DEVELOPMENT AND CONTROL OF STRENGTH ANISOTROPY AND CRYSTALLOGRAPHIC TEXTURE DURING EXTRUSION OF ALUMINUM 2195 AND 7075

A Dissertation
Presented to
The Academic Faculty

by

Judith M. Dickson

In Partial Fulfillment
of the Requirements for the Degree
Doctor of Philosophy in the
School of Materials Science and Engineering

Georgia Institute of Technology
August 2017

DEVELOPMENT AND CONTROL OF STRENGTH ANISOTROPY AND CRYSTALLOGRAPHIC TEXTURE DURING EXTRUSION OF ALUMINUM 2195 AND 7075

Approved by:

Dr. Thomas H. Sanders, Jr., Advisor
School of Materials Science and Engineering
Georgia Institute of Technology

Dr. Naresh N. Thadhani
School of Materials Science and Engineering
Georgia Institute of Technology

Dr. Hamid Garmestani
School of Materials Science and Engineering
Georgia Institute of Technology

Dr. Richard W. Neu
The George W. Woodruff School of Mechanical Engineering
Georgia Institute of Technology

Victor Dangerfield
Research and Development
Universal Alloy Corporation

Date Approved: May 2, 2017

ACKNOWLEDGEMENTS

I would like to first express my gratitude to my mom, Anne Keeven-Dickson, for teaching me the value of commitment and for supporting my endeavors regardless of success, failure, or broken bones. To my advisor, Dr. Tom Sanders, I also owe particular thanks for his support. He has allowed me the opportunity to pursue my doctoral research without sacrificing my pursuit of athletic aspirations. I am also grateful to him for facilitating my experience in France as a teaching assistant. I want to recognize and express my gratitude to Vic Dangerfield and Dr. Justin Lamb of the Universal Alloy Corporation in Canton, GA. They have always been willing to offer invaluable advice and guidance in addition to materials and financial support. I would like to express my appreciation to my other committee members, Dr. Naresh Thadhani, Dr. Hamid Garmestani, and Dr. Richard Neu, for their support, time, and advice throughout my years as a graduate student. I want to recognize and thank Dr. Yong-ho Sohn and Dr. Ashley Paz y Puente who challenged me to pursue a Ph.D.

I gratefully acknowledge the funding I received from the Department of Defense (DoD) through the National Defense Science & Engineering Graduate Fellowship (NDSEG) Program as well as the funding and internship opportunity I received from the Universal Alloy Corporation that made this dissertation possible. This work would not have been successful without the technical support of many people. Thank you to Dr. Thomas Dorin and Dr. Alireza Vahidgolpayegani of Deakin University in Australia for performing microscopy and mechanical testing. I also appreciate the hot torsion work performed by and the expertise of Dr. Kip Findley and Blake Whitley at the Colorado School of Mines in Golden, CO. I would like express my gratitude to Narendra Singh from Altair for his assistance with HyperXtrude, William "Bill" Krumme of Vista Metals in Adairsville, GA for working with me to supply material for this research, and Dr. Marat Latypov at Georgia Tech Lorraine for his advice on image analysis and his conversations regarding texture simulations.

At Georgia Tech in Atlanta, thanks to Todd Walters for training on the TEM. Special thanks to Ameer David Tavakoli for training on the XRD and for answering my late night and holiday text messages and phone calls for help when I inevitably ran into issues with the machine. I also want to thank Lauren O'Hara and Meghan Toler for their assistance with writing a Matlab script that saved me many hours of tedious work. To my office mates and pseudo-office mates, Dr. Justin Lamb, Dr. Ricky Whelchel, Dr. Peter Marshall, Dr. Rachel Muhlbauer, and Peter Chamberlain for their technical and many non-technical conversations and for their willingness to occasionally move me up notches, not just down. To my graduate school classmates, Stefany Holguin, Brian Doyle, Alex Bryant, and Dan Gordon, thank you for always being willing ears for problems and willing participants for celebrations.

Lastly, immeasurable gratitude is extended to my family and friends, particularly the rugby community, for supporting me on those days when I felt near my fracture point or after I had actually fractured bones. You are the alloying additions that ultimately give me strength and toughness. I appreciate my mom, dad, and Sarah and Chris Chandler for putting up with my ridiculous schedule. I am also indebted to the Atlanta Harlequins Women's Rugby Football Club. My teammates have always shown me that I am capable of far more than I imagined, both on the field as a player and off the field as a leader. In particular, to my teammate, colleague, and friend, Dr. Jordan Ciciliano, I owe a large sum of gratitude for her assistance editing this dissertation and for sanity saving afternoon coffee and gym breaks. Lastly, for being one of the most reasonable and understanding humans throughout my final days completing this dissertation, thank you to Meredith Whitten.

What do you call an aluminum alloy raised on a mountain?

Peak aged.

TABLE OF CONTENTS

LIST OF TABLES

LIST OF FIGURES

SUMMARY

Material development in the aerospace industry is driven by a need for low density materials with high strengths, fracture toughnesses, and good corrosion properties that are easy and affordable to manufacture. Aluminum alloys are one of the most commonly used materials, comprising nearly 80% of the weight of modern commercial aircraft. The addition of lithium to 2xxx-series, Al-Cu, alloys results in densities and properties competitive with composite materials. Through three generations of alloy development, the Al-Cu-Li alloy, Al 2195, was created for use as the external fuel tank on the space shuttle, Discovery. Al 2195 is a commercially relevant alloy that can be manufactured through the established thermo-mechanical methods of extrusion and rolling.

However, regions of low aspect ratio Al-Cu-Li extrusions have longitudinal strengths greater than regions of higher aspect ratios, a small difference between the longitudinal and transverse yield strengths, a small spread between the yield and ultimate tensile strength, and a low transverse ductility. These anisotropic mechanical properties are undesirable and typically not observed in non-lithium containing alloys. Some authors attribute the anisotropy to crystallographic texture development, others blame the preferential growth of the primary strengthening phase, and still others state a complex interaction between crystallographic texture and the second phase particles. Unfortunately, many of these studies were performed on complex extrusions profiles with no comparison to non-lithium containing alloys and they convolve the effects of aspect ratio, extrusion ratio, and transition regions. There also exist conflicting reports on how to control crystallographic texture development. This study offers a systematic investigation on the effects of extrusion aspect ratio and use of processing variables for control of strength anisotropy and crystallographic texture.

Simple rectangular sections with constant extrusion ratios of Al 2195 and Al 7075 were industrially extruded over a range of aspect ratios (AR) from AR2-AR15 to systematically study the effects of composition and aspect ratio on strength anisotropy, crystallographic texture, and microstructure. The AR2 and AR3 Al 2195 extrusions had more of the Copper texture component than either the Brass or S textures while the low AR Al 7075 samples had a typical plate-like texture with Brass in the highest amount and Copper in the lowest fraction. This increase in Copper texture was associated with poor mechanical properties in the T8 condition, but not in the T3 condition. The undesirable mechanical performance of low AR Al 2195 extrusions was attributed to the interaction of the second phase particles with the Copper texture. Methods of controlling the Copper texture, including processing temperatures and speeds, were investigated through a series of rolling studies.

The initial microstructure of Al 2195 was found to contain nearly 50% secondary phases. Variation in the starting microstructure can affect final properties and microstructures. Plates were rolled at 343°C, 454°C, and 515°C with dwell times before and between rolling passes of 1, 4, 8, and 24 hours. At 343°C and 454°C, second phase particles varied in fraction and morphology with processing conditions and the Copper texture decreased with time before and between rolling passes. The lowest fractions of the Copper texture, and the most plate-like macrotextures, were found in the plates rolled at 515°C, which had less than 1% second phase particles. Based on these results, it was concluded that higher extrusion temperatures and slower ram speeds might reduce the Copper texture and resulting strength anisotropy. However, experimentally studying the effects of press parameters on final properties and microstructure is difficult, particularly at the industrial scale, due to imperfect press repeatability. Multiple parameters often vary between extrusions such that effects of a single parameter cannot be isolated. For this reason, and its cost-effectiveness, finite element modeling (FEM) is an attractive option for investigation of the effect of press parameters on final strength anisotropy since individual parameters can be systematically varied within a computational framework.

The commercially available FEM software, HyperXtrude, was used to accurately predict load curves for the Al 2195 and Al 7075 extrusions used in this study. Flow stress data

from literature was used to model the high temperature deformation behavior of Al 7075. Although high temperature torsion tests were performed to generate flow stress data for Al 2195, a numerical fit to the hyperbolic sine law using HyperXtrude's Relative Extrudability Approach most accurately predicted the load curves and was used for further simulations. Comparison of simulated and experimental strain fields indicated accurate prediction near edges but under-prediction of strain near the center of the billet. HyperXtrude was not able to predict the difference in yield strength between low and high aspect ratio extrusions, and the Hall-Petch relationship used by the software is incapable of predicting anisotropic properties since it fundamentally assumes equiaxed grains. The Barlat Method for prediction of anisotropic yield strengths was recommended for integration into the HyperXtrude solver so that computational parametric studies on the effects of extrusion variables on final strength anisotropy can be performed.

CHAPTER 1

INTRODUCTION

Research and development in the aerospace industry is driven by the need for improved properties while continually decreasing weight. Aluminum alloys played a vital role in the success of the Wright Brother's historic first flight in 1903 when a precipitation hardened aluminum alloy flew along as the crankcase [1]. Since 1903, aluminum has been one of the leading materials for aerospace applications, comprising approximately 80 weight percent of most modern aircraft [2]. Aluminum's affordability, high formability, low working temperatures, and recyclability make it both an economical and environmentally friendly choice. With the introduction of composites, attention has been focused on lithium containing aluminum alloys which offer high properties with lower densities than conventional high strength aluminum alloys. For every 1 wt. % lithium added, the density is decreased 3% and the stiffness increased 5-6% [3].

The addition of varying amounts of Li to the Al-Cu system can result in a different precipitates, namely δ' (Al_3Li), θ' (Al_2Cu), T_1 (Al_2CuLi), and T_2 (Al_6CuLi_3), the formation of which can have significant impacts on final properties. The first two generations of Al-Li alloys contained 2 wt. % or more of Li and had very low densities. However, these alloys suffered from high anisotropy, low toughness, and were difficult to manufacture due to the presence of the δ' and T_2 phases [4, 5]. The third generation Al-Cu-Li alloy, Al 2195, contains 0.8-1.2 wt.% Li, relies on the T_1 phase for strengthening, offers low density, and has displayed yield strengths up to 700 MPa [6, 7].

Despite lowered lithium contents and improved properties, third-generation lithium containing alloys are prone to develop what some authors have termed "chunkiness" or the "Al-Li fiber texture problem" during thermo-mechanical processing [8, 9]. This problem is typically seen in low aspect ratio regions of lithium containing extrusions. Low aspect ratio regions display higher longitudinal yield strengths, lower transverse yield strengths,

lower transverse ductility, and a smaller spread between the longitudinal yield and ultimate tensile strengths than their high aspect ratio and non-lithium containing counterparts. Typically, this problem is blamed on the development of preferred orientations (also referred to as crystallographic texture development) and/or the presence of the T_1 phase which has a {111} habit plane and grows as a thin plate. Many of the studies that reported "chunkiness" used complex extrusion profiles. In these complex sections, transition zones were labeled as low aspect ratio and regions of varying aspect ratio also has different local extrusion ratios. While most authors link the crystallographic texture and the directionality of the T_1 phase to the poor mechanical performance, few investigations offer any comparison to the texture and phase development in non-lithium containing alloys. A systematic investigation at the industrial scale on the effects of aspect ratio on strength, microstructure, and crystallographic texture development for both a lithium-containing alloy and a non-lithium containing alloy has not been performed.

In this work, Al 2195 and a non-lithium containing counterpart, Al 7075, were industrially extruded over a range of aspect ratios from 2-15 all while maintaining a constant extrusion ratio. All other extrusion parameters within an alloy system were held relatively constant (i.e. initial billet temperature, container temperature, die temperature, ram speed, etc.) This allowed for an isolated study on the effects of extrusion aspect ratio. Using optical, scanning electron (SEM), and transmission electron microscopy (TEM), the microstructural evolution of these extrusions was characterized. Nano-hardness measurements and tensile tests were conducted to measure strength in the longitudinal and transverse directions in the T3, underaged, and T8 conditions. Electron backscatter diffraction (EBSD), x-ray diffraction (XRD) techniques, and the code, MTEX, were used to characterize and quantify the associated crystallographic texture development.

It is well documented that crystallographic texture results in anisotropy in many metallic and ceramic systems. However, controlling the development of texture before, during, and after thermo-mechanical processing is challenging. Methods for control post-processing, including variation of heat treatments, are often unsuccessful. Control of crystallographic texture before and during thermo-mechanical processing of Al 2195 was investigated via a

series of systematic rolling studies. Plates were rolled at 343°C, 454°C, and 515°C with dwell times before and between rolling passes of 1, 4, 8, and 24 hours. The microstructural and crystallographic developments with temperature and dwell time were characterized via optical, SEM, TEM, and XRD.

Another method of controlling crystallographic texture is variation of the extrusion press parameters such as billet temperature and ram speed. Despite sophisticated feedback control systems, these variables are nearly impossible to systematically vary. Particularly at the industrial scale, the number of variables and imperfect press repeatability often result in slight variations of multiple variables leaving the true cause of final microstructures and properties unknown. These variables, however, can be systematically varied and controlled in a computational framework. While several commercially available programs for finite element modeling (FEM) of aluminum extrusions exist, the literature is absent of Al-Cu-Li alloy simulations, and the constitutive parameters necessary for simulating the high temperature deformation behavior of Al 2195 have not been reported. The ability to use computational modeling to simulate the effects of aspect ratio on mechanical strength has also not been addressed in the literature.

The commercially available code, HyperXtrude, was used to simulate the Al 2195 and Al 7075 experimental extrusions. High temperature flow stress data available in the literature and the values for the hyperbolic sine constitutive equation available from the HyperXtrude database were used to predict the load curves for Al 7075. Since no flow stress data or constitutive parameters existed in the literature to describe the high temperature deformation of Al 2195, hot torsion testing was performed at temperatures and strain rates commonly experienced during manufacturing. Additionally, HyperXtrude's numerical Relative Extrudability Approach was used to find parameters to fit the hyperbolic sine law. The sets of data that most accurately predicted the load curves for Al 2195 and Al 7075 were used for further simulations. Comparisons of strain fields, grain sizes, and yield strengths between experimental data and HyperXtrude predictions were made and critically assessed. Recommendations were made for modeling and computationally predicting anisotropic mechanical properties.

The objectives of this study were to:

1. Characterize the effect of extrusion aspect ratio on strength, crystallographic texture, and microstructure in Al 2195 and Al 7075.

2. Investigate methods of controlling texture development during thermo-mechanical processing.

3. Evaluate the effectiveness of the FEM software, HyperXtrude, for use in computational investigations of aluminum extrusions.

CHAPTER 2

BACKGROUND

For the purpose of studying thermo-mechanical processing of Al 2195 and Al 7075, it is important to have a fundamental knowledge of processing methods, phase formation in the alloys, development of crystallographic texture and anisotropy, and previous attempts at computational modeling. These topics are addressed in the following sections.

2.1 Phase Formation in Al 2195

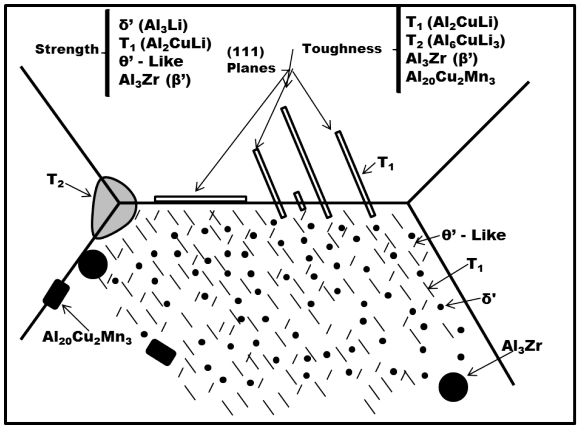

Figure 1: Schematic of precipitates and dispersoids that contribute to strength and toughness in Al 2099 and 2199. Adapted from Guimmarra et al. [4]. (Missing S′ (Al_2CuMg) and the Al_6Mn dispersoid.)

The development of modern, third generation, Al-Li alloys began with the need for a weldable aluminum alloy for aerospace launch vehicles and cryogenic tanks. Lockheed Martin modified Al 2219 with Ag and Li to create Weldalite for this purpose [6, 10]. Further research led to Al 2195 whose composition is given in Table 1 [7]. Copper and lithium form strengthening precipitates. Magnesium and silver were added to act as nucleating agents for the preferred precipitate (T_1). Manganese and zirconium form dispersoids which aid in preventing recrystallization [6]. Zinc stays in solid solution and helps to lower the electrochemical potential between the grain boundary and the matrix possibly by stimulating the

desaturation of Cu from the matrix [11–13]. Iron and silicon contents were lowered as much as economically possible in modern Al-Li alloys because the formation of $Al_{12}(FeMn)_3Si$ and Al_7Cu_2Fe lead to poor ductility and recrystallization [6]. The trace amount of titanium present in Al 2195 acts as a grain refiner and typically takes the form of the TiO_2 impurity [14, 15]. Titanium can also form tetragonal Al_3Ti which has a solubility range of 36.5 to 37.5% Ti [14, 16].

Lithium containing alloys incorporate precipitation sequences from the Al-Li, Al-Cu, Al-Cu-Li, and Al-Cu-Mg systems. Alloys with approximately 1 wt.% Li (such as Al 2195 and Al 2198) are typically dominated by the T_1 (Al_2CuLi) and θ' phases. Figure 1 shows the complexity of the phases which can be seen in Li containing alloys. This schematic was created specifically to describe Al 2099 and 2199, but is generally applicable to 2xxx series Li alloys [4]. Specifically in Al 2195, intermetallic particles, Guinier-Preston (GP) zones, θ'', θ', θ, δ', T_1, T_B, T_2, and S' phases, as well as precipitate free zones (PFZs) have been identified [17–21]. The presence of secondary phases during thermo-mechanical processing can have a significant effect on the mechanical response of a material; therefore, each of the phases possible in Al 2195 will be discussed in greater detail in the remainder of this section.

2.1.1 T_1, T_2, and T_B Precipitates

One of the primary strengthening phases in Al-Li alloys is the T_1 (Al_2CuLi) precipitate. It is prominent in Al 2195 microstructures [18, 21]. T_1 has a hexagonal crystal structure with a c/a ratio of 1.885 and forms as hexagonal shaped platelets on the {111} set of habit planes [10, 22–24]. Using atom probe tomography and transmission electron microscopy, T_1 was studied in T8 temper Al 2195 and found to deviate from its stoichiometry due to Mg enrichment [21]. This suggests that there may be a non-equilibrium version of T_1 [21]. The T_2 phase, which does not have a habit plane, has also been observed in alloys similar to Al 2195 [4, 23, 25]. Hardy and Silcock [23] determined the composition of T_2 to be Al_6CuLi_3; however, they were unable to identify the structure. Further research has been inconclusive as to whether T_2 has a five-fold icosohedral symmetry or if this observed symmetry is the

Table 1: Registered compositions for Li containing alloys and their non-lithium counterparts [7].

	Registered Composition (wt. %)											
Alloy	**Si**	**Fe**	**Cu**	**Mn**	**Mg**	**Cr**	**Zn**	**Ti**	**Ag**	**Li**	**Zr**	**V**
2219	0.20	0.30	5.8-6.8	0.2-0.4	0.02	-	0.10	0.02-0.1	-	-	0.1-.25	0.05-0.15
7075	0.40	0.50	1.2-2.0	0.30	2.1-2.9	0.18-0.28	5.1-6.1	0.20	-	-	-	-
2195	0.12	0.15	3.7-4.3	0.25	0.25-0.8	-	0.25	0.10	0.25-0.6	0.8-1.2	0.08-0.16	-
2090	0.10	0.12	2.4-3.0	0.05	0.25	0.05	0.10	0.15	-	1.9-2.6	0.08-0.15	-
2198	0.08	0.10	2.9-3.5	0.50	0.25-0.8	0.05	0.35	0.10	0.10-0.50	0.8-1.1	0.04-0.18	-
8090	0.20	0.30	1.0-1.6	0.10	0.6-1.3	0.10	0.25	0.10	-	2.2-2.7	0.04-0.16	-

result of double diffraction caused by very fine (5 nm) crystallites comprising the particles [26, 27]. Less commonly observed or studied in literature is the T_B phase ($Al_{7.5}Cu_4Li$) which has a {100} habit plane [25, 28].

T_1 is known to precipitate on dislocations and subgrain boundaries; therefore, cold working prior to aging reduces the aspect ratio and size of T_1 while increasing the overall density [10, 29]. One study suggested that the additions of Mg and Ag aided in the creation of monolayer GP zones which then acted as nucleation sites for T_1 [29]. After thermo-mechanical processing, solution heat treatment, and often stretching, T_1 nucleation begins around 250°C and dissolution ends around 500°C [30]. A fine dispersion is maintained for long aging times as T_1 is resistant to coarsening [31]. Particles as thin as 1-4 atomic layers and less than 100-200 nm long were observed in Al 2198 [30, 32]. It has been suggested that T_2 nucleates on Al-Li oxide particles, clusters of impurities, Al_7Cu_2Fe particles, clusters of Al_3Zr dispersoids, and high angle grain boundaries; it grows to form 1200-2500 nm particles [26, 33].

In studies on aged Al-Cu-Li alloys, T_1 plates less than 2 nm thick were sheared by dislocations; the critical size for transition from shearing to by-passing was unclear [31, 34]. More macroscopically homogeneous deformation (evidenced by a lack of shear bands) associated with the presence of T_1 may be attributed to the shearing mechanism or the build-up of internal stresses by Orowan looping or dislocation tangles [31, 34, 35]. T_1 may also be prone to octahedral slip [25]. Models based on the shearing mechanism were able to accurately predict the yield strength evolution for particles with diameters between 20-55 nm, but overestimated the strength for highly over-aged samples [36]. T_2 is associated with excellent formability in Al 2090-O temper sheet but reduced fracture toughness [26, 37]. T_1 and T_2 both result in the formation of precipitate-free zones (PFZs) which can have a negative impact on properties as discussed in Section 2.1.5 [33, 35].

2.1.2 δ and δ' Precipitates

In the binary Al-Li system, as well as alloys containing more than 2 wt.% Li, the δ' and δ phases dominate the precipitation process as expected based on the binary phase diagram

[38, 39]. In alloys containing less then 2 wt.% Li, such as Al 2195, δ' has also been observed [17, 18, 20]. The metastable δ' (Al_3Li) phase has an L1 superlattice structure and is coherent with the matrix; the equilibrium, stable δ (AlLi) phase has a B32 crystal structure and is incoherent with the matrix [39–42].

The equilibrium, δ phase has been shown to nucleate on grain boundaries, while the coherent and metastable δ' phase nucleates homogeneously within the matrix as well as on existing Al_3Zr (β') dispersoids to form a composite precipitate [33, 43]. As expected with homogeneous nucleation, the δ' phase grows as spheres and maintains coherency up to approximately 50 nm [33]. Discontinuous precipitation of δ' was observed by Williams and Edington [44]. Coarsening of the grain boundary precipitates via dissolution of δ' near the grain boundary leads to a precipitate-free zone [42, 43]. The addition of Zr increases the precipitation kinetics of δ' [45]. Palmer, Lewis, and Crooks [46] found that the size of δ' increased from 10-30 nm in the under-aged condition, 30-50 nm in the peak-aged condition, and grew up to 200 nm in the over-aged condition (Al-3Li-2Cu-0.2Zr alloy).

The δ' phase is also considered to be a strengthening precipitate; however, microstructures with primarily δ' exhibit lower strain hardening and higher sensitivity to strain localization [31]. This was attributed to dislocations shearing δ' precipitates [35].

2.1.3 θ, θ', and, θ'' Precipitates

The θ' (Al_2Cu) phase is another strengthening phase in Al-Cu-Li alloys. It is widely accepted that the precipitation sequence follows: $\alpha_{ssss} \rightarrow$ GP zones $\rightarrow \theta'' \rightarrow \theta' \rightarrow \theta$ where α_{ssss} is aluminum supersaturated solid solution [47, 48]. GP zones are two-dimensional copper-rich disk shaped regions in the matrix oriented parallel to the {100} planes [14, 47]. One of the intermediate phases, θ'', is sometimes referred to as GP-II zones and is described as a three dimensional (few atomic layers thick) GP-I zone [14]. The other intermediate phase, θ', forms platelets parallel to the {100} planes because it nucleates on Guinier-Preston (GP) zones [14, 33]. Due to its constrained coherency with the {100} Al planes, the metastable θ' has a tetragonally distorted cubic flourite structure [49]. Quist and Narayanan [33] stated that formation of θ' in lithium containing alloys was only observed when the Cu:Li ratio was

above 1:3; they did not state whether this ratio was atomic or weight %. However, Palmer, Lewis, and Crooks [46] reported θ' in an Al-3Li-2Cu-0.2Zr alloy which agrees with a weight % ratio grater than 1:3. The size of θ' was shown to remain 1 μm long and 10-15 nm thick in the peak-aged and over-aged conditions [46]. The equilibrium phase, θ, is tetragonal and incoherent with the matrix [49]. The θ phase is associated with a decrease in hardness. Thus, the formation of the equilibrium phase is considered undesirable [49]. Occasionally, the formation of a modified θ' phase, referred to as Ω (Al_2Cu with Mg and Ag at the boundary), is observed in Ag containing alloys [10, 50]. Its structure has been described as monoclinic, hexagonal, orthorhombic, and tetragonal having a coherent boundary with the matrix [10].

2.1.4 S and S′ Phase

The S′ (Al_2CuMg) phase is another strengthening precipitate observed in Al-Cu-Li alloys. The S phase is stable Al_2CuMg with a face centered orthorhombic structure; the structure of S′ is debated to either be the same as S or a strained face centered orthorhombic structure [51]. The S′ phase nucleates heterogeneously as rods or needles aligned with the $\langle 100 \rangle$ direction [33, 35]. S′ is coherent on the $\{021\}$ matrix planes [14]. Coarsening or overaging of the S′ phase results in the formation of the incoherent, S phase (Al_2CuMg) as indicated by the precipitation sequences: $\alpha_{ssss} \rightarrow$ GP zones $\rightarrow$ S′ $\rightarrow$ S [14] and $\alpha_{ssss} \rightarrow$ GP zones $\rightarrow$ S″ $\rightarrow$ S′ $\rightarrow$ S [52].

Grain boundary precipitation of the incoherent S phase was observed by Crooks [35]. The growth of S on low- and high-angle grain boundaries did not result in the formation of precipitate free zones (see Section 2.1.5) [33]. Homogeneous nucleation of S phase was reported for critical combinations of vacancy concentrations and Cu/Mg supersaturation [53].

The S phase reduces the propensity for slip coplanarity and improves toughness [54]. The S phase reportedly homogenizes slip (as expected for a non-coherent phase which dislocations would bypass) [35, 37, 54]. Dislocation bypassing, however, has not been observed experimentally. Dislocation tangles have been associated with a fine dispersion of both the

S′ and T_1 phases [35]. The S′ phase was shown to reduce the Portevin-le Chatelier effect (serrated yielding) in an Al-Li-Cu-Mg-Zr alloy by reducing the amount of Cu and Mg in solution [55]. Overall, the distinction between S, S′, and S″ is not consistent throughout literature, the existence of the S″ phase is debated, and the structure of the GP zones remains unclear [51].

2.1.5 Precipitate Free Zones

Precipitate free zones (PFZs) are solute denuded zones typically found near grain boundaries. Along with a decrease in fracture toughness and corrosion resistance, large PFZs can be responsible for a lack of ductility in Al-Cu-Li alloys [33, 35]. In an Al-3Li-2Cu-0.2Zr alloy, PFZs were reported to have widths of 100-150 nm in the under-aged condition and 200 nm in peak-aged samples [46]. Increasing Li content increases the growth kinetics of the PFZ [42].

2.2 Strengthening Precipitates in Al 7075

The primary strengthening phases in the Al-Zn-Mg-Cu alloy, Al 7075, are GP zones and η'. The η' phase evolves from coherent, spherical GP zones [14]. These GP zones reach a maximum diameter of approximately 1.2 nm after natural aging, and diameters around 2-3.5 nm after artificial aging [14]. η' has a hexagonal crystal structure, a c/a ratio of 2.83, and the basal planes are partially coherent with the {111} matrix planes while the interface between the matrix and the c direction of the precipitate is incoherent [14, 56]. η' forms as thin plates on the $\{111\}_{Al}$ plane [57]. Li et al. [58] observed η' using high resolution transmission electron microscopy and reported a very fine dispersion of η' precipitates with a diameter around 5 nm. The highest strengths are obtained with a microstructure consisting of GP zones and some η' [14, 56]. The non-equilibrium, η' can transform into the equilibrium intermetallic η ($MgZn_2$) phase [14]. Equilibrium η also has a hexagonal (C14) crystal structure and forms coarse plates on multiple habit planes at aging temperatures below 190°C [56, 57].

Alternatively, a non-equilibrium T′ phase can form from GP zones which transform into the equilibrium intermetallic T ($Mg_3Zn_3Al_2$ also reported as $(Al,Zn)_{49}Mg_{32}$) phase [14, 59].

Equilibrium T phase has a cubic structure and forms with aging temperature above 190°C [56]. Formation of the T phase is typically considered detrimental as it leads to reduced corrosion resistance and fracture toughness [60]. At high aging temperatures (300-400°C), the formation of the S phase, as discussed in Section 2.1.4, was observed by Cogan et al. [61] but was not observed by Wert [62] in Al 7075.

2.3 Recovery and Recrystallization

Recrystallization and recovery can occur during deformation (dynamic) or during solution heat treatment (static). Recrystallization and recovery are processes driven by the thermodynamic instability of dislocations present in the deformed subgrain structure. While these processes are not phase changes, they are structural transformations that result in the annihilation of dislocations and low angle grain boundaries. Just as the presence of secondary phases can play a role in the mechanical response of an alloy, so too, can recovered and recrystallized grains affect the mechanical behavior of a material.

Recovery is generally defined as any change in the microstructure driven by stored energy that does not involve the movement of high angle grain boundaries [63]. Dynamic recovery is often a softening mechanism during deformation of aluminum alloys. Thus, the strain hardening or softening behavior depends on the balance between creation and annihilation of dislocations via recovery.

Recrystallization is the formation of a new grain structure in a deformed material by the formation and migration of high angle grain boundaries. Dynamic recrystallization occurs once a critical strain is reached and results in a decrease in the flow stress [64]. Static recrystallization is common and often results in a layer of completely recrystallized grains at the edge of a plate or extrusion [65]. For aerospace applications, recrystallization is typically undesirable because fracture toughness decreases with decreasing substructure, and subsequent grain growth occurring after recrystallization reduces strength. However, because recrystallization reverses the formation of texture, it is sometimes desirable to have a final microstructure with fine recrystallized grains [66].

2.4 Presence of Second Phase Particles

During deformation, secondary phase particles can be thought of as either deforming with the matrix or retaining their original shape. Deformation is determined by the lattice mismatch, modulus difference, Peirls-force mismatch, and antiphase boundary energy [67]. The interaction of second phase particles with the surrounding matrix determines the amount of shear strain a particle is subject to, which in turn affects the deformation mechanism, as shown in Figure 2 [25, 63].

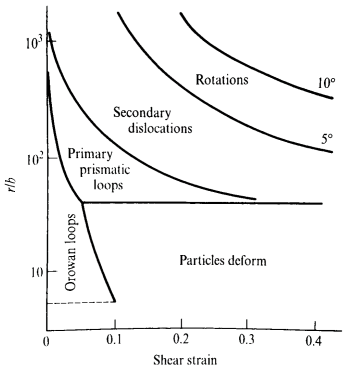

Figure 2: Deformation mechanism map by Martin [63] for a copper matrix containing silica particles.

For particles that do not deform with the matrix, dislocations either shear or bypass (also referred to as looping) the obstacle. Shearing or cutting of a particle reduces its effective size and can result in localization, while bypassing effectively enlarges the obstacle [37]. Shear/strain localizations and shear bands result in a drop on the stress-strain diagram [68]. The deformation mechanisms around second phase particles were related to crystallographic texture development by Lucke, Engler, and Hirsch [69, 70] (see Section 2.6 for an overview of crystallographic texture). Shearable particles lead to planar slip, shear band formation, and strong Goss and Brass orientations [69, 70]. An increase in the number of shearable particles results in increased shear band formation and a reduction in texture.

Humphreys and colleagues [71–75] studied the behavior of non-shearable second phase particles that were bypassed during plastic deformation because of a large mismatch between the matrix modulus and particle modulus. Much of their work focused on a transition in the mechanical response of a material at a critical strain rate, which is a function of strain

rate, temperature, and particles size [73]. For small, non-shearable particles, the strain was relaxed via prismatic loops; whereas, for larger particles and larger strains, local lattice rotations were observed [71]. Similarly, Engler et al. found that non-shearable particles caused dislocation pile-ups and thus deformation zones around the particles [76]. For a large number of non-shearable particles these deformation zones generally led to a decrease in rolling texture, but for an intermediate number of particles it led to a more rolling-type crystallographic texture [76]. In order to understand mechanisms for the development of anisotropy and crystallographic texture in Al 2195 and Al 7075, it is critical to know about the phases present and how they behave during deformation.

2.4.1 Intermetallic Particles: Equilibrium, Dispersoids, and Constituent Phases

The equilibrium phases, T_1, δ, θ, S, η, and T (as discussed in more detail in Sections 2.1-2.2) can be present in 2xxx and 7xxx series alloys after homogenization and air-cooling. The volume fraction and structure of these phases present during deformation can therefore affect the deformation mechanisms and final microstructure. In Al 2195, equilibrium T_1 (Al_2CuLi) is often present in the homogenized billet. It is hexagonal, and as with the metastable form, dissolution begins above 300°C and ends around 500°C [10, 22–24, 30] The equilibrium, stable δ (AlLi) phase has been shown to nucleate on grain boundaries, has a B32 crystal structure, and is incoherent with the matrix [39–42]. The equilibrium phase, θ (Al_2Cu), is tetragonal, incoherent with the matrix, and associated with a decrease in hardness [49]. Based on the binary phase diagram, θ in Al 2195 would begin to dissolve around 450-500°C (Figure 3) [77]. The S phase is stable Al_2CuMg with a face centered orthorhombic structure that is incoherent with the aluminum matrix [51, 52]. S phase is also present in many 7xxx-series alloys. In 7xxx-series alloys, the non-equilibrium, η' can transform into the equilibrium intermetallic η ($MgZn_2$) phase [14]. Equilibrium η also has a hexagonal (C14) crystal structure and forms coarse plates on multiple habit planes [56, 57]. The equilibrium intermetallic T ($Mg_3Zn_3Al_2$) phase can also form, and it has a cubic structure [14, 56, 59].

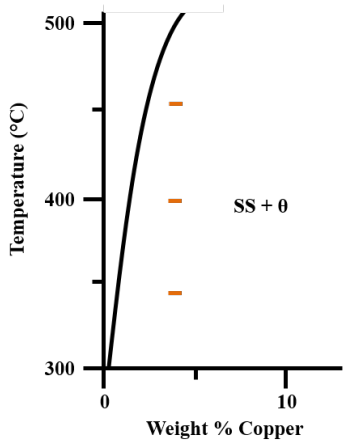

Figure 3: Aluminum-Copper binary phase diagram where the dashes indicate the composition of Al 2195. Adapted from the ASM Binary Phase Diagram [77].

Dispersoids are low solubility, intermetallic particles that primarily precipitate during homogenization and do not dissolve during solution heat treatment. Al 2195 contains a small amount of Zr and Mn that form dispersoids. Both help to reduce recrystallization, but have opposite effects regarding strain localizations.

Zirconium results in the formation of Al_3Zr (β') [4]. Al_3Zr has reported diameters of 20 nm in an Al-Li-Zr alloy and 23.8-58.7 nm in 7xxx alloys containing similar levels of Zr [45, 78]. This coherent dispersoid helps to prevent static recovery and recrystallization, as well as acts as a preferential site for nucleation of the δ' phase [33, 40, 45]. Higher Zr content leads to strain localization and sharper texture development, likely because Zr-rich dispersoids are sheared by dislocations [6, 37].

To help alleviate the strain localization and increased texture associated with high Zr content, Mn was added. Manganese can result in the formation of $Al_{20}Cu_2Mn_3$ and Al_6Mn [6]. In Al-Cu-Li alloys, $Al_{20}Cu_2Mn_3$ is incoherent with the matrix, works to increase fatigue and fracture toughness, and helps to refine grain size during solidification [48, 79]. Dislocation build up has been observed surrounding $Al_{20}Cu_2Mn_3$ particles in friction stir welds of Al 2199 [80]. The incoherent, rod-like Al_6Mn dispersoid forms approximately 200 nm particles in solution heat treated Al-Mg-Li alloys and Al-Li-Mn alloys, but does not seem to be favorable in Al-Cu-Li [48, 67]. Due to their incoherent nature, Mn dispersoids are

often looped or bypassed by dislocations and therefore disperse slip [37]. This dispersion of slip or homogenization of strain aids in reducing texture development.

Intermetallic particles that range from 1,000-10,000 nm in size; are rich in Fe, Si, and Cu; and are formed during casting are referred to as constituent phases. The Fe and Si contents are minimized in third generation Al-Li alloys. However, the formation of these phases cannot be disregarded. Crooks studied an Al-Cu-Li-Mg-Zr alloy and observed the Al_7Cu_2Fe and Mg_2Si phases [19, 35]. In other Al-Li alloys, the $Al_{12}(FeMn)_3Si$ phase was also observed [81].

2.5 Thermo-Mechanical Processing

Wrought aluminum alloys require further processing after casting in order to obtain their final shape and properties. This processing chain generally consists of homogenization, thermo-mechanical working, and subsequent heat treatment. Homogenization is performed after casting to reduce solute segregation, remove eutectics, and precipitate dispersoids. Thermo-mechanical processing includes both rolling and extrusion. In the case of rolling, the three orthogonal directions in the rolled samples are defined as the rolling (RD), transverse (TD), and short normal (ND) directions. The designations of longitudinal (L), longitudinal transverse (TT), and short transverse (ST) are used in the extrusion industry. Figure 4 shows these orientations. Both rolling and extrusion work harden the material as well as introduce preferred crystallographic and morphological orientations that result in anisotropic properties. The following sections detail thermo-mechanical processing.

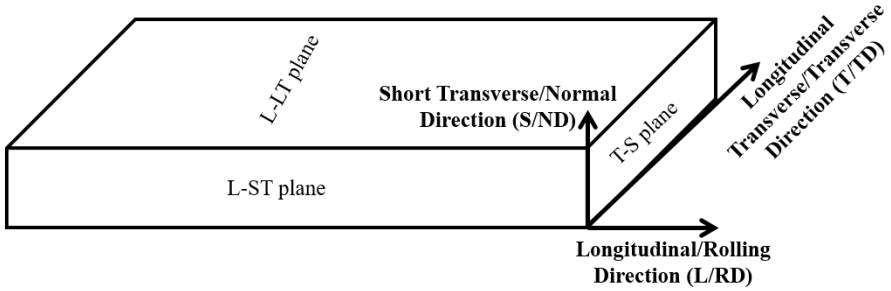

Figure 4: Rolling and extrusion directions and planes.

2.5.1 Rolling

Rolling is used for the production of plate or sheet metal. Large ingot blocks are passed through two (or a system of many) cylindrical rollers to a set reduction. Multiple reductions are performed until the final thickness is achieved. The overall reduction is represented as R_r as given in Equation 1 where h is the initial height (thickness in the normal direction) and h_f is the final height. This number is often multiplied by 100 and reported as a reduction percentage.

$$R_r = h - h_f \tag{1}$$

Strain in the material during each rolling pass can be approximated as plane strain ($d\epsilon_2 = 0$) [82]. A method for calculating mean strain and strain rate was proposed by Sellars and Whiteman [64]. The von Mises equivalent strain (ϵ) during a single pass is represented using the original thickness of the plate (h_o) and the final thickness for the i^{th} step (h_i) as given in Equation 2 [64].

$$\epsilon = 1.155 ln \frac{h_o}{h_i} \tag{2}$$

The strain rate is then calculated using the peripheral velocity of the rolls (V_{roll}) and the radius of the roll (r) [64].

$$\dot{\epsilon} = \frac{V_{roll}\epsilon}{\sqrt{r(h_o - h_i)}} \tag{3}$$

2.5.2 Extrusion

Extrusion is a widely used method for production of net-shape or near net-shape parts for aerospace and other industries. The aerospace industry is the most common user of high strength 2xxx and 7xxx series aluminum extruded alloys. There are two main types of extrusion presses, direct and indirect, as shown in Figure 6, which produce different types of flow (Figure 7) [83]. For both methods, extrusion parameters include: ram speed, initial billet temperature, pre-heat time, container temperature, and profile geometry (Figure 5). Typical working temperatures for aluminum alloys are between 300 and 600°C [84].

Calculating strain rate ($\dot{\epsilon}$) for the extrusion process can be accomplished using several different methods. Two of the more common methods are the Feltham (Equation 4) and

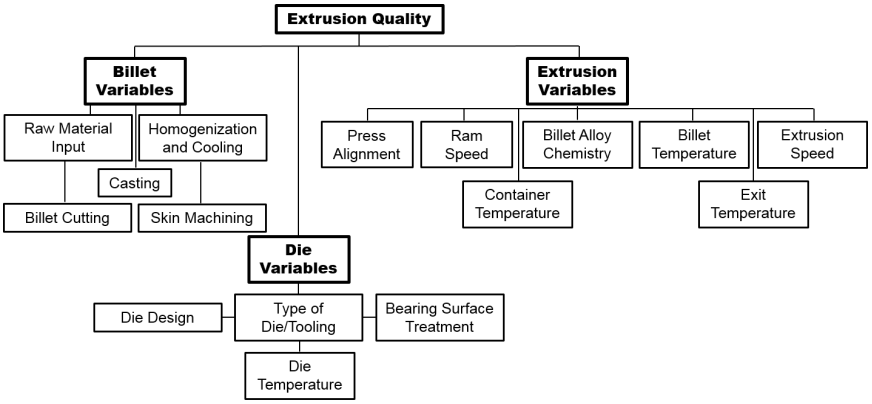

Figure 5: Flow chart demonstrating the multi-variable nature of the extrusion process adapted from [85].

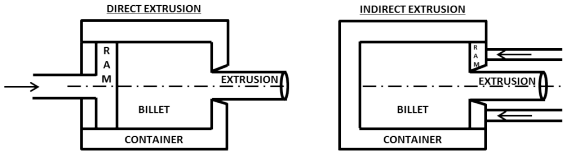

Figure 6: Schematics of direct extrusion and indirect extrusion.

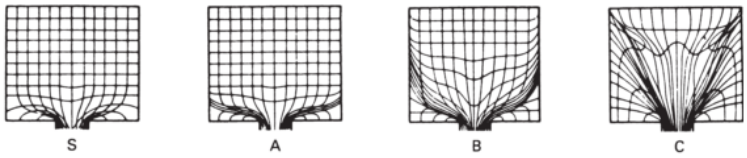

Figure 7: Flow patterns that develop during direct (type B pattern) extrusion and indirect (type A pattern) extrusion from Laue and Stenger [83].

Modified Feltham (Equation 5) approximations [86, 87]. The Feltham approximation is based on the steady state assumption, and extrusion pressures calculated via this assumption can be expected to fall below average [86–88].

$$\dot{\epsilon}_{Feltham} = \frac{6D_B^2 V_{ram} ln(ER)}{D_B^3 - D_E^3} \tag{4}$$

$$\dot{\epsilon}_{ModifiedFeltham} = \frac{6V_{ram} D_B^3 (0.171 + 1.86 lnER) tan(38.7 + 6.9 lnER)}{D_B^2 - D_E^2} \tag{5}$$

In these equations, ER is the extrusion ratio given by $ER = D_B^2/D_E^2$, D_B is the diameter of the billet, D_E is the equivalent diameter of the extrusion (diameter to achieve the same extrusion cross sectional area), and V_{ram} is the ram speed. The coefficients reported for Equation 5 vary in the literature [86, 89]. A modified extrusion ratio (ER$'$) was suggested

to account for the difference in the periphery of the actual extrusion cross section (P_{actual}) versus the periphery of a rod of equivalent cross sectional area ($P_{equivalent}$) as given in Equation 6 [90]. This is one method of accounting for the effects of profile shape and frictional forces.

$$ER' = ER\sqrt{\frac{P_{actual}}{P_{equivalent}}} \tag{6}$$

Estimation of the strain rate can be circumvented by considering that the peak pressure during an extrusion run represents the energy required to initiate plastic deformation. Since peak pressure incorporates a material's thermo-mechanical deformation response, it can be considered as a validation tool for modeling the extrusion process. For the past 40 years, Sheppard and colleagues [86] have done considerable research investigating the extrusion process, both experimentally and via computer simulations. Sheppard suggested Equation 7 to relate peak pressure (p) to the Zener-Hollomon parameter (Z) where a, b, and c are fitting parameters and α, n, and A are the same as Equation 9 [91]. The Zener-Hollomon parameter, discussed more in Section 2.5.3, is a function of strain rate and temperature, both of which affect dislocation mobility [92]. Based on fitting Equation 7 to data for indirect and direct extrusion of Al 7075, Sheppard suggested that the sign of the a parameter may be related to the amount of solute in solution as well as the friction conditions [91].

$$p = \frac{1}{\alpha n}[a + blnER + cln(Z/A)] \tag{7}$$

2.5.3 Constitutive Equation

Modeling of thermo-mechanical processes often utilizes a temperature compensated strain rate, also referred to as the Zener-Hollomon (Z) parameter, to make correlations between the processing parameters and resulting microstructure and properties. The Zener-Hollomon parameter helps to account for the increase in flow stress with increasing strain rate and decreasing temperature. Equation 8 is one method of calculating Z where $\dot{\epsilon}$ is the strain rate, Q is the activation energy for deformation, R is the universal gas constant, and T is the absolute temperature.

$$Z = \dot{\epsilon}exp(\frac{Q}{RT}) \tag{8}$$

There is also a constitutive relationship for the calculation of Z known as the hyperbolic sine law, or Sellars-Tegart model [93]. In Equation 9, σ is the flow stress, while the stress multiplier (α), stress exponent (n), and reciprocal strain factor (A) are all coefficients which can be obtained via regression analysis of tension, compression, or torsion test data [86].

$$Z = A[sinh(\alpha\sigma)]^n \tag{9}$$

Methods of calculating $\dot{\epsilon}$ for rolling and extrusion are discussed in Sections 2.5.1 and 2.5.2. Typically, a mean value is used since strain rate varies not only along the cross section, but also along the length of rolled and extruded products. Similarly, temperature during rolling and extrusion varies along the length of the ingot/billet and along the length of the final product. Often, the initial billet temperature is used in Equation 8. Changing the initial microstructure is also equivalent to changing the material constants. Thus, if secondary phases nucleate and grow prior to, or during, deformation, the activation energy (and corresponding α, n, and A) would also need to be adjusted.

2.6 Crystallographic Texture

Crystallographic orientations describe how the atomic planes in a crystal are positioned relative to a fixed frame of reference. In polycrystalline materials, the development of preferred crystallographic orientations during processing results in what is referred to as crystallographic texture or simply, texture (not to be confused with grain morphology which is referred to as "texture" by some authors). Average texture is sometimes referred to as macrotexture. Alternatively, microtexture combines microstructural and texture information to yield a distribution mapping of the orientation of each grain [94]. Understanding texture not only allows for greater control of material properties, but can also aid in tracing the processing history. The exact mechanisms by which preferred orientations develop, however, are still not completely understood [82, 94]. In his book, W. A. Backofen [82] states "it is an experimental fact that FCC crystals of common orientation but different compositions are not alike in the extent to which they elect one [texture development path] or the other." However, there is currently no theroy to explain the variation in texture with composition in face-centered cubic metals such as aluminum. Lithium containing aluminum

alloys are known to be sensitive to texture development during thermo-mechanical processing, as discussed in Section 2.7.4. This section offers an introduction to the fundamentals of crystallographic texture including notations, methods of quantification, and commonly observed crystallographic textures.

In this work, cylindrical Euler space using Bunge notation $(\varphi_1, \phi, \varphi_2)$ is used as shown in a rolling reference space in Figure 8 [94]. Other notations seen in literature include Kocks (Ψ, Θ, ϕ) and Roe $(\Psi, \Theta, \Phi$ (sometimes $\gamma))$ [94]. Miller indices are also used to specify crystallographic orientations where the indicated plane, (hkl), is perpendicular to the normal direction and the crystallographic direction, $[uvw]$, is parallel to the rolling direction [95, 96]. These indices have no bearing to the active slip mechanisms [96]. Use of Miller indices, however, makes quantitative analysis difficult.

The quantification of macrotexture is performed using x-ray diffraction (XRD), and microtexture can be obtained via electron backscatter diffraction (EBSD) techniques. Both yield orientation information that can be used to generate pole figures and orientation distribution functions (ODFs).

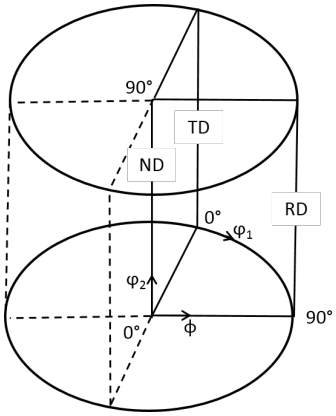

Figure 8: Euler angles (Bunge notation) in reference to the rolling orientations adapted from Engler and Randle [94].

To understand how pole figures and ODFs are generated, imagine that a single grain, or crystallite, is taken out of the matrix and placed inside a unit sphere. For generation of a pole figure, a line is drawn perpendicular to that particular crystallographic plane (i.e. for the {111} pole figure, a line is drawn perpendicular to the {111} plane). The intersection of

this line with the unit sphere is a point. Each grain is represented by a point on the sphere, so if there is a preferred orientation, it will result in a grouping of points on the sphere. Once all of the grains are accounted for, a stereographic projection of this sphere becomes the 2D pole figure. Again, regions of high intensity on a pole figure represent preferred orientations.

To generate an ODF, a grain is taken out of the matrix and placed inside a unit sphere. Instead of drawing perpendicular lines, the grain is rotated such that it falls in line with a reference orientation. The three rotations needed to get a particular grain into the reference orientation can be represented by three Euler angles, $(\varphi_1, \phi, \varphi_2)$. These angles then represent the orientation of a grain with respect to a frame of reference. Each grain is represented by a point in 3-dimensional Euler space (instead of (x,y,z), Euler space is (φ_1, ϕ, φ_2). This 3D plot is known as an orientation distribution function (ODF) where regions of high intensity represent preferred orientations.

Over time, researchers noticed patterns in the high intensity regions on pole figures and ODFs. For convenience, they began to refer to these commonly observed crystallographic textures by names such as the Brass texture, Copper texture, or S texture. Table 2 gives the names and ideal locations of commonly observed textures. Figure 9 shows the locations of commonly observed deformation textures on a {111} pole figure as well some experimental pole figures for Li-containing aluminum alloys. Figure 10 shows the locations of "fibers" or lines of intensity commonly observed in an ODF.

While Table 2 presents the commonly observed locations, or "ideal" locations of certain textures, the locations of the actual maximums representing a texture may shift from ideal. In Figure 10b, the ideal location of the β-fiber is represented by a line, but the range of possible locations is represented by a tube [94]. As described by Kocks, Tome, and Wenk [100], texture can be thought of as a mountain range consisting of ridges and valleys. A fiber shift would be analogous to a slight shift in the mountain ridge. Hirsch and Lucke [99] showed that the β-fiber systematically shifts to smaller φ_1 and higher ϕ values with increasing strain.

Table 2: Commonly observed crystallographic textures in FCC metals.

Name	Plane	Direction	Euler Angles ($\varphi_1, \phi, \varphi_2$)	Reference
		Deformation Textures		
Brass (Bs)	{011}	⟨211⟩	35° 45° 90°	[94]
Copper (Cu)	{112}	⟨111⟩	90° 30° 45°	[94]
S	{123}	⟨634⟩	59° 33° 65°	[94]
Shear_1	{001}	⟨110⟩	45° 0° 0°	[97]
		Recrystallization Textures		
Cube	{001}	⟨100⟩	0° 0° 0°	[97]
Goss	{011}	⟨100⟩	0° 45° 0°	[94]
R	{124}	⟨211⟩	55° 75° 25°	[97]
P	{011}	⟨122⟩	65° 45° 0°	[97]
Q	{013}	⟨231⟩	55° 20° 0°	[97]
		Fiber Textures		
α	-	⟨011⟩//ND	0° 45° 0° - 90° 45° 0°	[94]
γ	-	⟨111⟩//ND	60° 54.7° 45° - 90° 54.7° 45°	[94]
τ	-	⟨011⟩//TD	90° 0° 45° - 90° 90° 45°	[94]
β	-	-	90° 35° 45° - 35° 45° 90°	[94]

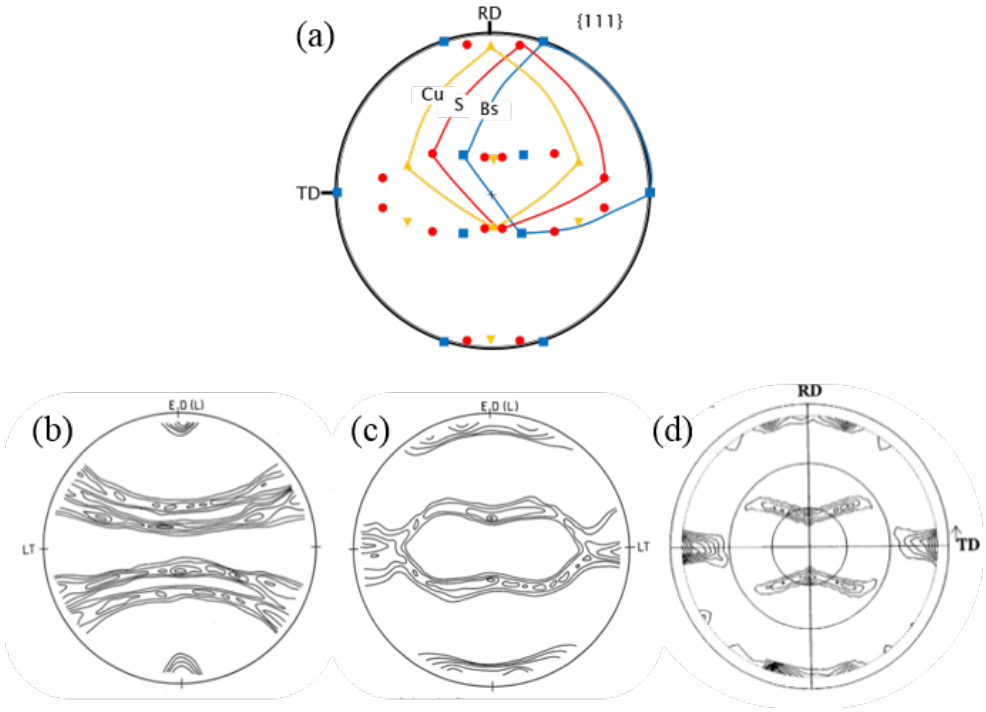

Figure 9: (a) General locations of commonly observed texture components on a {111} pole figure adapted from [94] and actual {111} pole figures from (b) low aspect ratio extruded Al 8090 [98], (c) high aspect ratio extruded Al 8090 [98], and (d) Al 2195 plate [97].

Characterizing and quantifying crystallographic texture development is important because texture can often result in anisotropic properties in thermo-mechanically processed

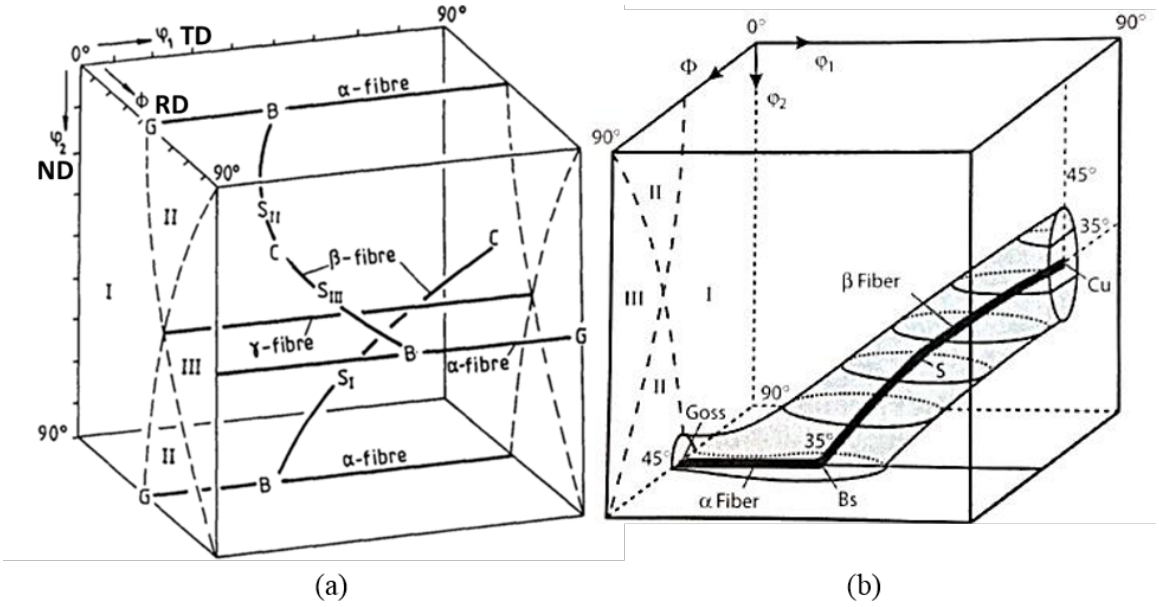

Figure 10: Locations of commonly observed fiber textures in Euler space for FCC metals from (a) [99] and (b) [94].

metals. The effects of preferred orientations on properties in aluminum alloys is discussed in Sections 2.7.4 and 2.7.5.

2.7 Anisotropy in Aluminum Alloys

The properties of a material often vary with respect to the direction of the applied load. This variation is referred to as anisotropy, and it develops during thermo-mechanical processing. Precipitation on habit planes, variation in grain morphology, and development of crystallographic texture can all result in a more anisotropic material. The degree of anisotropy varies between metals and alloy systems but is generally undesirable. A final part with isotropic properties is desirable for most aerospace applications. Aspect ratio has been shown to play an important role in the final properties of aluminum alloys. The role of aspect ratio in affecting anisotropy, mechanisms for anisotropy, and methods of controlling the anisotropy are discussed in this section. In this section, reference will be made to the type of extrusion (i.e. whether it was a simple rectangular cross section or a more "complex profile"). A complex profile will refer to any extrusion that was not a rectangular bar or cylindrical rod, such as a stringer or an integrally stiffened panel. For these shapes, the investigators defined aspect ratios for particular regions.

2.7.1 Aspect Ratio Effects

Low aspect ratio (AR) regions in Al-Li extrusions display what some authors [8] term "chunkiness:" high longitudinal tensile yield strength (TYS), low transverse TYS, low transverse ductility, and a small spread between the TYS and ultimate tensile yield strength (UTS). The effect of varying aspect ratio on longitudinal TYS and UTS is shown in Figure 11 for a lithium containing alloy, Al 8090, and a non-lithium containing alloy, Al 7475 (plotted from reported data) [98, 101]. From these plots, it is clear that the lithium containing alloy shows a greater dependence on aspect ratio. From AR1 to AR10 the longitudinal TYS decreased approximately 14% (75 MPa) while for Al 7475 the longitudinal TYS only decreased approximately 4% (25 MPa)[1].

Although the longitudinal TYS increased in low aspect ratio extrusions, the strength and ductility in the transverse direction decreased (Figure 12) [9]. A cylindrical extrusion (AR1) of Al 2099-T83 had a longitudinal TYS of approximately 600 MPa and a longitudinal

[1] 75 MPa (10.9 ksi); 25 MPa (3.6 ksi)

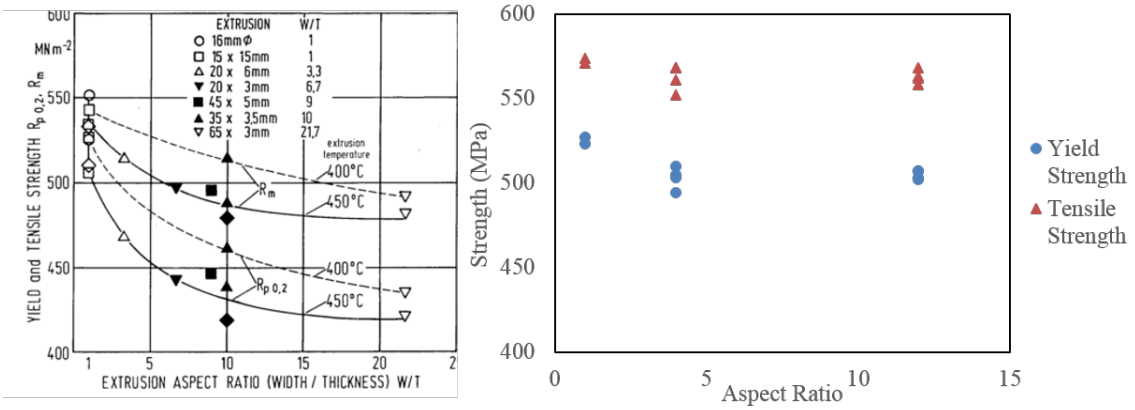

(a) Al 8090 (b) Al 7475

Figure 11: Variation in yield strength with extrusion aspect ratio for (a) a lithium containing alloy [98] and (b) a non-lithium alloy [101].

UTS of 625 MPa; whereas, for the same extrusion, the transverse TYS was approximately 440 MPa and the transverse UTS was approximately 505 MPa[2]. This equates to a 27% decrease in the TYS between the longitudinal and transverse directions and spread between the longitudinal UTS and TYS of 25 MPa for an aspect ratio of one[3].

A complex profile of Al 2099-T83 was also studied, and the variation in longitudinal versus transverse strength properties was greatest in regions of low aspect ratio [102]. Low strength in the transverse direction is undesirable, and for regions of AR4 and less, the TYS in all directions would ideally be above 414-483 MPa or less than 20% variation[4] [8, 103]. In addition to a high longitudinal TYS and a low transverse TYS, low aspect ratio extrusions also displayed a small spread between the UTS and TYS for lithium containing alloys (Figure 13) [9, 103]. For low aspect ratio regions, this spread between TYS and UTS would ideally be greater than 27.6 MPa[5] [8, 103]. Lithium containing aluminum alloys show a greater dependence on aspect ratio than their non-lithium containing counterparts. In low aspect ratio regions of lithium-containing extrusions, a high longitudinal TYS, a low transverse TYS, low transverse ductility, and a small spread between the UTS and TYS were observed.

[2]All values were extracted from Figure 8a in [32] and therefore may not be exact.
[3]600 MPa (87 ksi); 625 MPa (91 ksi); 440 MPa (64 ksi); 505 MPa (73 ksi); 25 MPa (3.6)
[4]414-483 MPa (60-70 ksi)
[5]27.6 MPa (4-4.5 ksi)

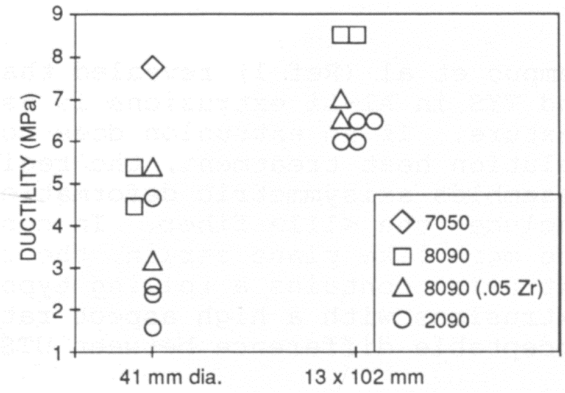

Figure 12: Variation in the transverse ductility for a non-lithium containing alloy (Al 7050) and lithium containing alloys (Al 8090 and 2090) at AR1 and AR8 [9].

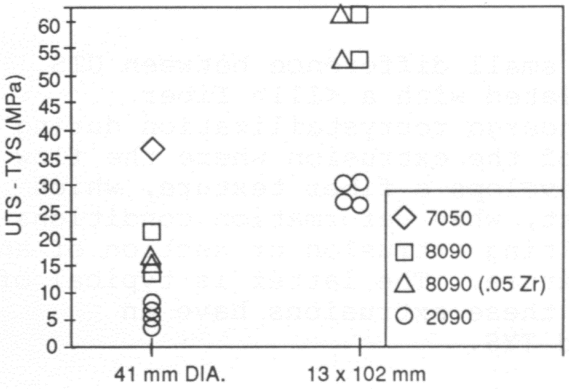

Figure 13: Spread in the longitudinal TYS and UTS for a non-lithium containing alloy (Al 7050) and lithium containing alloys (Al 8090 and 2090) at AR1 and AR8 [9].

Possible causes of these undesirable properties—including precipitation, microstructural variations, and crystallographic texture—are discussed in the following sections.

2.7.2 Precipitation Effects

A primary strengthening mechanism in heat treatable aluminum alloys is precipitation hardening, as discussed in Section 2.1 for Al-Li alloys. Tempus, Calles, and Scharf [104] found that for Al 8090, the precipitation kinetics were different for regions of varying aspect ratio. In low aspect ratio regions, the longitudinal UTS was reached sooner, and was higher, than that in the high aspect ratio region. Martin, Doherty, and Cantor [63] similarly reported variation in the homogenization kinetics amongst different geometries. If the precipitation kinetics are changed with the aspect ratio of a sample, one might conclude

that the strengthening precipitates play a significant role in anisotropy; however, reports on this relationship vary.

In 1990, Vasudevan et al. [105] performed tensile tests at 0° and 45° to the rolling direction at various stages in the heat treatment process for Al 2090 sheet (3.9 mm) and concluded that the anisotropic behavior was due to a "complex interaction between texture and microstructure." They attributed changes in anisotropy in part to the evolution of slip systems that accompany the evolution of T_1, θ', θ' coated in δ', T_2, and PFZs (Figure 14). In 1993, Kim and Lee [24] performed similar studies on rolled Al 2090 sheet and similarly concluded that "while the crystallographic texture development during thermo-mechanical treatment [was] directly responsible for most of the anisotropy observed, it also [had] an indirect effect by resulting in heterogeneous distribution of T_1 precipitates among four possible {111} habit planes." These early reports indicated that anisotropy is in some way dependent, whether directly or indirectly, on the precipitates that form. Later studies indicated no dependency or no conclusive correlation between anisotropy and precipitates.

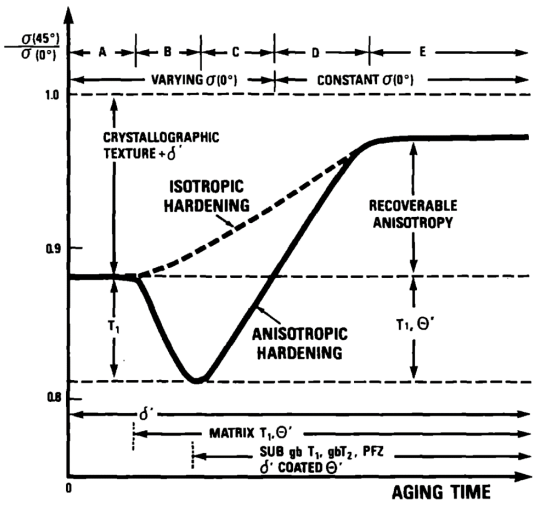

Figure 14: Schematic representation of the relationship between the yield stress anisotropy and microstructure in Al 2090 [105].

In 1998, Crooks et al. [106] studied in plane anisotropy of Al 2195 plates and extruded parts and found that "the strengthening precipitates had no discernible effect on the amount of anisotropy, nor did attempts to vary the distribution of these precipitates have any effect." They reported no significant difference in anisotropy between as-quenched (T8 + solution

heat treatment) and T8 samples [106]. However, Jata, Panchanadeeswaran, and Vasudevan [25] saw approximately a 10% difference in anisotropy between as-extruded (F-temper) and peak aged while the peak aged and solution heat treated anisotropies were similar (Figure 15). In 2016, Bois-Brochu et al. [3] studied the T_1 precipitate density as a function of aspect ratio and found that they could not conclude whether the precipitate density did or did not have an effect on the anisotropy. They stated that it "merely indicated that [their] results of the characterization of the sub-structure were not sufficiently different between the two extrusions sections as to quantitatively measure variations in density of precipitates [3]." However, they later concluded that a "tendency for lower precipitate density was observed for $\langle 111 \rangle$ orientation [3]." An earlier study by Tempus, Scharf, and Calles showed no difference in precipitation state between an AR1 and an AR10 region of a complex profile [104].

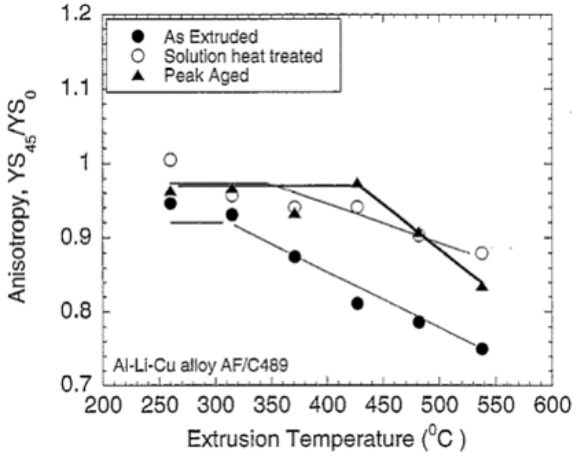

Figure 15: Effect of temper and extrusion temperature on anisotropy in AR5 extruded aluminum bars [25].

Overall, the literature is divergent on how great a role precipitation may play on the final anisotropy. Regardless of how great or minimal an effect the precipitates may have, it is clear that anisotropic precipitation is not solely responsible for anisotropy in Al-Li alloys; other mechanisms must also be at play.

2.7.3 Microstructural Effects

Microstructural control is a common method of varying properties in aluminum alloys. Decreasing the grain size is known to increase strength via the Hall-Petch relationship, but the effects of grain size, subgrain size, and grain morphology on anisotropy are less well defined. Tempus, Calles, and Scharf [104] analyzed the microstructure in AR1 (20 x 20 mm) and AR10 (20 x 2 mm) regions of a complex profile (representative cross section in Figure 16a) and found an as-extruded microstructure and similar precipitation in both[6]. In the AR10 region, they noted pancake-shaped grains and a slightly higher volume fraction of recrystallized grains. They did not note however the type of grains observed in the AR1 region. In all, they concluded that these variations were "unlikely to cause the remarkable difference in strength" [104].

(a) Tempus, Scharf, and Calles (b) Hales and Hafley

Figure 16: Representative cross sections of complex extrusion profiles from (a) [104] and (b) [97].

Hales and Hafley [97] also studied a complex profile; however, they included a transition zone as the low aspect ratio region as demonstrated in Figure 16b. They found layered, pancake-like grains in the high AR region along with a high transverse TYS and a low longitudinal TYS [97]. In the low AR (transition zone) they found distorted layers consisting of half pancake-like and half cigar grains along with a low transverse TYS and a high longitudinal TYS [97]. In both regions, the authors found a large spread (45-50 MPa) between the UTS and TYS[7] [97]. This acceptable range in UTS and TYS was attributed to the mixed grain structure since this region also showed a typical asymmetric crystallographic texture, discussed in Section 2.7.4.

[6] 20 x 20 mm (0.8 x 0.8"); 20 x 2 mm (0.8 x 0.08")
[7] 45-50 MPa (6.5-7.3 ksi)

Bois-Brochu et al. found roughly equiaxed grains at the center of the cylindrical extrusion and more elongated grains at 0.5*radius due to increased shear [32]. Bois-Brochu et al. [32] found no correlation between grain width (varying from 10-40 μm) and tensile strength anisotropy, similar to Tempus, Calles, and Scharf [104].

Jata, Panchanadeeswaran, and Vasudevan [25] studied anisotropy in AR5 aluminum extrusions deformed at temperatures from 250-550°C. They found that the solution heat treated microstructures evolved from coarse and recrystallized to finer and unrecrystallized with increased extrusion temperature [25]. These authors did not point directly to the grain morphology affecting the anisotropy. Instead, they suggested that the yield strength anisotropy "may be due to combined synergistic effect of particles and crystallographic texture" noting that platelet particles had higher volume fractions and smaller inter-particles spacing in the F-temper low extrusion temperature samples [25].

The presence of other secondary phases such as dispersoids and constituent particles can also affect grain size and shape. In 1987, Dorward studied the effects of dispersoids on grain control in Al-Cu-Li alloys. He found that Zr dispersoids resulted in an unrecrystallized microstructure consisting of elongated grains while Mn-Cr dispersoids resulted in recrystallized, elongated pancake grains (Figure 17) [107]. Both alloys followed the same aging curve and exhibited similar anisotropy between the transverse and longitudinal yield strength [107]. Bois-Brochu et al. [32, 102] also found that an alloy containing Al_3Zr dispersoids consisted of mostly unrecrystallized elongated grains with subgrains thereby indicating dynamic recovery. Further discussion on the effects of recrystallization is presented in Section 2.7.5.

Bois-Brochu et al. found no variation in the size, distribution, or volume percent (0.14-0.23%) of constituent particles (likely $Al_{20}Mn_3Cu_2$ and Al_6(Mn,Fe)) through the thickness of a cylindrical extrusion or in various regions across a complex profile [32, 102]. However, the volume percent in AR4.7 transition regions (three total regions spanning the diameter of the billet) was 0.68% [32]. The authors offered no explanation for this variation in constituent particle distribution.

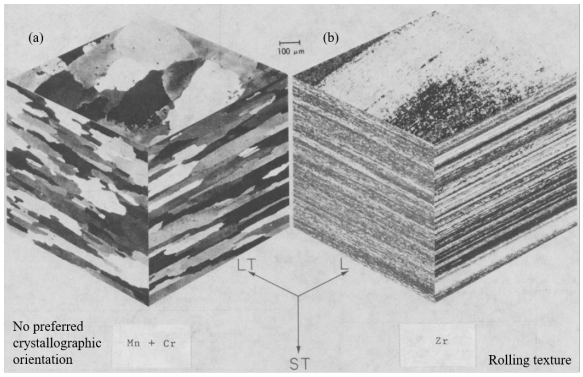

Figure 17: Variation in microstructure of an Al-Cu-Li alloy with (a) Mn-Cr and (b) Zr dispersoids [107].

Although microstrucutral variations occur between low aspect ratio and high aspect ratio extrusions, the literature indicates that variations in grain morphology, grain size, and fraction of constituent phases do not play a role in the strength anisotropy. However, in a low aspect ratio transition zone [97], the spread between UTS and TYS was above the target 27.6 MPa value likely due to the mixed grain structure[8].

2.7.4 Crystallographic Texture Development in Al-Li Alloys

Crystallographic texture development, by definition, is the development of preferred orientations. This preference often leads to anisotropy. The anisotropy described in Section 2.7.1 (i.e. the increased longitudinal yield strength, small difference between the UTS and TYS, and the low ductility in the transverse direction) has been attributed primarily to texture development and has even been termed the "Al-Li fiber texture problem" [9]. This section discusses the various observed textures in Al-Li alloys from the studies reported in Table 3. Some discussion on the correlation between crystallographic texture and grain morphology, as noted in Figure 17 will also be presented. For a review of crystallographic texture see Section 2.6.

Experimental investigations on rolled Al 2195 reported elongated, pancake (weak texture) and laminar (strong β-fiber texture) grains with Brass, Copper, and S along with some Goss, Cube, R, and P components [25, 97, 109]. A $\langle 111 \rangle + \langle 100 \rangle$ double fiber texture

[8] 27.6 MPa (4 ksi)

Reference	Alloy(s)	Temper(s)	Type
[54]	Al-Li-Mg-Cu	under-, peak-, over-aged	Sheet
[104]	8090	T6, T8	Extruded rod and complex profile
[108]	2090	T8E41	Plate
[105]	2090	T8	Sheet
[13]	Al-Cu-Li-Zn-Mn-Mg-Zr, 2090	T8	Plate/Sheet
[98]	8090, 8091	W, T8	Extruded rod, bar, and complex profiles
[103]	Al-Cu-Li-Zn-Mn-Mg-Zr-V, 2090, 2091, 8090	T8	Complex profile
[9]	2090, 8090, 8090-type, 7050	W, T6, T86	Extruded rod and bar of constant ER
[24]	2090	Reverted, Re-solutionized, under-aged, T9E41	Sheet
[66]	AF/C489, 2090, 2091, 8090, 7150, 7055	F, W, T6, T8	Plate
[97]	2195	T8	Plate and T-stiffened extrusion
[25]	AF/C489	F, W, T6	Extruded bars (9x46x1016 mm)
[106]	2195	W, T8	Plate and integrally T-stiffened extrusion
[109]	2195	T6	Sheet
[8]	2090	T8	Complex extrusion
[3, 32, 102]	2099	T83	Extruded rod and integrally stiffened panel

Table 3: Summary of previous studies on texture development in Al-Li alloys from 1985 (first row) to 2016 (last row).

typically resulted after axisymmetric extrusion or in low AR transition regions [9, 97, 98]. In a complex Al 2195 extrusion, the texture and grain morphology were shown to vary throughout the cross section [97]. As discussed in Section 2.7.3, Hales and Hafley reported pancake-like grains with Brass and Cube texture in high AR regions to a mixture of pancake- and cigar-like grains with a double fiber texture in a low AR transition region [97]. Textures typically vary through the thickness or along the cross section of a plate or extrusion. Vasudevan, Przystupa, and Fricke, Jr. [108] studied through thickness variations and found that the center of an extrusion had the highest longitudinal yield strength accompanied by the highest percentages of Brass, S, and Copper textures. Conversely the longitudinal yield strength near the surface was lower than that at the center and associated with a rise in Cube and Goss textures, likely due to a increase in recrystallization near the surface [108].

The "Al-Li fiber texture problem" with Al-Li alloys was termed by Denzer, et al. [9] of Alcoa Laboratories in a study comparing Al 2090, 8090, and 7050. While this study presented the texture developed in the Li-containing alloys it did not present any pole figure data for Al 7050. Denzer, et al. [9] did note that 7050 had the same fiber components as the Li-containing extrusion. Jata, Hopkins, and Rioja [66] also studied Al-Li alloys and compared them to 7xxx-series alloys. They concluded that reducing the Brass texture component reduced the in plane anisotropy to levels seen in conventional alloys (Figure 18a). Their data also suggested that reducing the Copper component resulted in in plane anisotropy similar to conventional alloys; a plot adapted from their data is presented in Figure 18b [66].

Tempus, Calles, and Scharf [104] associated the $\langle 111 \rangle$ fiber texture with the small difference between the UTS and TYS. Similarly, Bois-Brochu et al. [3, 32, 102], found that the intensity of the $\langle 111 \rangle$ fiber texture was highly correlated to the evolution of anisotropic tensile mechanical properties for Al 2099-T83 extrusions ranging from AR1 to 4.7. However, their work also showed a correlation between the $\langle 100 \rangle$ fiber intensities and aspect ratio, with no correlation between strength anisotropy and the Taylor factor [32]. Based on the degree of correlation (using an ANOVA with a significance level of five percent, the residuals correlation matrix, and step-by-step modeling) the authors hypothesized that there was

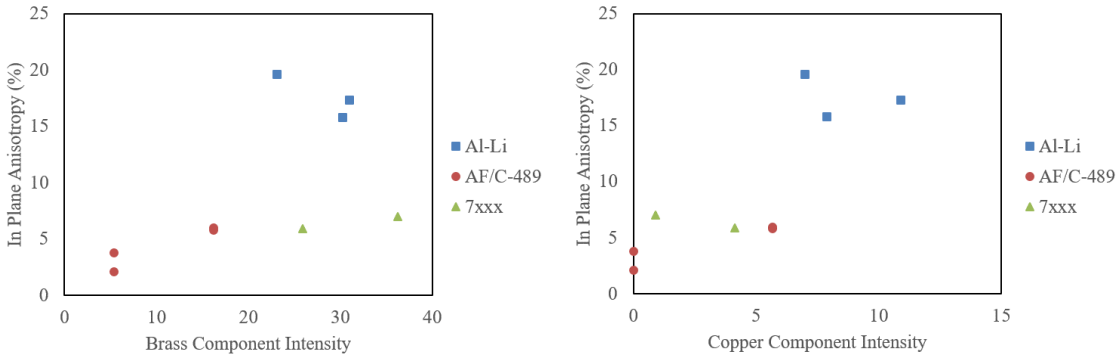

(a) Brass texture vs. Anisotropy

(b) Copper texture vs. Anisotropy

Figure 18: Plots of texture components versus anisotropy where (a) was plotted in [66] and (b) was plotted from data presented in [66]

most likely a cause and effect relationship between the ⟨111⟩ fiber intensity and the yield strength anisotropy [32, 102]. Bois-Brochu et al. made explicit in their reporting that their analysis was based on correlation and that any reports of causation were speculation.

While it is clear that crystallographic texture development results in anisotropy, the literature is inconclusive as to the exact origin and extent. Many studies pointed to strong ⟨111⟩ fiber texture while others noted the Brass component. More definitive conclusions regarding the mechanism behind strength anisotropy can be made through demonstration of control of the anistropy through control of the identified source.

2.7.5 Control of Anisotropy in Al-Li Alloys

In a review paper published in 1998, Rioja [110] stated six approaches previously used to reduce anisotropy of mechanical properties of Al-Li alloys. These methods of controlling anisotropy, in addition to three others (Approaches 7-9), will be discussed in this section.

1. Changing the dispersoid type
2. Recrystallization
3. Recrystallization intermediate step

Approaches 1, 2, and 3 are related. Observed variations in properties with a change in composition or dispersoid type is often due to the change in recrystallization behavior. As discussed in Section 2.7.3 and shown in Figure 17, changing the dispersoid type from Zr to

Mn-Cr, resulted in a change in microstructure but did not have an effect on the anisotropy [107]. In another study, a zirconium content of (0-0.15 wt. %) was reported to improve toughness and ductility in the short transverse direction of rolled plate [13]. Later, the Zr content was varied an unreported amount and only a slight difference in properties was achieved [9]. Although Zr is a popular alloying element for dispersoid formation, there are other elements that can be used. Recrystallization can be controlled with zirconium, chromium, cerium, hafnium, vanadium, manganese, and scandium through the formation of various dispersoids, and recrystallization is sometimes induced during an intermediate stage in the rolling process as stated in Approach 3 [13].

An intermediate step wherein the product is raised to a temperature sufficiently high to cause recrystallization (ranging from partial to complete) was reported to improve the short transverse properties [13]. The resulting product lacked "intense work texture characteristics," but no discussion of specific texture characteristics or pole figures was presented. A later study by Jata, Hopkins, and Rioja [66] revealed that both the Brass and Copper texture components were reduced in Al-Li plate with an intermediate recrystallization treatment and by reducing the stretch (Approach 4). The Brass and Copper textures were also lowered by Trinca et al. [109] using Approach 4. They found that they could reduce these texture components and reduce yield strengths by rolling at an angle of 45° [109]. Rodgers and Prangnell [111] studied rolled Al 2195 in the T8 temper with varied pre-strain percentages (Approach 4) from 3-15%. They reported an increase in the TYS and UTS from approximately 585 MPa and 655 MPa at 4% pre-strain to 665 MPa and 685 MPa at a pre-strain of 15%[9] [111]. The ductility decreased from approximately 11% at 3% pre-strain to 7.5% at 15% pre-strain [111].

4. Stretching or cold rolling in different directions or percentages

5. Reducing the amount of wrought deformation

6. Heat treatment/overaging

[9]585 MPa (84.8 ksi); 655 MPa (95.0 ksi)

Unsurprisingly, the intensity of the Brass texture and anisotropy were found to be lower for heavy gauge plate compared to thinner plate or sheet (Approach 5) [110]. However, changing the geometry or reduction percentage is often not an option in industrial practice. A more practical option would be adjusting the heat treatment after processing (Approach 6).

Arehart et al. claimed that, for extruded Al 2195, skipping the solution heat treatment and aging at 160°C (320°F) for 28 hours resulted in a reduction in anisotropy [112]. Their report did not include any information about the aspect ratio of the extrusions used in testing, it showed some issues with tensile testing, and the reduced anisotropy sample still showed a difference of 59 MPa between the longitudinal and short-transverse TYS. Gregson and Flower [54], reported that overaging results in a significant decrease in TYS anisotropy (underaged varied by 60 MPa, while overaged varied by 10 MPa)[10]. This effect was observed in sheet consisting primarily of δ', and was attributed to the "overaged condition containing copious S phase precipitation" [54]; recall that the S phase has been shown to homogenize slip as discussed in Section 2.1.4. However, overaging resulted in too great a reduction in fracture toughness; therefore, commercial tempers do not include overaging [110].

7. Varying the composition

8. Varying extrusion/rolling temperature

9. Use of a spreader die during extrusion

Instead of changing the heat treatment, Approach 7 involves changing the alloy composition. Keeping the Mg/Zn ratio in the range of 0.2-0.8 wt. % (Approach 7) reportedly reduced the hot worked texture as well as the anisotropy in rolled plate [13]. Increasing the Zn content in the binary Cu-Zn system reportedly increased the Brass texture while decreasing the Copper texture in rolled plates [95, 113]. A similar transition from Copper to Brass texture was also reported for the addition of phosphorous to copper [113]. No mechanism for these observed variations in texture and anisotropy were discussed, and as

[10] 59 MPa (8.5 ksi); 60 MPa (8.7 ksi); 10 MPa (1.5 ksi)

previously discussed, there is no theory as to why some face-centered cubic materials elect one texture path versus another [82].

Unlike rolling, extrusion does not easily allow for intermediate steps or a change in the deformation direction. The easily changed extrusion variables are ram speed and extrusion temperature (Approach 8). Jata, Panchanadeeswaran, and Vasudevan [25] studied direct extrusions of rectangular bars made of an Al-Li-Cu alloy (AF/C489). Extrusion temperatures were varied between 260-540°C (500-1004°F). Raising the temperature above 300°C (527°F) led to an increase in the Brass component intensity and increased anisotropy in as-extruded samples. This increase in Brass texture was associated with an increase in dissolution, an increase in shear band formation, a decrease in particle stimulated nucleation during solution heat treatment, and a larger subgrain boundaries [25]. The Brass texture was also related to an increase in strain localization [106]. Alternatively, decreasing the extrusion temperature resulted in a lower Brass intensity, increased Cube component, and more recrystallization [25]. A discussion on the effect of deformation temperature on texture development in rolled plate by Rollett and Wright [113], however, indicated the opposite trend (i.e. decreasing the rolling temperature led to an increase in the Brass texture and a decrease in the Copper texture).

Other research has shown that the texture, and resulting strength, was affected more by aspect ratio (or specimen geometry) than temperature or extrusion ratio in Al 2090, 8090, 8091, and Al 7050 for direct extrusion [9, 98]. However, the reports do not offer values or ranges for extrusion speeds or temperatures.

Denzer et al. of Alcoa Laboratories were able to reduce the texture development of extruded Al 2090 and Al 8090 products using a proprietary process [9]. Later, some of the same authors reported use of a spreader die to obtain a TYS of at least 483 MPa and an UTS of at least 510 MPa in regions of low aspect ratio (defined as AR4 and less) of Al 2090[11] [8]. They stated that their method reduced texture; however, they did not report on the texture development.

[11] 483 MPa (70 ksi); 510 MPa (74 ksi)

Each of the nine approaches listed results in a decrease in anisotropy. Most of the studies correlated the decrease in anisotropy to a decrease in worked texture, specifically the Brass and Copper components, this decrease in anisotropy was often accompanied by recrystallization or an increase in the Cube component. While a completely recrystallized part would be far more isotropic, it would also not offer the strength or fracture toughness necessary for structural aerospace applications. The most applicable approach for use in controlling texture and strength development during extrusion of a fixed shape and for a fixed alloy is variation in the initial billet temperature or ram speed (Approach 8). None of the existing literature offers a systematic study of the crystallographic texture, precipitate, and microstructural evolutions with varying aspect ratio that occur during industrial extrusion of Al-Li alloys. Further investigations into the mechanisms behind anisotropy and methods of controlling these specific mechanisms, while maintaining high strengths, are still needed.

2.8 Finite Element Modeling of Aluminum Extrusions

Finite element modeling (FEM) is a valuable tool for the aluminum extrusion industry. Experimental extrusion trials require expensive materials and valuable press time. It is also very challenging to systematically vary one variable while holing others constant over multiple runs due to imperfect press repeatability. Modeling is a more economical method that allows for isolation and systematic variation of single press parameters within a computational frame-work. There are two main categories of FEM based on their frame of reference: Eulerian and Lagrangian formulations. In the Eulerian formulation, the mesh and nodal points are fixed in space. In the Lagrangian formulation, the mesh and nodal points move through a fixed frame. Because the Eulerian mesh is fixed in space, it does not allow for the free surface of a profile to be modeled [88]. The Lagrangian formulation, however, requires re-meshing, which can be a computational burden. A third option, the Arbitrary Lagrangian Eulerian (ALE) formulation, combines the best aspects of Eulerian and Lagrangian codes: instead of fixing the reference frame to the mesh or at a location in space, it is attached to an arbitrary computational reference system [88].

There are several codes available for modeling aluminum extrusion: ALMA2π, Deform3D, Forge, and HyperXtrude. ALMA2π is a 2D Eulerian code [114], Deform3D and Forge are Lagrangian codes [115, 116], and HyperXtrude by Altair is an ALE based code [88]. Bastani found that 3D simulations in HyperXtrude agreed with 2D ALMA2π simulations[114]. Kloppenborg et al. [117] compared HyperXtrude and Deform3D and found that both accurately predicted flow lines, but did not comment on other thermo-mechanical predictors such as temperature and load curves. Since it uses an ALE formulation, HyperXtrude offers the widest range of capabilities, allowing for re-meshing, steady-state analysis, transient analysis, and prediction of profile deflection.

2.8.1 Previous Studies in HyperXtrude

There are a number of studies that utilize HyperXtrude modeling but do not offer any experimental validation [118–121]. This section will focus on the studies that offer experimental comparison to the simulated results. The first half is dedicated to studies at the laboratory scale and the second half focuses on results obtained from industrial scale experiments and simulations. This section addresses the ability of HyperXtrude to accuratley predict load and temperature as these are the key indicators of the validity of a thermo-mechanical simulation.

In 2007, Kumar and Vijay performed laboratory scale extrusions of Al 2024 billets, 45 mm (1.8") in length and 25 mm (1.0") in diameter [122]. They compared experimentally determined power to theoretical power calculated based on HyperXtrude results for various shapes (L, T, H, and two-hole cylinders) extruded through a flat die. They found that the HyperXtrude power was 0.13 to 0.18 W greater than experimentally calculated [122]. Kloppenborg et al. [123] showed that HyperXtrude was able to qualitatively predict profile exit speed (fastest versus slowest) for multi-hole AA6060 extrusions on a 10 MN (1004 ton) direct press. Later, Kloppenborg et al. [117, 124] extruded Al 6063 through a porthole die with feeder plates on a vertical laboratory 5 MN (502 ton) press for flow pattern analysis. They determined that HyperXtrude "very accurately" predicted flow lines for Al 6063. Parkar et al. performed a more comprehensive study [125, 126]. They extruded

laboratory scale cylinders of Al 1100 and AM30 from a 25 mm (1") billet and found that for three different test conditions HyperXtrude accurately predicted the peak load, but underestimated the load past peak force. For a more complex alloy, AZ61, Parkar found that HyperXtrude underestimated the peak load [125]. The under prediction was rectified by creating a user-defined function that allowed for a strain dependent constitutive equation [125]. Temperature profiles were well captured by the simulation [125]. Their study also indicated that ram speed did little to affect load curves while the billet temperature had a much larger effect [126].

All of the industrial scale extrusion studies that compared simulated to experimental data were published between 2010-2011 [88, 127–129]. Bastani, Aukrust, and Brandal industrially extruded an AA6060 U-section from a 800 mm (31.5") long billet [88, 127]. They found that HyperXtrude underestimated the peak load by less than 5 MN (562 tons), and precisely simulated the later portion of the load curve for two temperatures and two ram speeds [88, 127].

Ockewitz et al. [129] analyzed the backward and forward extrusion of AA6005A cylindrical rods at FZS Berlin for multiple extrusion ratios, billet temperatures, and ram speeds from billets measuring 125 mm (5") in diameter [129]. They found good agreement between simulated temperature and force curves and the experimental values for backward extrusion, but observed that HyperXtrude over predicted the temperature and force for forward extrusion by approximately 50°C and 1 MN (100 tons), respectively [129]. They attributed this over prediction to the additional friction between the billet and container during forward extrusion. Since none of the built-in friction models improved results, they suggested a new friction model [129]. Ockewitz et al. [129] also offered a model for predicting grain size and recrystallization which was implemented in HyperXtrude via a user function.

Pinter and El Mehtedi [128] performed hot torsion on Al 7020, 6005, and 6063 to fit constitutive parameters, and subsequently performed experimental and simulated extrusions of these alloys. Experimental extrusions were performed using a 50 MN (5620 ton) direct extrusion press at ETEM S.A. in Magoula, Greece [128]. Although this paper discussed experimental results, Pinter and Mehtedi only presented or plotted HyperXtrude

results. As shown in Table 4, the constitutive parameters reported [128] differ from those in the HyperXtrude database [130]. Pinter and El Mehtedi state that their simulated exit temperatures were approximately 10°C above the experimentally measured exit temperatures [128]. While this minimum level of discrepancy suggested accurate thermodynamic simulation, when it came to the mechanical response, Pinter and El Mehtedi found that HyperXtrude overestimated the peak load under both transient and steady-state conditions. They stated that this was "mainly due to the adoption of the Zener-Hollomon equation, in which the flow stress is not dependent on the strain, since it relates the peak strength of the alloy with thermo-mechanical parameters [128]."

Table 4: Constitutive parameters for Al 6063 reported by various sources.

Parameter	Symbol	Unit	Al 6063 [128]	Al 6063 [130]
Stress Exponent	n	-	5.12	5.385
Activation Energy	Q	J/mol	204,078	141,550
Reciprocal Strain Factor	A	-	6.67000E+12	5.91052E+09
Stress Multiplier	α	1/MPa	0.045	0.040

While some sources stated that load curves were under ([125]) or over ([128]) estimated due to a non-strain dependent constitutive equation, another pointed to an improper friction model causing overestimation [129]. Further work involving simulation of industrial extrusions is necessary to evaluate the accuracy of HyperXtrude at predicting load, temperature, and ultimately, strength anisotropy.

CHAPTER 3

EXPERIMENTAL PROCEDURES

The purpose of this work is to study the effects of extrusion aspect ratio on strength anisotropy and crystallographic texture in Al 2195 and Al 7075, as well as methods of controlling and predicting this anisotropy. Experimental methods are discussed in this chapter.

3.1 Materials

Homogenized billets of Al 2195 and Al 7075 were provided by Vista Metals in Adairsville, GA for extrusion. Vista also provided homogenized billet slices of Al 2195, which were machined into ingots for rolling as described in Section 5.2. The registered composition of Al 2195 (in wt.%) is 3.7-4.3 Cu, 0.8-1.2 Li, 0.25-0.8 Mg, 0.25-0.6 Ag, 0.25 Mn, 0.25 Zn, 0.08-0.16 Zr, 0.15 Fe, 0.12 Si, 0.10 Ti and remainder Al [7]. Al 7075 is a non-lithium containing alloy with a composition of (in wt. %) 5.1-6.1 Zn, 1.2-2.2 Cu, 2.1-2.9 Mg, 0.30 Mn, 0.50 Fe, 0.40 Si, 0.20 Ti, 0.18-0.28 Cr, and remainder Al [7].

3.2 Microscopy

Optical microscopy, scanning electron microscopy (SEM), and transmission electron microscopy (TEM) were employed to better understand the microstructural differences that occurred with aspect ratio and between alloy systems. Prior to optical and SEM, samples were polished using silicon carbide grinding paper down to 1200 grit, diamond paste down to 1 μm, and 0.04 μm colloidal silica. Samples were prepped for optical microscopy with various etchants. Keller's etchant (2-5% nitric acid, 1-5% hydrochloric acid, 0-5% hydrofluoric acid, water remaining) was swabbed across polished samples for approximately 10-12 seconds. For a phosphorous etch (10% of 85+% H_3O_4P and 90% H_2) samples were left

to soak for 20 minutes. To perform polarized light optical microscopy, samples were electropolished for 15 seconds followed by 45 seconds of etching with Barker's reagent (98.2 mL distilled water and 1.8 mL flouroboric acid (H_3OBF_4)).

TEM samples were taken from mid-thickness of the plate (where the texture measurements were taken). The plate was mechanically ground into a foil of approximately 0.1-0.2 mm and then punched into 3 mm diameter disks. These disks were electrolytically thinned on a Struers Tenupol unit until a small hole was created. A solution of 75% methanol and 25% concentrated nitric acid by volume was used. An operating voltage between 10-11 V and a solution temperature of -20 to -15°C was maintained. After thinning, each sample was cleaned in four stages of methanol. TEM was performed on a Hitachi HT7700 microscope. Some scanning transmission electron microscopy (STEM) with energy-dispersive x-ray spectroscopy (EDX) and TEM with x-ray photoelectron spectroscopy (XPS) was performed by Thomas Dorin at Deakin University.

3.3 Texture Analyses

Samples for XRD texture analysis were taken from the L-T plane (see Figure 4), midway through the thickness of the sample. Previous studies on cold rolled Al 2195 indicate a texture gradient exists through the thickness of the rolled plate [131]. Thus, all samples used for pole figure analysis in this study were sectioned such that the measurements were taken from mid-thickness and mid-width of the plates and extrusions. A PANalytical Materials Research Diffractometer (MRD) with a point detector was used to obtain pole figures. Scans were run using Cu-K_α radiation and an operating voltage of 45 kV with a current of 40 mA. An aperture size of 2 x 2 mm was used. For each sample, the exact 2θ locations of the (111), (200), (220), and (311) peaks were recorded. A specific range of ϕ values was set for each 2θ value. In order to prevent the beam from spilling off the sample, the range was set to 0-65° for the (111) peak, 0-70° for the (200) peak, 0-75° for the (211) peak, and 0-85° for the (311) peak.

MTEX 3.5.0 (with Matlab 2014a) code was used to convert the raw data into calculated pole figures and orientation distribution functions (ODFs). The code performs a fitting

routine to the experimental pole figure data [132]. MTEX then solved for the ODF using the general solution of the Darboux differential equation, which governs the pole density function corresponding to an orientation density function [132–134]. This approach was developed by Hielscher and Schaeben [133] and a detailed discussion can be found in their original paper. The reference system used by MTEX is shown in Figure 19 and these coordinates were used in all plots presented.

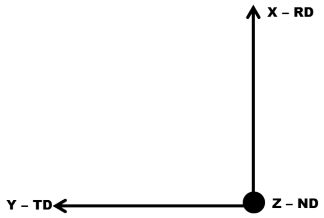

Figure 19: Reference coordinated system used in MTEX.

Pole figures were generated using the "antipodal" command which ensures the calculated figures follow Friedel's law and can be compared to experimental data. Volume fractions of all commonly found texture components, as summarized in Table 2, were also calculated. Intensities along the ideal β-fiber were found, and a routine was used to locate values and positions of the shifted local maxima. The specific commands and the β-fiber routine, written by Lauren O'Hara and Meghan Toler of Georgia Tech, used in MTEX can be found in Appendix B.

While pole figures and ODFs offer quantitative information about the macrotexture development, specific grain orientation mapping cannot be performed with these results. Electron backscatter diffraction (EBSD) and nano-hardness mapping were performed at Deakin University to investigate microtexture.

3.4 Heat Treatment

Samples designated F-temper were taken from the air cooled extrusions with no further heat treatment. A Paragon furnace was used for all heat treatments performed at Georgia Tech. Temperature was monitored with an external thermocouple attached to an aluminum block of similar volume to the samples. Samples of Al 2195 and Al 7075 were treated to a

W-temper for studying surface recrystallization. The Al 2195 samples were held at 515°C for 24 hours and the Al 7075 samples were held at 480°C for 2 hours. Both alloy systems were water quenched. Al 2195 samples sent to Deakin University were solution heat treated at 500°C for 24 hours, stretched, and naturally aged to a T3 temper. After solution heat treatment and stretch, samples sent to Deakin University were aged at 144°C for 8 hours to an underaged temper or aged at 144°C for 50 hours to a T8-temper.

3.5 Tensile Testing

Tensile tests and measurements were conducted at Deakin University. Flat tensile specimen were machined from the middle L-LT plane with the testing direction oriented in the longiudinal and transverse directions. These specimen had a gauge length of 22 mm, a width of 5.25 mm, and a thickness of 1.5 mm[1]. Tests were performed at room temperature in the T3-temper, underaged condition, and T8-temper at a strain rate of 0.01/s.

3.6 Differential Scanning Calorimetry

Differential scanning calorimetry (DSC) scans were performed to determine processing temperatures for Al 2195. DSC was performed on a PerkinElmer DSC 8000 at a heating rate of 20°C/min while flowing argon gas at a rate of 20 ml/min. Samples were machined from the center of the billet into discs approximately 6.35 mm in diameter and 0.5 mm thick. Samples were mounted in a 10 μL aluminum pan and run against a reference empty aluminum 10 μL pan. Onset of melting for Al 2195 was observed via DSC to be 516°C (960°F).

3.7 High Temperature X-Ray Diffraction

In situ, high temperature x-ray diffraction (XRD) was performed on a PANalytical X'Pert Pro Multi-Purpose Diffractometer (MPD) using Cu k-α radiation. Scans were taken over the 2θ range 4-150° at 45 kV and 40 mA. A 0.25° incident anti-scatter slit and a 5 mm divergent scatter slit were used. Samples were heated at a rate of 60°C per minute to the temperature of interest and held for 5 minutes to allow transfer of heat to the sample before a scan was taken. Scans were then taken once an hour for the duration of the 24 hour run.

[1] 0.87x0.21x0.06"

3.8 Hot Torsion Tests

Hot torsion tests were performed by Blake Whitley at the Colorado School of Mines on a Gleeble 1500 over a range of strain rates and temperatures typically experienced during thermo-mechanical processing of Al 2195 (Table 5). Samples, as shown in Figure 20, were machined from the homogenized billet of Al 2195 received from Vista Metals. Once machined, these samples were heated to the listed temperatures at a rate of 25°C/min., held at temperature for 10 minutes, and then deformed until failure under fixed-end conditions at the strain rates indicated in Table 5. Strain and strain rate were measured at the outer surface of the gauge. Temperature was monitored via a thermocouple at the left shoulder, and it did not deviate more than +5°C from the set point.

Table 5: Experimental matrix for hot torsion testing of Al 2195.

Temperature (°C)	Shear Strain Rate (1/s)
400	0.1
400	1
400	10
450	0.01
450	0.1
450	1
450	10
500	0.1
500	1
500	10

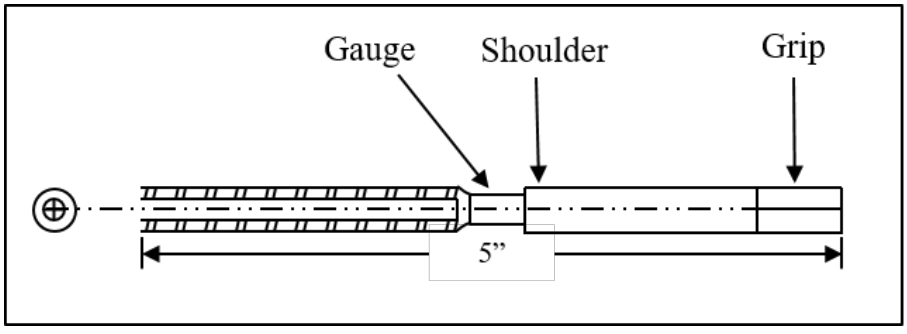

Figure 20: Torsion specimen drawing with regions of interest labeled.

3.9 Macro-Etching

Macro-etching was performed by submersing the billet butt in a caustic bath (100 mL distilled water/20 g NaOH) for approximately 5 minutes. This was followed by a water rinse and 5 minutes in a nitric solution (50 mL distilled water/50 mL HNO_3). After the nitric bath, all samples were thoroughly cleaned with water and photographed.

CHAPTER 4

EFFECTS OF ASPECT RATIO ON EXTRUDED AL 2195 AND 7075

As discussed in Section 2.7, the literature indicates that lithium containing aluminum alloys develop more pronounced anisotropy than their non-lithium containing counterparts, particularly at lower aspect ratios. However, many of these investigations were performed on complex shapes with transition zones labeled as low aspect ratio regions, and most of the previous studies reported on regions of varying aspect ratio that also had different local extrusion ratios. Many researchers suggest that crystallographic texture was the primary cause of increased anisotropy in Li containing alloys, but did not offer a comparison to the texture that developed in a non-lithium extrusion of the same cross section. No study currently exists in the literature that systematically investigates the effects of changing aspect ratio at the industrial scale on the resulting microstructure and properties of an Al-Cu-Li alloy and a non-lithium containing counterpart. In this chapter, the evolution of strength, texture, and microstructure with changes in aspect ratio are characterized for Al 2195 and Al 7075.

4.1 Extrusion Procedure

Extrusions were performed at Universal Alloy Corporation in Canton, GA (UAC-Canton) on an industrial scale direct press. Systematic variations in aspect ratio were performed as reported in Table 6 and seen in Figure 21 while a constant cross-sectional area and extrusion ratio (ER = 20) were maintained. Similarly, all other processing parameters were held constant to ensure any variations were due solely to aspect ratio. Data was collected real-time via the process monitoring software, Historian. Extrusion pressure, speed, initial billet temperature (IBT), container temperature, and dwell time were all recorded. Exit temperature was not recorded because of an error in the monitoring system. Ram speed was controlled within +/- 0.1 inches per minute (IPM) from target for Al 2195 AR2-AR8 extrusions. However, Al 2195 AR15 was run at a ram speed approximately 3 times slower.

The Al 7075 ram speeds were controlled within +/- 0.3 IPM from the target. All extrusions were allowed to air cool. The front and rear 20% of the extrusions were marked and set aside. All samples were taken from the middle 60% of the extrusion. After extrusion, select Al 2195 billet butts were cross sectioned, milled to obtain a fine finish, and macro-etched (see Section 3.9 for details) to observe the flow pattern.

Table 6: Experimental matrix for extrusion of Al 2195 and Al 7075.

Alloy	Aspect Ratio (AR)	Extrusion Ratio (ER)
Al 2195	2 3 5 7 8 15	19.2
Al 7075	2 7 8 15	19.2

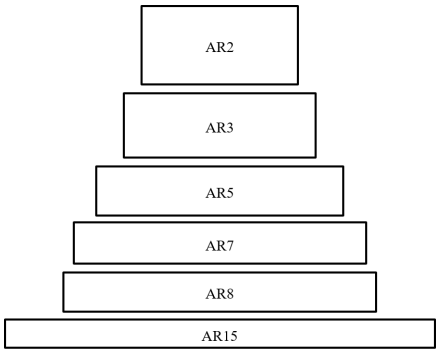

Figure 21: Variation in aspect ratio while maintaining a constant cross-sectional area and extrusion ratio (ER).

4.2 Characterization of the Al 2195 Billet

The as-received billet of Al 2195 had equiaxed grains, various secondary phases, and a random texture (Figure 22). The large plate-like particles in the grain interior were likely T_1 (Al_2CuLi) based on the morphology and the energy-dispersive x-ray spectroscopy (EDX) mapping shown in Figure 23. Based on this mapping, the grain boundary phase was Cu-rich and likely Al_2Cu. A transmission electron microscope (TEM) equipped with x-ray

photoelectron spectroscopy (XPS) revealed Zr-rich dispersoids, likely Al_3Zr (Figure 24). Figures 22a and 23 indicate the presence of precipitate free zones (PFZs) near the grain boundary. A complete discussion of possible phases in lithium containing alloys can be found in Section 2.1.

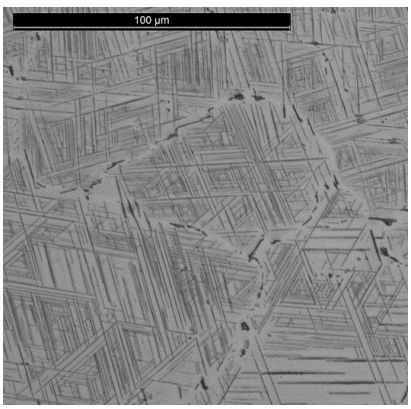

(a) Optical

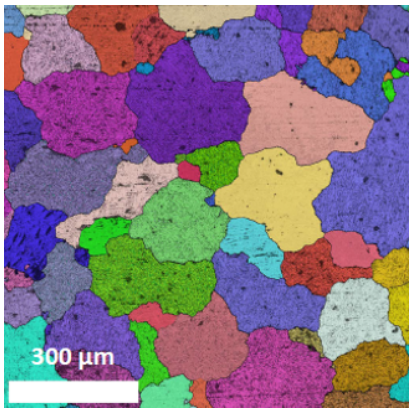

(b) EBSD

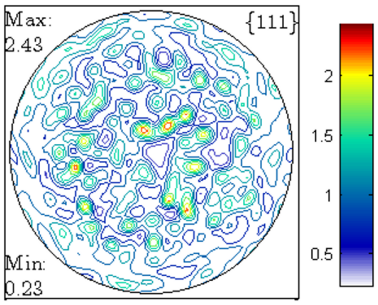

(c) {111} Pole figure

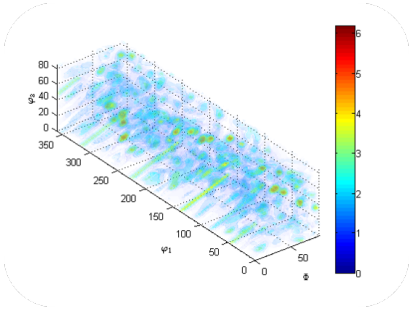

(d) ODF

Figure 22: Characterization of the as-received Al 2195 billet.

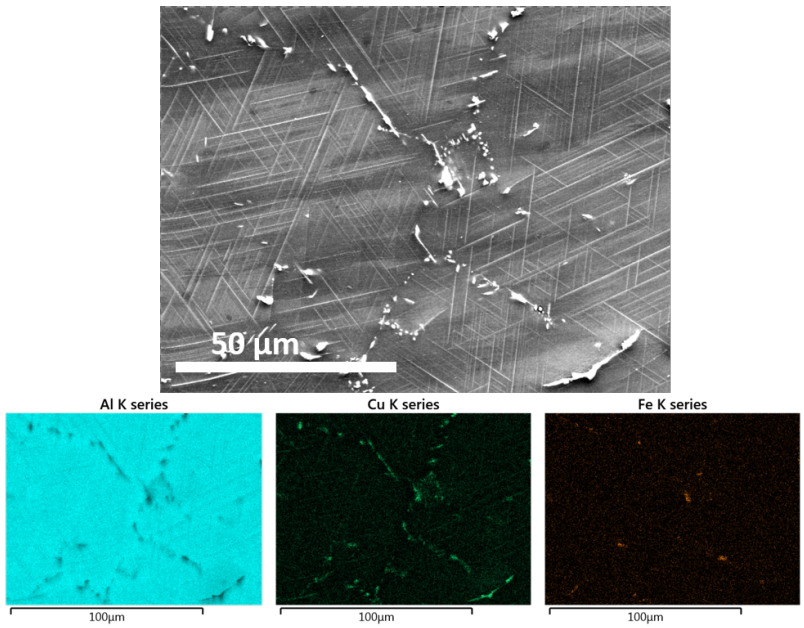

Figure 23: SEM and EDX mapping of the as-received Al 2195 billet. Courtesy of Dr. Thomas Dorin at Deakin University.

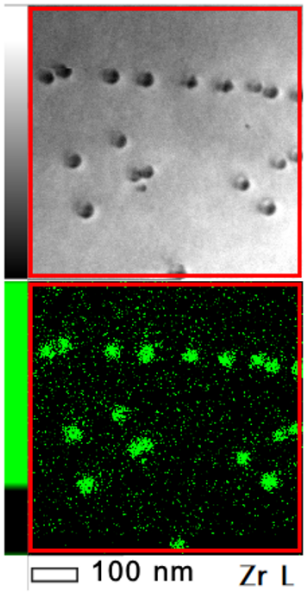

Figure 24: TEM image and XPS mapping of zirconium in the as-received Al 2195 billet. Courtesy of Dr. Thomas Dorin at Deakin University.

4.3 Precipitation in Al 2195 Extrusions

Extrusions were investigated in the F (air cooled after extrusion), T3 (solution heat treated, stretched, and naturally aged), and T8 (T3 + artificial aging to peak strength) conditions

as detailed in Section 3.4. All samples were stretched to the same percentage. Samples were sent to Deakin University where scanning transmission electron microscopy (STEM) was used for phase identification. STEM observation revealed the presence of T_1 on 111 planes and θ' on the 100 planes in the T8 condition as shown in Figure 25. No δ (AlLi) was observed. The precipitates in heat treated Al 7075 are likely GP zones and η' as discussed in Section 2.2. TEM was not performed on the Al 7075 samples in this study; however, the microstructure was reported by Marlaud et al. [135] as shown in Figure 26. The precipitates in Al 7075 are not only smaller, but Marlaud et al. [135] reported that the aspect ratio of these precipitates was 0.4; whereas, in Al 2195, the precipitate aspect ratio was much more pronounced. However, T_1 and η' both have a HCP crystal structure and grow on {111} habit planes.

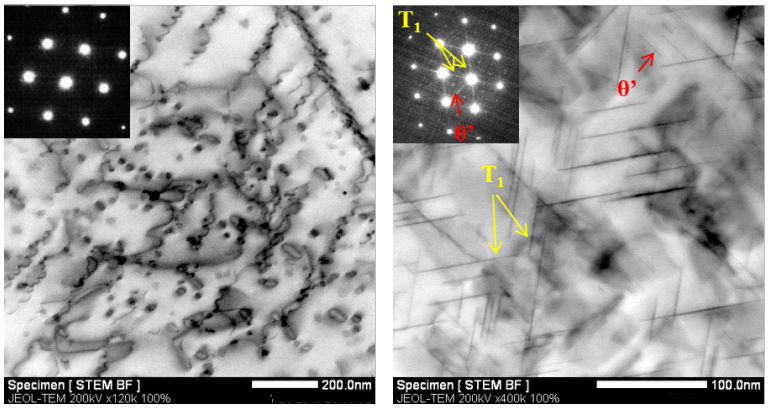

(a) Al 2195 T3 (b) Al 2195 T8

Figure 25: Bright field STEM images and diffraction patterns from Al 2195 in the (a) T3 and (b) T8 conditions. Courtesy of Dr. Thomas Dorin at Deakin University.

Al 2195 samples were also sent to Deakin University where 400 nanohardness indentations were performed on AR2 and AR15 in the T3 and T8 conditions. Each nanohardness measurement is represented by a point on the nanohardness maps (Figure 27) which indicate that in the peak aged condition, the hardness of AR2 was less homogeneous than AR15. In order to further investigate the strength and crystallographic texture development, tensile tests and x-ray diffraction analyses were performed on all aspect ratio samples.

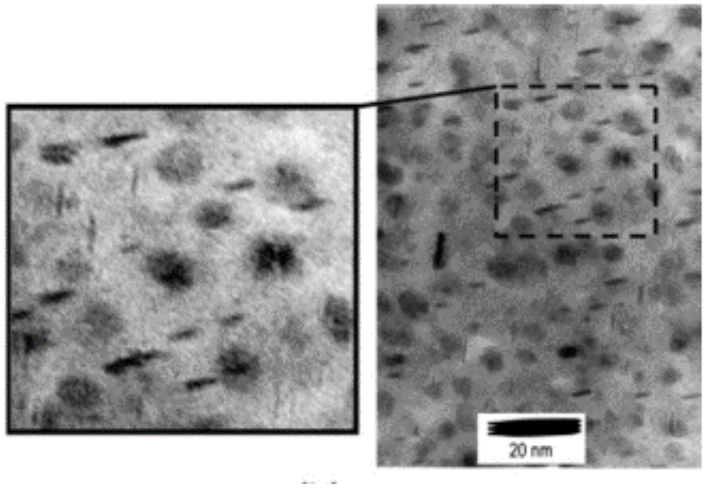

Figure 26: Bright field TEM images and from Marlaud et al. [135] of Al 7075 after retrogression and re-aging.

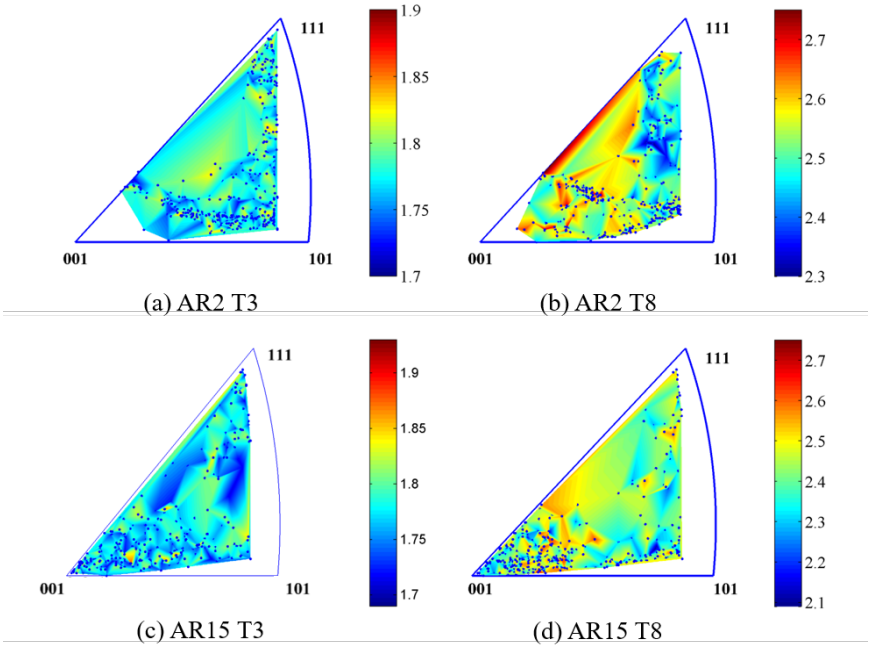

Figure 27: Nanohardness maps for Al 2195 (a) AR2 T3, (b) AR2 T8, (c) AR15 T3, and (d) AR15 T8. Courtesy of Dr. Thomas Dorin at Deakin University.

4.4 Strength Anisotropy with Aspect Ratio in Al 2195

As discussed in Section 2.7.1, low aspect ratio extrusions of lithium containing alloys are prone to high longitudinal tensile yield strengths (TYS) (14% higher than high AR regions), low transverse TYS (27% lower than the longitudinal TYS), and a small spread between the ultimate tensile strength (UTS) and the TYS (less than 27.6 MPa). Non-lithium containing alloys, such as Al 7075, typically show less variation between the longitudinal TYS in low and high aspect ratio sections, a smaller difference between the longitudinal and transverse TYS, a larger difference between the longitudinal TYS and UTS, and a higher transverse ductility.

In order to systematically quantify the variation in mechanical properties with aspect ratio for Al 2195, tensile tests were performed at Deakin University on the Al 2195 extrusions. Tests were conducted on samples in the T3, underaged, and T8 conditions and in the longitudinal and transverse directions. Average values are reported here. A set of tests in the transverse direction for the T3 condition was not performed for AR2, AR8, and AR15, and the AR3-AR7 T3 transverse results are not plotted since no trends were observed. The complete data set is reported in Appendix A.

With an increase in the aspect ratio, there was a corresponding decrease in the longitudinal strength (Figure 28) and an increase in the transverse strength (Figure 30) seen most prominently in the T8 condition. The longitudinal ductility in the T8 condition increased from AR2 to AR15, while in the T3 and underaged conditions, the longitudinal ductility decreased from AR2 to AR3 and then increased from AR7 to AR15 (Figure 29).

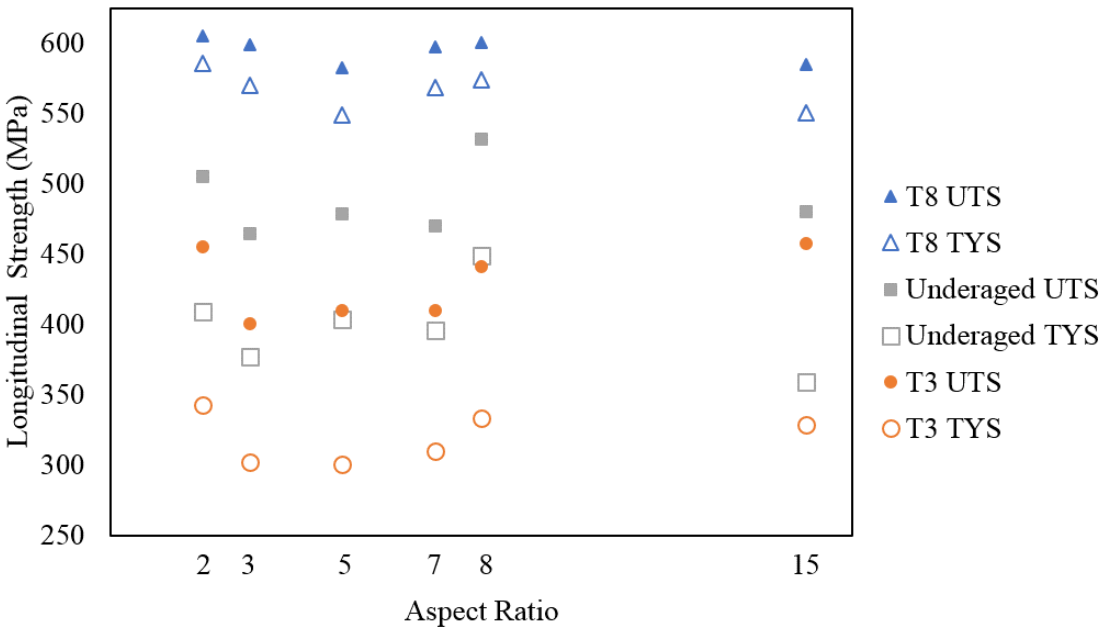

Figure 28: Longitudinal tensile yield and ultimate tensile strength variation with aspect ratio for T3, underaged, and T8 Al 2195 extrusions.

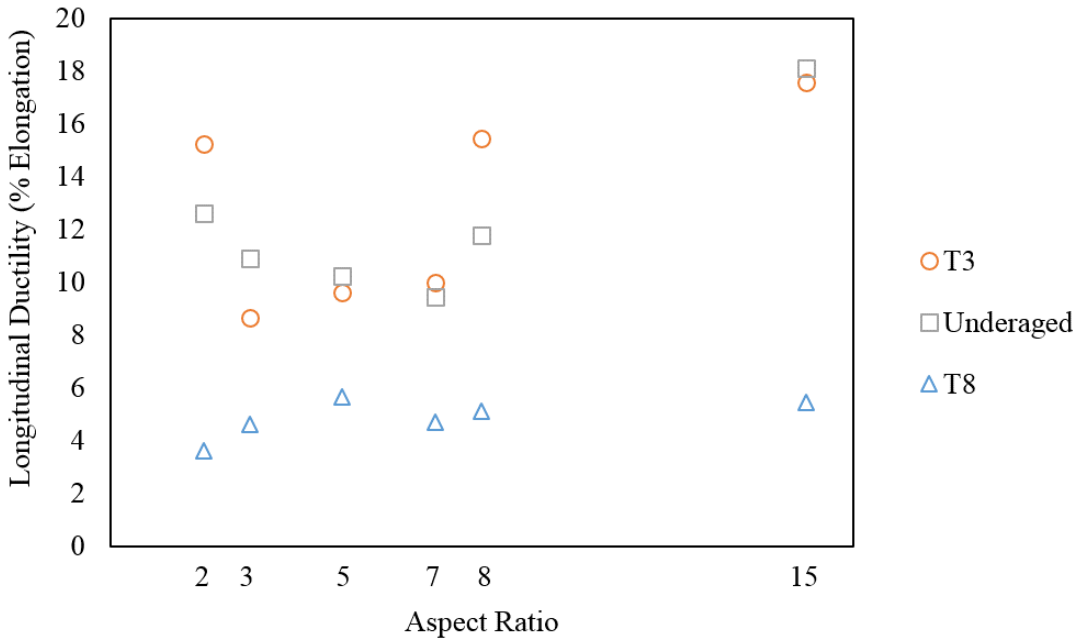

Figure 29: Longitudinal ductility variation with aspect ratio for T3, underaged, and T8 Al 2195 extrusions.

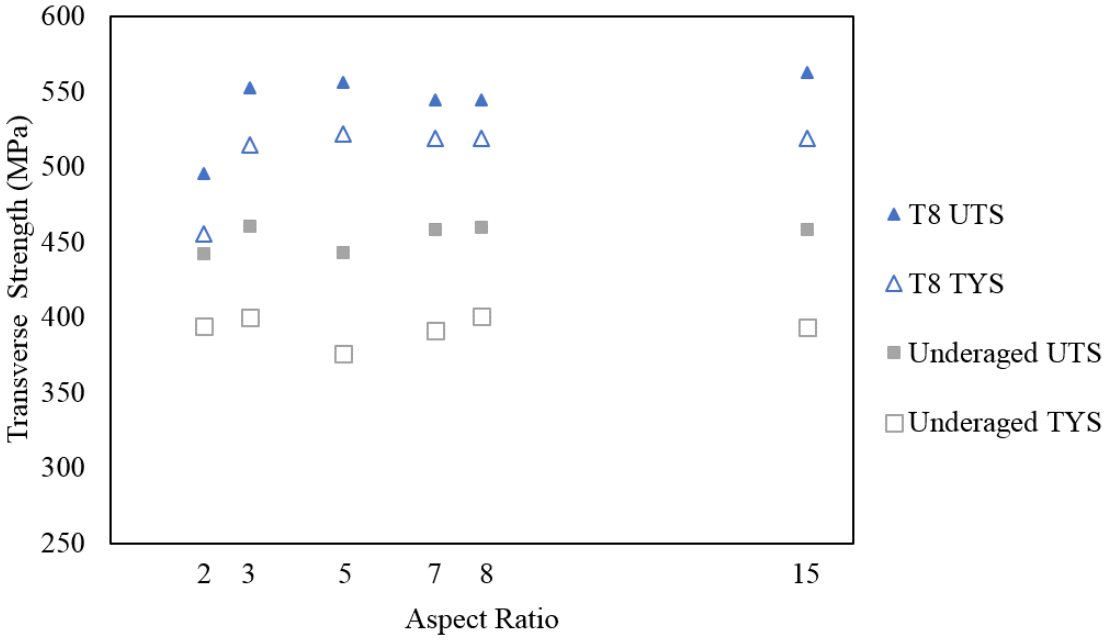

Figure 30: Transverse tensile yield and ultimate tensile strength variation with aspect ratio for underaged and T8 Al 2195 extrusions.

Based on the performance of non-lithium containing alloys reported in the literature, the following criteria were set for ideal performance of Al 2195 and will be referred to as Criterion 1, Criterion 2, Criterion 3, and Criterion 4.

1. Less than 4% difference between longitudinal TYS in low and high aspect ratio sections
2. Less than 20% difference between the longitudinal and transverse TYS
3. A spread between the longitudinal TYS and UTS greater than 27.6 MPa (4 ksi)
4. A transverse ductility greater than 4% elongation

The level to which Al 2195 did or did not meet Criteria 1-4 can be seen in Figures 31-34, respectively. From AR2 to AR15, the longitudinal TYS decreased most (12%) in the underaged condition. In the T8-temper, only AR5 and AR15 failed Criterion 1, with more than a 4% decrease in the longitudinal TYS from AR2. There did not appear to be a systematic variation in Criterion 1.

AR2 T8 was the only sample to fail Criterion 2, with a 22% variation between the longitudinal and transverse TYS (Figure 32). All of the other T8 and underaged samples had a variation between the longitudinal and transverse TYS of 15% or less and did not reveal any trends of systematic variation (the T3 data set was incomplete).

The spread between the longitudinal TYS and UTS (Criterion 3) was well above the target minimum for samples in the T3 and underaged conditions. Samples in the T3 and underaged conditions had a spread between the longitudinal TYS and UTS of 73 MPa or greater. However, only AR15 was above the target minimum for samples tested in the T8 condition (Figure 33). In the T8 condition, AR2 failed Criterion 3 with a longitudinal UTS-TYS spread of 20.2 MPa, the spread then hovered around the target value of 27.6 MPa from AR3-AR8, and finally exceeded Criterion 3 at AR15 with a spread of 34.4 MPa[1].

AR2 and AR3 in the T8 condition failed Criterion 4 (transverse ductility greater than 4%) with transverse ductilities of 2.0% and 3.9% elongation, respectively. The T8 samples

[1] 73 MPa (10.6); 20.2 MPa (2.9 ksi); 27.6 MPa (4.0 ksi); 34.4 MPa (5.0 ksi)

with an aspect ratio of 5 and greater had transverse ductilities of at least 4.6% (Figure 34). The T3 and underaged samples all had transverse ductilities well above 4%.

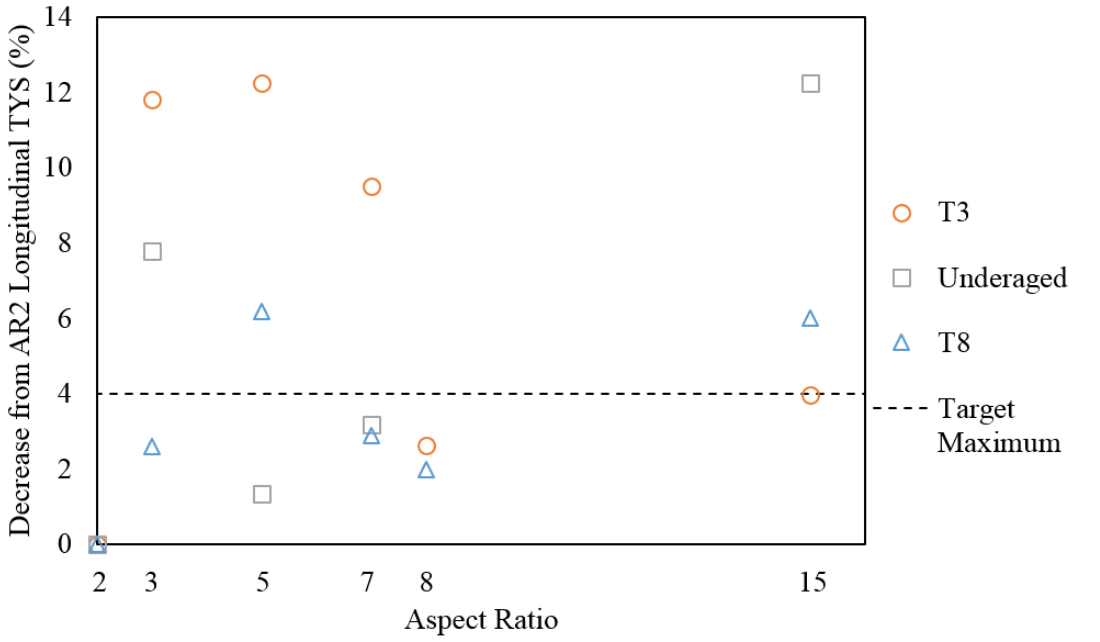

Figure 31: Decrease in the longitudinal TYS for AR3-AR15 from the longitudinal TYS of AR2 Al 2195 extrusion.

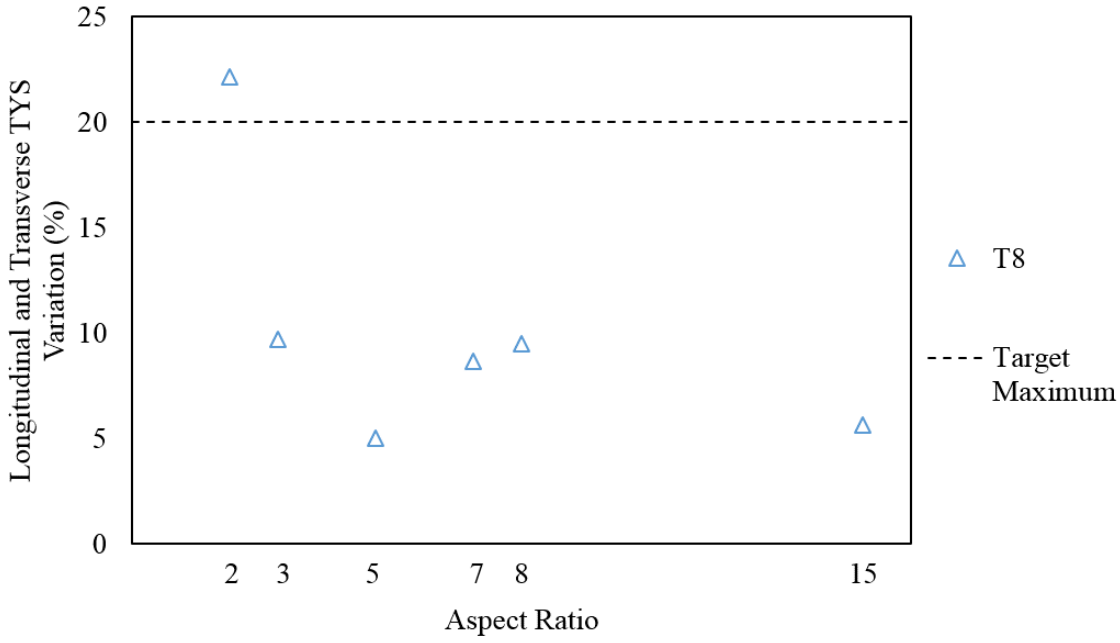

Figure 32: Percent variation between the longitudinal and transverse TYS's for T8 Al 2195 extrusions with various aspect ratios.

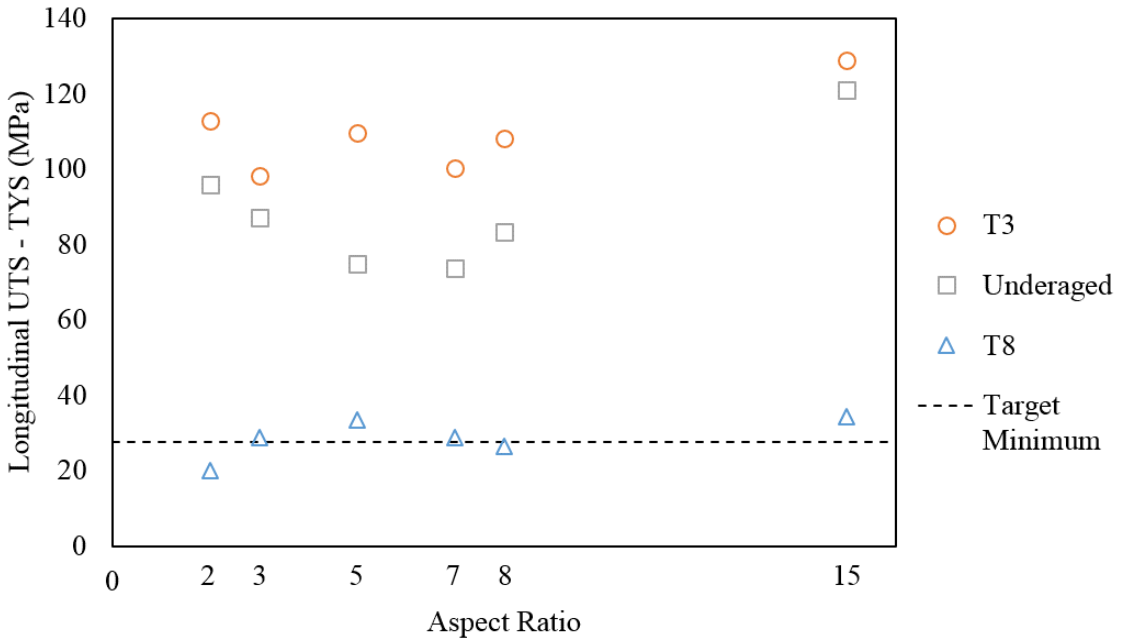

Figure 33: Difference between the longitudinal UTS and TYS variation with aspect ratio for T3, underaged, and T8 Al 2195 extrusions.

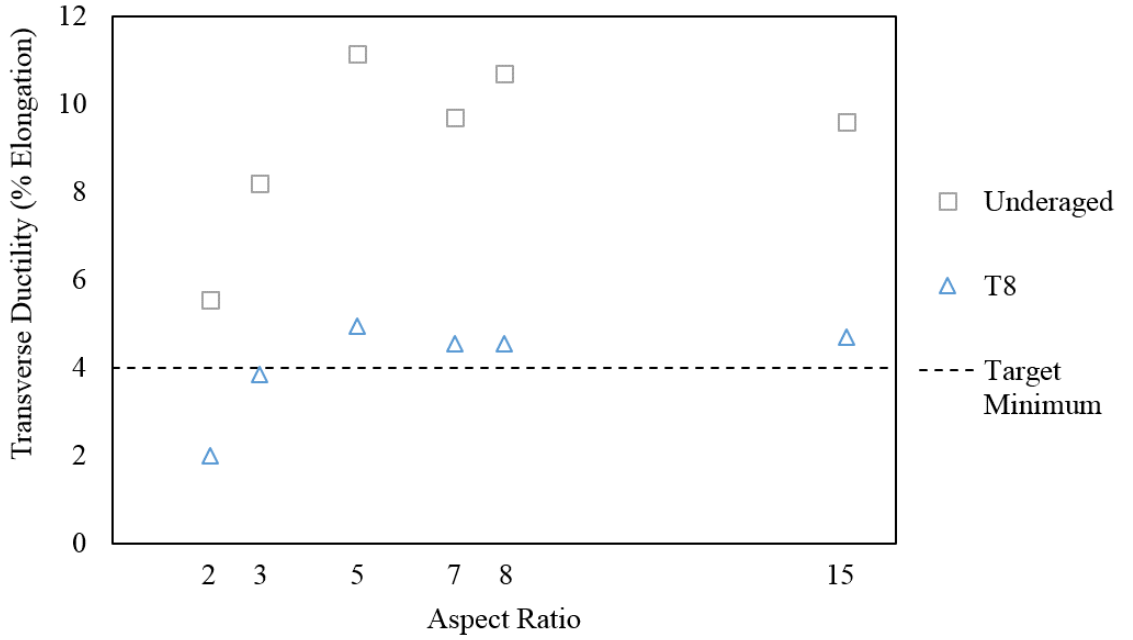

Figure 34: Transverse ductility variation with aspect ratio for underaged and T8 Al 2195 extrusions.

4.5 Texture Evolution with Aspect Ratio

X-ray diffraction (XRD) was performed on each extrusion to analyze macrotexture. The Al 2195 pole figures and orientation distribution functions (ODFs) can be seen in Figures

35-41. The Al 7075 pole figures are given in Figure 38-40. Qualitatively, it is evident that macrotexture changes with aspect ratio (AR) despite each profile having the same extrusion ratio (ER = 20). In the {111} pole figures, the transition from double-fiber to plate-like texture appears to occur between AR5 and AR8 for Al 2195 and Al 7075. Similarly, in Figures 41-42 the transition in the ODFs seems to occur gradually between AR5 and AR8 for both Al 2195 and Al 7075.

If macrotexture is the primary cause of anisotropy in Al 2195, then a similar texture evolution would not be expected to occur in more traditional alloys such as Al 7075. It appears that Al 2195 and Al 7075 exhibit similar texture evolutions from double-fiber to plate-like, with the transition falling between AR5 and AR8. Based on these results, macrotexture cannot be the primary cause of yield strength anisotropy observed in Al 2195. If it were, similar anisotropy should occur in Al 7075, and it is known that Al 7075 does not display the degree of yield strength anisotropy that Al 2195 does. Therefore, a more detailed analysis of the texture is required to determine possible mechanisms for yield strength anisotropy in Al 2195.

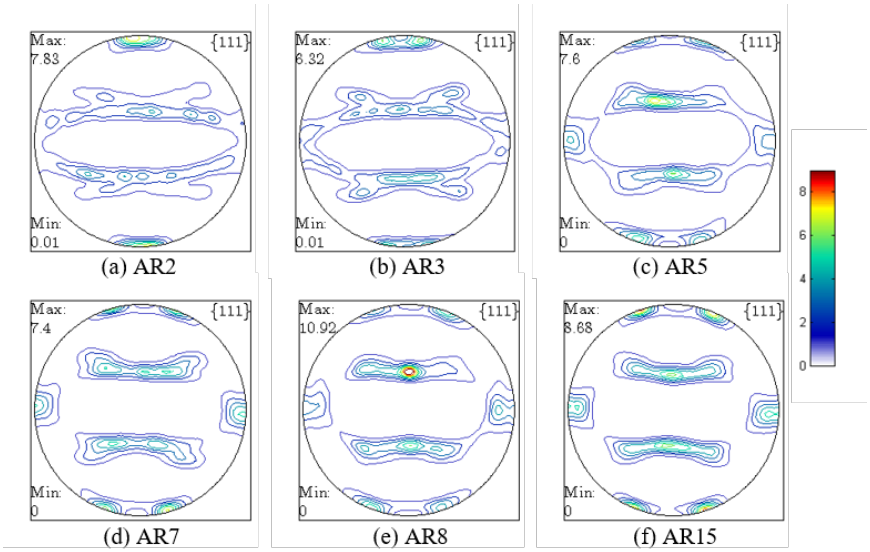

Figure 35: {111} Pole figures from F-temper Al 2195 extrusions.

A more quantitative way to represent texture is to identify the location of the intensity maximums in Euler space. For instance, the commonly observed β-fiber has an "ideal" or expected location; however, the location of the actual maximums is often shifted by several

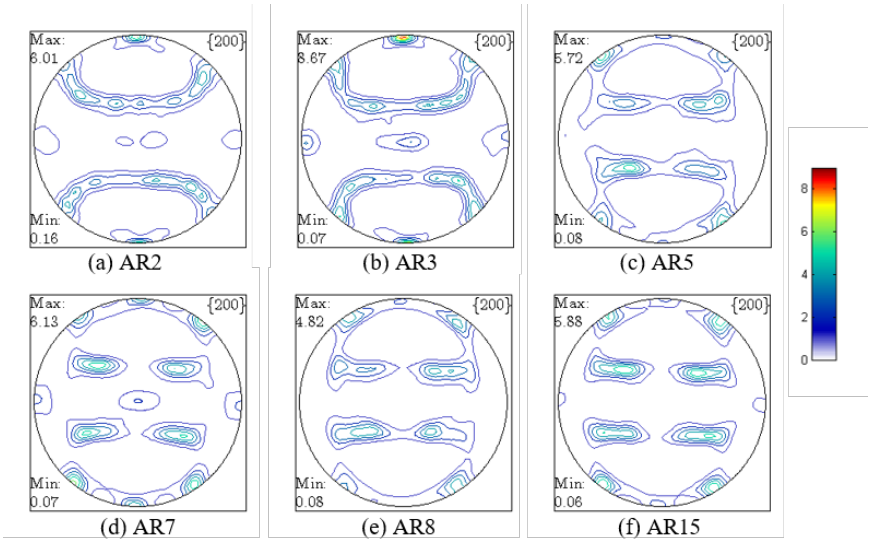

Figure 36: {200} Pole figures from F-temper Al 2195 extrusions.

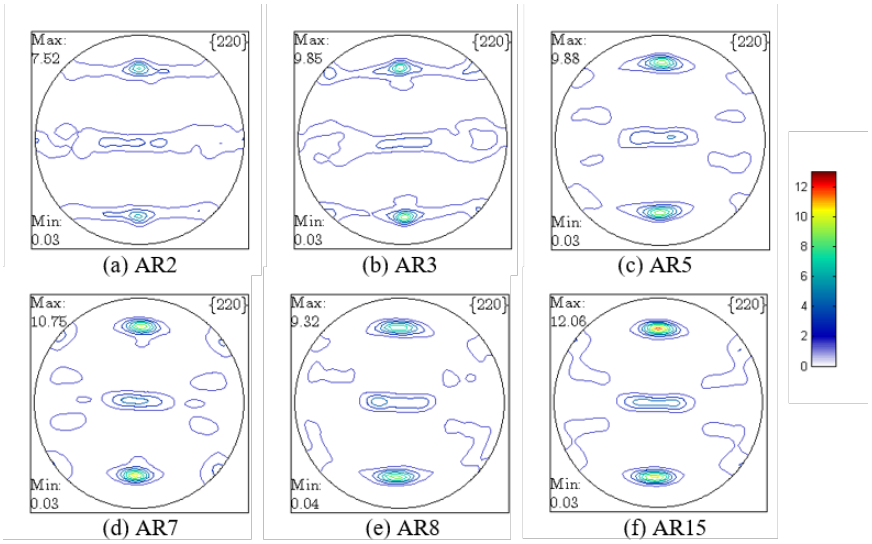

Figure 37: {220} Pole figures from F-temper Al 2195 extrusions.

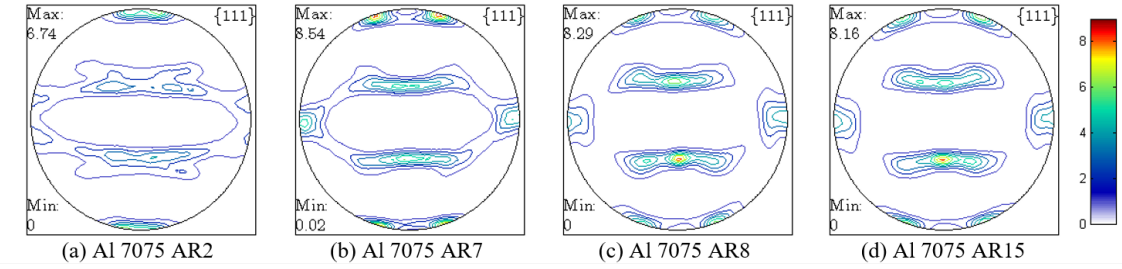

Figure 38: {111} Pole figures from Al 7075 F-temper extrusions.

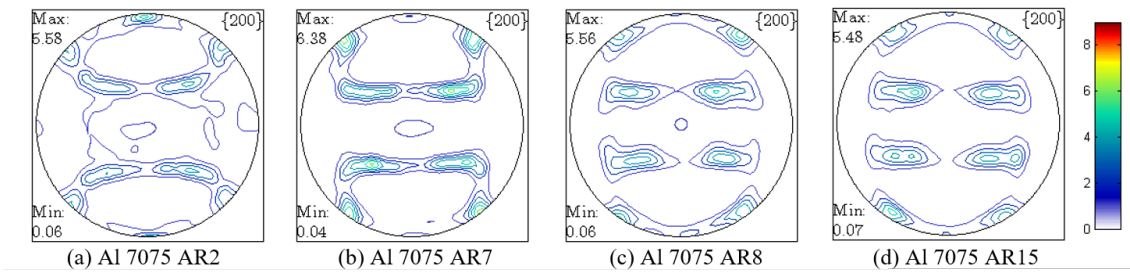

(a) Al 7075 AR2 (b) Al 7075 AR7 (c) Al 7075 AR8 (d) Al 7075 AR15

Figure 39: {200} Pole figures from Al 7075 F-temper extrusions.

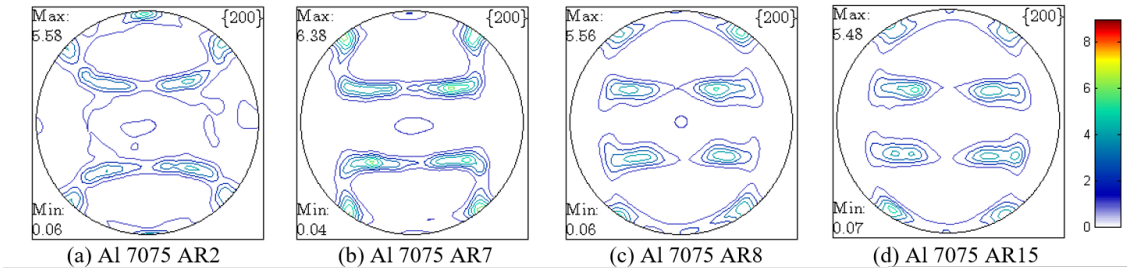

(a) Al 7075 AR2 (b) Al 7075 AR7 (c) Al 7075 AR8 (d) Al 7075 AR15

Figure 40: {220} Pole figures from Al 7075 F-temper extrusions.

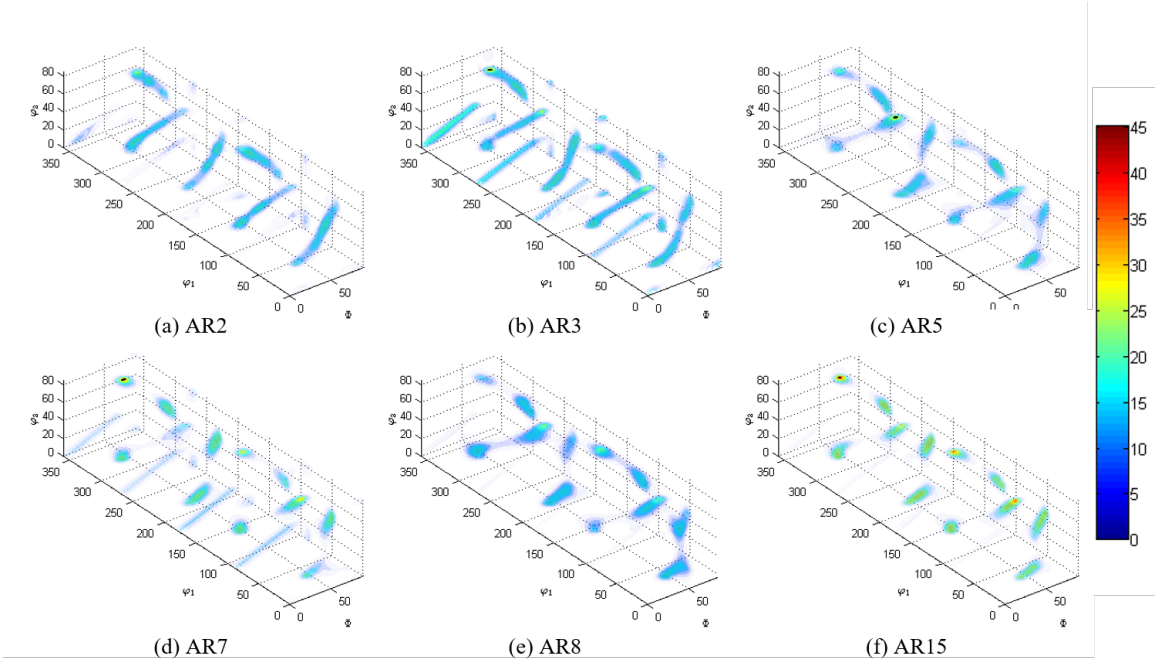

(a) AR2 (b) AR3 (c) AR5

(d) AR7 (e) AR8 (f) AR15

Figure 41: ODFs from F-temper Al 2195 extrusions.

degrees in Euler space as shown in Figure 43. Recall, that Hirsch and Lucke [99] reported that the β-fiber systematically shifts to smaller φ_1 and higher ϕ values with increasing

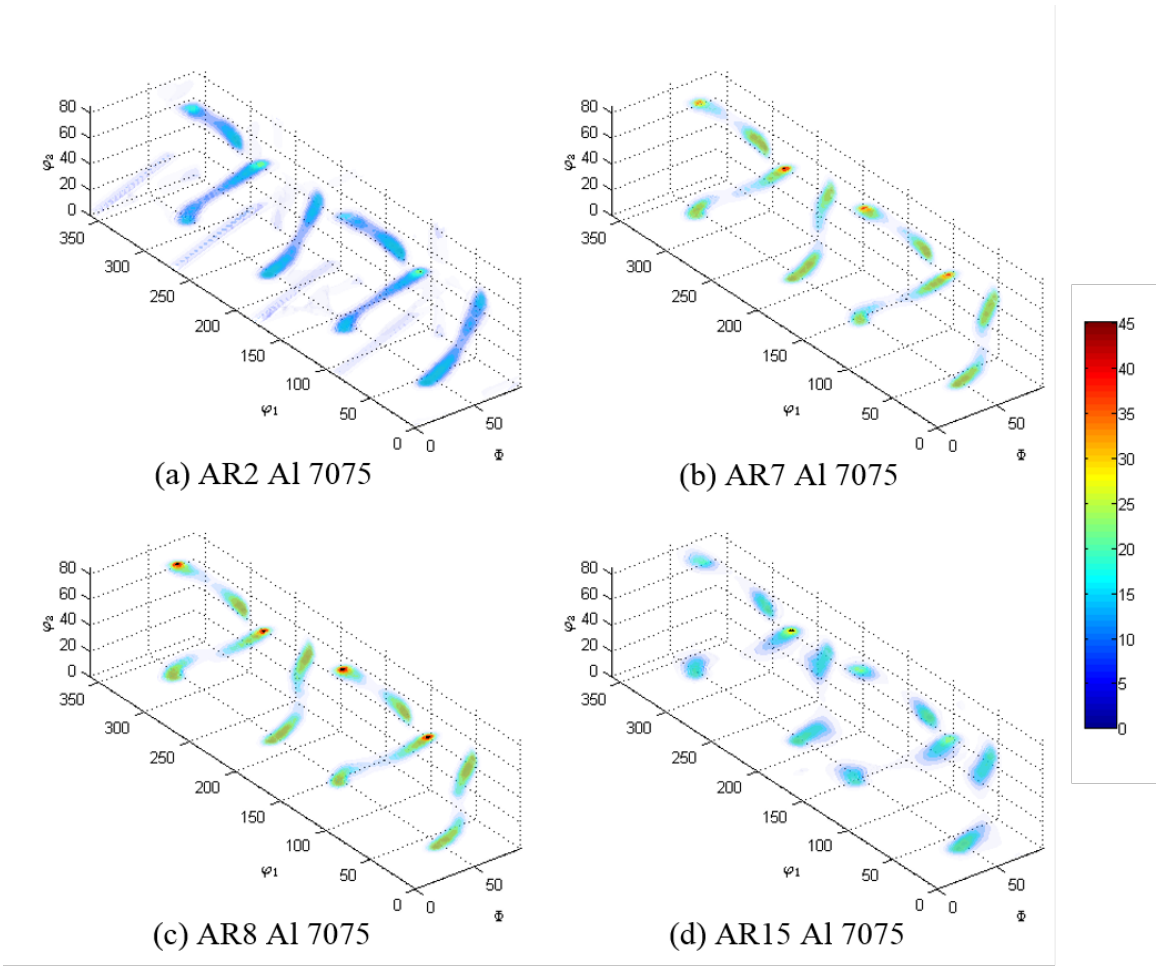

Figure 42: ODFs from Al 7075 F-temper extrusions.

strain. The location of the ideal and shifted β-fiber along φ_2 was plotted in Figure 44 for Al 2195. In this plot it is clear that the location of the β-fiber shifts from above the ideal value of φ_1 to below the ideal value around AR5. The location of AR5 appears to fall above the ideal φ_1 for low φ_2 values, along ideal φ_1 for intermediate φ_2 values, and then below ideal φ_1 for higher φ_2 values. This shift in the β-fiber quantitatively indicates that the transition in macro-texture occurs at AR5 for Al 2195. The location of the shifted β-fiber for Al 7075 is plotted in Figure 45. The shift in Al 7075 appears to occur around AR7-AR8. A systematic shift in the β-fiber has been reported with variation in strain [100]; however, this shift is likely not responsible for the difference in properties between low aspect ratio Al 2195 and Al 7075 extrusions.

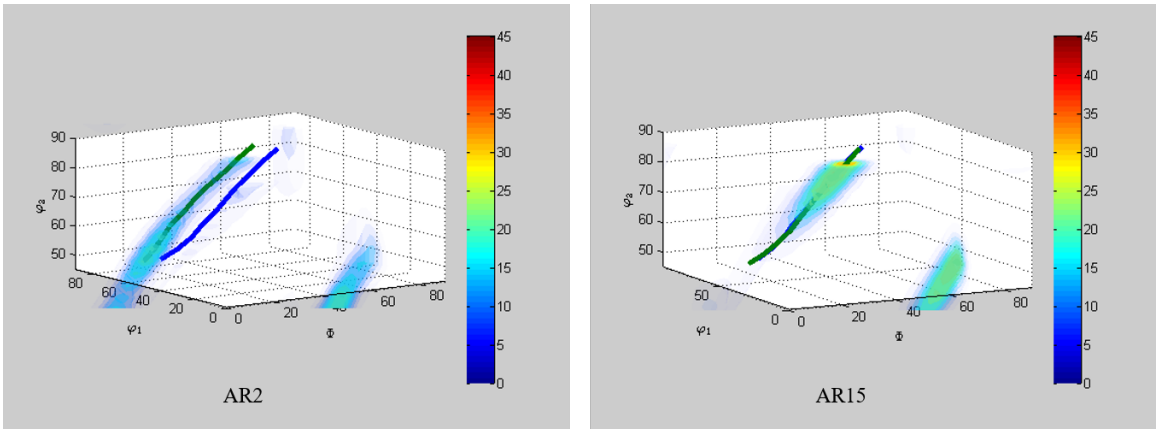

Figure 43: Location of the ideal and shifted β-fiber in Euler space for Al 2195 AR2 and AR15.

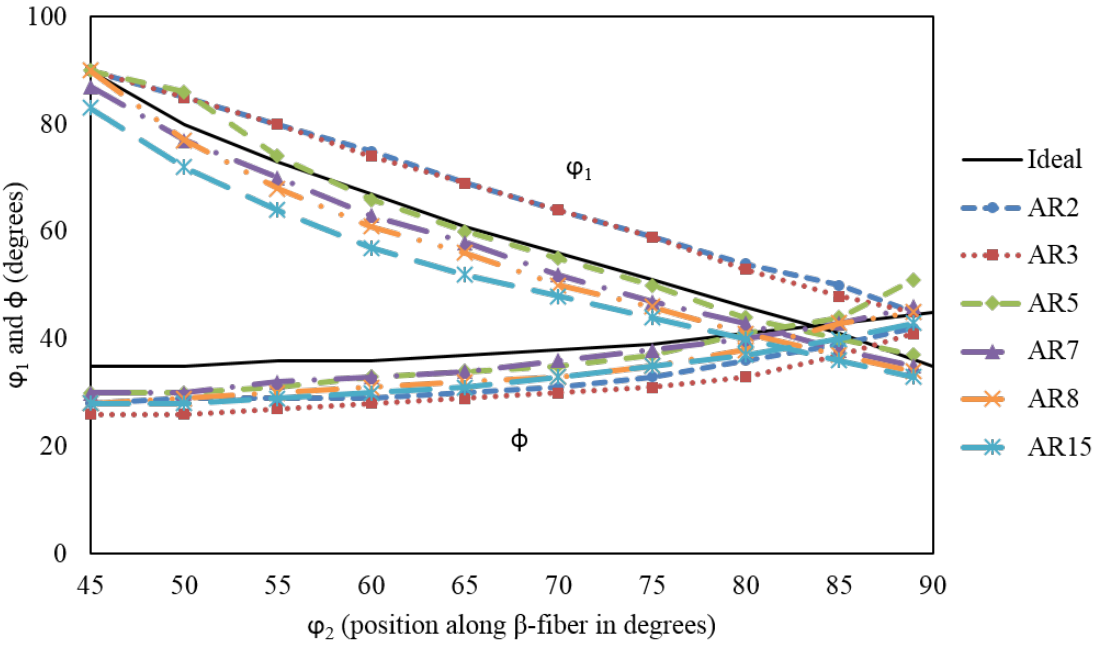

Figure 44: Location of the ideal and shifted β-fiber along φ_1 for Al 2195 extrusions.

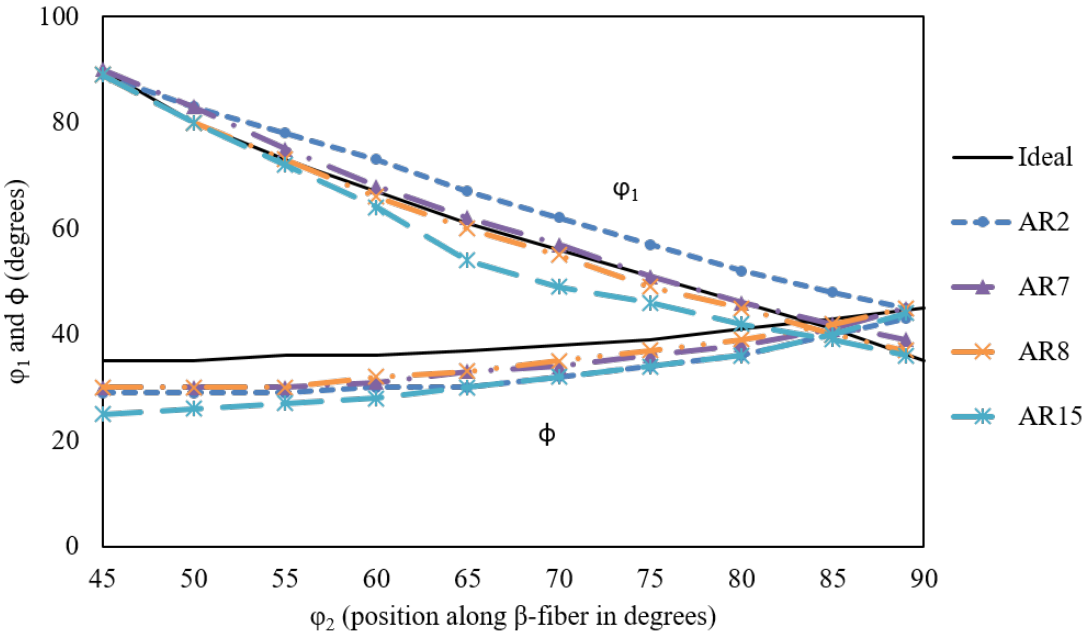

Figure 45: Location of the ideal and shifted β-fiber along φ_1 for Al 7075 extrusions.

Pole figures and ODFs offer an excellent visual representation of the macrotexture. The Al 2195 and Al 7075 AR2 {200} pole figures appear to differ; however, it is often difficult to decipher individual texture components from these plots. Instead, a computational component analysis was performed in MTEX to determine the percentage of each texture component from the ODFs. The primary deformation components in aluminum alloys are the Brass, S, and Copper components. Figure 46 shows how the percent of each component changes with aspect ratio for Al 2195 while Figure 47 shows this change for Al 7075. In Al 2195 and Al 7075, the Brass component increases with increasing aspect ratio and the Copper component decreases with increasing aspect ratio. The S component increased for Al 2195 but stayed relatively flat for Al 7075. Between the two alloy systems, Al 7075 had a higher overall percentage of the Brass texture while Al 2195 had a higher percentage of the Copper texture at AR2 and AR3.

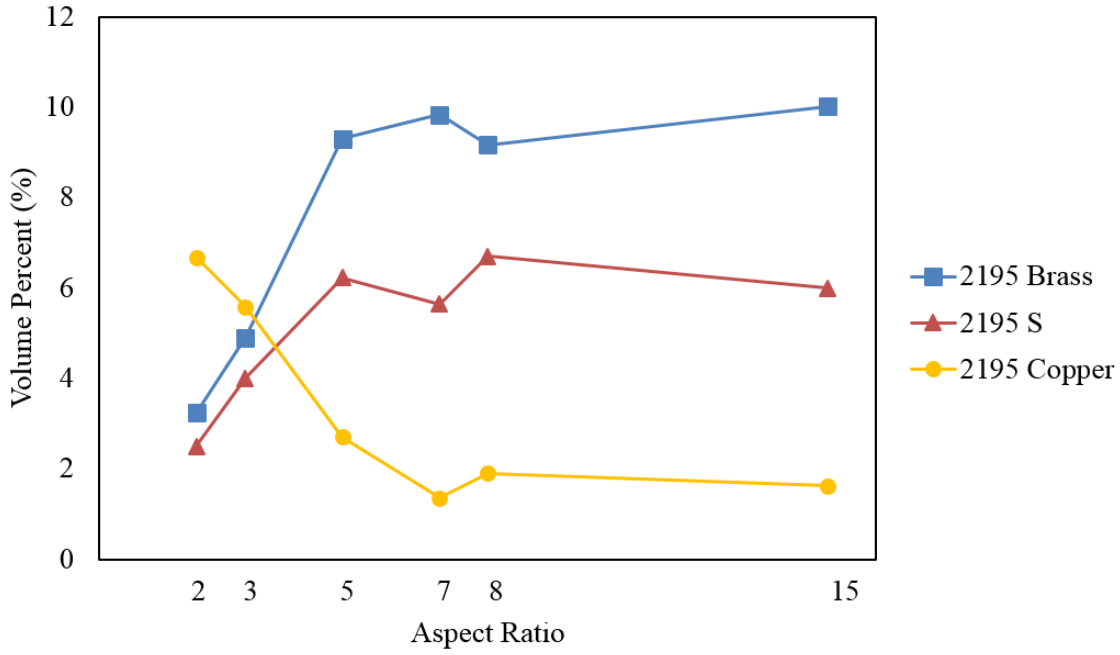

Figure 46: Volume percent of the Brass, S, and Copper components in F-temper Al 2195 extrusions.

The difference in the Copper component (located at (90°, 30°, 45°) in Euler space) between Al 2195 and Al 7075 can be seen in cross sections of the ODFs at φ_2 of 45° in Figure 48. The difference between Al 2195 and Al 7075 is also highlighted by plots of the

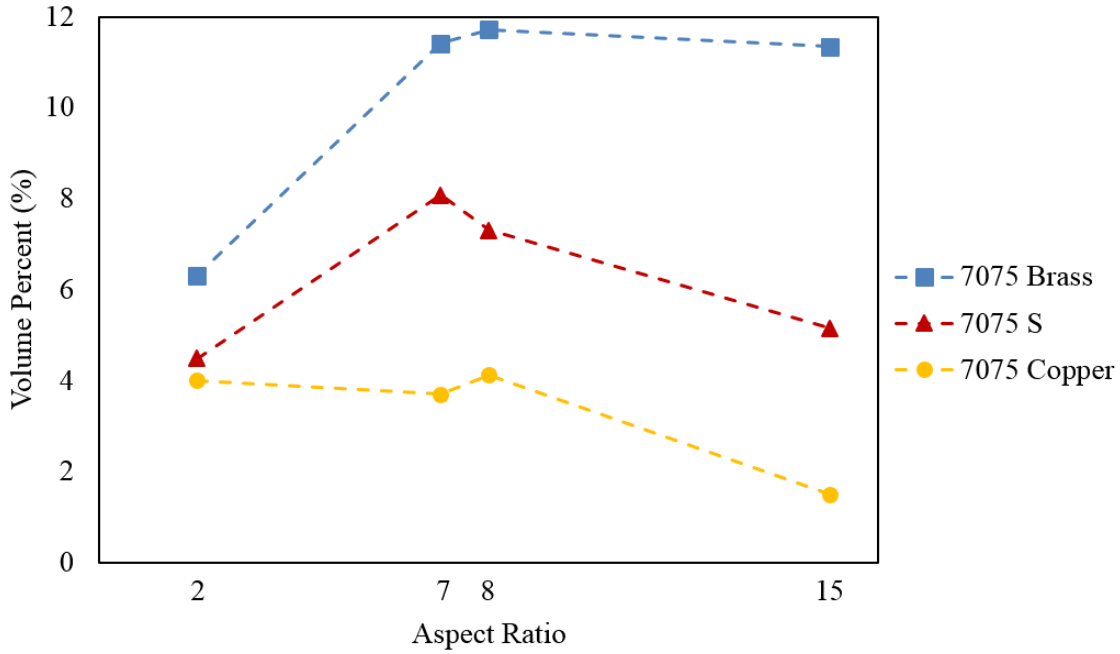

Figure 47: Volume percent of the Brass, S, and Copper components in F-temper Al 7075 extrusions.

β-fiber intensity along φ_2 where there is an increased intensity at φ_2=45° for AR2 and AR3 in Al 2195 (Figure 49) but not in Al 7075 (Figure 50). The S and Brass components are located at φ_2 of 65° and 90°, respectively.

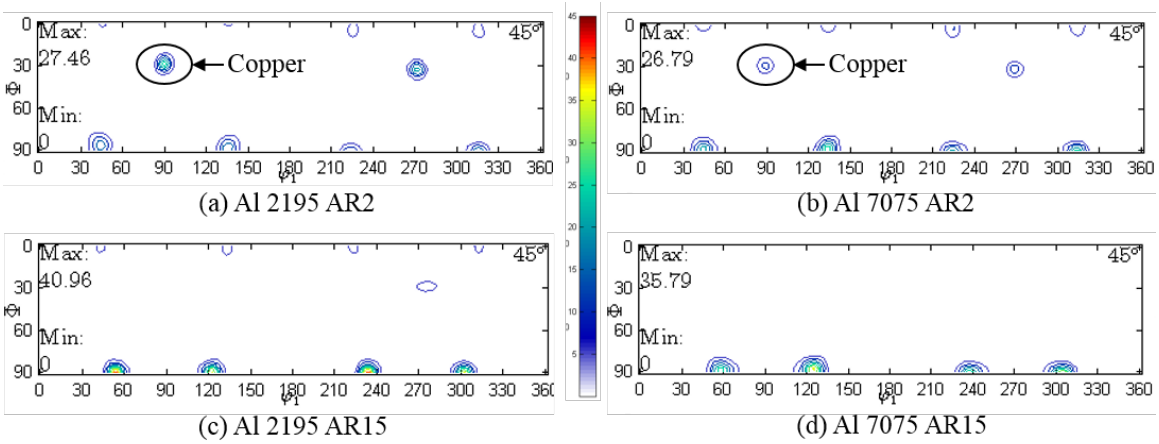

Figure 48: ODF cross sections at $\varphi_2 = 45°$ indicating the increased copper texture observed in the low aspect ratio Al 2195 extrusions versus Al 7075.

While it is clear that the Copper texture component was higher in the Al 2195 low AR samples, the Brass, S, and Copper components all vary simultaneously with aspect ratio in

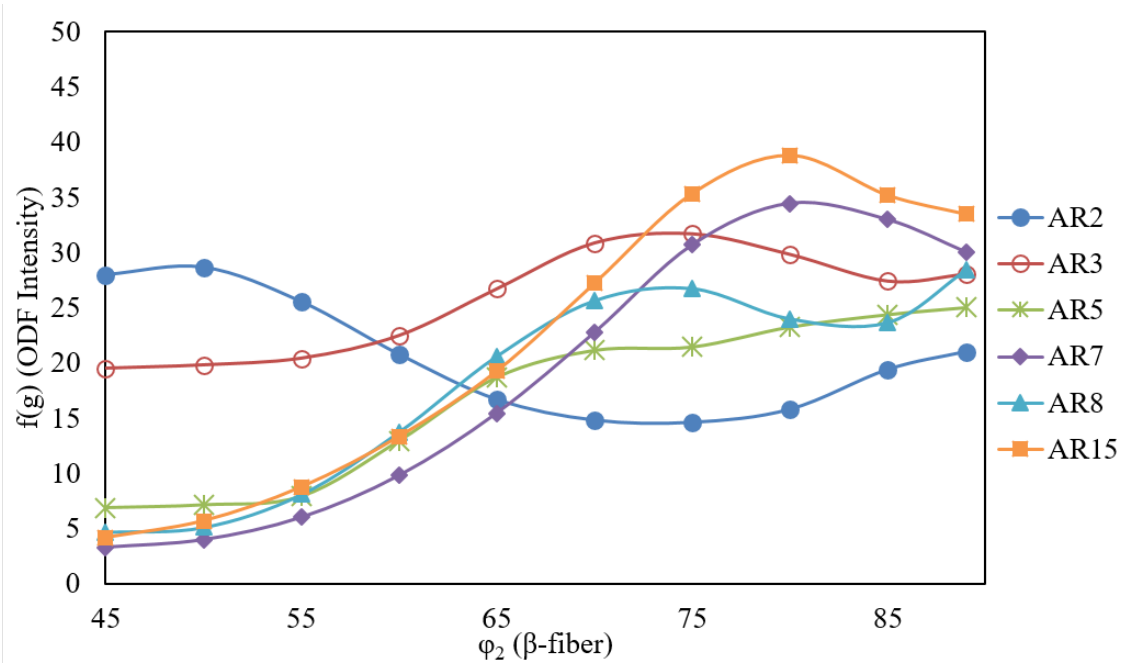

Figure 49: Intensity of the shifted β-fiber along φ_2 for F-temper Al 2195 extrusions.

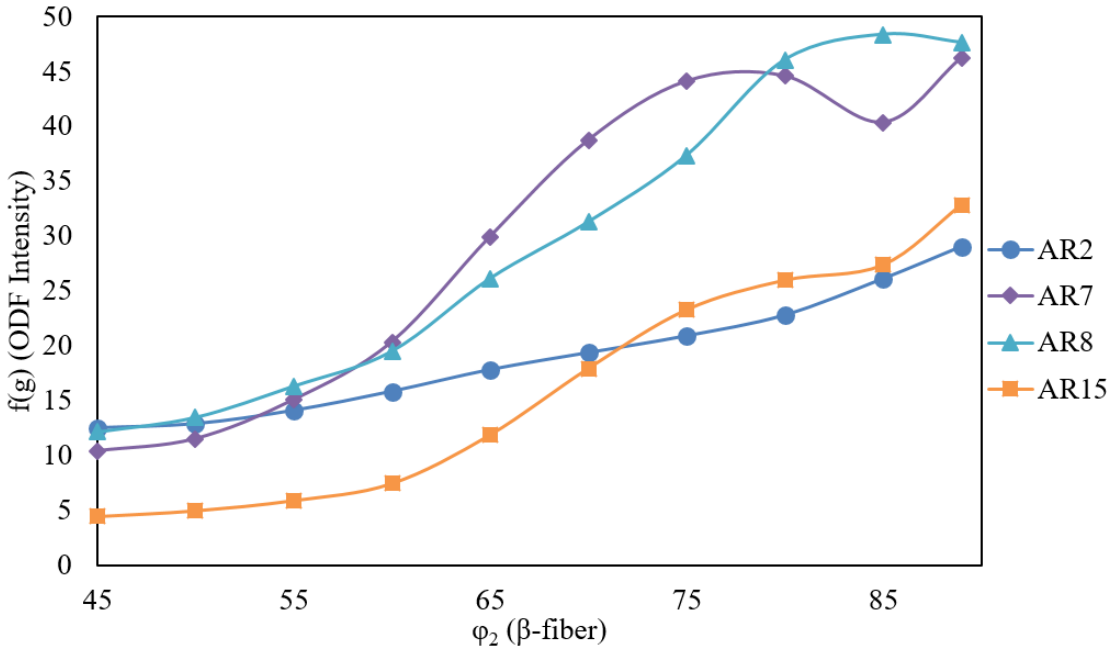

Figure 50: Intensity of the shifted β-fiber along φ_2 for F-temper Al 7075 extrusions.

both Al 2195 and Al 7075. In order to capture this complex variation in a single parameter, a new method of quantifying these commonly observed texture components was developed. Plates typically contain the Brass, S, and Copper textures, where Brass is present at the

highest concentration and Copper at the lowest. Based on the relative amounts of Brass, S, and Copper typically observed, Equation 10 was derived to determine the relative "plate-likeness" of a rolled sample.

$$PL \quad Number = \frac{(Bs - S) + (S - Cu) + (Bs - Cu)}{Bs + S + Cu} = \frac{2(Bs - Cu)}{Bs + S + Cu} \tag{10}$$

In this equation, $PLNumber$ is the Plate-Like Number, Bs is the volume percent of the Brass component, S is the volume percent of the S component, and Cu is the volume percent of the Copper component. This equation assumes that a large spread between the Brass, S, and Copper components creates an over-all more plate-like macrotexture which is represented by a higher PL Number. A PL Number equal to 0 corresponds to equal fractions of Brass and Copper. Using this parameter, it was found that a negative PL Number corresponds to a higher fraction of the Copper texture than the Brass texture. A negative PL Number, as seen in Figure 51, was only observed for Al 2195 AR2 and AR3 extrusions.

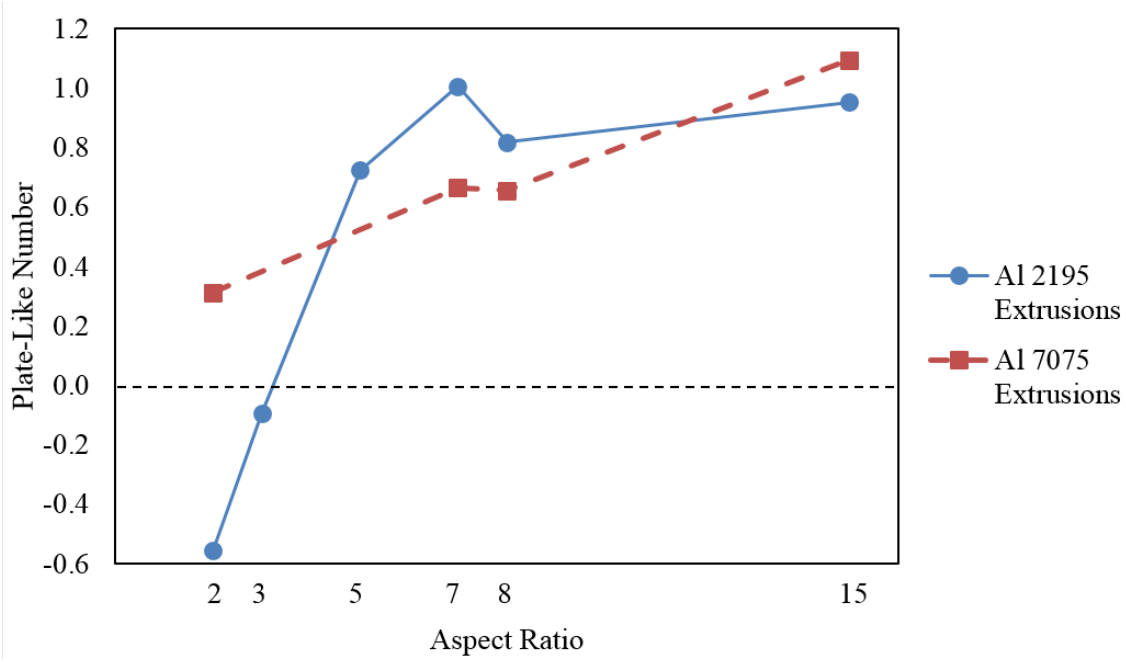

Figure 51: Variation in the plate-like number with aspect ratio for Al 2195 and Al 7075 extrusions.

4.6 Microstructural Evolution with Aspect Ratio

Micrographs were taken from the middle of each of the three planes (L-ST, T-ST, and L-LT as indicated in Figure 4) and used to construct 3D images to visualize the grain and particle morphologies. The microstructures of Al 2195 (Figure 52) and Al 7075 (Figure 53) evolved as the aspect ratio was changed, despite each profile having the same extrusion ratio. For Al 2195, the AR2 and AR3 samples had long, cylindrical grains, often referred to as cigar-like grains. At AR5 the grains began to flatten and become more pancake-like. Similarly, for Al 7075, cigar-like grains were observed in the AR2 Al 7075 sample and pancake-like grains in the AR15 sample. Polarized light microscopy was also performed on AR2 and AR15 for both Al 2195 and Al 7075 to highlight the difference between cigar-like and pancake-like grains (Figures 54-55).

The area of the grains in the L-ST plane for Al 2195 decreases with aspect ratio (108 μm^2 for AR2, 69 μm^2 for AR8, and 46 μm^2 for AR15) based on electron backscatter diffraction (EBSD) performed at Deakin University on the center of the L-ST planes (Figure 56). A misorientation threshold was set to greater than 15° so only high angle grain boundaries were captured.

Particle morphologies in the F-temper Al 2195 extrusions were observed at 500X as seen in Figures 57, 58, and 59. With increasing aspect ratio, the second phase particles became smaller and more spherical, with the most drastic change occurring between AR8 and AR15. This change can be seen most predominately in the L-LT plane where long, elongated, plate-like particles are observed in AR2-AR8 (Figures 59a-e), but no such particles are seen in AR15 (Figure 59f). The plate-like particles in AR2 and the spherical particles in AR15 were observed throughout the thickness in the L-ST plane as shown in Figure 60 where the extrusion surface is at the top of the image. The microstructural variation in Al 2195 is represented in three-dimensional space at 500X for AR2 and AR15 in Figure 61. No such change in particle morphology was observed in the F-temper Al 7075 extrusions. The second phase particles in Al 7075, as shown in Figure 62b, appear spherical in nature for both AR2 and AR15.

To investigate recrystallization, F and W-temper L-ST (longitudinal) samples from Al 2195 and Al 7075 were Barker's etched and observed under polarized light microscopy. At the center of the L-ST plane, substructure was observed in Al 2195 F-temper samples (Figures 63a and c). After solution heat treatment, this substructure was mostly recovered with some substructure still visible in the grain interiors as indicated by the variation in shading (Figures 63b and d). Solution heat treatment of Al 2195 induced primarily static recovery with negligible recrystallization in the interior of the extrusions. Images from the middle of the L-ST plane for Al 7075 (Figure 64) also indicated negligible static recrystallization. Increased strain at the surface of extrusions, however, often leads to a layer of large, fully recrystallized grains.

From images taken at the surface of the Al 2195 F-temper samples, Figure 65, it appears that the bulk does not experience dynamic recrystallization. The surface of AR15, seen in Figure 65d, shows a thin layer of recrystallized grains. The extrusions were air-cooled so this layer was likely due to static recrystallization during cooling. The Al 2195 solution heat treated, W-temper, samples showed distinct recrystallized surface layers (Figures 66-67). Five micrographs were taken at 50X and five measurements were made on each micrograph for a total of 25 measurements per sample. The average layer thicknesses are reported in Table 7. There was no significant correlation between aspect ratio and the thickness of the recrystallized surface layer for Al 2195. Similarly, the Al 7075 W-temper samples also demonstrated no dynamic recrystallization and no correlation between aspect ratio and thickness of the recrystallized surface layer. Thin layers across the entire sample were observed for AR2 and AR15 (Figures 68a and d). Only patchy regions of recrystallized surface grains were observed in AR7 and AR8 (Figures 68b and c).

Table 7: Average thickness of the recrystallized surface layer in Al 2195 extrusions after solution heat treatment.

Aspect Ratio	Thickness of the Recrystallized Surface Layer (μm)
2	84.6 ± 13.4
3	93.7 ± 15.5
5	90.2 ± 10.3
7	87.0 ± 12.6
8	101.5 ± 11.9
15	194.6 ± 18.9

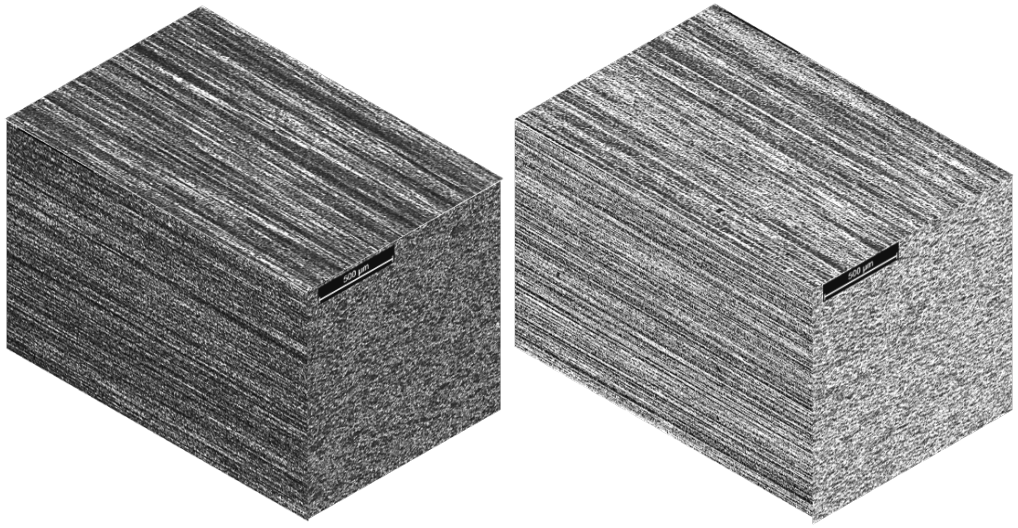

(a) AR2

(b) AR3

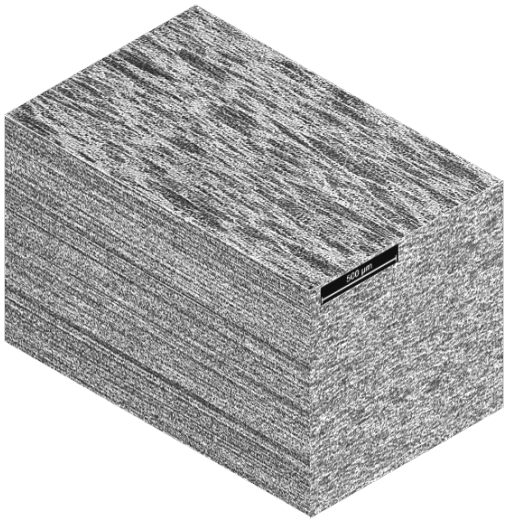

(c) AR5

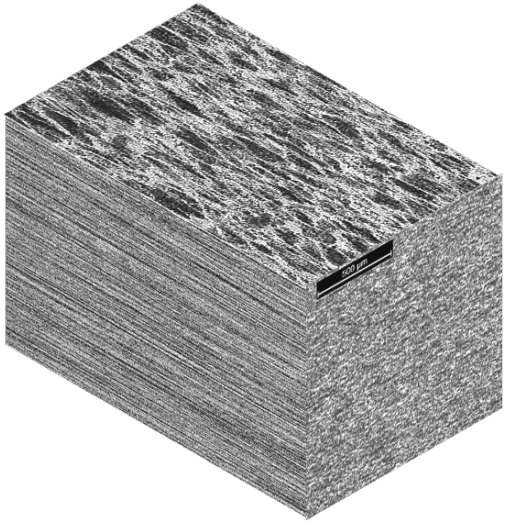

(d) AR7

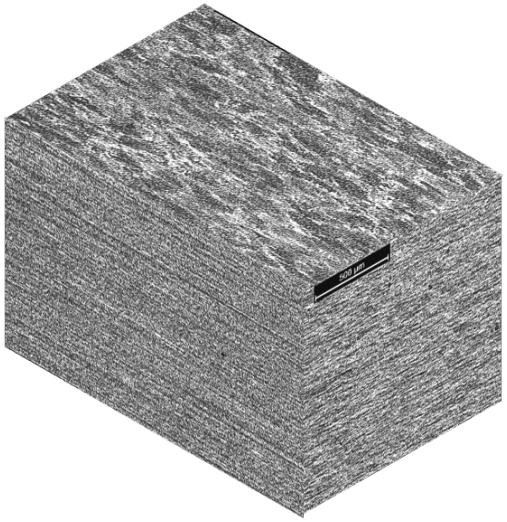

(e) AR8

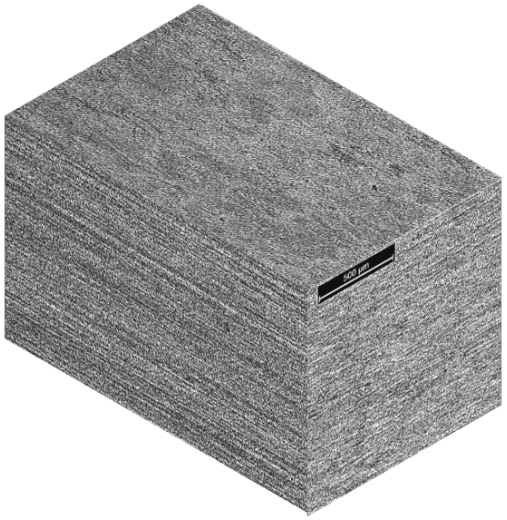

(f) AR15

Figure 52: Bright field optical micrographs (Keller's etch 50X) showing the three dimensional grain structures of Al 2195 F-temper (a) AR2, (b) AR3, (c) AR5, (d) AR7, (e) AR8, and (f) AR15 extrusions.

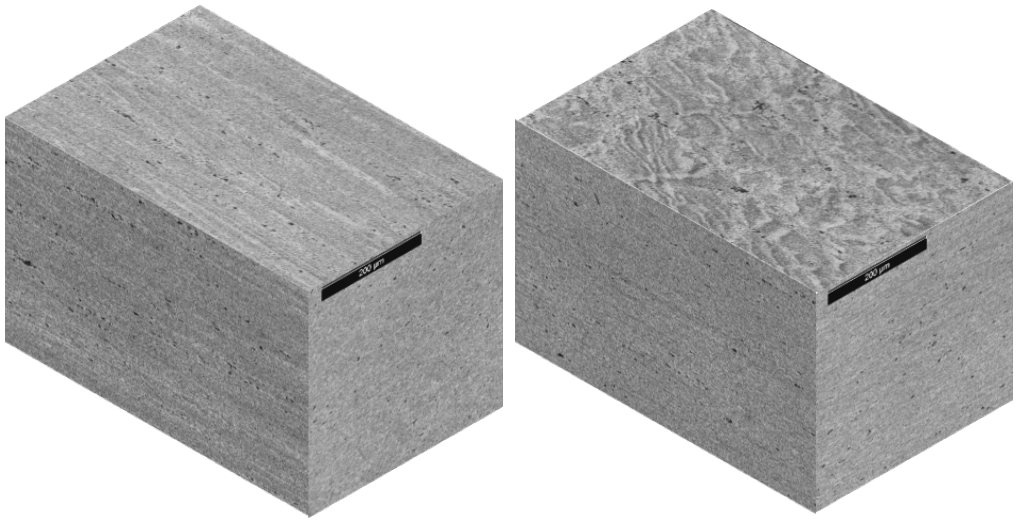

(a) Al 7075 AR2 (b) Al 7075 AR15

Figure 53: Bright field optical micrographs (Keller's etch 200X) showing the three dimensional grain structures of Al 7075 F-temper (a) AR2 and (b) AR15 extrusions.

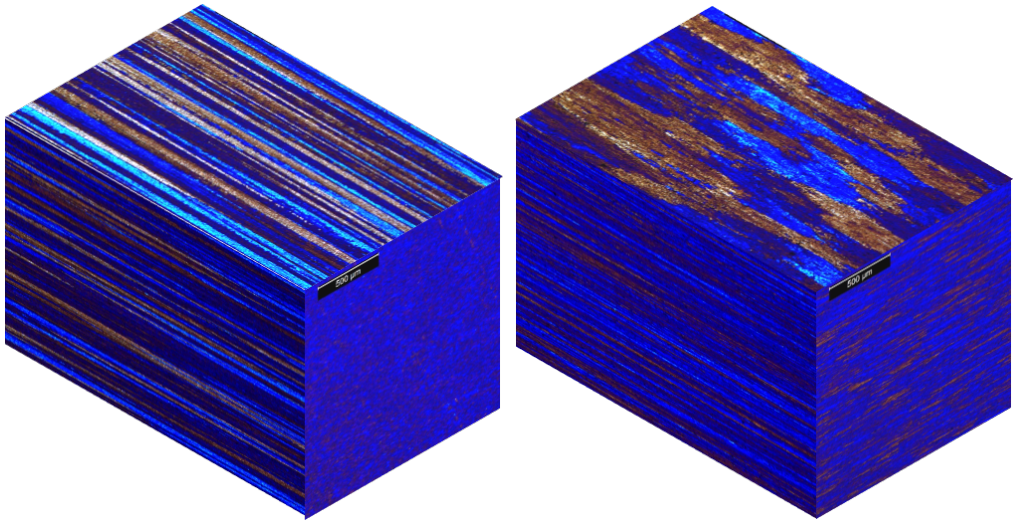

(a) AR2 (b) AR15

Figure 54: Polarized light micrographs (Barker's etch 50X) showing the three dimensional microstructures of Al 2195 F-temper (a) AR2 and (b) AR15 extrusions.

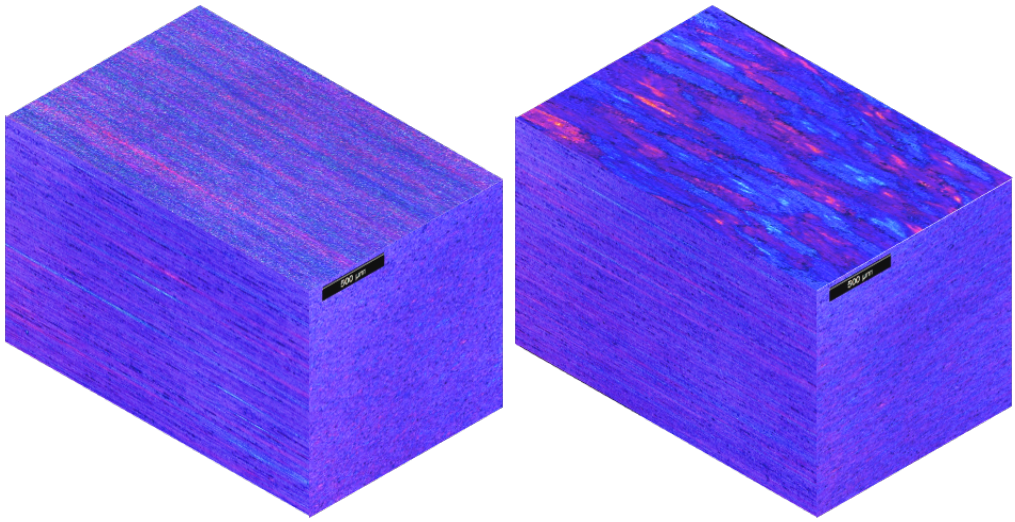

(a) AR2 (b) AR15

Figure 55: Polarized light micrographs (Barker's etch 50X) showing the three dimensional microstructures of Al 7075 F-temper (a) AR2 and (b) AR15 extrusions.

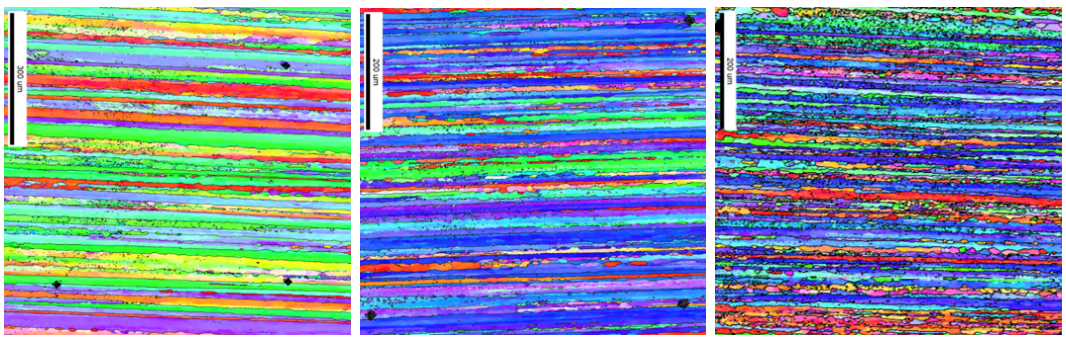

(a) AR2 (b) AR8 (c) AR15

Figure 56: EBSD images from the L-ST plane of F-temper Al 2195 (a) AR2, (b) AR8, and (c) AR15 extrusions. Courtesy of Dr. Thomas Dorin at Deakin University.

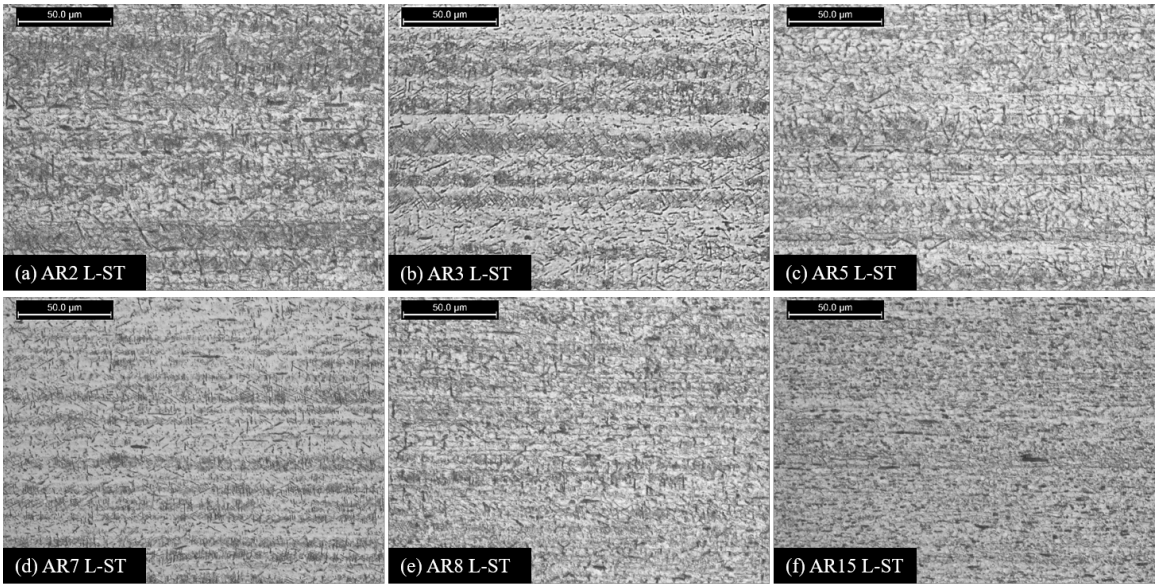

Figure 57: Bright field optical micrographs (Keller's etch) of F-temper Al 2195 from the middle of the L-ST (longitudinal) plane at 500X.

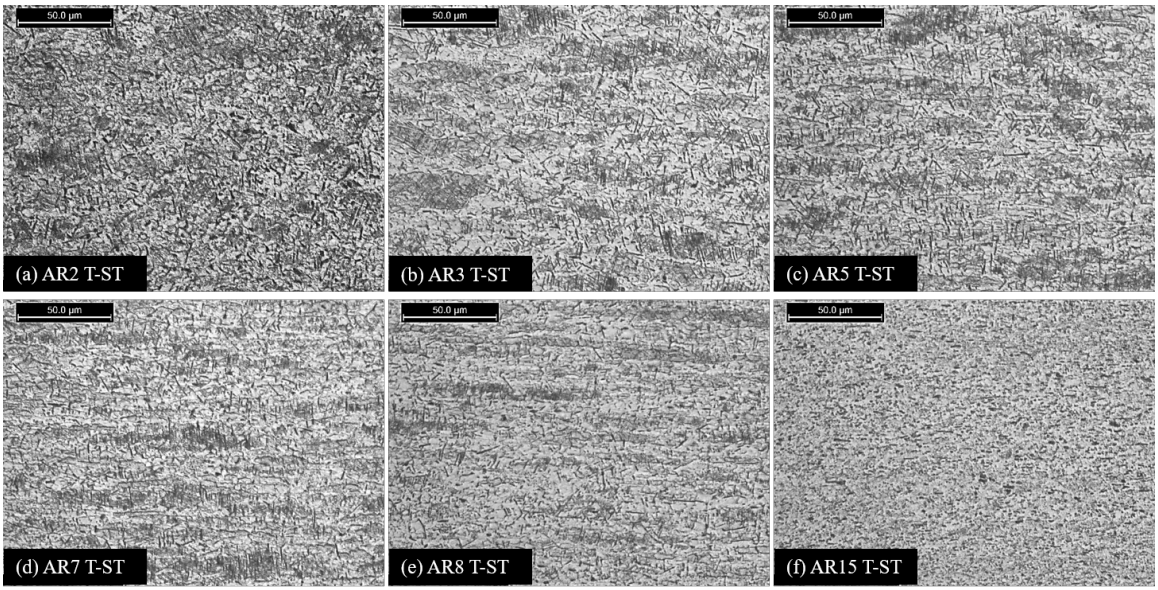

Figure 58: Bright field optical micrographs (Keller's etch) of F-temper Al 2195 from the middle of the T-ST (transverse) plane at 500X.

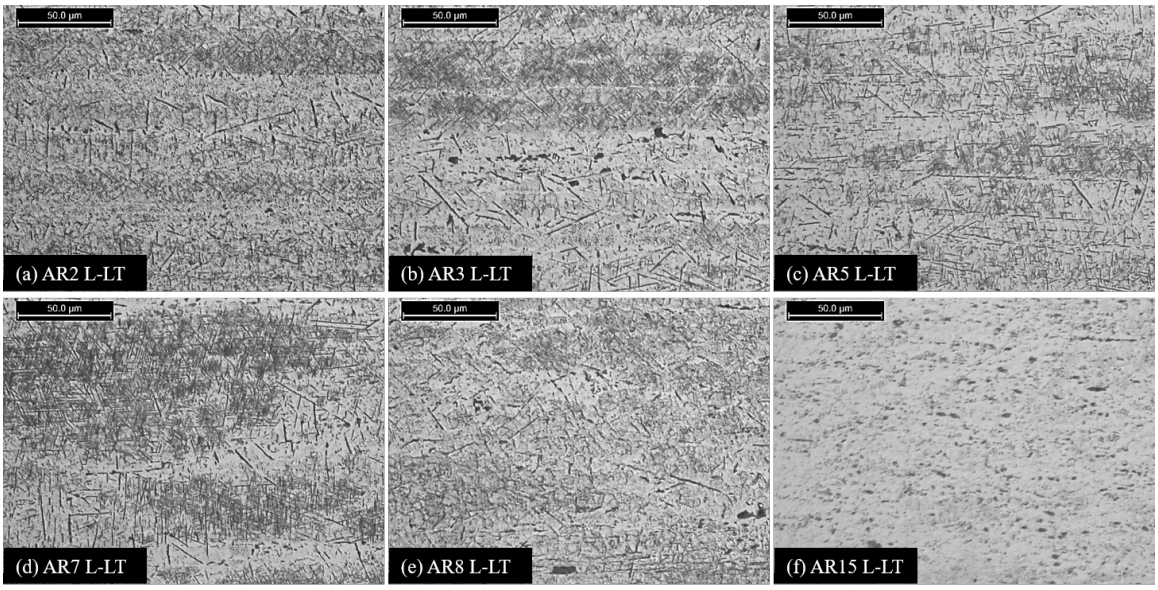

Figure 59: Bright field optical micrographs (Keller's etch) of F-temper Al 2195 from the middle of the L-LT plane at 500X.

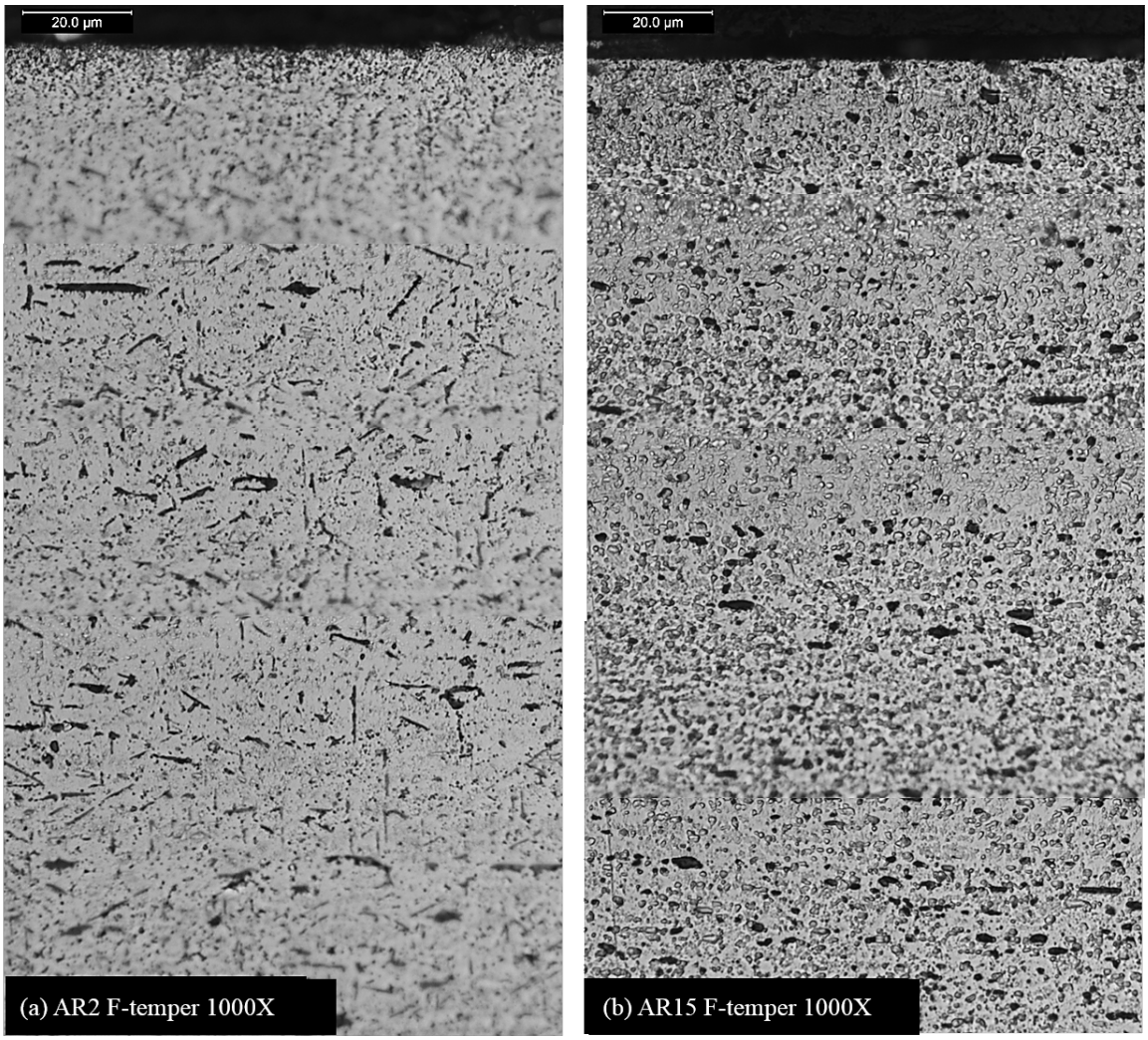

Figure 60: Bright field optical micrographs (Keller's etch) of F-temper Al 2195 showing the through-thickness variation in particle morphology for (a) AR2 and (b) AR15 at 1000X.

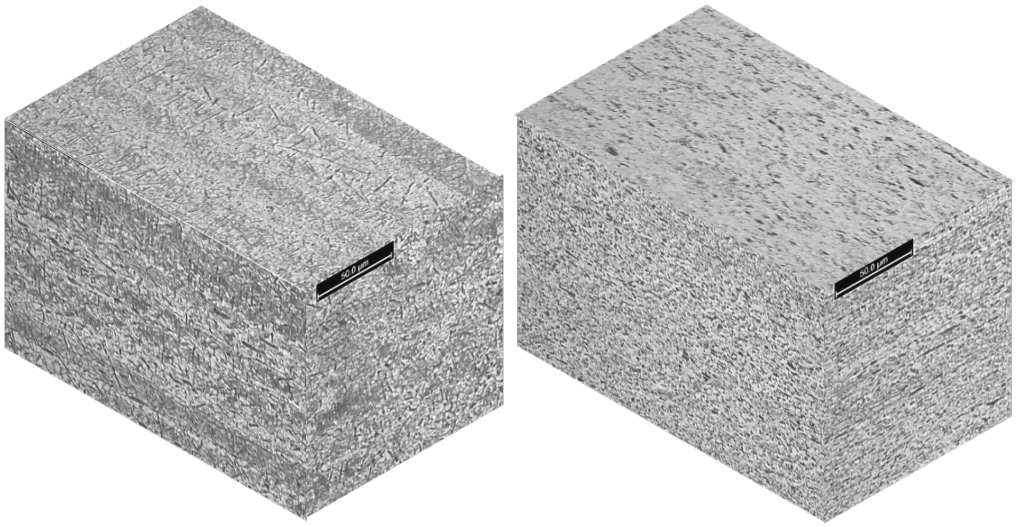

(a) Al 2195 AR2 (b) Al 2195 AR15

Figure 61: Bright field optical micrographs (Keller's etch 500X) showing the three dimensional microstructures and particle morphologies of Al 2195 F-temper (a) AR2 and (b) AR15 extrusions.

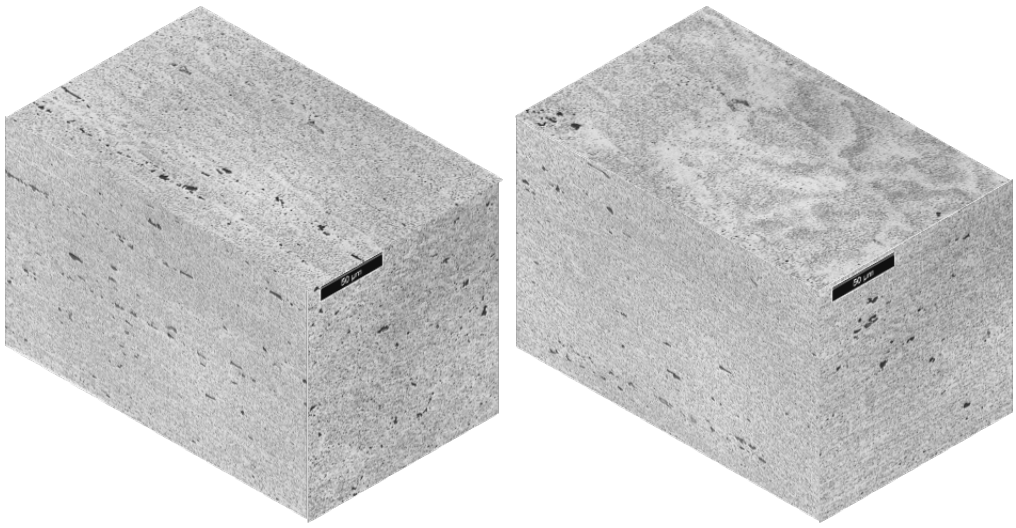

(a) Al 7075 AR2 (b) Al 7075 AR15

Figure 62: Bright field optical micrographs (Keller's etch 500X) showing the three dimensional microstructures and particle morphologies of Al 7075 F-temper (a) AR2 and (b) AR15 extrusions.

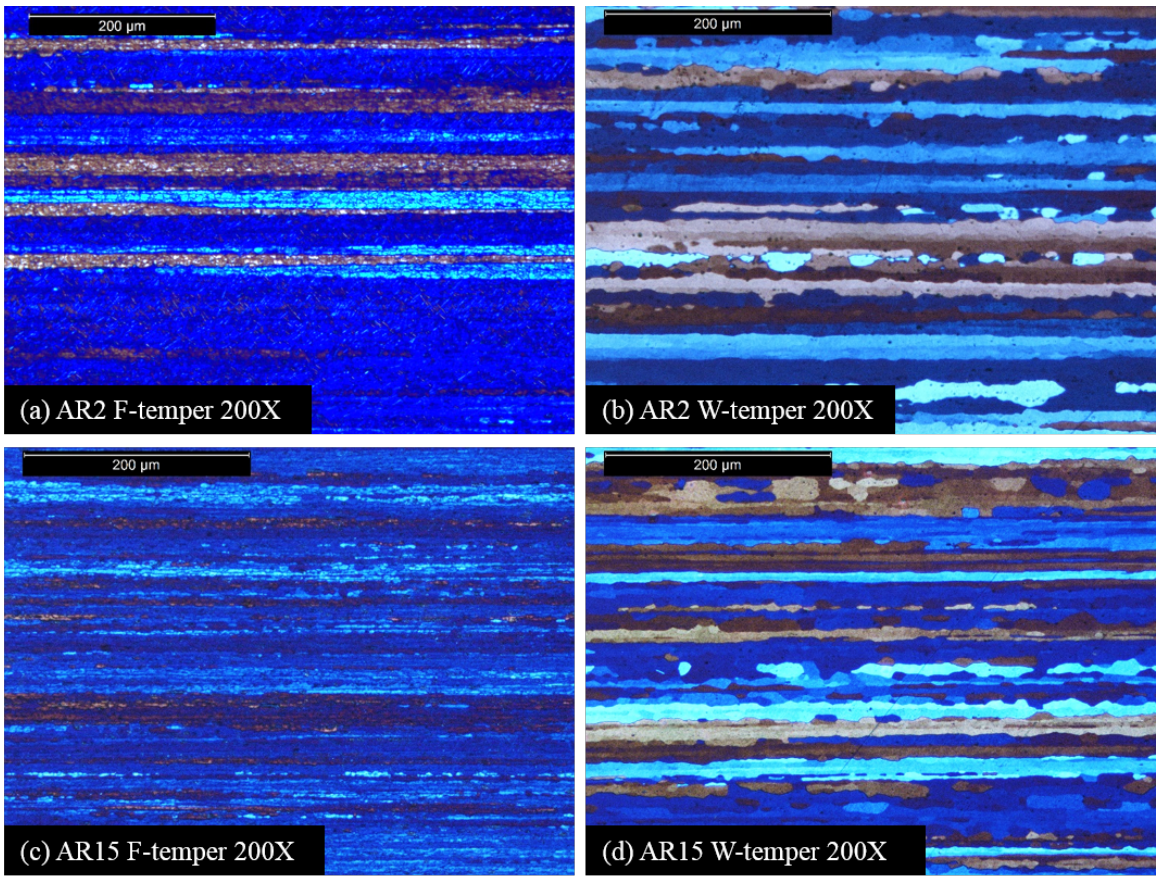

Figure 63: Polarized light optical micrographs (Barker's etch 200X) of Al 2195 extrusions from the middle of the L-ST plane for (a) AR2 F-temper, (b) AR2 W-temper, (c) AR15 F-temper, and (d) AR15 W-temper.

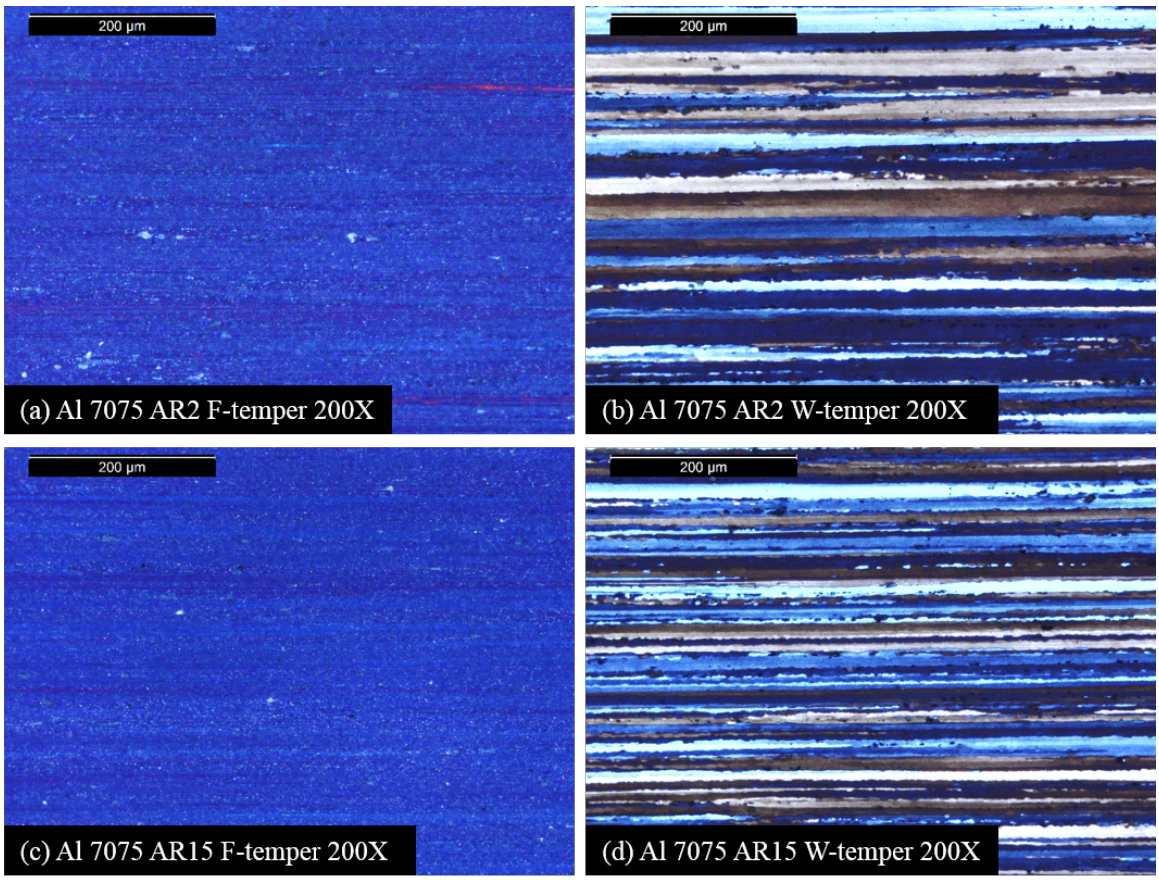

Figure 64: Polarized light optical micrographs (Barker's etch 200X) of Al 7075 extrusions from the middle of the L-ST plane for (a) AR2 F-temper, (b) AR2 W-temper, (c) AR15 F-temper, and (d) AR15 W-temper.

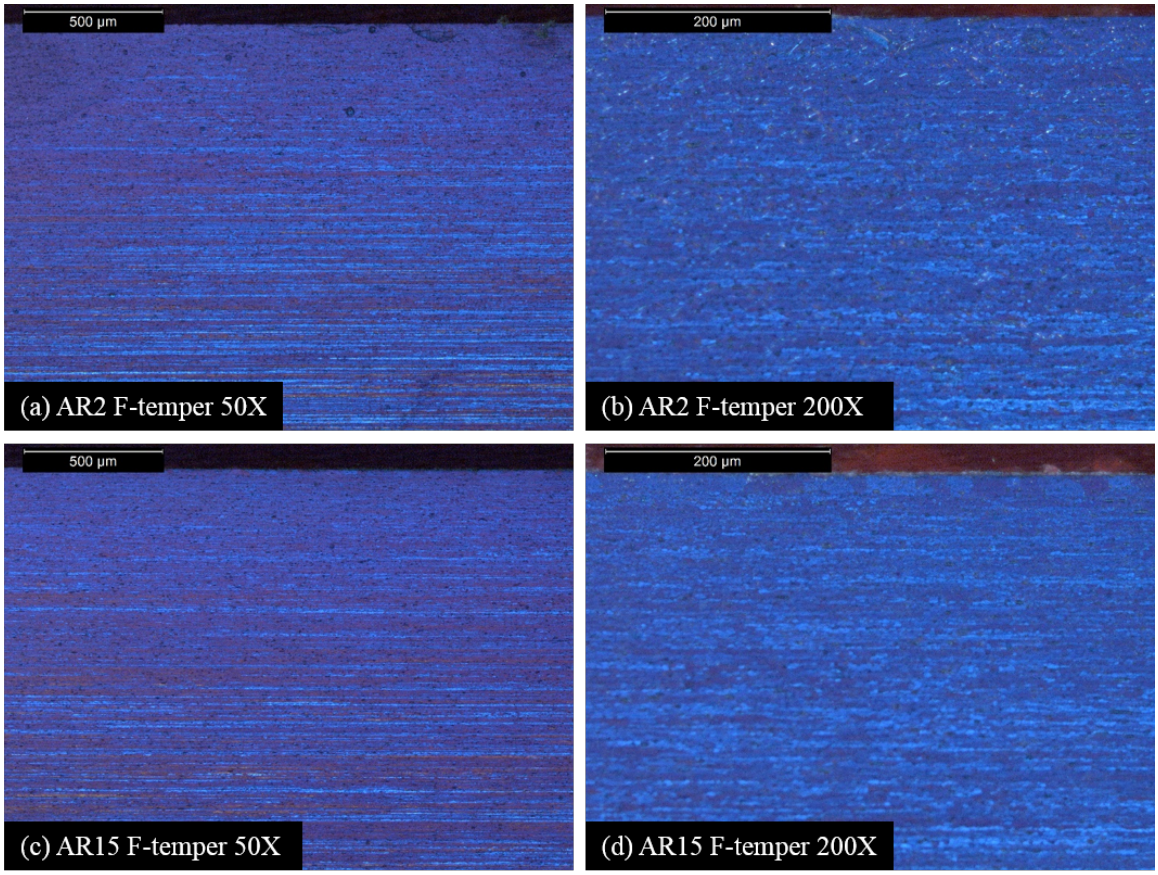

Figure 65: Polarized light optical micrographs (Barker's etch) of F-temper Al 2195 extrusions from the edge of the L-ST plane for (a) AR2 at 50X, (b) AR2 at 200X, (c) AR15 at 50X, and (d) AR15 at 200X.

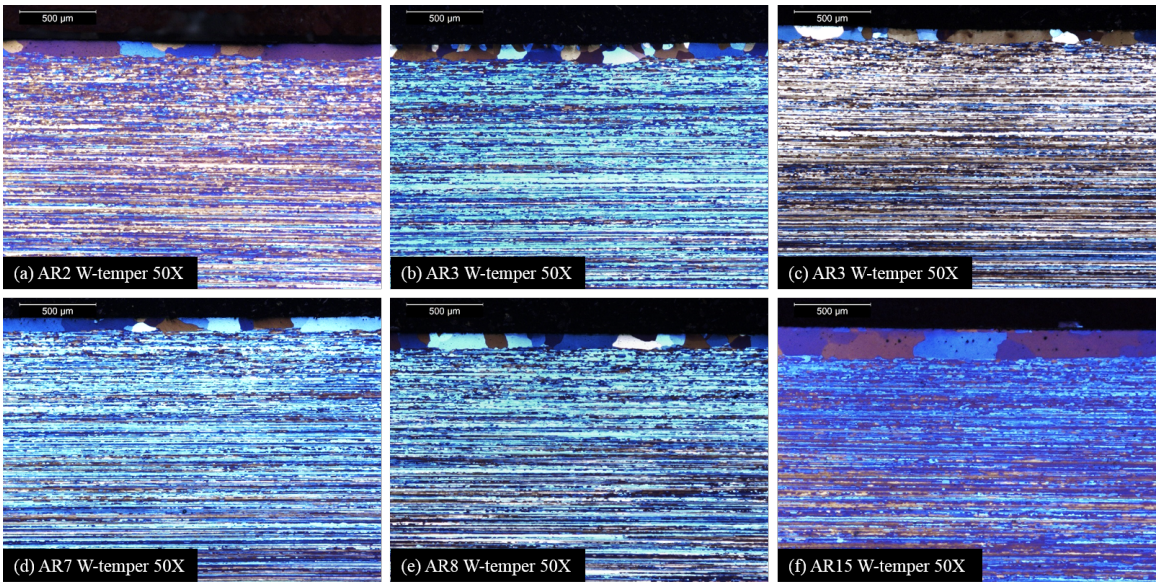

Figure 66: Polarized light optical micrographs (Barker's etch 50X) of W-temper Al 2195 extrusions from the edge of the L-ST plane for (a) AR2, (b) AR3, (c) AR5, (d) AR7, (e) AR8, and (f) AR15.

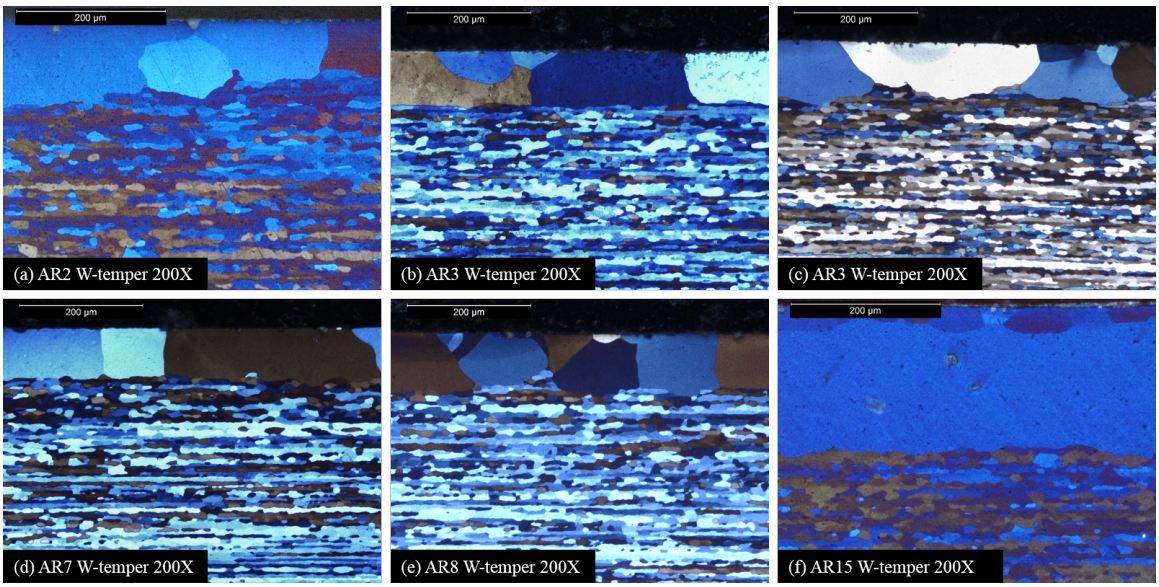

Figure 67: Polarized light optical micrographs (Barker's etch 200X) of W-temper Al 2195 extrusions from the edge of the L-ST plane for (a) AR2, (b) AR3, (c) AR5, (d) AR7, (e) AR8, and (f) AR15.

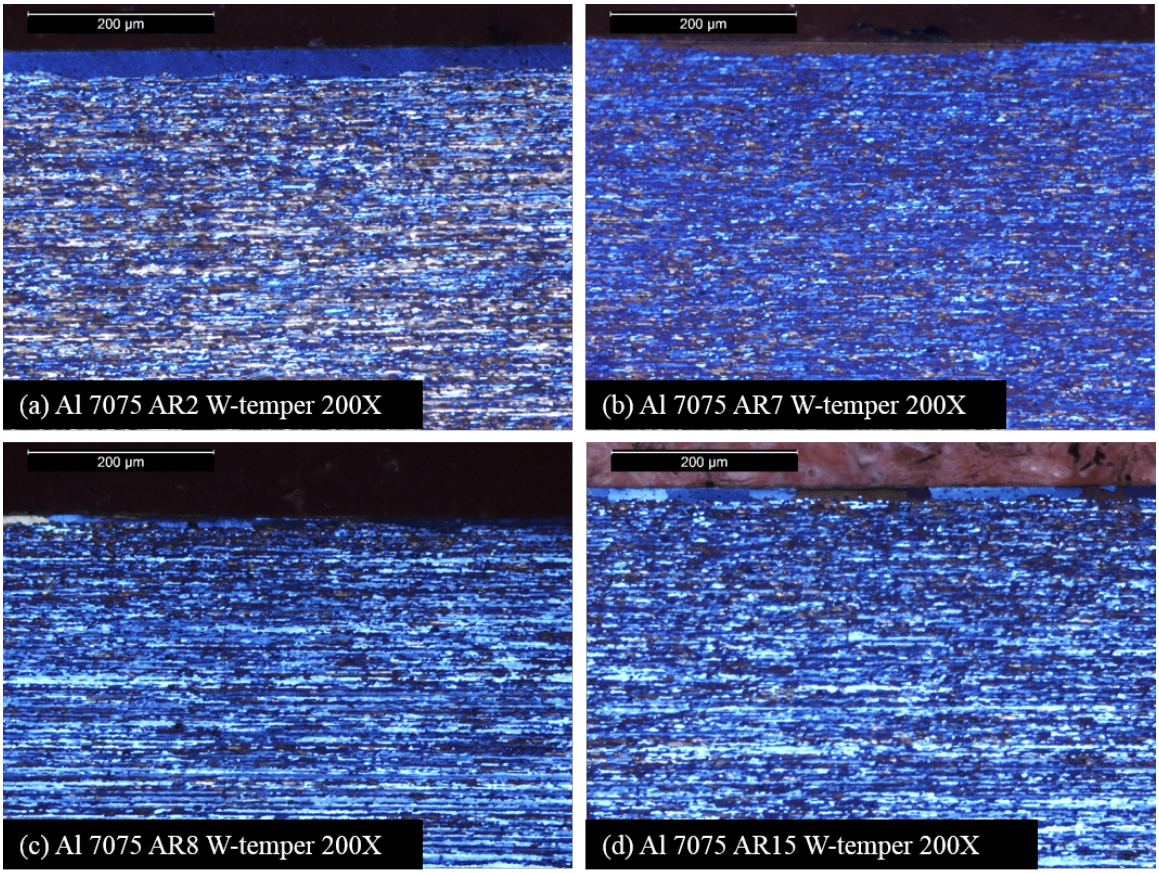

Figure 68: Polarized light optical micrographs (Barker's etch 200X) of W-temper Al 7075 extrusions from the edge of the L-ST plane for (a) AR2, (b) AR7, (c) AR8, and (d) AR15.

4.7 Discussion

Many authors suggest that the undesirable mechanical properties observed in low AR Al-Li extrusions (i.e. the "Al-Li fiber texture problem" also referred to as the development of "chunkiness") are primarily due to crystallographic texture development. This "chunkiness" is not typically observed in non-lithium containing alloys such as Al 7075. In this study, an increase in the Brass and S crystallographic texture components was observed in Al 2195 and Al 7075 extrusions with increasing aspect ratio while a decrease in the Copper texture was observed in both alloy systems with increasing aspect ratio. Similar results were reported by Jata, Hopkins, and Rioja (Figure 18) [66]. A look at the relative amounts of Brass, S, and Copper components in Al 2195 versus Al 7075 through use of the PL Number, however, indicates that only the Al 2195 AR2 and AR3 extrusions had a negative PL Number (Figure 51). None of the other observed variations with aspect ratio (i.e. location of the β-fiber, grain morphology, or particle morphology) correlated well with the mechanical properties of Al 2195 while also not being observed in Al 7075. The negative PL Numbers were due to the Al 2195 AR2 and AR3 samples having a higher volume fraction of the Copper texture component than Brass or S. In the Al 2195 T8 system, the volume fraction of the Copper component followed the same trend as the longitudinal TYS (Figure 28), the small spread between the UTS and the TYS (Criterion 3 plotted in Figure 33), and the variation in transverse ductility (Criterion 4 plotted in Figure 34). These results are summarized in Figure 69. Recall from Section 2.6, grains of Copper texture are oriented with the {112}

Aspect Ratio (-)	Copper Texture (%)	T8 Longitudinal TYS (MPa)	T8 Longitudinal UTS-TYS (MPa)	T8 Transverse Ductility (%)
2	6.7	586	20	2.0
3	5.6	570	29	3.9
5	2.7	549	34	5.0
7	1.4	569	29	4.6
8	1.9	574	27	4.6
15	1.6	550	34	4.7

Figure 69: Observed texture and strength trends of Al 2195 with variation of extrusion aspect ratio.

planes parallel to the rolling plane, or for an extrusion parallel to the L-LT plane, and the

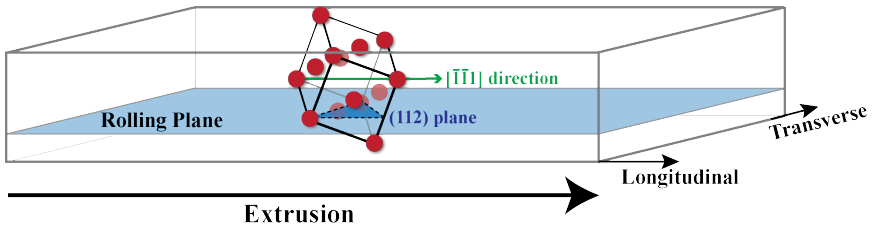

Figure 70: Visualization of the Copper texture within an extruded section. Courtesy of Dr. Jordan C. Ciciliano.

⟨111⟩ directions parallel to the extrusion direction. A {112} plane and a ⟨111⟩ direction within a face centered cubic (FCC) unit cell are shown in Figure 70. Using a theoretical approach, Barlat and Richmond [136] modeled the yield surfaces for an isotropic material, a material comprised of 50% Brass texture, a material comprised of 50% S texture, and a material comprised of 50% Copper texture. The Copper texture resulted in the most deformed yield surface, with a contracted transverse direction and a flat region near biaxial stretching compared to the isotropic material [136]. The contraction of the yield surface in the transverse direction due to the Copper texture is likely the mechanism responsible for the decreased transverse TYS in Al 2195 since stress states beyond the yield surface result in plastic deformation [95].

The Copper texture alone, however, cannot be the sole cause of increased longitudinal TYS, a low spread between the longitudinal UTS and TYS, and a low transverse ductility in Al 2195, as these correlations were only observed in the T8 temper. This suggests that the interaction of the T_1 and θ' phases with the Copper texture is the primary cause of undesirable mechanical properties, specifically as it relates to the large variation in the longitudinal and transverse TYS (Criterion 2 Figure 31) and the small spread between the longitudinal UTS and TYS (Criterion 3 Figure 33) as these trends were only seen in Al 2195 in the T8 temper, and not in the T3 or underaged conditions. This conclusion of a "complex interaction" or "synergistic effect" between the texture and precipitates is in agreement with Vasudevan, Przystupa, and Fricke [105] and Jata, Panchanadeeswaran, and Vasudevan [25]. However, Jata, Panchanadeeswaran, and Vasudevan [25] concluded that the Brass texture was primarily responsible for anisotropy. A "complex interaction" is in

disagreement with Crooks et al. [106] who reported no variation in Al 2195 anisotropy with changes to the precipitation treatments. Based on the results in this study, Al 7075 may also display undesirable mechanical properties if it developed increased Copper texture since η' and T1 are both HCP with {111} habit planes.

In addition to relating the Copper texture to the mechanical performance of low aspect ratio extrusions, the results presented in this chapter also highlights the importance of considering aspect ratio, in addition to extrusion ratio, for all metallic extrusions. Despite having the same extrusion ratio (ER=20) the Al 2195 and Al 7075 extrusions showed variation in grain morphology from cigar-like at low aspect ratios to pancake-like at high aspect ratios. Variations in grain morphology can play a role in mechanical, electrical, and electro-chemical properties as the morphology affects the total grain boundary area per unit volume. The extrusions did not show any variation in recrystallization behavior with aspect ratio. The solution heat treated microstructures in the bulk of the Al 2195 and Al 7075 samples were similarly recovered with minimal recrystallization. The surface recrystallization layer showed no significant variation for Al 2195 AR2-AR8 and Al 7075 AR2-AR15. The Al 2195 W-temper AR15 extrusion, however, showed a recrystallized surface layer nearly twice as thick as that observed in AR2-AR8. The Al 2195 AR15 sample was also the only sample with a slower ram speed than its counterparts. All of the other Al 2195 ram speeds were held relatively constant, and all of the Al 7075 ram speeds were held relatively constant. As reported by Sweet et al. [65], the nucleation rate was more affected by ram speed than the growth rate of recrystallized grains. At very slow ram speeds there are fewer recrystallization nuclei per unit volume, which could account for the increased thickness in the Al 2195 AR15 extrusion. The AR15 Al 2195 sample also showed more spherical second phase particles in the F-temper. Unfortunately, it is unclear whether this is due to the increased aspect ratio or the decreased ram speed.

4.8 Summary

Variations in properties, crystallographic textures, and microstructures with aspect ratio were analyzed for Al 2195 and Al 7075 extrusions. Four quantifiable criteria for measuring

the performance of Al-Li extrusions were established. Based on these criteria, the Al 2195 T8 extrusions with aspect ratios (AR) of 2 and 3 had undesirable mechanical properties. A new method of quantifying the plate-like nature of a sample's texture was introduced and is referred to as the Plate-Like Number (PL Number). A higher PL Number was associated with a more plate-like macrotexture. The Al 2195 AR2 and AR3 samples had negative PL Numbers, due to high volume fractions of the Copper component. The AR5-AR15 Al 2195 samples and all of the Al 7075 extrusions had positive PL Numbers. The undesirable mechanical performance of low aspect ratio Al 2195 extrusions was attributed to the interaction of the strengthening precipitates with the Copper texture component. It is therefore desirable to determine a method of decreasing the Copper component in extruded Al 2195 to obtain more isotropic properties.

CHAPTER 5

CONTROLLING CRYSTALLOGRAPHIC TEXTURE IN AL 2195

Although the Copper crystallographic texture component is not the sole cause of anisotropy in Al 2195, the interactions with second phase particles and negative Plate-Like (PL) numbers (corresponding to high fractions of the Copper texture) were shown in Chapter 4 to result in a large variation between the longitudinal and transverse tensile yield strengths, a small spread between the longitudinal ultimate and yield strengths, and low transverse ductility in low aspect ratio Al 2195-T8 extrusions. Therefore, if the PL Number can be increased, it is inferred that the mechanical properties will improve. The only way to have a non-negative PL Number is with a higher fraction of the Brass texture than the Copper texture. Therefore, the primary goal of this chapter is to determine a method of decreasing the Copper crystallographic texture during extrusion. For a fixed shape and alloy, the most applicable method of controlling texture is through variation in the extrusion speed and temperature. Previous reports alternatively indicate that decreases in processing temperature resulted in a decrease in the Copper texture [113], an increase in the Copper texture [25], and little change to the texture [9, 98] for various alloy systems. Clearly, more work in needed to understand the effects of processing temperature and speed on texture development in the Al-Cu-Li system. In this chapter, methods of controlling the Brass, S, and Copper texture components in Al 2195 will be investigated, including deformation temperature, time at temperature before deformation, and time at temperature during deformation.

5.1 Effects of Time at Temperature on the Initial Microstructure

The microstructure of the as-received Al 2195 billet was shown to have a large number of second phase particles, distinct precipitate free zones, Al_3Zr dispersoids, and a random texture as reported in Section 4.2. High temperature x-ray diffraction (XRD) was run on the as-received Al 2195 billet at 454°C, and select patterns are shown in Figure 71. From 0 to 24 hours at 454°C (Figures 71a to b), the intensity of the [111], [200], and [220] peaks

all increased significantly. From 1 to 24 hours, the intensity of these peaks decreased, while more low angle peaks began to appear. The systematic change in peak intensities with time at temperature indicates changes in the phases present. However, it was difficult to match these peaks to reference patterns for the possible secondary phases (T_1, θ', and S) because reference patterns were not found in the database. Instead, principle component analysis (PCA) in PANalytical's HighScore Plus software was performed to quantify the variation in the patterns. PCA of XRD patterns is analogous to the calculation of the principle stresses from a stress tensor to allow for simplified comparison between one stress state and another.

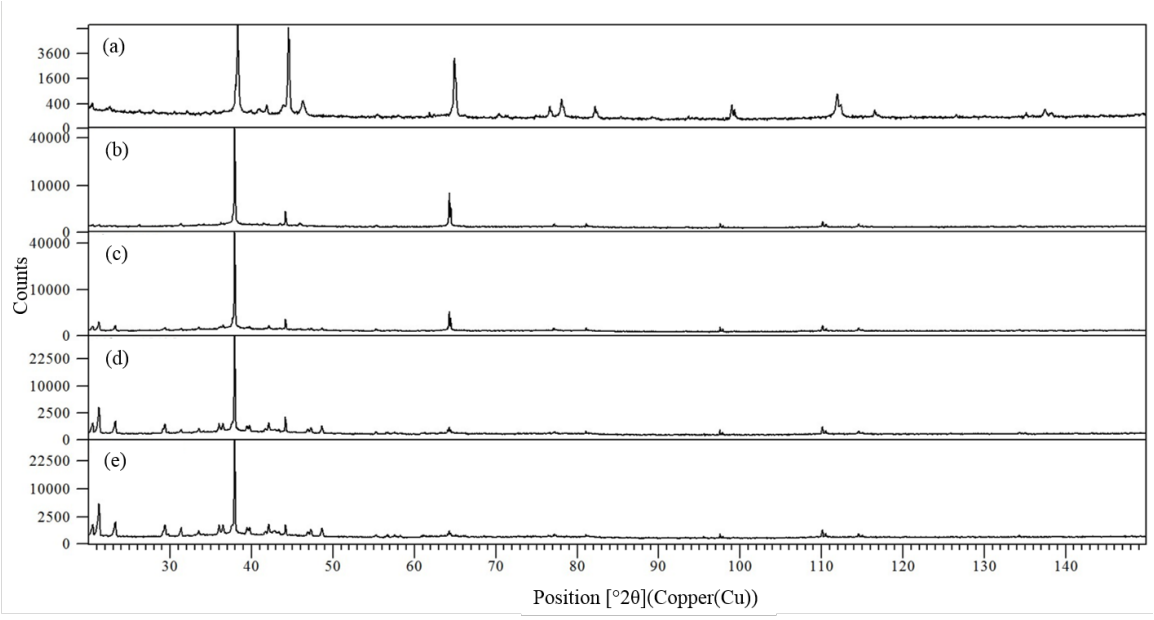

Figure 71: Representative XRD patterns from (a) the as-received billet and after (b) 5 minutes, (c) 1 hour, (d) 12 hours, and (e) 24 hours at 454°C.

The HighScore PCA algorithm is proprietary, but in general, the procedure begins with calculation of a correlation matrix. For this analysis, the correlation matrix quantitatively compares the similarity of each XRD pattern to every other pattern. Eigenvectors were then calculated from the correlation matrix. Each eigenvalue accounts for a percentage of variation between patterns. The first three eigenvalues represent over 99% of the variation between the patterns. Therefore, the first three values are designated principal component 1, principal component 2, and principal component 3. The three principal components act as coordinates for each XRD pattern in 3-dimensional principal component space. A more

detailed discussion on PCA can be found in reference [137]. The ability to interpret a 3D principal component plot is sufficient for investigating the variations in the microstructure with time at temperature.

In 3D principal component space, each point represents an XRD pattern. The further points are from one another in principal component space, the larger the variation between the patterns. If, for instance, two patterns are exactly alike, the points representing them are coincident in principal component space. Figure 72 shows variations between patterns taken over time at 454°C. In this plot, point 1 corresponds to the XRD pattern taken at room temperature, point 2 is from the scan taken after 5 minutes at 454°C, and points 3 through 26 represent scans taken every hour for 24 hours at 454°C. The microstructure evolves with time over 24 hours at 454°C, with the greatest variation occurring during the first 1-2 hours at temperature.

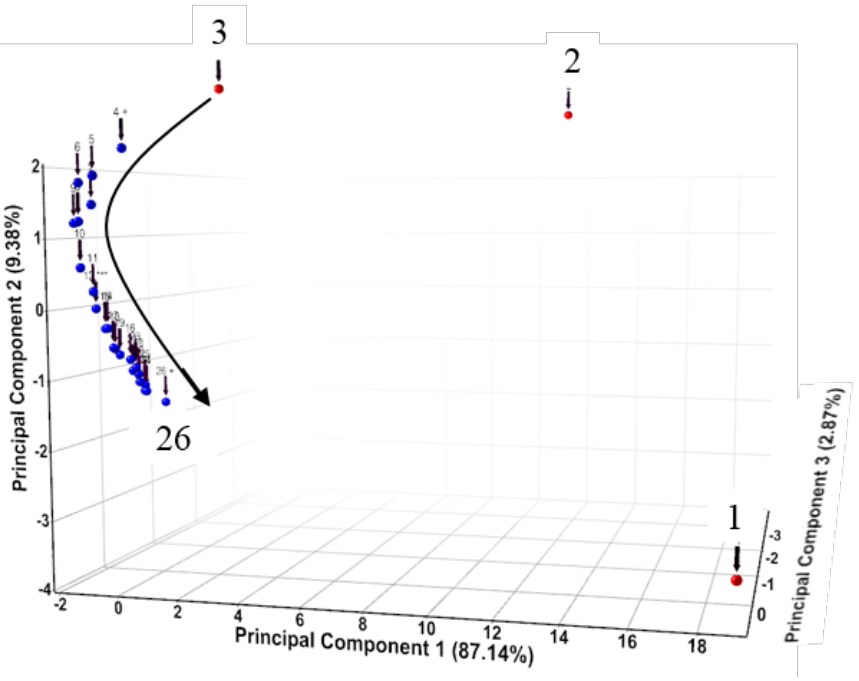

Figure 72: PCA demonstrating that the Al 2195 initial microstructure evolves with time at 454°C.

In order to further investigate the evolution of the microstructure with time at temperature, samples of the as-received billet were held at 343°C, 454°C, and 515°C for 1, 2, 4, 8, and 24 hours. Samples were water quenched, sectioned into 3 samples, and Keller's etched

to analyze the L-LT plane via optical microscopy. Similarly, samples were taken from the as-received billet without any heat treatment. At a magnification of 50X, the volume fraction of secondary phases was observed to decrease as a function of temperature with 1 hour dwells (Figure 73). A magnification of 500X was necessary to resolve the phases for volume fraction analysis (Figures 74-76). Quantitative microstructural analysis was required to make definitive statements about the change in microstructure observed in Figures 73-76.

Three samples were cut, mounted, and prepped for metallography from each time at each temperature. Ten total micrographs at 500X were taken at random locations from each of the three samples for a total of 600 images (30 per time at temperature). Volume fraction analysis of secondary phases was performed using MATLAB. All images were converted to binary and individually thresholded. An example of a thresholded image is shown in Figure 77b. In a binary image, the T_1 and Cu-rich grain boundary phases were not distinguishable from one another; only the volume fraction of total secondary phases could be calculated. The initial Al 2195 microstructure consisted of 54% secondary phases (Figure 78). At 343°C the area fraction of secondary phases decreased to 37% over the course of 24 hours at temperature. At 454°C, the phases decreased to 34% in the first hour, 11% after two hours, and 9% after 24 hours. After less than 1 hour at 515°C, the area fraction decreased to less than 1%. This evolution agreed with the PCA results, as the largest changes in the microstructure occurred during the first hour at temperature.

Based on the development of the billet microstructure at elevated temperatures, the amount of time that a billet is held at the deformation temperature before processing cannot be neglected. Reported pre-heat times vary from 1-30 hours [13]. As a billet sits in a furnace waiting to be extruded or rolled, the microstructure is evolving. As discussed in Section 2.5.3, changing the microstructure is equivalent to changing the material altogether from the perspective of constitutive equation parameters. What role does this change in initial microstructure have on the final texture and microstructure? Can this microstructural evolution be utilized in Al 2195 to control properties? Samples of Al 2195 were rolled at various temperatures with various dwell times and analyzed as described in the proceeding

sections to investigate possible effects of processing temperatures and dwell times on the final crystallographic texture and microstructure.

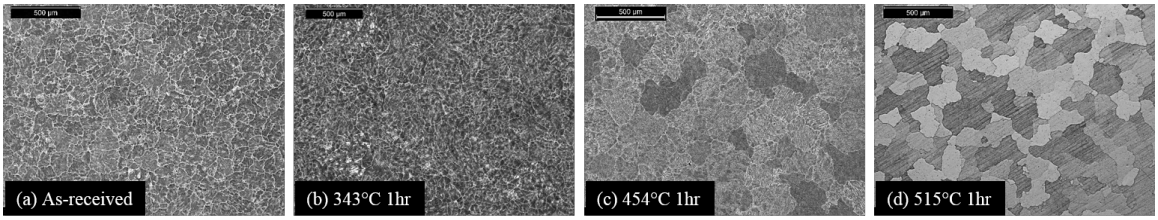

Figure 73: Bright field optical micrographs (50X) of the (a) initial microstructure and with 1 hour dwells at (b) 343°C, (c) 454°C, and (d) 515°C.

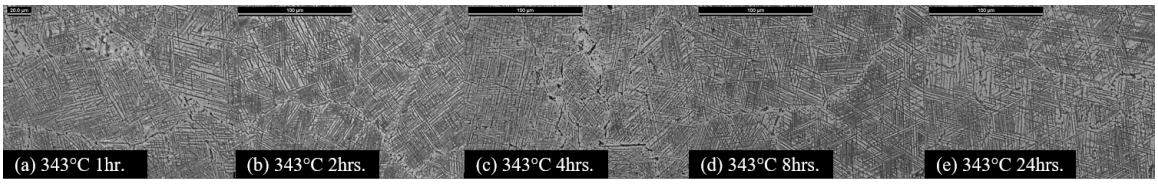

Figure 74: Bright field optical micrographs (500X) of the Al 2195 billet held at 343°C for (a) 1 hour, (b) 2 hours, (c) 4 hours, (d) 8 hours, and (e) 24 hours.

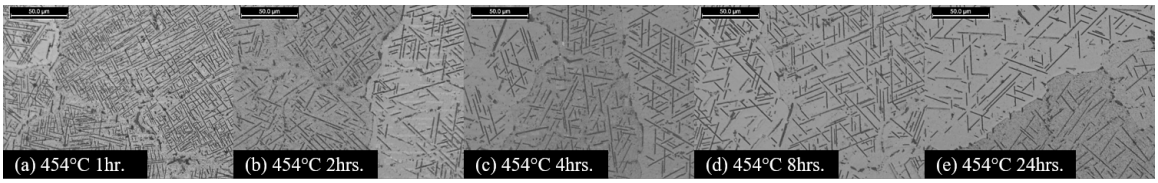

Figure 75: Bright field optical micrographs (500X) of the Al 2195 billet held at 454°C for (a) 1 hour, (b) 2 hours, (c) 4 hours, (d) 8 hours, and (e) 24 hours.

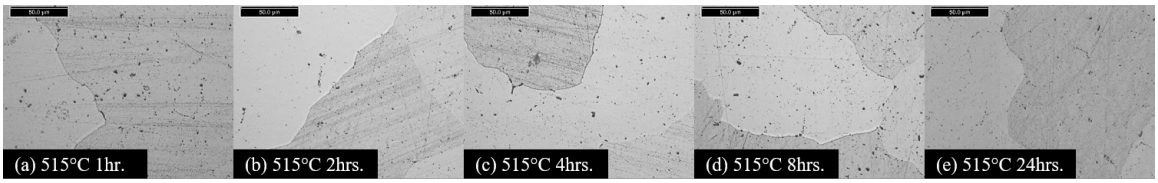

Figure 76: Bright field optical micrographs (500X) of the Al 2195 billet held at 515°C for (a) 1 hour, (b) 2 hours, (c) 4 hours, (d) 8 hours, and (e) 24 hours.

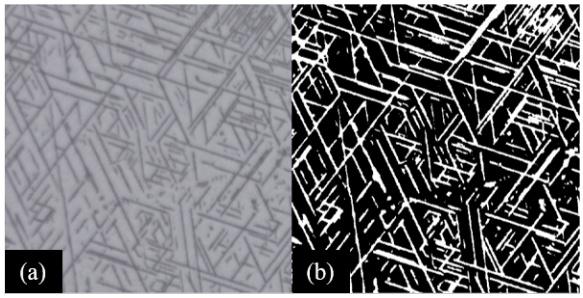

Figure 77: Representative (a) original micrograph and (b) thresholded image.

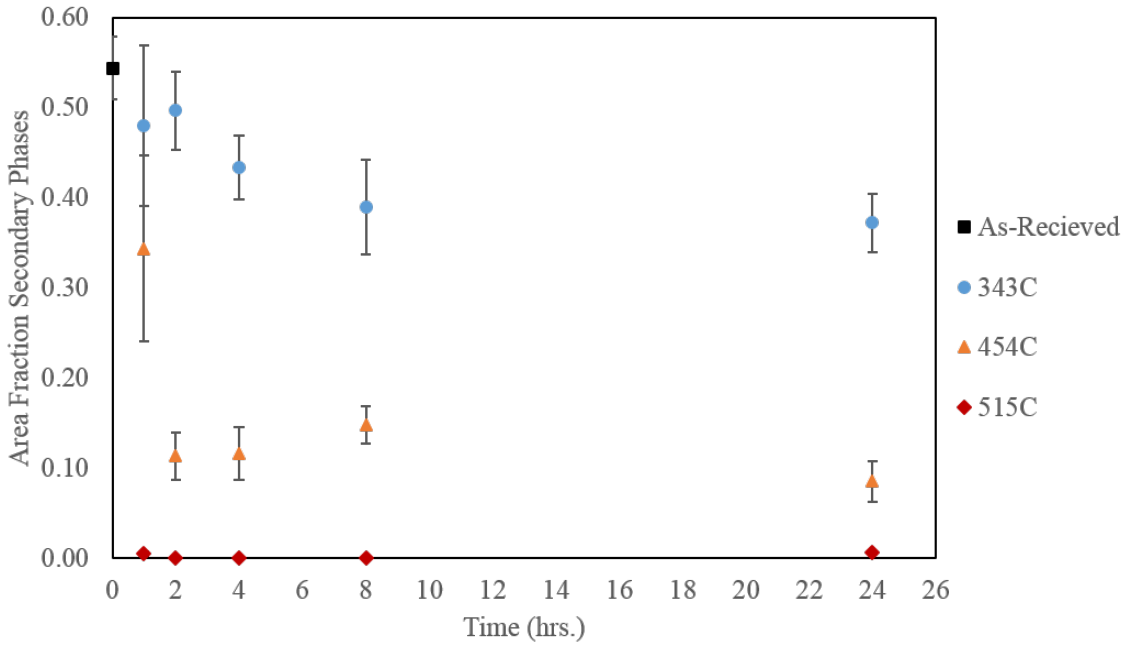

Figure 78: Evolution of the Al 2195 homogenized billet microstructure with time at 343°C, 454°C, and 515°C.

5.2 Rolling Procedures

Billet slices of Al 2195 were machined into tapered ingots of approximately 7.6 x 12.7 x 1.9 cm[1]. The ingots were pre-heated to 343°C, 454°C, and 515°C for 1, 4, 8, and 24 hours (Table 8). Processing temperatures were chosen to stay below the onset of melting temperature of the homogenized billet, which observed via differential scanning calorimetry to be 516°C for the as-received Al 2195. A total reduction goal of 75% was chosen to achieve a rolled microstructure; actual reduction values are reported in Table 8.

[1] 3 x 5 x 0.75 inches

Table 8: Rolling times, temperatures, and reductions for Al 2195.

Temperature (°C)	**Temperature (°F)**	**Pre-Heat Time (hrs.)**	**Reduction %**
343	650	1	79
343	650	4	77
343	650	8	79
343	650	24	80
454	850	1	68
454	850	4	77
454	850	8	79
454	850	24	78
515	959	1	78
515	959	4	76
515	959	8	78
515	959	24	78

The reduction was achieved through three passes of 25% each with a dwell time between passes equivalent to the pre-heat temperature and time. For example, an ingot of Al 2195 was pre-heated to 454°C for 8 hours, rolled to a 25% reduction, heated at 454°C for 8 hours, rolled another 25% reduction, heated at 454°C for 8 hours, and rolled again to a 25% reduction for a total reduction of 75% and a total time at temperature of 24 hours. After the final pass, samples were water quenched to maintain the high temperature microstructure. A representative schematic of the rolling procedure is shown in Figure 79. A Paragon box furnace was used for heating, with a K-type thermocouple attached to a block of aluminum for temperature monitoring. To more closely replicate an extruded microstructure, cross rolling was not performed. The front and rear 20% of the plates were discarded in accordance with industrial procedure wherein only the product processed under steady-state conditions is sold.

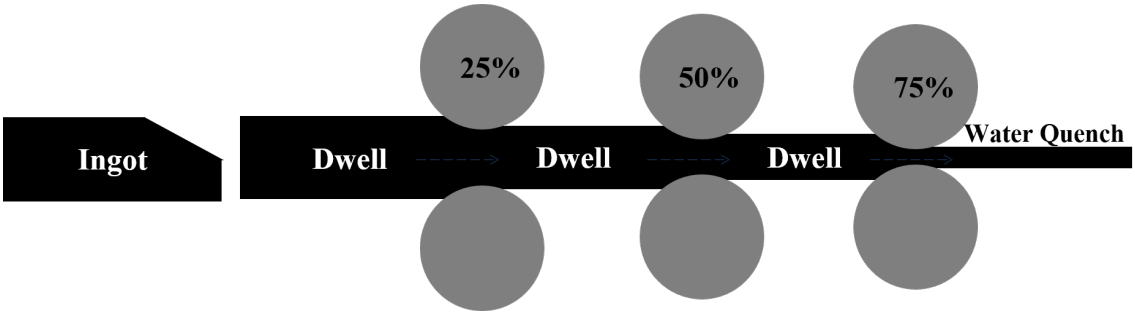

Figure 79: Schematic showing the procedure used for rolling at various temperatures and dwell times.

5.3 Effects of Rolling Time and Temperature on Texture

XRD was performed for macro-texture analysis of the rolled plates (see Section 3.3 for detailed experimental procedures). All of the plates developed plate-like macrotextures[2]. Representative plate-like pole figures are shown in Figures 9c-d. There were slight changes to the macrotexture observed due to dwell times as well as processing temperatures. At 343°C the pole figures in Figure 80 do not show significant variation between the 1, 4, 8, and 24 hour samples. The texture is less evenly distributed with increased dwell time at 343°C, an effect that is seen more predominately in the ODFs in Figure 81. The texture observed at 343°C with 24 hour dwells (Figure 81d) is more indicative of a plate-like texture than that after 1 hour dwells at 343°C (Figure 81a). The development of an increasingly plate-like texture is more pronounced at 454°C than at 343°C and can be observed in the pole figures in Figure 82 as well as the ODFs in Figure 83. The most plate-like textures were observed for a processing temperature of 515°C (Figures 84-85). All of the pole figures and ODFs presented in Figures 80-85 suggest that with increased rolling temperature and increased dwell time between rolling passes, the texture became more plate-like. This effect is shown more clearly in Figures 86-87.

[2]Complete pole figures (including {200} and {220}) and ODFs can be found in Appendix C.

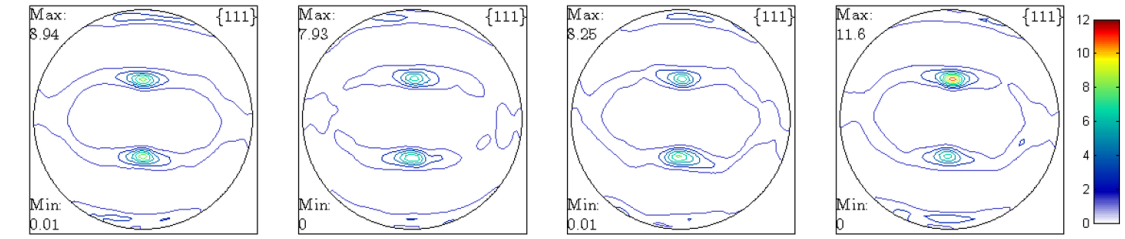

(a) 343°C 1 hr. (b) 343°C 4 hrs. (c) 343°C 8 hrs. (d) 343°C 24 hrs.

Figure 80: {111} Pole figures from F-temper Al 2195 rolled at 343°C with (a) 1, (b) 4, (c) 8, and (d) 24 hour dwells.

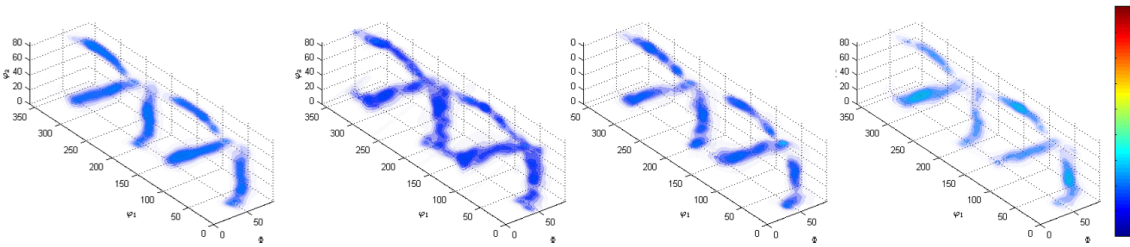

(a) 343°C 1 hr. (b) 343°C 4 hrs. (c) 343°C 8 hrs. (d) 343°C 24 hrs.

Figure 81: ODFs from F-temper Al 2195 rolled at 343°C with (a) 1, (b) 4, (c) 8, and (d) 24 hour dwells.

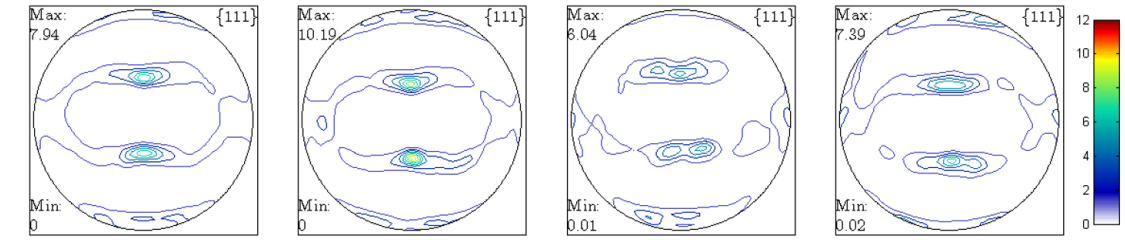

(a) 454°C 1 hr. (b) 454°C 4 hrs. (c) 454°C 8 hrs. (d) 454°C 24 hrs.

Figure 82: {111} Pole figures from F-temper Al 2195 rolled at 454°C with (a) 1, (b) 4, (c) 8, and (d) 24 hour dwells.

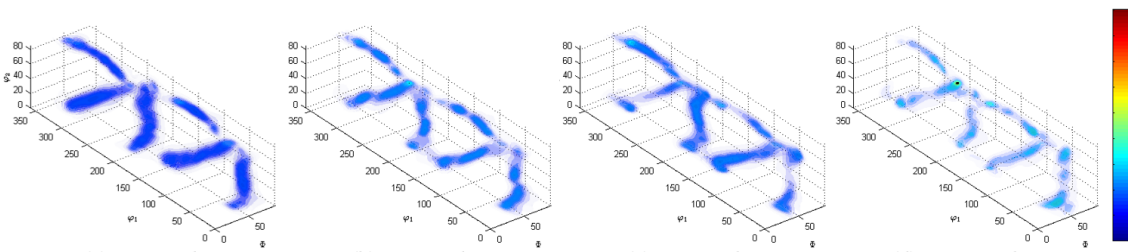

(a) 454°C 1 hr. (b) 454°C 4 hrs. (c) 454°C 8 hrs. (d) 454°C 24 hrs.

Figure 83: ODFs from F temper Al 2195 rolled at 454°C with (a) 1, (b) 4, (c) 8, and (d) 24 hour dwells.

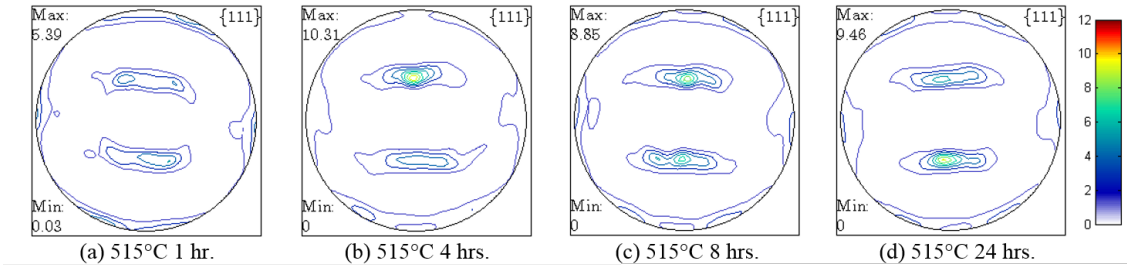

(a) 515°C 1 hr. (b) 515°C 4 hrs. (c) 515°C 8 hrs. (d) 515°C 24 hrs.

Figure 84: {111} Pole figures from F-temper Al 2195 rolled at 515°C with (a) 1, (b) 4, (c) 8, and (d) 24 hour dwells.

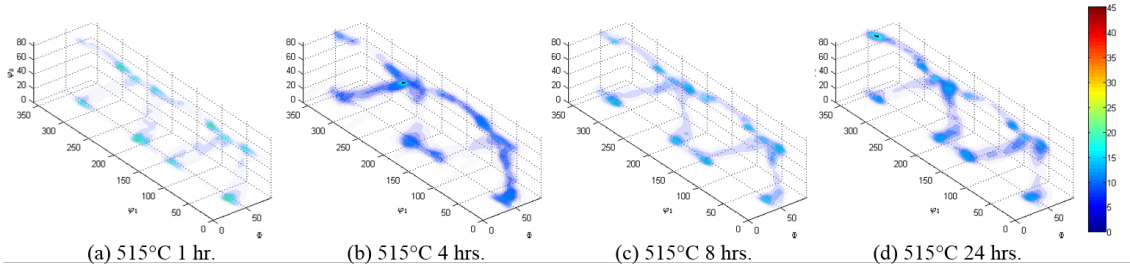

(a) 515°C 1 hr. (b) 515°C 4 hrs. (c) 515°C 8 hrs. (d) 515°C 24 hrs.

Figure 85: ODFs from F-temper Al 2195 rolled at 515°C with (a) 1, (b) 4, (c) 8, and (d) 24 hour dwells.

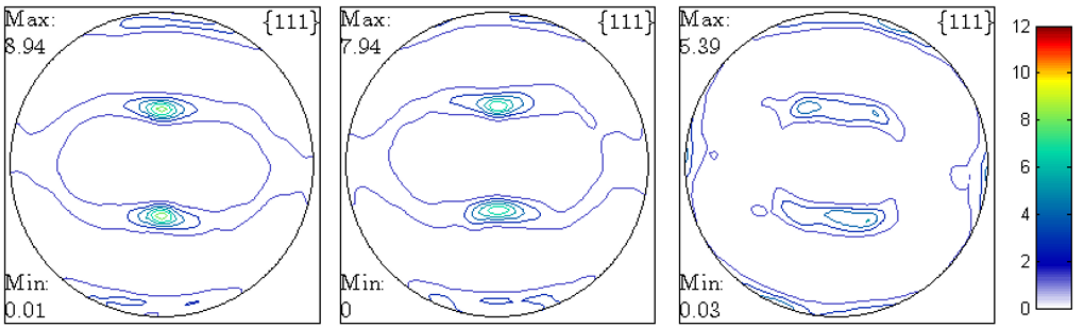

(a) 343°C 1 hr. (b) 454°C 1 hr. (b) 515°C 1 hr.

Figure 86: {111} Pole figures from F temper Al 2195 rolled at (a) 343°C, (b) 454°C, and (C) 515°C with 1 hour dwells.

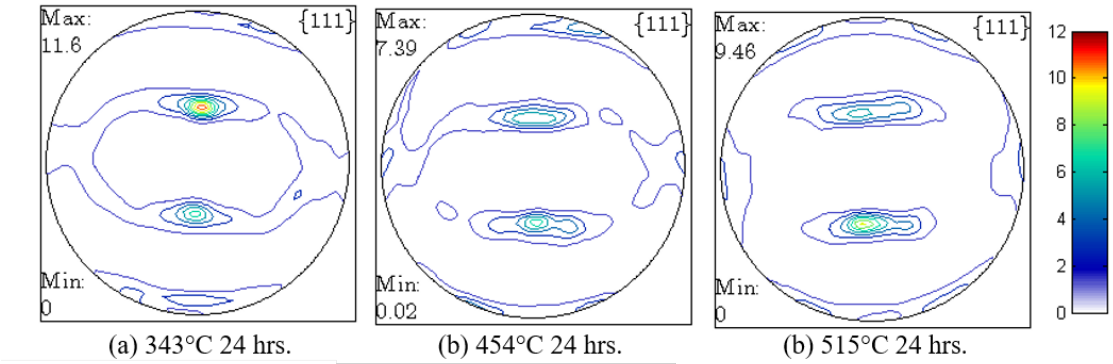

Figure 87: {111} Pole figures from F temper Al 2195 rolled at (a) 343°C, (b) 454°C, and (c) 515°C with 24 hour dwells.

While pole figures and ODFs qualitatively described the changes in texture, a more quantitative analysis can be performed using volume percents of particular texture components. There is no clear trend between the Brass texture and dwell time; however, the 343°C plates consistently had the lowest fraction of the Brass component (Figure 88a). Conversely, the samples rolled at 515°C consistently had the lowest percentages of the S and Copper components (Figures 88b-c). The 343°C samples had the highest amounts of Copper and S components, except at a dwell time of 4 hours. The 515°C 4 hour samples had the lowest volume percent of Copper and S components.

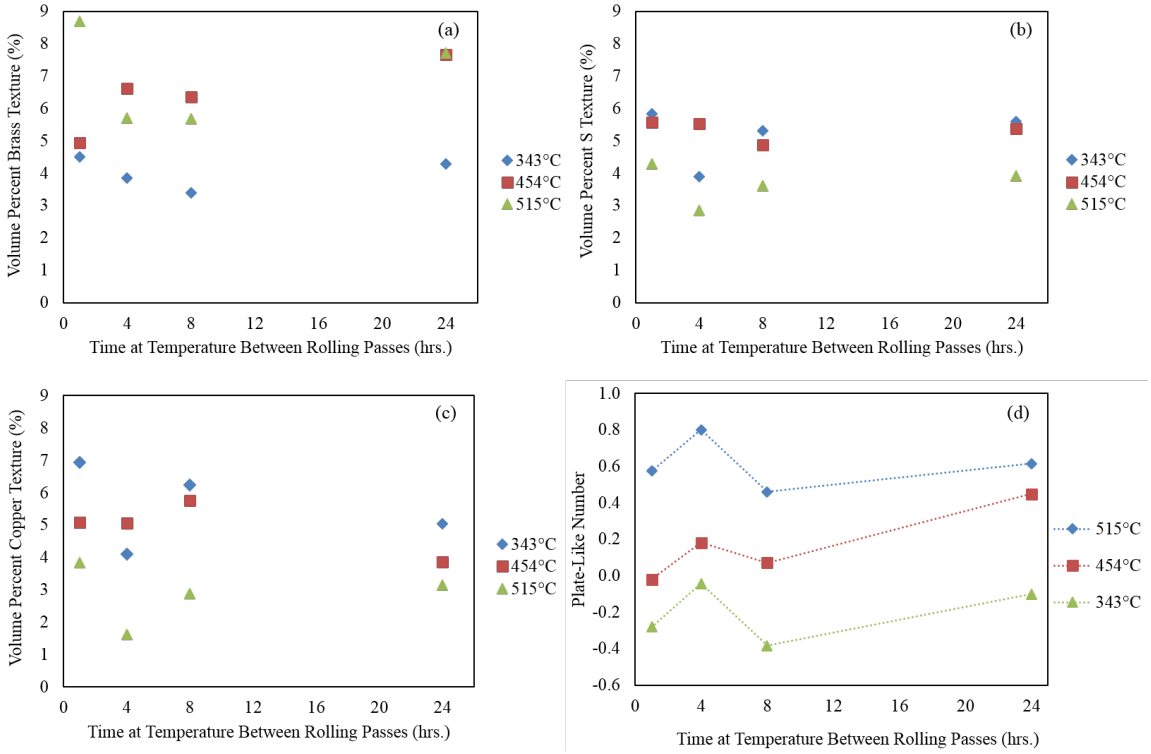

Figure 88: Variation in the volume percent (a) Brass, (b) S, and (c) Copper texture components and in (d) the Plate-Like Number with rolling temperature and dwell time.

It is difficult to determine which samples had the most plate-like textures simply by looking at the variations in the Brass, S, and Copper textures with temperature and dwell time (Figures 88a-c). As discussed in Section 4.5, plates typically contain the Brass, S, and Copper textures, where Brass is present in the highest concentration and Copper in the least [105]. Equation 10 was introduced to determine the relative "plate-likeness" of a sample where a higher PL Number is associated with a more plate-like macrotexture. The

PL Number is plotted for the Al 2195 plates in Figure 88d. Using the PL Number, it is easy to identify which samples had the most plate-like macrotextures. The PL Number was highest for the 515°C plates and decreased with temperature. The 515°C plate with 4 hour dwells had the highest PL number. The 454°C samples showed an increase in the PL Number with increasing dwell time. All of the 343°C samples had negative PL Numbers. In the extruded samples, only the Al 2195 samples with aspect ratios of 2 and 3, which showed poor mechanical properties, had negative PL Numbers. This indicates that rolling Al 2195 at 343°C would lead to similar properties as those observed for low aspect ratio Al 2195 extrusions.

5.4 Effects of Rolling Time and Temperature on Microstructure

Not only did texture change with rolling dwell time and temperature, but the microstructure also changed. Backscatter scanning electron microscopy (SEM) and corresponding energy-dispersive x-ray (EDX) mapping was performed on the as-received billet and on the 343°C 24 hour and 454°C 24 hour plates (Figure 89). The T_1 phase began to dissolve at 343°C (Figure 89b), and at 454°C the T_1 phase had almost completely dissolved (Figure 89c). The dissolution of the T_1 phase in the rolled product agrees with the decrease in area fraction of second phase particles observed in the homogenized billet when held at elevated temperatures (Figure 78). What could not be observed from the billet study was the coarsening of the grain boundary, Cu-rich phase which was evident in the 454°C 24 hour plate (Figure 89c).

Bright field optical microscopy indicates that the second phase particles spherodize as the dwell time increases (Figures 90-91). The spherodizing effect occurs more rapidly and in a more pronounced manner at 454°C and in a less pronounced manner at 343°C. Based on the dissolution and coarsening observed via SEM, the change in microstructure seen in the optical micrographs is likely due to the dissolution of plate-like T_1 and the coarsening of the more spherical grain boundary phase.

Utilizing results from Section 5.1, it was assumed that all of the second phase particles dissolved with processing at 515°C. Polarized light microscopy was performed on the 515°C

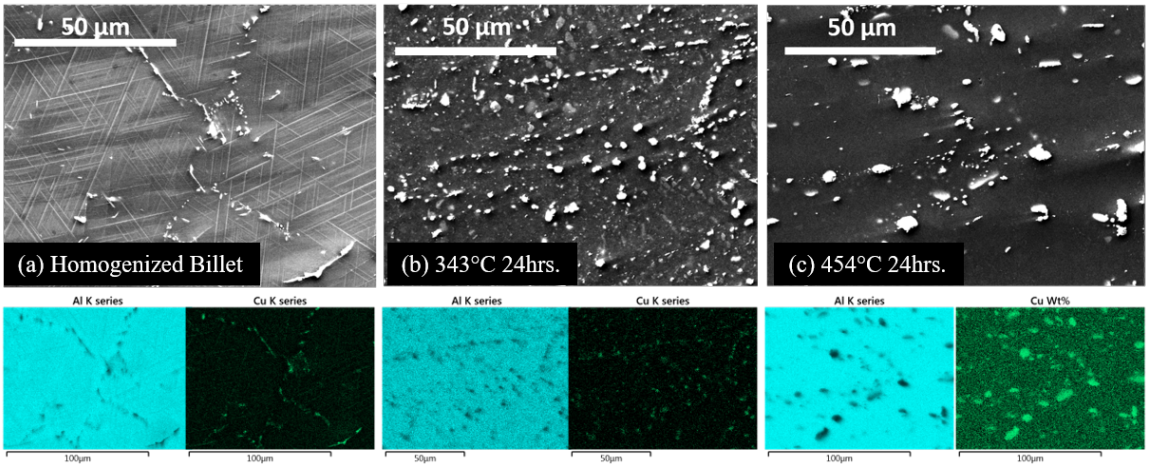

Figure 89: Backscatter SEM images from the (a) homogenized billet (b) 343°C 24 hour plate, and (c) 454°C 24 hour plate with corresponding EDX elemental maps. Courtesy of Dr. Thomas Dorin at Deakin University.

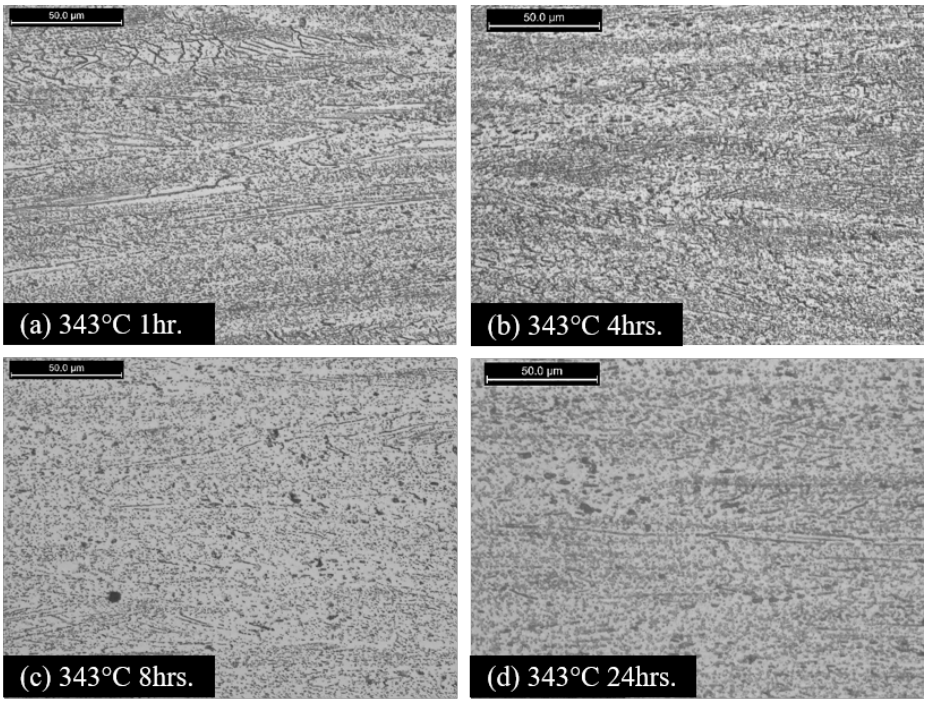

Figure 90: Bright field optical micrographs of longitudinal sections (500X Keller's etch) from F temper Al 2195 rolled at 343°C with (a) 1, (b) 4, (c) 8, and (d) 24 hour dwells.

plates since bright field images did not reveal second phase particles or grain morphology. Typical rolled grain morphologies were observed in the longitudinal plane (Figure 92).

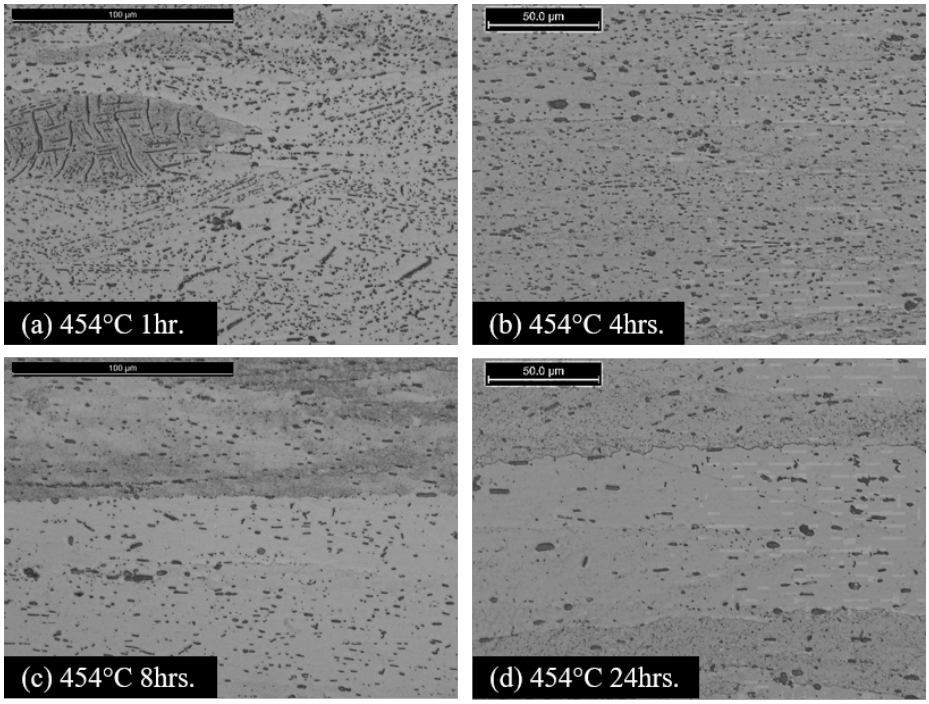

Figure 91: Bright field optical micrographs of longitudinal sections (500X Keller's etch) from F temper Al 2195 rolled at 454°C with (a) 1, (b) 4, (c) 8, and (d) 24 hour dwells.

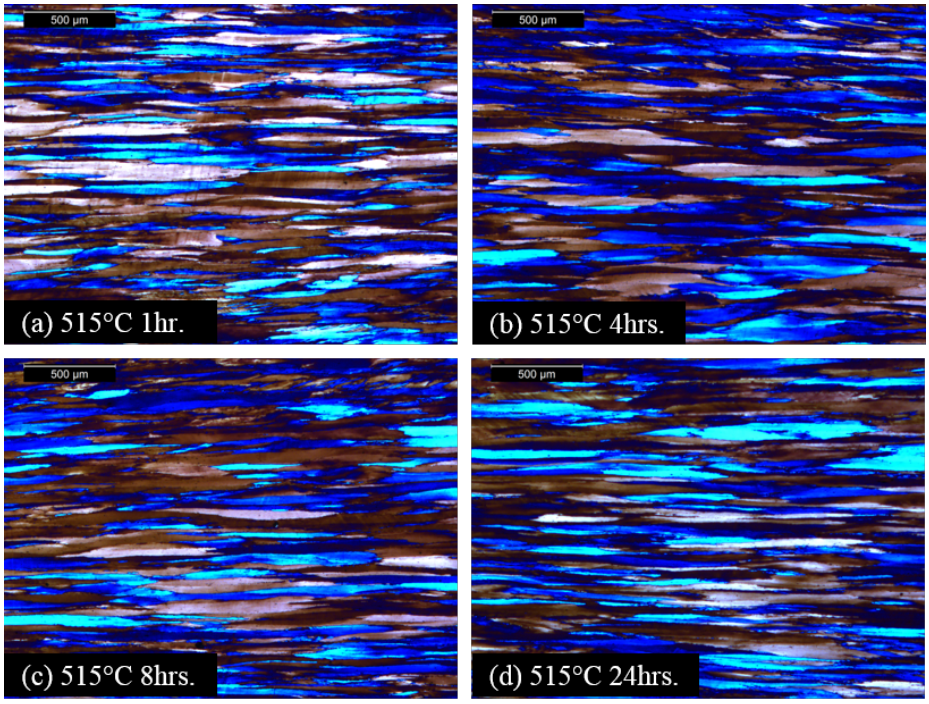

Figure 92: Polarized light optical micrographs of longitudinal sections at (50X Barker's etch) from F temper Al 2195 rolled at 515°C with (a) 1, (b) 4, (c) 8, and (d) 24 hour dwells.

5.5 Discussion

The presence of secondary phase particles can affect the texture that develops in thermo-mechanically processed metals (discussed in Section 2.4) [66, 69, 70]. Any variation in the initial microstructure is equivalent to changing the material, as discussed in Section 2.5.3. Jata, Panchanadeeswaran, and Vasudevan [25] concluded that increasing extrusion temperatures above 300°C led to dissolution of second phase particles and an increase in the Brass texture component in an Al-Li-Cu alloy, AF/C489. Rollett and Wright [113] concluded the opposite: that the Brass texture decreased with increasing rolling temperature. In this study, no correlation was made between the Brass texture and processing temperatures or dwell times. However, systematic variation in the PL Number, or plate-like nature of the macrotexture, was observed.

The initial Al 2195 microstructure consisted of over 50% secondary phases. At processing temperatures of 343°C and 454°C, these phases dissolved and coarsened. A sample held at 343°C for 24 hours still had nearly 40% secondary phases, and the resulting textures still had a negative PL Number, indicating that they did not become completely plate-like (Figure 93a-b). At 454°C, however, the fraction of second phase particles dropped to approximately 10% after 2 hours at temperature. With dissolution of T_1 and coarsening of the grain boundary phase, the morphology of the particles also evolved. The particles appeared the most spherical at 454°C with 24 hour dwells, and this sample had the fewest number of particles and the highest PL Number (most plate-like texture) of the second phase containing samples (Figure 93d).

At 515°C, after 1 hour at temperature, the microstructure consisted of less than 1% second phase particles. This homogeneous microstructure resulted in the highest PL Numbers with little variation between 1 and 24 hour dwell times (Figures 84 and 88d). Slight variations in the texture development with dwell time at 515°C might be due to recovery and recrystallization kinetics. The longer a sample sits between rolling passes, the more time it has for static recovery and recrystallization. The polarized light optical micrographs of the final microstructure did not reveal any significant differences in the high temperature microstructure after the final pass. Interrupted microstructural characterization would be

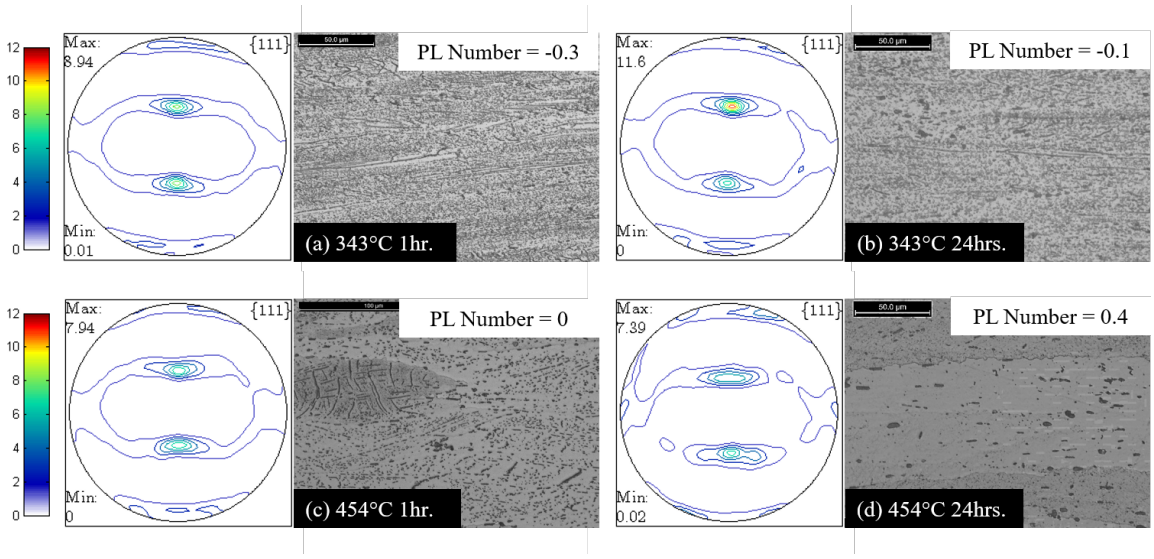

Figure 93: Optical micrographs and {111} pole figures demonstrating the relationship between crystallographic texture development and microstructure during processing.

required to identify sources of variation in the 515°C samples. The goal of this study, however, is to identify mechanism for control of crystallographic texture during the extrusion process. Dwell time between rolling passes and associated static recovery or recrystallization that may occur during these dwell time is not applicable to the extrusion industry. The effects of rolling temperature and dwell time on texture and microstructural development can be applied to the extrusion of Al 2195. Higher extrusion temperatures would likely lead to similar results as higher rolling temperatures (i.e. more plate-like texture and lower fractions of secondary phases) and slower ram speed would likely result in similar results as longer dwell times, particularly near an extrusion temperature of 454°C (i.e. more spherical second phase particles and more plate-like textures).

5.6 Summary

Controlling texture through post-processing heat treatment methods proved unsuccessful. Instead, the effects of varying the initial microstructure and the microstructure during processing were investigated through a series of rolling studies. Variation in the volume fractions and morphologies of second phase particles was achieved through adjustments to the rolling temperature (343°C, 454°C, and 515°C) and time between passes (1, 4, 8, and 24 hours). The most plate-like textures were observed in the plates rolled at 515°C

which had less than 1% secondary phases in the started microstructure. Plates rolled at 343°C and 454°C had initial microstructures consisting of 9-50% second phase particles. Of the 343°C and 454°C plates, the most plate-like macrotexture was associated with the 454°C plate with 24 hours dwells. Based on these results, it was hypothesized that higher extrusion temperatures and slower ram speeds may lead to products with lower Copper texture and therefore better mechanical properties. Systematic investigation of the effects of billet temperature and ram speed through industrial scale experimental press trials, however, is costly and often leads to convoluted results due to imperfect press repeatability. Instead, the effects of press parameters on texture and anisotropy are ideally studied through computational methods.

CHAPTER 6

VALIDATION OF HYPERXTRUDE

Variation in press parameters, such as billet temperature and ram speed, can affect the final microstructure and properties of extruded products. Running experimental trials to understand the effects of press parameters on a particular alloy can be expensive and time consuming. This investment is often not worthwhile because of imperfect press repeatability. Ideally, these effects can be computationally investigated via finite element analysis (FEM). Altair's HyperXtrude is commercially available software for the modeling of aluminum extrusions. However, the literature lacks experimentally verified industrial scale simulations, and simulations have not been performed on lithium containing alloys (Section 2.8).

Finite element modeling requires a constitutive equation or flow stress data to describe the material's behavior. The hyperbolic sine law (Equation 11), also known as the Garofalo relationship, is commonly used to describe the flow behavior for high temperature deformation of metals. In Equation 11, $\dot{\epsilon}$ is strain rate, A is the reciprocal strain factor, α is the stress multiplier, σ is flow stress, n is the stress exponent, Q is the activation energy for deformation, R is the universal gas constant, and T is the absolute temperature.

$$\dot{\epsilon} = A[sinh(\alpha\sigma)]^n exp(-\frac{Q}{RT}) \tag{11}$$

The constitutive parameters (A, α, n, and Q) necessary to utilize this equation have been determined and published for Al 7075 and are available in the HyperXtrude database. High temperature flow stress data are also available in the ASM International Hot Working Guide [138]. Neither constitutive parameters nor high temperature flow stress data exist in literature for Al 2195.

In this chapter, the constitutive parameters and flow stress data for Al 7075 are used to assess HyperXtrude's load curve prediction capability for industrial scale extrusions. Load curves can be used for validation because the activation energy for deformation (Q)

is a thermo-mechanical parameter that represents the activation energy required to initiate dislocation motion and, as shown in Equation 7, this parameter can be replaced with peak pressure/load. Therefore, in this work, accurate prediction of load curves was assumed to represent accurate prediction of a material's thermo-mechanical response.

After ascertaining the level of accuracy achieved for Al 7075 using the hyperbolic sine law and a flow stress table, three techniques for predicting the behavior of Al 2195 are investigated: 1. fitting the hyperbolic sine law via a built-in HyperXtrude numerical method, 2. fitting the hyperbolic sine law with hot torsion data, and 3. use of a flow stress table. An analysis of the validity of the load curve results is offered and an acceptable method for further FEM modeling of Al 2195 extrusion is presented.

6.1 Modeling Procedures

The computer aided design (CAD) of the flat-faced extrusion die was created in SolidWorks and the .STEP file was imported into Click2Extrude 2017. Click2Extrude generated billet and profile geometries and meshed them using combinations of tetras and rectangular prism elements as shown in Figure 94. Click2Extrude was used to create and export the data deck. The data deck included a .hx file and a .grf file that were edited to reflect the boundary conditions for direct extrusion (Table 9) and actual experimental parameters before submitting the job to HyperXtrude 14.0.130.12 for solving[1]. A ram speed acceleration of 0.0 seconds was used since the experimental ram speeds were held constant and HyperXtrude does not model the billet-upsetting process. The non-linear iteration tolerance was set to 0.01 for transient analysis and 0.001 for steady-state analysis. The maximum number of non-linear iterations was set to 25 for both types of analysis. Variable time steps were adjusted to calculate data every 1.0 second to match data recorded at the press.

[1]HyperXtrude 13.0.110.31 led to unsatisfactory load curve predictions for Al 7075.

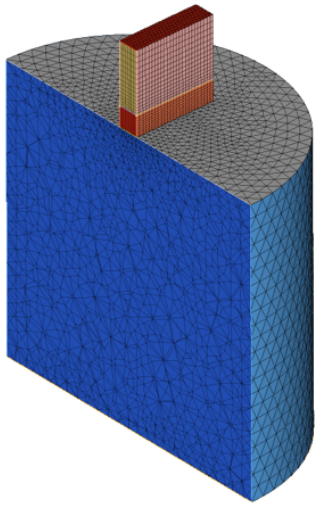

Figure 94: Cross section of a representative billet and profile CAD and FEM mesh created by Click2Extrude.

Table 9: Boundary conditions used to model Al 2195 and Al 7075 extrusions.

Interface	HyperXtrude Boundary Condition
Billet-Dummy Block	Inflow
Billet-Die	SolidWall
Billet-Container	SolidWall
Bearing-Die	Bearing (Viscoplastic friction model)
Free surfaces	FreeSurface
Exit	Outflow

6.2 Prediction of Load Curves for Al 7075

The values for the hyperbolic sine (sinh) law for Al 7075 from HyperXtrude's database are given in Tables 10 and 11. These values and the experimental press parameters for AR2, AR8, and AR15 were used to simulate the load curves. This method is referred to as "Al 7075 Sinh." Using Al 7075 Sinh, HyperXtrude predicted peak loads that fell 25% (AR2), 22% (AR8), and 18% (AR15) below experimental values (Figure 95). A new feature in HyperXtrude 2017 allows for the direct entry of flow stress data into a material file in tabular format (Appendix F). A flow stress material file was created from strain rate, strain, and stress data presented in The ASM Hot Working Guide [138] for as-cast Al 7075 where the values were corrected for adiabatic temperature rise. As shown in Figure 7, use of the flow stress table, referred to as Al 7075 Flow, led to a more accurate simulation of

the load curves. The flow stress data may have performed better than the HyperXtrude Sinh model because it accounted for the adiabatic temperature rise. Using the Al 7075 Flow approach, the predicted values for peak load fell only 9% (AR2), 8% (AR8), and 2% (AR15) below experimental. It is reasonable to expect simulated peak loads to fall within 10% of the experimental values when using a valid method for capturing the high temperature deformation behavior of the material. For Al 7075, a flow stress table, Al 7075 Flow, was a better method than using the hyperbolic sine law, Al 7075 Sinh.

Table 10: Parameters for the hyperbolic sine law for Al 2195 from the HyperXtrude database.

Parameter	Symbol	Unit	Al 7075
Stress Exponent	n	-	5.41
Activation Energy	Q	J/mol	129,400
Reciprocal Strain Factor	A	-	1.03E+09
Stress Multiplier	α	1/Pa	1.41E-08

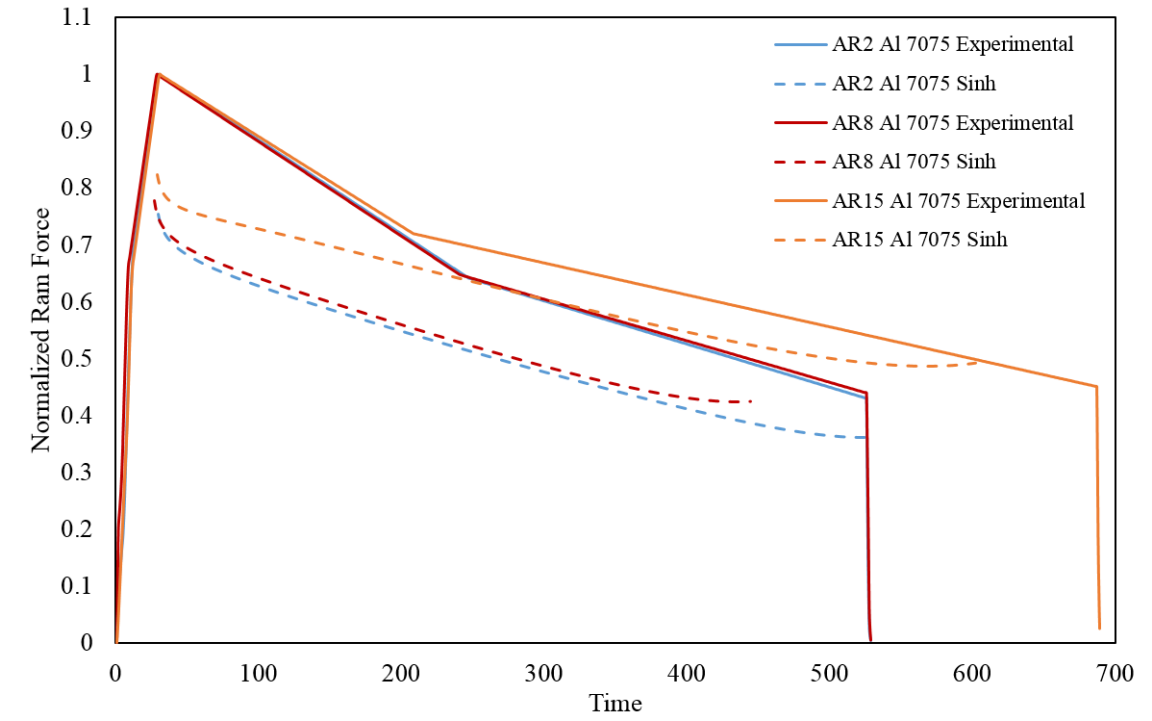

Figure 95: Experimental load curves compared to those predicted by HyperXtrude using the sinh law for Al 7075.

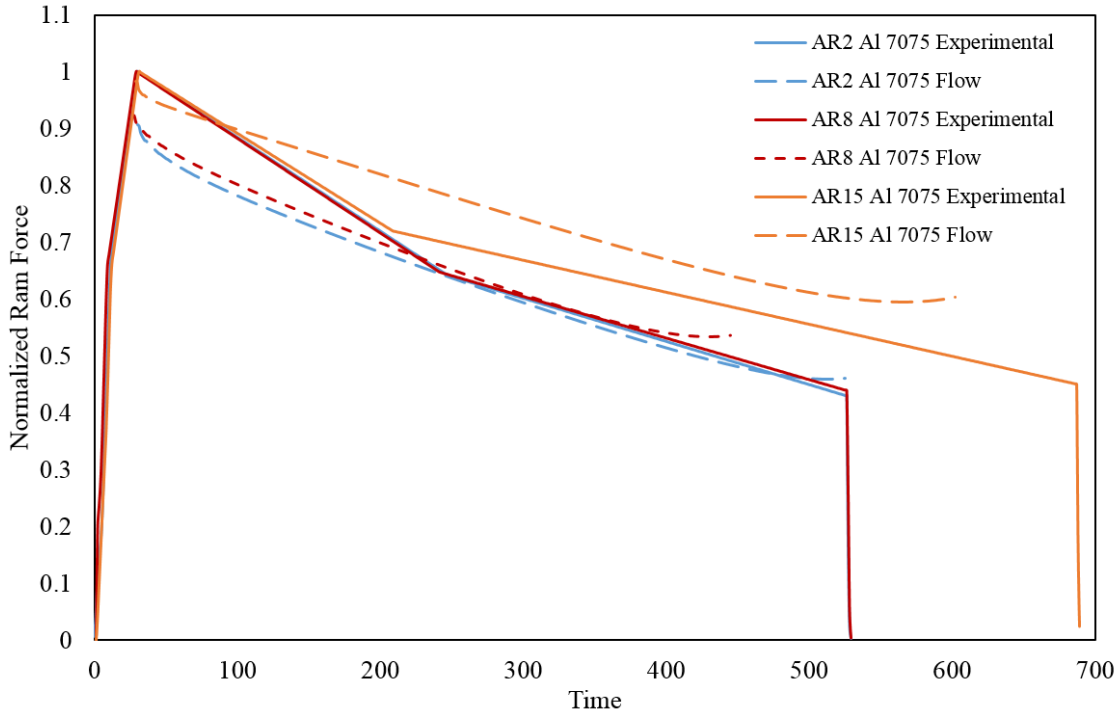

Figure 96: Experimental load curves compared to those predicted by HyperXtrude using high temperature flow stress data for Al 7075.

6.3 Prediction of Load Curves for Al 2195

There are no pre-existing parameters in the HyperXtrude database for Al 2195 and there currently exists no published hot flow data. Therefore, various methods were used to model the Al 2195 AR2, AR8, and AR15 experimental load curves. Thermodynamic parameters for Al 2195 were obtained using JMatPro, a Sente Software, in partnership with UAC-Canton, as reported in Table 11.

Table 11: Thermodynamic parameters used for modeling Al 2195 and Al 7075.

Parameter	Unit	Al 2195	Al 7075
Density	kg/m	2,681	2,810
Specific Heat	J/kgK	1,100	960
Conductivity	W/mK	139.91	173
Coefficient of Thermal Expansion	1/K	2.80E-05	1.00E-05
Volumetric Heat Source	W/m^3	0	0
Reference Temperature	K	700	700
Liquidus Temperature	K	970	908
Solidus Temperature	K	960	750
Young Modulus	Pa	5.88E+10	4.00E+10
Poisson Ratio	-	0.354	0.350

6.3.1 HyperXtrude Numerical Method

The Relative Extrudability Numerical Approach is HyperXtrude's built-in method for fitting the hyperbolic sine law referred to as the Relative Extrudability Numerical Approach [139]. This approach compares the extrudability of an unknown alloy to Al 6063 based on the actual press data of the unknown alloy. Relative extrudability (R_{ex} in Equation 12) is the ratio of the experimental peak pressure ($P_{experimental}$) for the alloy of interest and the HyperXtrude peak pressure for Al 6063 (P_{6063}) run with the same parameters. Al 6063 is used as the baseline because it has an extrudability equal to 100 [130]. For the Relative Extrudability Approach, peak pressure is found using a steady-state analysis.

$$R_{ex} = \frac{P_{experimental}}{P_{6063}} \tag{12}$$

Comparison of the extrusion data for AR15 to the Al 6063 simulation resulted in an extrudability number of 255.7 for Al 2195. This R_{ex} falls between that of Al 2024 and Al 5054 [130]. Once the relative extrudability number was calculated for Al 2195, a new material was created using HyperXtrude's "fit material" option, wherein the constitutive parameters were calculated by HyperXtrude based on the relative extrudability number.

This numerical fit, "Numerical Sinh", was then used to re-model the extrusion. The load curves predicted by Numerical Sinh are shown in Figure 97. The predicted peak loads fell 15% (AR2), 10% (AR8), and 17% (AR15) below experimental values. These variations are outside of the acceptable +/- 10% range established using the Al 7075 results. According

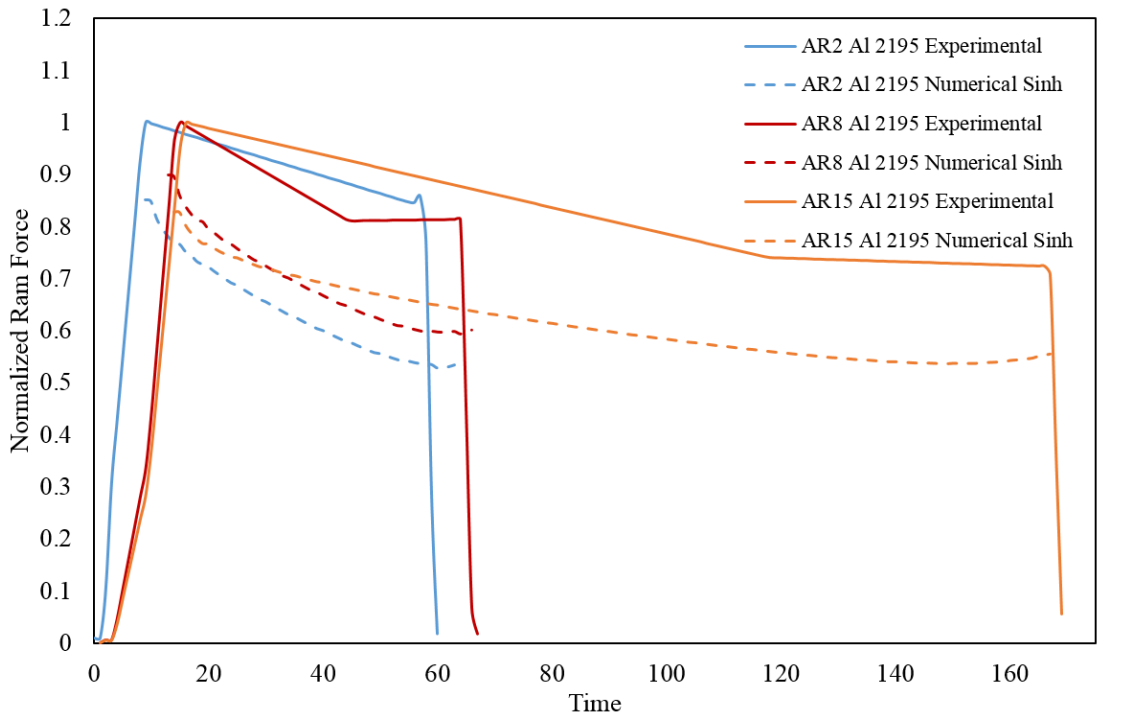

Figure 97: Experimental load curves compared to those predicted by HyperXtrude using the sinh Numerical Fit for Al 2195.

to HyperXtrude [139], adjustments to the numerical fit should be made until the predicted breakthrough pressure and exit temperature match with the experimental values. While exit temperature data was not available, peak ram force, or load, was considered an accurate predictor of a material's thermo-mechanical behavior.

A study of the effects of systematically changing each variable in the hyperbolic sine law was performed (Appendix G). Based on these results, systematic, manual adjustments of Numerical Sinh was iteratively performed to decrease the variation in peak pressures

Table 12: Parameters for the hyperbolic sine law for Al 2195 fit from HyperXtrude numerical methods.

Parameter	Symbol	Unit	Numerical Sinh	Adjusted I	Adjusted II
Stress Exponent	n	-	5.08344	15.8	9.7
Strain Rate Offset	-	-	0.01	0.01	0.01
Activation Energy	Q	J/mol	149,337	185,500	360,160
Reciprocal Strain Factor	A	-	1.31E+10	1.31E+10	1.63E+10
Universal Gas Constant	R	J/mol-K	8.314	8.314	8.314
Stress Multiplier	α	1/Pa	1.57E-08	1.70E-08	6.10E-08

to less than 0.5% for AR15. The first result of this manual adjustment is referred to as "Adjusted I." If this was a unique solution and the parameters, such as Q and n, accurately represented the material's deformation behavior then a second round of manual adjustments should lead to the same result. Using Numerical Sinh as the starting point, a second round of adjustments was performed which led to a second set of parameters, referred to as "Adjusted II." Compared to the experimental values, the predicted peak loads for Adjusted I (Figure 98) are 2% below for AR2, 0.3% above for AR8, and 6% below for AR15. The peak loads for Adjusted II (Figure 99) are 2% (AR2), 0.4% (AR8), and 5% (AR15) below experimental values.

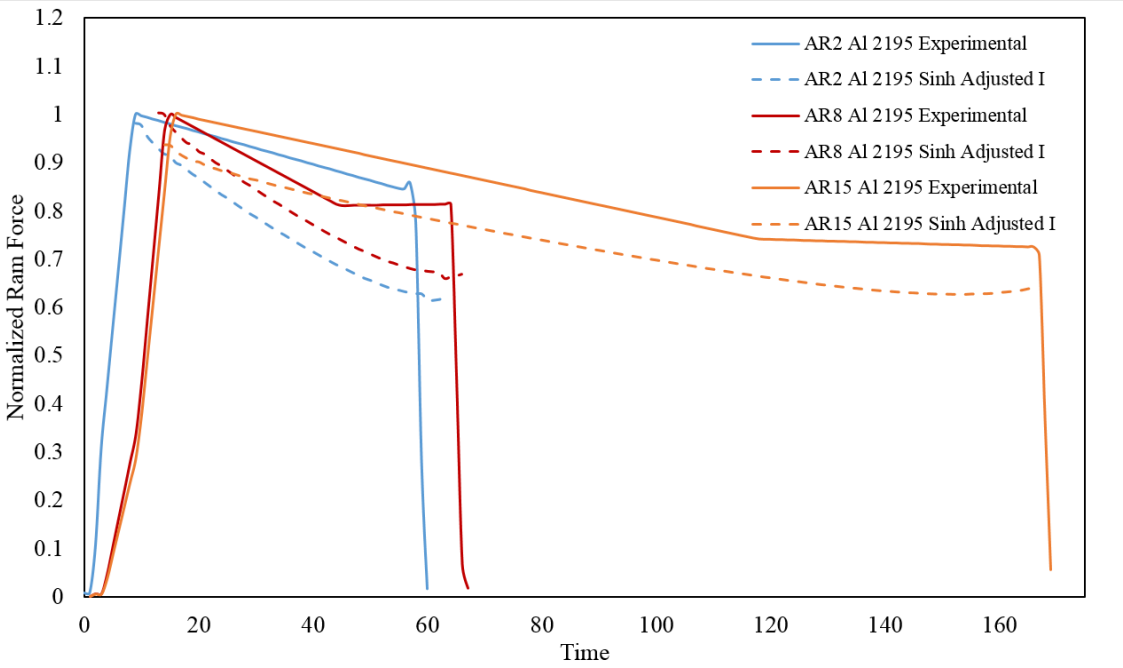

Figure 98: Experimental load curves compared to those predicted by HyperXtrude using the Adjusted I Sinh for Al 2195.

Since the Adjusted I and Adjusted II parameters, given in Table 12, are non-unique solutions but both accurately predicted the load curves for Al 2195 extrusions, these parameters do not have physical significance. For example, the activation energy for deformation, Q, was 186 kJ/mol for Adjusted I and 360 kJ/mol for Adjusted II. Typically, the higher the activation energy, the more difficult a material is to extrude. These values, however, were

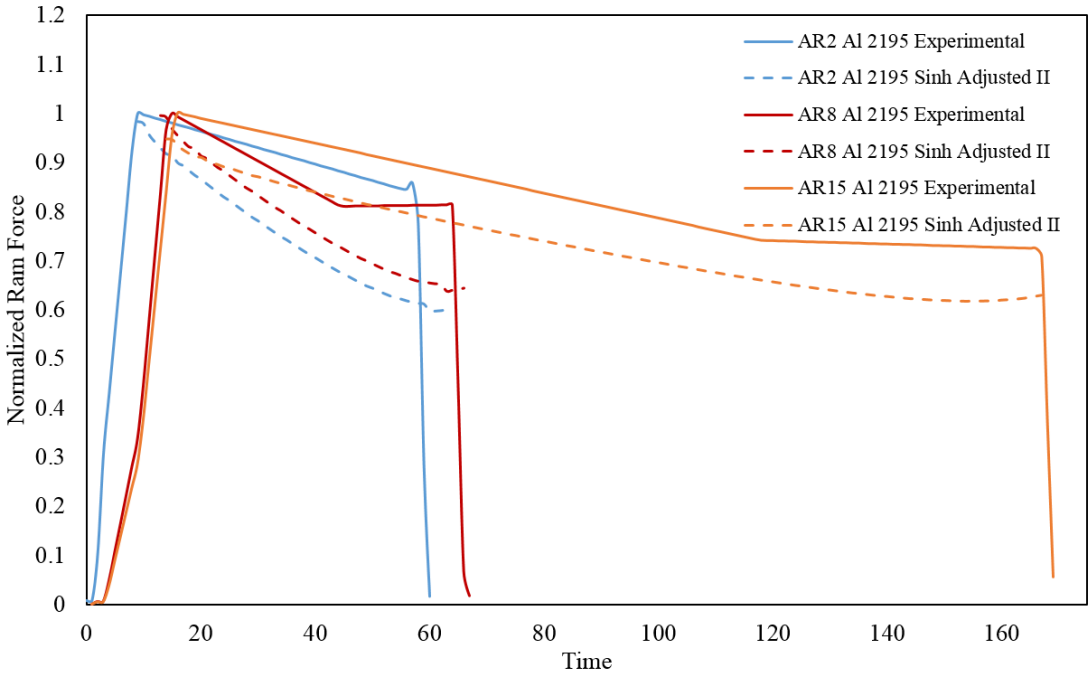

Figure 99: Experimental load curves compared to those predicted by HyperXtrude using the Adjusted II Sinh for Al 2195.

reached in an arbitrary manner, so conclusions about Al 2195's deformation behavior cannot be drawn based on the individual parameters of these fits. The peak loads predicted by Adjusted I and Adjusted II, however, are all within the +/- 10% from experimental range which was deemed acceptable based on the Al 7075 simulations.

6.3.2 Flow Stress Methods

The high temperature deformation behavior of a material can be experimentally studied using tensile, compression, and torsion tests. Due to necking, tensile tests are generally limited to a maximum strain of 0.3. The barreling phenomenon in compression tests limits the maximum strain to 1.0-2.0 [86]. Torsion tests do not suffer from these limitations, and can achieve maximum strains of greater than 20. Extrusion is a high temperature and high strain forming method; therefore, a test method that can achieve similarly high strains is recommended. For this reason, torsion tests were performed to obtain flow stress data for use in fitting constants to the hyperbolic sine constitutive equation. The procedures for hot torsion testing can be found in Section 3.8.

The grip region (Figure 20) of each torsion sample was not exposed to any strain, or temperatures above 100°C. Therefore, by performing optical microscopy in this region, it was confirmed that all of the samples had the same starting microstructure (Figure 100). The resulting shear stress vs. shear strain plots can be seen in Figure 101. At 400°C and 500°C the peak stress increased and the ductility decreased with increasing strain rate, which is the expected deformation behavior. However, at 450°C (Figure 101b) the low strain rate tests resulted in a higher than expected peak stress. Initially, this was thought to be an experimental error. Therefore, the 450°C 0.1/s test was re-run, resulting in a similarly high peak stress. A test performed at 0.01/s and 450°C confirmed that the material seemed to strengthen at 450°C for strain rates of 0.1/s and 0.01/s. These points were excluded when fitting the hyperbolic sine law as they were anomalous with respect to the general material behavior.

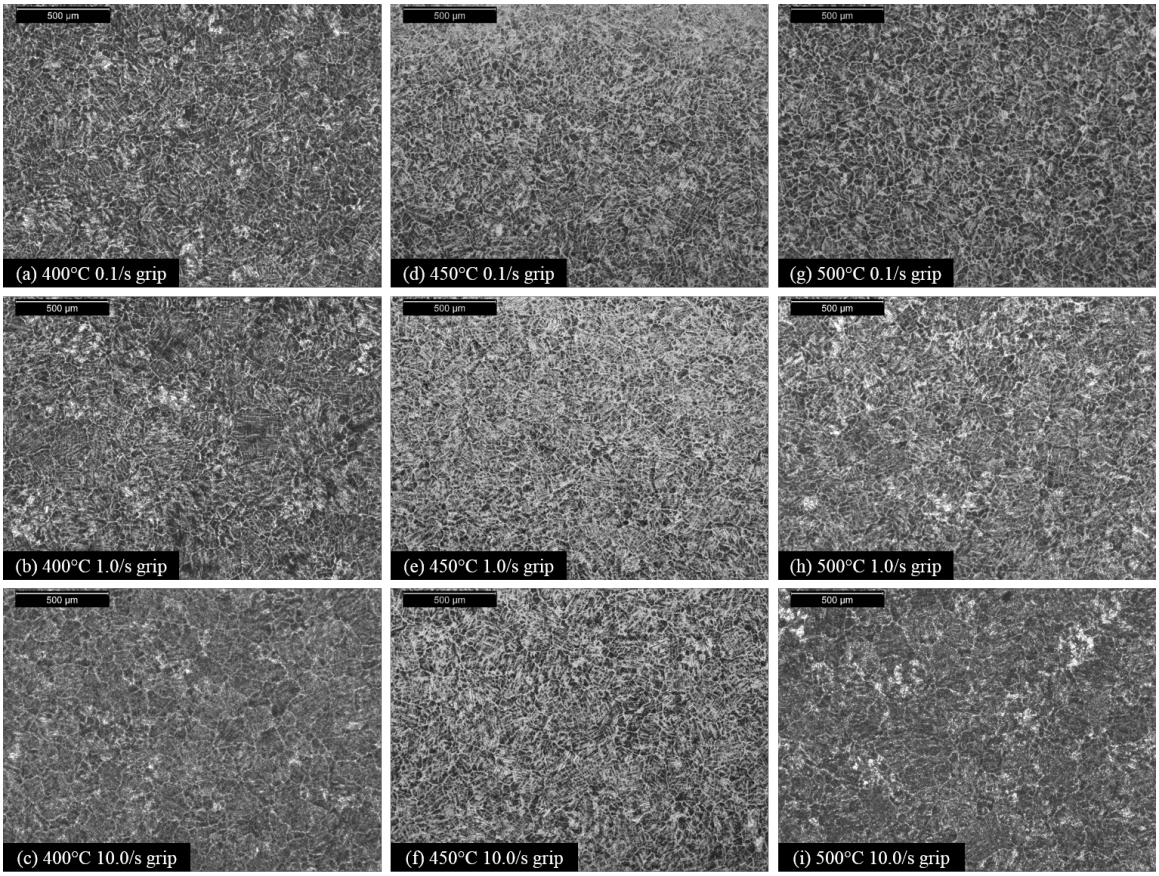

Figure 100: Microstructures from the grip region of each torsion sample (50X Keller's etch).

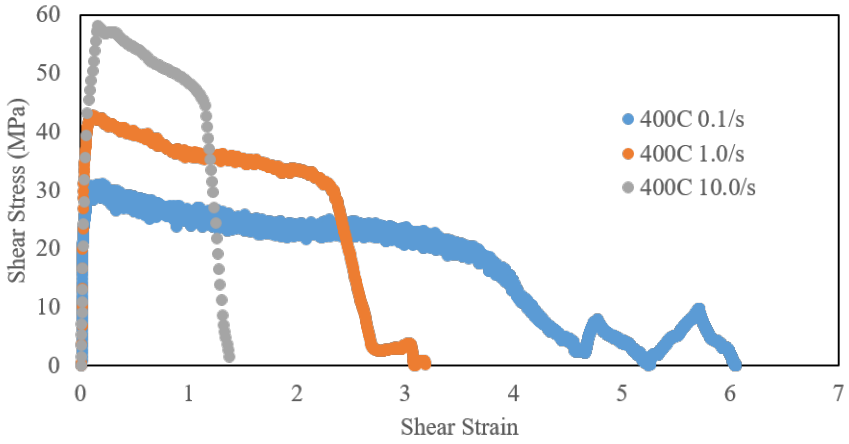

(a) 400°C

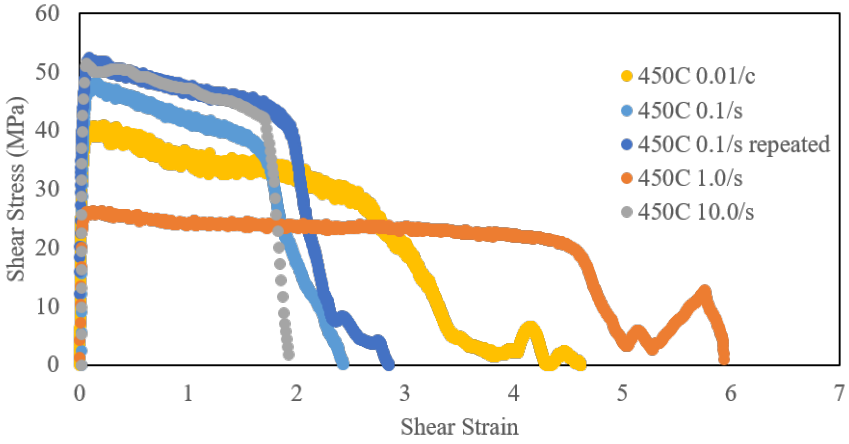

(b) 450°C

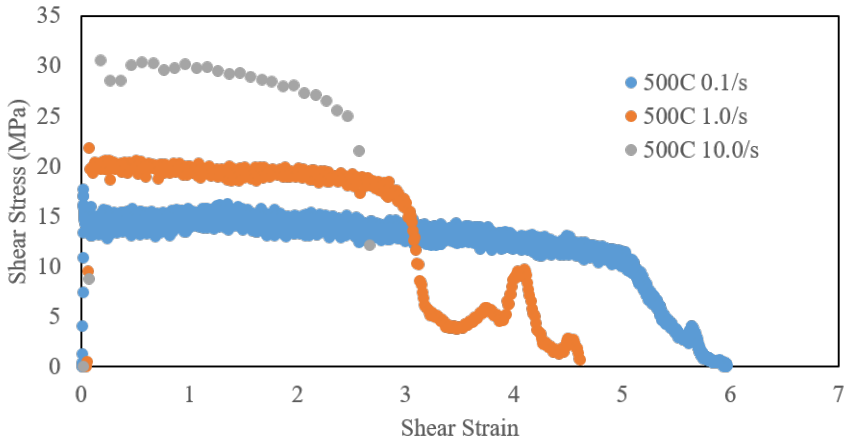

(c) 500°C

Figure 101: Shear stress versus shear strain plots for all torsion samples

Hot torsion tests produce time (seconds), temperature (°C), thrust (N), torque (Nm), and torsion (radians) data. These were converted into equivalent stress (MPa) and strain, and multiple regression analysis was performed to find parameters for the hyperbolic sine constitutive equation. Below are the steps used for extracting constitutive parameters from raw torsion data. Several references were used to construct and confirm this approach [86, 128, 140–146].

1. Plot log(strain rate) vs. log(peak torque), take the average slope, and set this equal to m, the strain hardening exponent.

2. Convert torque (Γ) into surface shear stress (τ) via Equation 13 where r is the radius of the solid rod and m is the strain rate sensitivity. The strain hardening exponent, k, is assumed equal to 0 at the peak stress and in the steady state regime at high deformation temperatures [141, 147].

$$\tau = [3 + m + k)(\Gamma)]/(2\pi r^3) \tag{13}$$

3. Convert shear stress (τ) into equivalent stress (σ) via Equation 14.

$$\sigma = \sqrt{3}\tau \tag{14}$$

4. Convert torsion (θ) into shear strain (γ) via Equation 15 where L is the gauge length of the rod and r is the radius.

$$\gamma = \frac{r}{L}\theta \tag{15}$$

5. Convert shear strain (γ) into equivalent strain (ϵ) via Equation 16.

$$\epsilon = \frac{\gamma}{\sqrt{3}} \tag{16}$$

6. Plot ln(flow stress) vs. ln(strain rate) as in Figure 102a, find the average slope, and set this equal to n_1.

7. Plot flow stress vs. ln(strain rate) as in Figure 102b, find the average slope, and set this equal to β.

8. Use $\alpha = \beta/n_1$ to calculate α.

9. Plot ln(sinh($\alpha\sigma$)) vs. ln(strain rate) as in Figure 102c, find the average slope, and set this equal to n.

10. Plot 1000/T vs. ln[sinh($\alpha\sigma$)] for a constant stress at various strain rates as in Figure 102d, find the average slope, and set this equal to S.

11. Use $Q = RnS$ to calculate Q.

12. Plot ln[sinh$\alpha\sigma$] as in Figure 103, fit the line, find the y-intercept, and use the linearized hyperbolic sine law ($lnZ = lnA + nln[sinh(\alpha\sigma)]$) to calculate A.

13. Use values of α, n, Q, and A found above in the hyperbolic sine law.

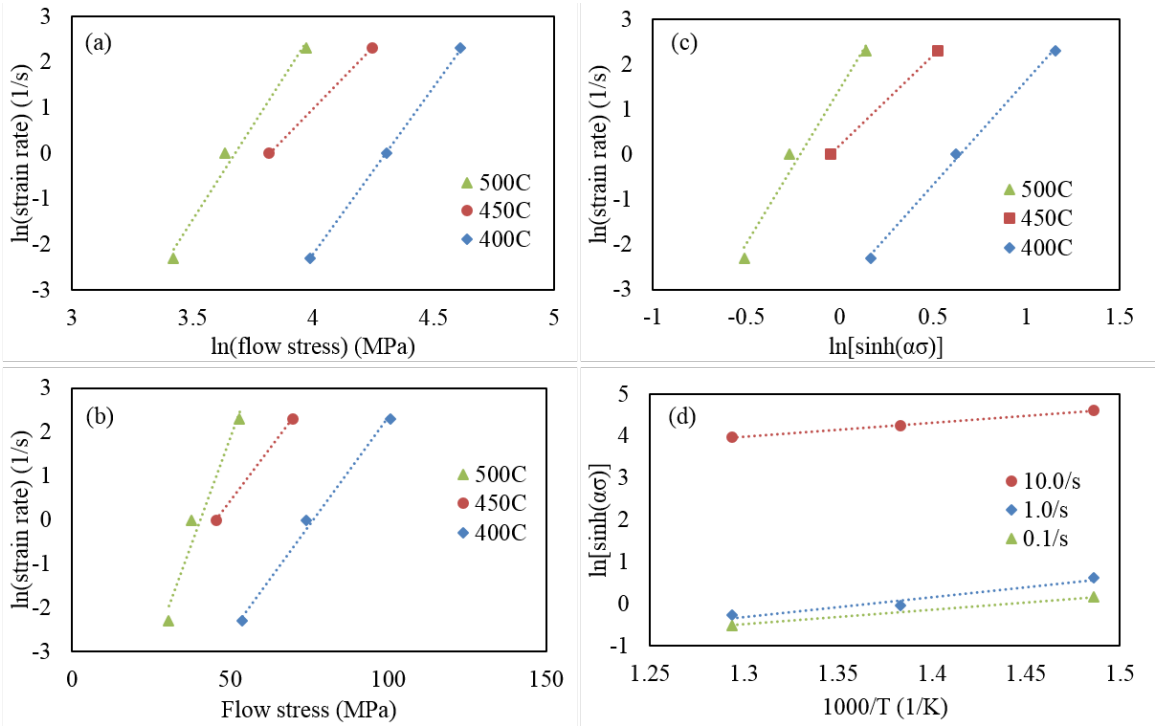

Figure 102: Plots used to fit parameters for the hyperbolic sine law from Al 2195 hot torsion test results.

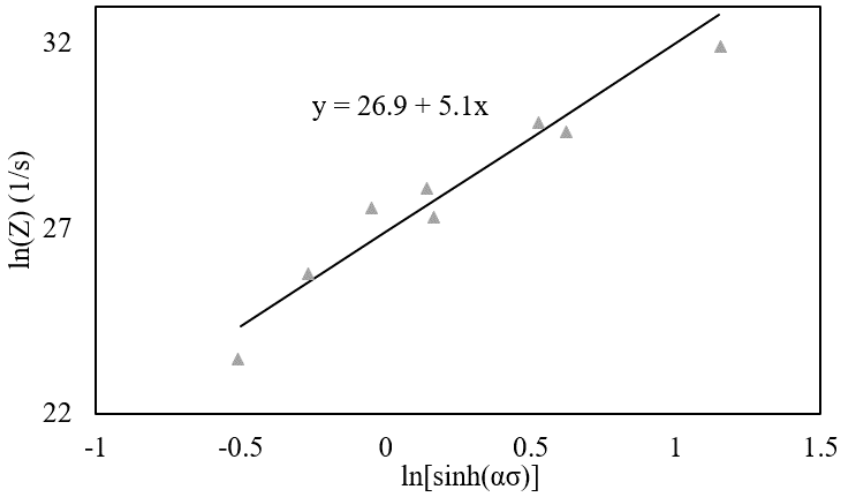

Figure 103: Plot used to fit the reciprocal strain factor (A) for Al 2195.

Table 13: Parameters for the hyperbolic sine law for Al 2195 fit from hot torsion data.

Parameter	Symbol	Unit	Torsion Result for Al 2195
Stress Exponent	n	-	5.1
Activation Energy	Q	J/mol	165,654
Reciprocal Strain Factor	A	-	4.80E+11
Stress Multiplier	α	1/Pa	1.86E-08

The resulting parameters for the hyperbolic sine law are reported in Table 13 and are referred to as the "Sinh Torsion" fit. The load curves predicted with the Sinh Torsion fit are significantly below the experimental values (Figure 104). The peak loads were 37, 33, and 38% below experimental for AR2, AR8, and AR15, respectively. This was not completely unexpected since the simulated load curves for Al 7075 using the sinh law were 18-24% below experimental values.

In an attempt to have better prediction of the peak loads, a flow stress table was created (Appendix F) and used to simulate the extrusions. The format of the flow stress material file did not allow for the omission of particular points, such as the 450°C 0.1/s data point. All data points from a particular temperature had to be either completely included or completely excluded. Therefore, a table was created with all of the flow stress data from 400°C, 450°C, and 500°C at strain rates of 0.1, 1.0, and 10.0/s. This material method is

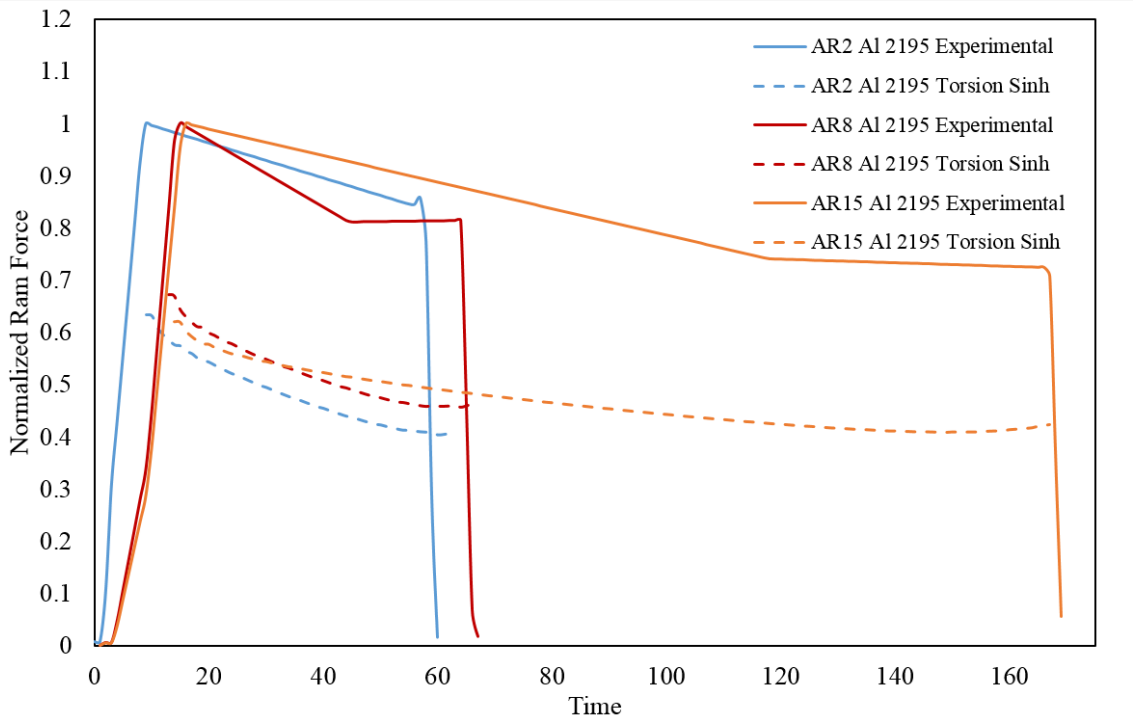

Figure 104: Experimental load curves compared to those predicted by HyperXtrude using the sinh fit from hot torsion data for Al 2195.

referred to as "FlowAll." The simulated peak load values using FlowAll are 43% (AR2), 34% (AR8), and 51% (AR15) below experimental (Figure 105).

Since FlowAll included the 450°C 0.1/s data point "Flow", was created including only the 400°C and 500°C data (Appendix F). The Flow table led to peak loads 49% (AR2), 44% (AR8), and 56% (AR15) below experimental values. It also predicted irregular shapes for the transient behavior (Figure 105). Next, a table with only the 450°C data at 0.01, 0.1, 1.0, and 10.0 (Appendix F), referred to as "FlowAnomalous", was used to simulate these extrusions. The predicted peak loads using FlowAnomalous fall 8% (AR2), 1% (AR8), and 15% (AR15) below experimental values.

Out of the four flow stress methods (Sinh Torsion, FlowAll, Flow, and FlowAnomalous), FlowAnomalous most closely predicted the peak loads. Based on the Al 7075 simulations, the acceptable range is defined as +/- 10%. Using FlowAnomalous, the AR2 and AR8 peak loads were within this range; however, the predicted load for AR15 was outside of the

acceptable range. Therefore, none of the physically based flow stress methods met the +/- 10% peak load prediction standard.

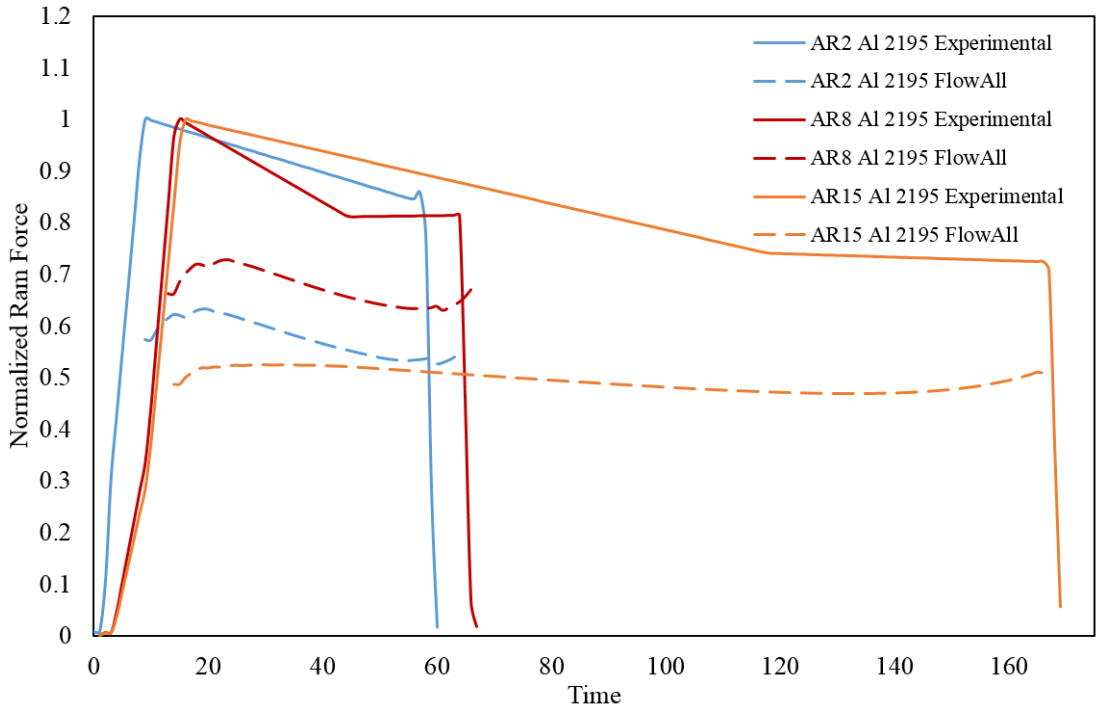

Figure 105: Experimental load curves compared to those predicted by HyperXtrude using the flow stress data from hot torsion tests of Al 2195 (including all 0.1, 1.0, and 10.0/s data).

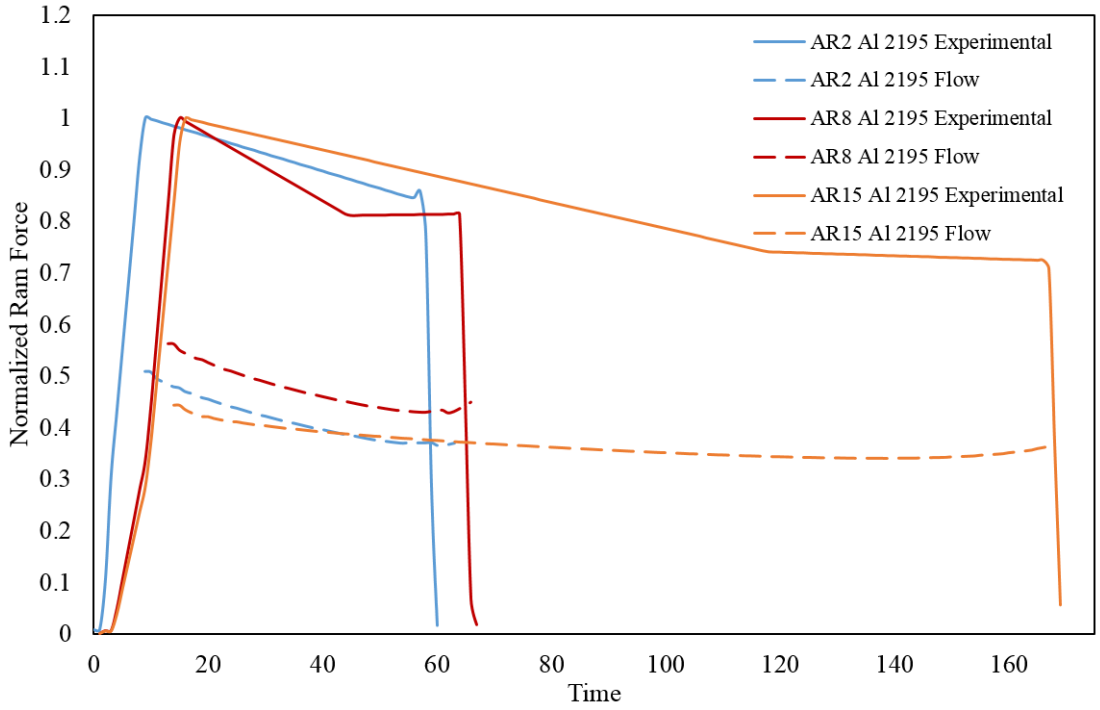

Figure 106: Experimental load curves compared to those predicted by HyperXtrude using the flow stress data from hot torsion tests of Al 2195 (excluding 450°C data).

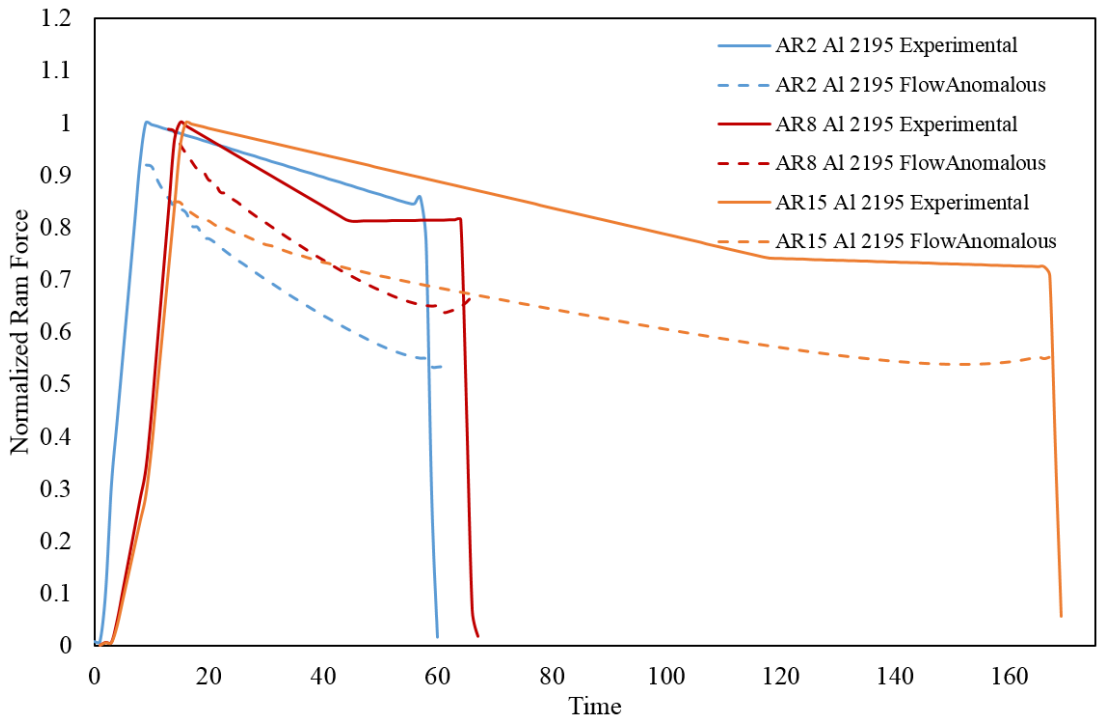

Figure 107: Experimental load curves compared to those predicted by HyperXtrude using only the 450°C flow stress data from hot torsion tests of Al 2195.

6.4 Discussion

In total, seven different fits/methods were used to model the load curve behavior of Al 2195.

1. Numerical Sinh: Initial fit as calculated by HyperXtrude's built-in Relative Extrudability approach
2. Adjusted I Sinh: Result of first round of manual adjustments
3. Adjusted II Sinh: Result of second round of manual adjustments
4. Torsion Sinh: Hyperbolic sine fit from torsion data
5. FlowAll: Flow stress table including all 400, 450, and 500°C, 0.1, 1.0, and 10.0/s data
6. Flow: Flow stress data excluding 450°C data
7. FlowAnomalous: Flow stress table including only 450°C data

Table 14: Variations between simulated and experimental peak loads for various methods of FEM modeling of Al 7075 and Al 2195.

Alloy	Method	Variation from Experimental Peak Load (%)			
		AR2	AR8	AR15	Average
Al 7075	Sinh	25	22	18	22
Al 7075	Flow Stress	9	8	2	6
Al 2195	Numerical Sinh	15	10	17	14
Al 2195	Adjusted I Sinh	2	0.3	6	3
Al 2195	Adjusted II Sinh	2	0.4	5	2
Al 2195	Torsion Sinh	37	33	38	36
Al 2195	FlowAll	43	34	51	43
Al 2195	Flow	49	44	56	50
Al 2195	FlowAnomalous	8	1	15	8

The load curve simulation results are summarized in Table 14. Al 7075 is an alloy with pre-existing parameters and flow stress data. Based on the results from this known alloy, a prediction of the peak load within +/- 10% was set as a standard level of desired accuracy. For Al 2195, the models with no physical basis, Adjusted I and Adjusted II, and that with the least amount of flow stress data, FlowAnomalous, predicted peak loads varying less than 10% from experimental. The flow stress data from hot torsion tests is presented in

Table 15. The 450°C values are represented by x's in Figure 108. Also plotted in Figure 108 are the flow stress curves represented by Adjusted I, Adjusted II, and Torsion Sinh fits to the hyperbolic sine law. If the strain rates for AR2, AR8, and AR15 were less than 1.0/s, then the anomalous 450°C 0.01 and 0.1/s hot torsion data points may best represent the extrusion behavior of Al 2195.

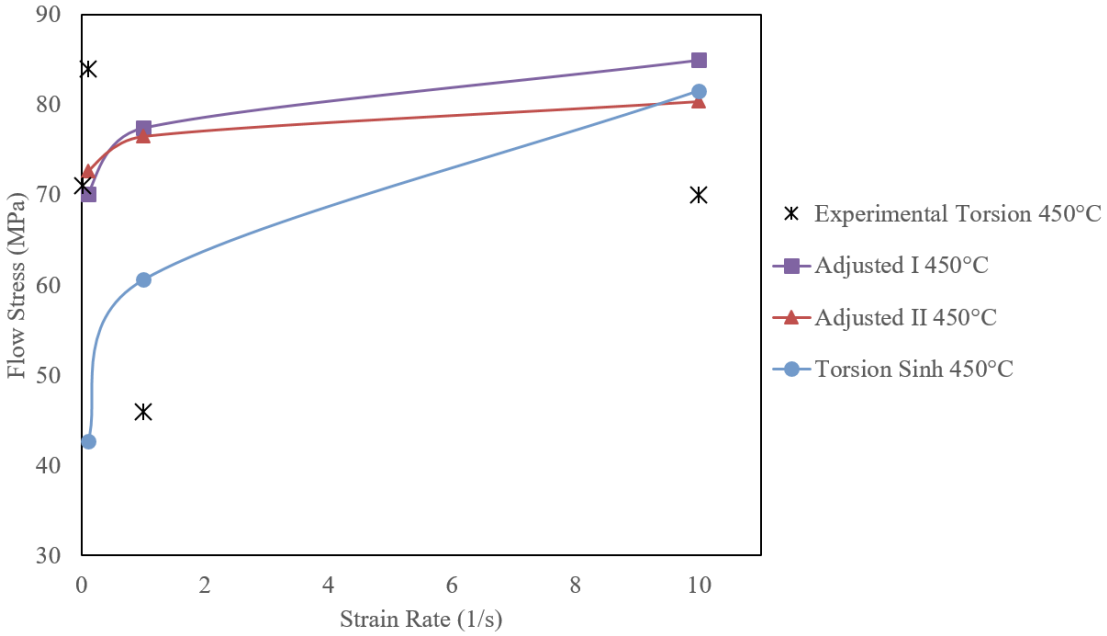

Figure 108: Hyperbolic sine law flow stress curves at 450°C compared to the hot torsion flow stress values.

The strain rate for each extrusion was estimated using Feltham's approximation (Equation 17) where $\dot{\epsilon}$ is strain rate, D_B is the diameter of the billet, D_E is the equivalent diameter of the extrusion, V_{ram} is the ram speed, and ER is the extrusion ratio. The average Feltham's strain rate for the Al 2195 extrusions was approximately 0.27/s for AR2, AR3, AR5, AR7, and AR8 and 0.09/s for AR15.

$$\dot{\epsilon}_{Feltham} = \frac{6D_B^2 V_{ram} ln(ER)}{D_B^3 - D_E^3} \tag{17}$$

Strain rate did not vary based on the constitutive equation used (i.e. the same values and patterns were found when simulating AR2, AR8, and AR15 with Al 6063 as were found using any of the above seven methods) so any fit method could be used to compare HyperXtrude's predicted strain rates to those calculated using Feltham's approximation. Although

Table 15: Equivalent peak stress values from hot torsion tests of Al 2195.

Temperature °C	Strain Rate (1/s)	Equivalent Peak Stress (MPa)	Equivalent Peak Stress (ksi)
400	0.1	53.9	7.8
400	1	74.2	10.8
400	10	100.7	14.6
450	0.01	70.9	10.3
450	0.1	90.9	13.2
450	0.1	83.6	12.1
450	1	45.6	6.6
450	10	69.7	10.1
500	0.1	30.6	4.4
500	1	37.9	5.5
500	10	53.0	7.7

HyperXtrude estimated strain rates as high as 13.0 near the edges of the extrusions, at the center, each displayed strain rates consistently below 1.0/s (Figure 109). Based on Feltham's approximation and HyperXtrude's prediction, the bulk of the profiles were exposed to strain rates less than 1.0/s.

It can be concluded that the seemingly anomalous behavior in the hot torsion data at 450°C 0.01/s and 0.1/s accurately describes the experimental material behavior. FlowAnomalous, Adjusted I, or Adjusted II should be used for modeling extrusions near this temperature in HyperXtrude. Theoretically, some change in dynamic recovery/recrystallization behavior or change in the deformation mode around second phase particles might cause this dramatic strengthening behavior. As discussed in Chapter 5, the microstructure of Al 2195 does evolve with time at temperature. Dissolution of the T_1 phase and coarsening of grain boundary θ occur around 450°C. However, each of these samples was held at 450°C for roughly the same amount of time (approximately 20 minutes) for the length of the test. Any hardening effect due to dissolution and coarsening is expected at all strain rates; however, it was only observed at the two lowest: 0.01/s and 0.1/s. Bright field optical and polarized light microscopy were performed on the cross sections of the gauge and shoulder regions of the torsion specimens to investigate this phenomenon (Appendix H). However, the optical micrographs did not yield any conclusive evidence. Further research is needed

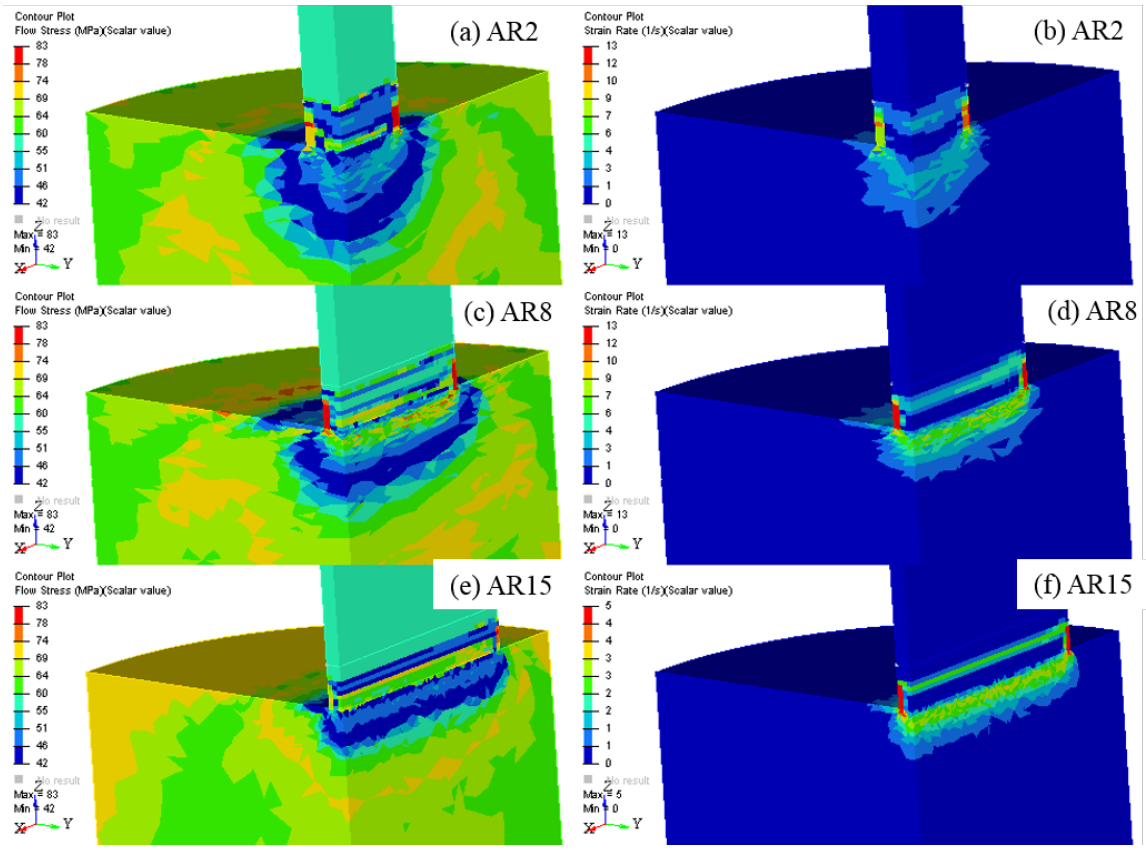

Figure 109: Flow stress and strain rate for AR2, AR8, and AR15 predicted by HyperXtrude using FlowAnomalous flow stress table.

to understand this anomalous hardening of Al 2195 at 450° 0.01/s and 0.1/s as discussed in Section 9.2.

6.5 Summary

A standard peak load prediction of +/- 10% from experimental was established using Al 7075. For the previously un-reported hot deformation behavior of Al 2195, the use of flow data from 450°C resulted in prediction of the load curves (+/- 15%) with physical significance for extrusions performed around this temperature. Use of a non-unique numerical fit to the hyperbolic sine law, Adjusted II, led to accurate prediction of all peak loads within 5% and had the lowest average variation of 2%. Since this set of constitutive parameters was the best fit for Al 2195, Adjusted II was used for further practical modeling of Al 2195 extrusions.

CHAPTER 7

PRACTICAL APPLICATIONS AND LIMITATIONS OF HYPERXTRUDE

The previous chapter focuses on finding a suitable method for modeling the high temperature deformation behavior of Al 7075 and Al 2195. These methods can be applied for finite element modeling (FEM) of Al 2195 and Al 7075 extrusions. Ideally, the effects of varying initial billet temperature and ram speed on the final mechanical properties of Al 2195 extrusions could be studied in a computation framework. This chapter examines the practical applications and limitations of FEM with HyperXtrude. Results from experimental and simulated strain fields, grain sizes, and yield strengths are presented and discussed. The current limitations of HyperXtrude with respect to prediction of yield strength anisotropy are also discussed and recommendations made for future improvements.

7.1 Predicted and Experimental Strain Fields

Simulations of Al 2195 AR2, AR8, and AR15 extrusions were run in HyperXtrude with the experimental press parameters using the Adjusted II material parameters (see Table 12). Strain fields were mapped along the cross section for the final time step (Figures 110a, 111a, and 112a). The billet butts from the Al 2195 AR2, AR8, and AR15 extrusions were air cooled, cross sectioned, and macro-etched. This macro-etch revealed strain fields as shown in Figures 110b, 111b, and 112b. The simulated strain fields accurately predicted regions of maximum strain at the die face, seen in red. The simulation also accurately predicted the dead metal zone, seen as the dark blue triangular region near the die entrance. The intake region, which appears as a triangle at the bottom and middle of the macro-etched butts, was not accurately predicted by HyperXtrude. The high strain flow lines seen in all of the Al 2195 extrusions are not represented in the strain contour plots. Quantitative comparison of the experimental and simulated strain fields could not be performed using the macro-etched billet butts.

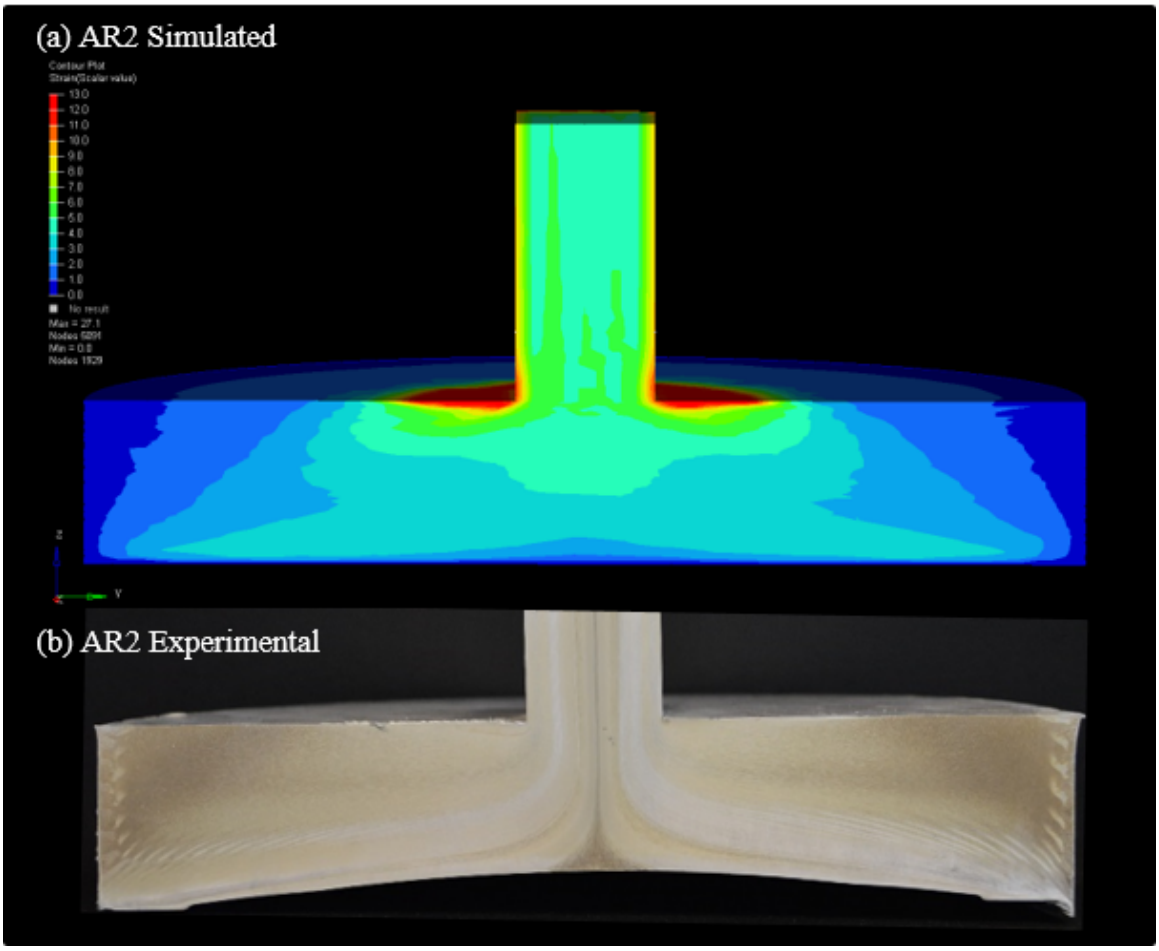

Figure 110: (a) Simulated and (b) experimental strain patterns from the AR2 Al 2195 billet butt.

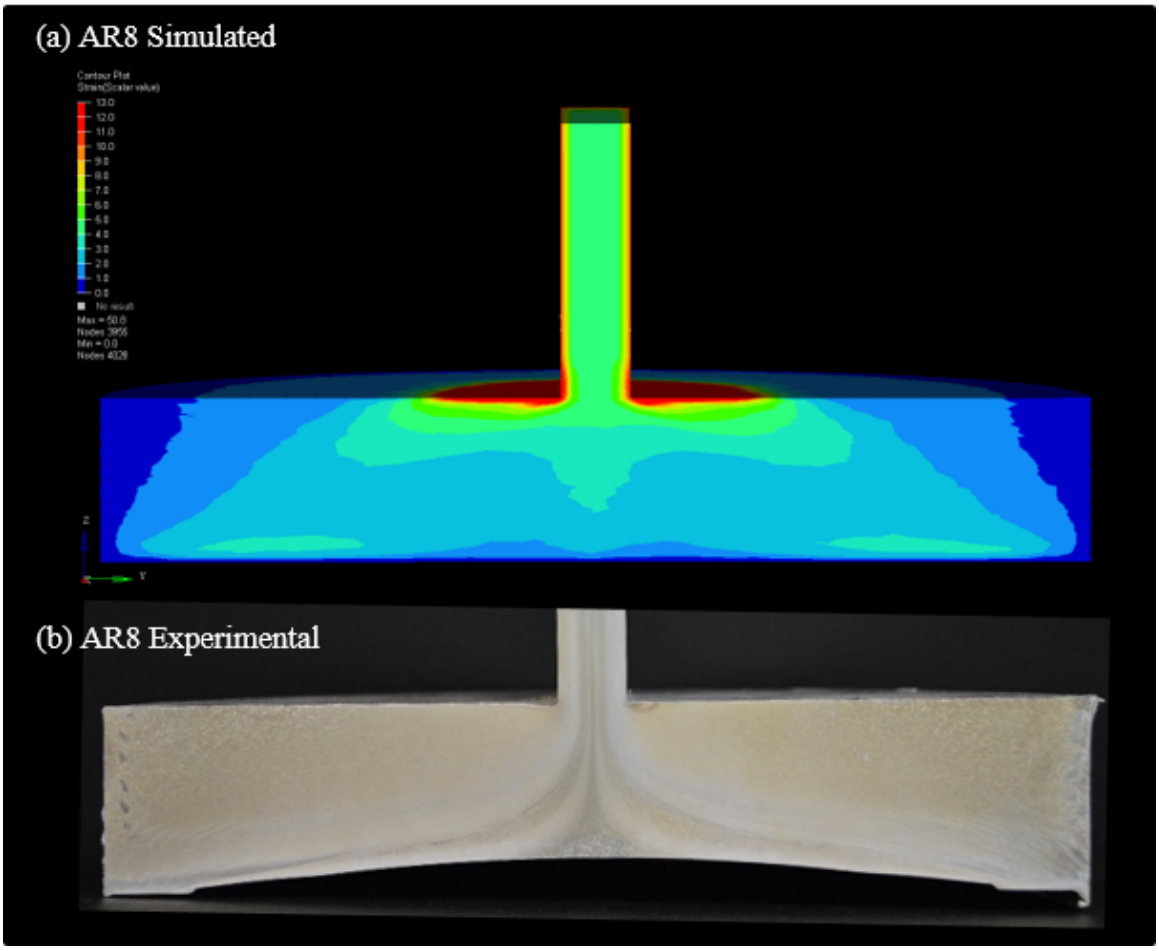

Figure 111: (a) Simulated and (b) experimental strain patterns from the AR8 Al 2195 billet butt.

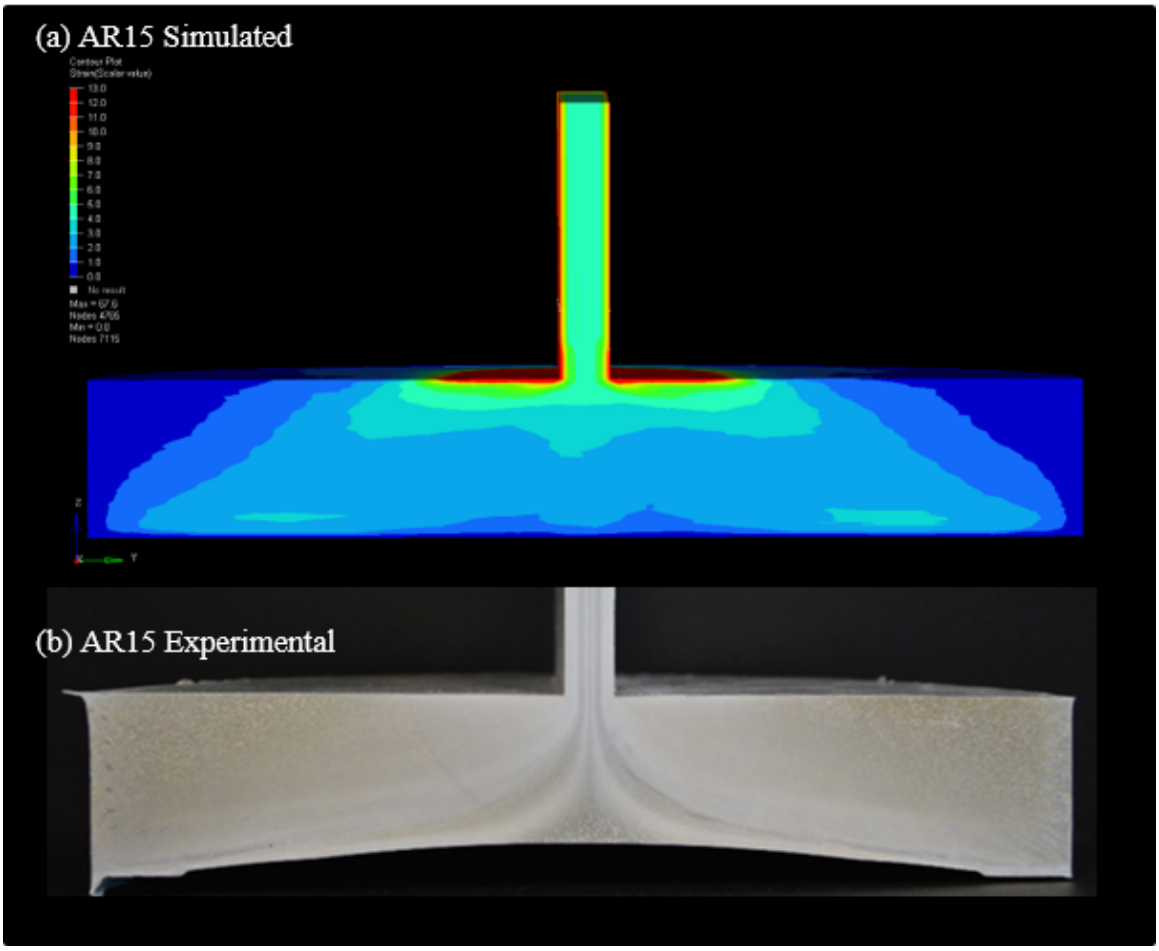

Figure 112: (a) Simulated and (b) experimental strain patterns from the AR15 Al 2195 billet butt.

Quantitative analysis can be performed using gridded billets. While gridded billets were not used in this study, Flitta and Sheppard [148] reported results from extrusion and FEM simulation of Al 2024. One of these gridded billets, shown in Figure 113a, was simulated in HyperXtrude using the parameters given in Table 16 from Flitta and Sheppard [148] with the billet dimensions from Niu, Velay, and Sheppard [116]. Similar to the results from simulation of strain fields for the Al 2195 extrusions performed in this work, HyperXtrude was able to predict the dead metal zone for Flitta and Sheppard's Al 2024 extrusion (Figure 113). Also similar to the Al 2195 strain fields, the simulated strain field for Al 2024 did not accurately predict the strain in the intake region, as denoted in Figure 114. Based on the gridded billet, two other regions, labeled as the horseshoe region and the domed region in Figure 114, were not accurately predicted. The gridded billet shows zero strain in the domed region while HyperXtrude predicts a strain of 0.3-0.5 in the domed region. HyperXtude then predicts zero strain in the horseshoe region while the elements in this region of the gridded billet are deformed indicating strain greater than zero.

Table 16: Extrusion parameters used to simulate Flitta and Sheppard's gridded billet [116, 148]

Parameter	Input Value
Alloy	AA2024
Billet Diameter	75 mm
Billet Length	95 mm
Ram Speed	3 mm/s
Butt Length	62 mm
Billet Temperature	450°C
Container Temperature	400°C
Die Temperature	400°C
Bearing Length	5 mm

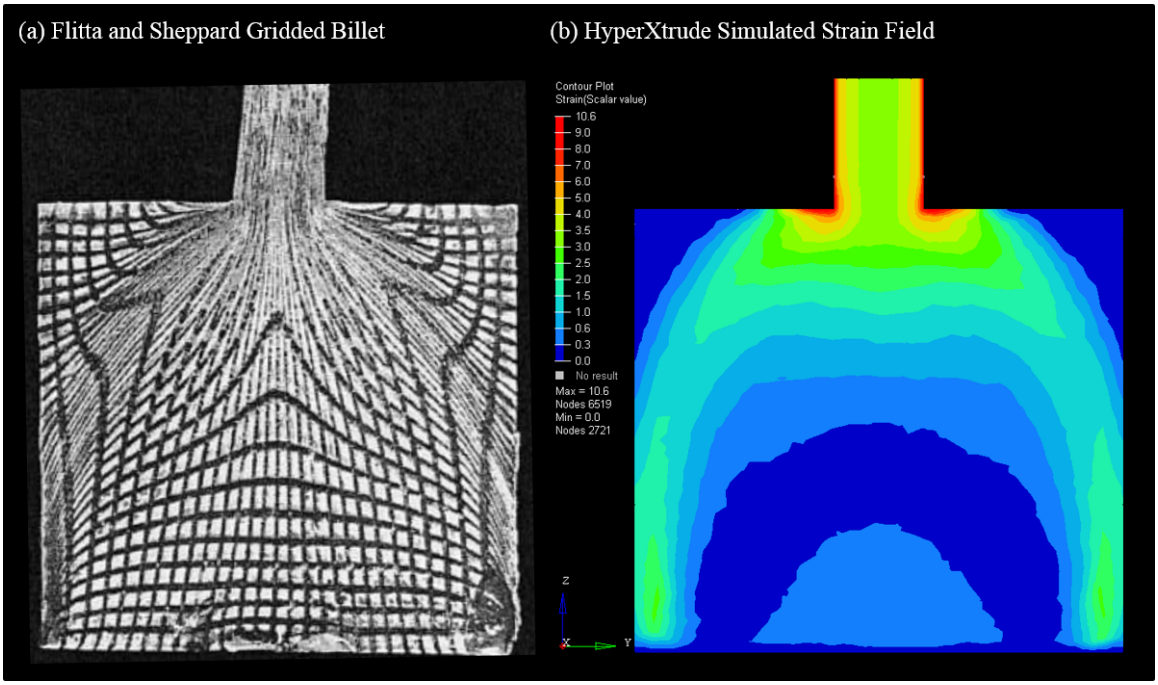

Figure 113: (a) Flitta and Sheppard's [148] experimental gridded billet and (b) the simulated strain field.

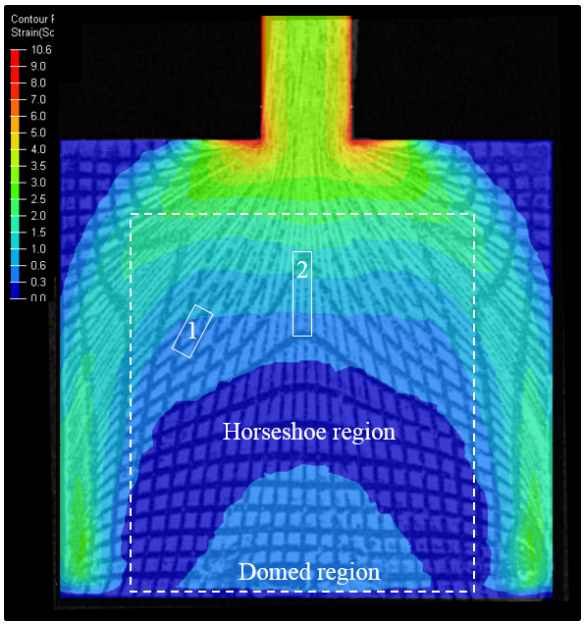

Figure 114: Flitta and Sheppard's experimental gridded billet [148] with an overlay of the simulated strain field. The dashed box indicates the region of poor simulation.

Equations 18-21 from Backofen [82], where the variables correspond to the lengths and angles in Figure 115, were used to make estimates for the strain tensors, $\epsilon_{region1}$ and $\epsilon_{region2}$. Region 1 and Region 2 are indicated on Figure 114. The estimated strain tensors are reported in Equations 22-23.

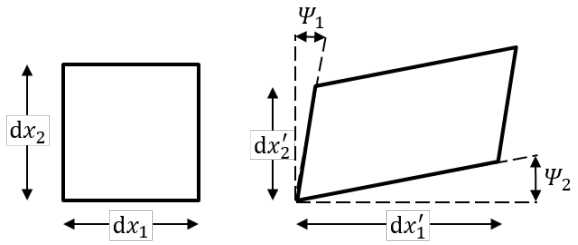

Figure 115: Undeformed grid element (left) and corresponding deformed grid element (right) adapted from [82].

$$\epsilon_{11} = (\frac{dx_1'}{dx_1}) - 1 \tag{18}$$

$$\epsilon_{22} = (\frac{dx_2'}{dx_2}) - 1 \tag{19}$$

$$\gamma_{12} = \gamma_{21} = \Psi_1 + \Psi_2 \tag{20}$$

$$\epsilon_{12} = \epsilon_{21} = \frac{\gamma_{12}}{2} \tag{21}$$

$$\epsilon_{region1} = \begin{bmatrix} 0.33 & 0.55 \\ 0.55 & 0.33 \end{bmatrix} \tag{22}$$

$$\epsilon_{region2} = \begin{bmatrix} -0.33 & 0 \\ 0 & 3.83 \end{bmatrix} \tag{23}$$

$$\epsilon_{max}, \epsilon_{min} = \frac{\epsilon_{11} + \epsilon_{22}}{2} \pm \sqrt{\left(\frac{\epsilon_{11} + \epsilon_{22}}{2}\right)^2 - (\epsilon_{12})^2} \tag{24}$$

Using Equation 24, an average of the minimum and maximum strains were used to find an average strain. Region 1 has an experimental average strain of approximately 0.33 and a predicted strain between 0.3-0.6. HyperXtrude accurately predicted the strain in Region 1. Region 2 has an experimental average strain of approximately 1.75 and a predicted strain

between 0.3-1.0. HyperXtrude underestimated the strain in Region 2, at the center of the billet, by approximately 63%.

For both the Al 2195 and Al 2024 extrusions, HyperXtrude was able to correctly predict the dead metal zone, the regions of increased strain near the die face, and the increased strain near the container wall (Region 1). The macro-etched butts of Al 2195 indicated a region of increased strain near the center of the billet. This region of increased strain was not represented on the strain contours predicted by HyperXtrude. Similarly, the strain in Region 2 from Flitta and Sheppard's [148] gridded billet of Al 2024 was not represented in the HyperXtrude strain contour. The domed and horsehoe regions (Figure 114) predicted by HyperXtrude should have been inverted (i.e. the horseshoe region should have had increased strain and the domed region should have had zero strain) based on Flitta and Sheppard's [148] gridded billet.

7.2 Grain Size and Yield Strength Limitations

There were slight variations in press parameters between each experimental extrusion (i.e. the ram speed, initial billet temperature, container temperature, etc. varied slightly between AR2-AR15) for the Al 2195 and Al 7075 extrusions discussed in Chapter 4. The appeal of FEM is that press parameters can be set as/forced to be constant. The effect of aspect ratio and press parameters on yield strength anisotropy and grain size can, in theory, be isolated and studied using HyperXtrude.

HyperXtrude predicts grain size using a continuous dynamic recrystallization model (CDRX) [149] developed by Hallberg, Wallin, and Ristinamaa [150]. The CDRX model was developed for prediction of grain sizes after equal channel angular extrusion (ECAP) of AA1050 processed at room temperature [150]. HyperXtrude then predicts the yield strength by applying the Hall-Petch relationship, Equation 25, to the predicted grain size where σ_y is the yield strength, σ_o is the material's inherent resistance to dislocation motion, k_y is an empirical constant, and D is the grain size.

$$\sigma_y = \sigma_o + \frac{k_y}{\sqrt{D}} \tag{25}$$

The predicted grain sizes did not vary for Al 2195 AR2 and AR15 simulated with the Adjusted II fit as shown in Figure 116. Similar results were obtained for simulation of the Al 7075 extrusions. This lack of grain size variation does not agree with the experimental

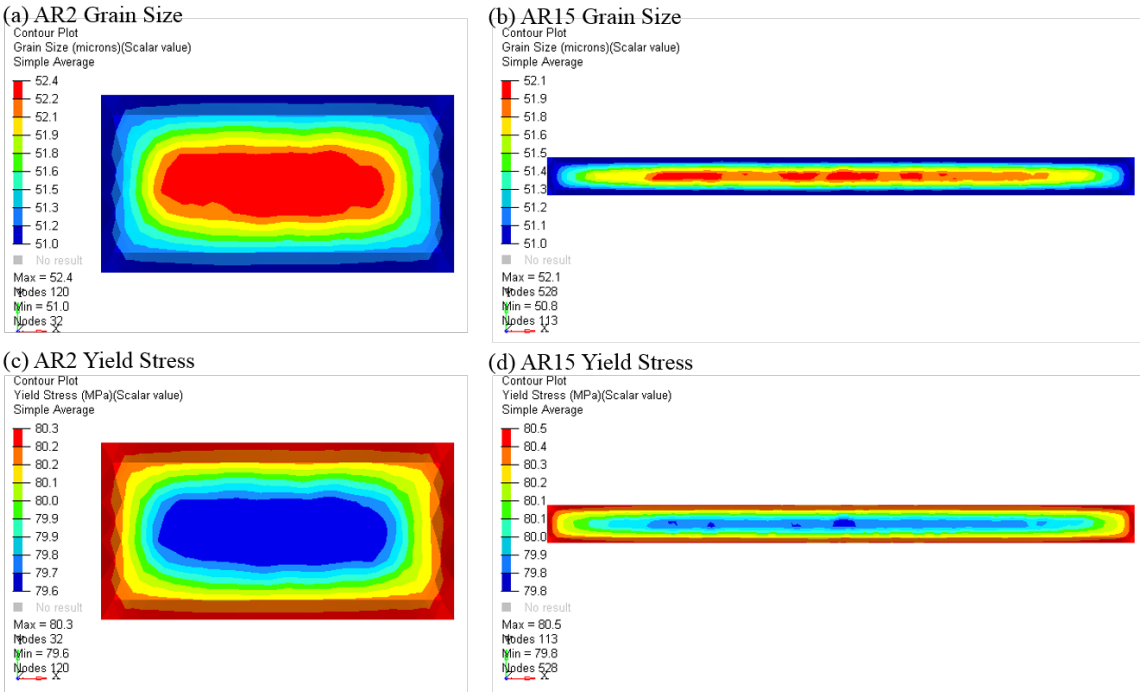

Figure 116: Simulated grain sizes and yield stresses across the profiles of Al 2195 AR2 and AR15.

results, which show variation in grain size and morphology with varying aspect ratio (Figures 52-54). This is likely because Al 2195 did not experience dynamic recrystallization (Section 4.6), and HyperXtrude uses a model based on continuous dynamic recrystallization AR2 and AR15 not only had different grain morphologies, but their longitudinal yield strengths should be 342 MPa and 329 MPa, respectively, in the T3-temper and 586 MPa and 550 MPa in the T8-temper (as reported in Section 4.4). The values from HyperXtrude at the center of the profile were only 79.6 MPa for AR2 and 79.8 MPa for AR15. HyperXtrude was likely not able to predict the variation between longitudinal and transverse yield strengths because the Hall-Petch relationship assumes equiaxed grains. Similarly, the commonly used equation relating subgrain size, d, to the temperature compensated strain rate (Z) through use of empirical constants, m, a, and b (Equation 26), does not account for anisotropy of

the substructure.

$$d^{-m} = a + blnZ \tag{26}$$

The concept of substructure morphology was briefly addressed by Hollinshead and Sheppard [151]; however, models relating subgrain size to strength follow the Hall-Petch form where the grain morphology is assumed to be equiaxed. Therefore they are not useful for prediction of anisotropic strength. Models that account for the morphology of both grains and subgrains are needed to predict yield strength anisotropy. Models that account for precipitate strengthening and anisotropy are also needed to fully predict yield strength and yield strength anisotropy in heat-treatable aluminum alloys. A phenomenological model developed for anisotropic materials by Barlat et al. might be more suitable than the CDRX model in conjunction with the Hall-Petch relationship for modeling of yield strength anisotropy of Al 2195 [136, 152]. Cazacu and Barlat [153] successfully applied this model to predict yield strengths at various angles from the extrusion direction for Al 2026-T3511 as shown in Figure 117.

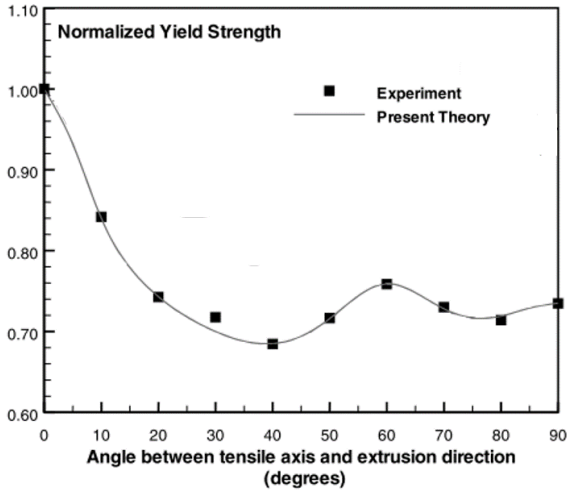

Figure 117: Application of the Barlat model for prediction of yield strength anisotropy in extruded Al 2026-T3511 by Cazacu and Barlat [153].

7.3 Summary

As reported in Chapter 6, HyperXtrude was able to accurately predict peak loads when using the correct material model. In this chapter, the ability of HyperXtrude to predict

strain fields, grain sizes, and yield strengths was assessed. HyperXtrude accurately predicted zero strain in the dead metal zone, increased strain at the die face, increased strain near the container wall, and the strain in Region 2 as shown in Figure 114. However, based on macro-etched billet of Al 2195 and a gridded billets of Al 2024, HyperXtrude was not able to accurately predict the strain fields in the central region of the billet during direct extrusion. While it was not investigated in this study, it is assumed that HyperXtrude's bearing optimization routine would aid in decreasing the time to design a bearing curve for a complex extrusion based on the accurate prediction of strain near the die entrance. Also not investigated in this study, preliminary results presented by Parkar [125] suggest the stress and strain tensors from HyperXtrude can be used to predict crystallographic texture. This will be discussed in more detail in Section 9.3.

HyperXtrude needs more robust phenomenological models for studying yield strength anisotropy. The grain sizes are predicted using a CRDX model developed for ECAP. This model is not applicable to the high temperature extrusion of complex aluminum alloys. The yield strength predictions in HyperXtrude are based on the Hall-Petch relationship, which assumes grains are equiaxed. Thus, it is incapable of predicting anisotropy. Furthermore, this simplified relationship does not consider for other strengthening mechanisms, namely crystallographic texture development and precipitation hardening, which account for a significant portion of the strength in many heat treatable aluminum alloys. While HyperXtrude is able to predict peak loads and the dead metal zone, the FEM software does not currently allow for prediction of yield strength anisotropy. The Barlat method [136, 152, 153] for prediction of yield strength anisotropy is suggested for integration into the HyperXtrude solver.

CHAPTER 8

SUMMARY AND CONCLUSIONS

This research investigates the high temperature deformation behavior of Al 2195 and Al 7075. The overall objectives of this research are to quantify the effects of extrusion aspect ratio on mechanical properties and crystallographic texture development, investigate a method for controlling crystallographic texture during thermo-mechanical processing, and to evaluate the effectiveness of finite element modeling (FEM) for prediction of the effects of extrusion press parameters on final properties of extruded aluminum alloys. Samples of Al 2195 and Al 7075 were extruded with aspect ratios (AR) varying from 2-15 while maintaining a constant extrusion ratio of 20 in order to isolate the effects of aspect ratio on properties and microstructure development. To investigate methods of controlling crystallographic texture during processing, plates of Al 2195 were rolled at temperatures of 343°C, 454°C, and 515°C with dwell times of 1, 4, 8, and 24 hours. Although experimental parameters such as temperatures and speed were kept relatively constant, fluctuations were unavoidable. Simulations via FEM offer an economical method for isolating and investigating the effects of particular experimental parameters. Flow stress tables and fits to the hyperbolic sine law were used to accurately predict the load curves for Al 2195 and Al 7075 extrusions in the commercially available FEM program, HyperXtrude. These fits were then used to simulate strain fields, grain sizes, and yields strengths which were compared to experimental results. The consequential conclusions from these investigations are listed below. More detailed discussion and summaries can be found within each specific chapter.

Chapter 4: Effects of Aspect Ratio on Extruded Al 2195 and Al 7075

1. The mechanical performance of Al-Li extrusions was quantified into four criteria.

2. A single parameter, the Plate-Like Number, was developed to quantify the similarity of a sample's texture to that typically observed in rolled plate.

3. Only the Al 2195 AR2-AR3 extrusions had a negative Plate-Like Number, indicating a deviation in the macrotexture from the typical ordering of the volume fractions of crystallographic components (i.e. Brass $\rightarrow$ S $\rightarrow$ Copper).

4. The undesirable mechanical performance of low aspect ratio Al 2195 extrusions was due to the interactions of the strengthening phases with the high volume fraction of the Copper texture.

5. 7xxx-series alloys might suffer from similar mechanical properties if the low aspect ratio regions developed higher volume fractions of the Copper texture.

6. No significant variation in recrystallization behavior with aspect ratio was observed for Al 2195 or Al 7075. There was an increase in the surface recrystallization observed in the Al 2195 AR15 sample, but this was likely due to slight variations in press parameters.

7. Despite having the same extrusion ratio, the grain morphologies of Al 2195 and Al 7075 varied from cigar-like grains at low aspect ratios to pancake-like grains at high aspect ratios.

8. In addition to the extrusion ratio, the extrusion aspect ratio should be reported along with material property data in the literature or for use in databases such as the Metallic Materials Properties Development and Standardization (MMPDS) data.

Chapter 5: Controlling Crystallographic Texture in Al 2195

9. The Al 2195 billet contained nearly 50% secondary phases which dissolved and coarsened over the range of processing temperatures; therefore, the amount of time a billet or ingot sits at temperature before processing should be controlled.

10. The volume percent of the Copper texture decreased with increasing rolling temperature and dwell time. The Brass and S textures did not systematically vary with dwell time or temperature.

11. The Plate-Like number, combining the effect of the Brass, S, and Copper textures, systematically increased (indicating a more plate-like texture) with increasing rolling temperature.

12. A decrease in the second phase particles in the matrix and their corresponding spherodization was also associated with a more plate-like macrotexture.

13. The most plate-like sample was the plate rolled at 515°C with 4 hour dwells.

14. Samples processed at 343°C had negative Plate-Like numbers, indicative of the poor mechanical properties observed in the AR2 and AR3 Al 2195 extrusions.

Chapter 6: Validation of HyperXtrude

15. Using flow stress data from literature, HyperXtrude was able to predict load curves for Al 7075 extrusions. Variation in the predicted peak loads was less than 10% from experimental values.

16. Hot torsion testing of Al 2195 indicated an anomalous strengthening at 450°C and strains of 0.01/s and 0.1/s. This behavior was confirmed by the experimental and simulated extrusion results and is discussed more in Section 9.2.

17. Using a numerical fit to the hyperbolic sine law, HyperXtrude was able to accurately predict load curves for Al 2195 extrusions.

Chapter 7: Practical Applications and Limitations of HyperXtrude

18. HyperXtrude accurately predicted the dead metal zone and the regions of increased strain at the die face and near the container wall.

19. Simulated strains around the center of the billet were below experimental values by approximately 63%.

20. The continuous dynamic recrystallization (CDRX) model used in HyperXtrude to predict grain size is not applicable to the high temperature deformation of aluminum alloys.

21. The Hall-Petch relationship utilized by HyperXtrude to predict yield strengths does not account for grain and subgrain morphologies, crystallographic texture, or precipitate strengthening, and is therefore unable to model anisotropy.

22. Integration of the Barlat Method [136, 152, 153] into HyperXtrude may allow for prediction of anisotropic properties.

CHAPTER 9

FUTURE WORK

The research presented herein aimed to be as comprehensive as possible. However, opportunities for future work exist. Relevant questions and avenues for investigation are briefly discussed in this chapter.

9.1 Texture Development in Complex Al 2195 Profiles

This study isolates the effects of aspect ratio on the development of texture, microstructure, and strength in Al 2195 and Al 7075. With this fundamental understanding, more complex profiles could be studied to investigate the effects of extrusion ratio and transition zones. Many of the previous studies on texture development with aspect ratio (Sections 2.7.4 and Table 3) were performed on complex profiles where the effective extrusion ratio varied between regions of different aspect ratios and transition zones were often labeled as low aspect ratio regions. Systematic variation of the extrusion ratio with constant aspect ratio as well as variation in the transition zone would allow for the effects of each of these factors to be isolated. A proposed set of geometries is presented in Figure 118a for studying the effect or extrusion ratio and Figure 118b for investigating the effects of the transition zone, as indicated by the dashed lines, while maintaining a constant aspect ratio.

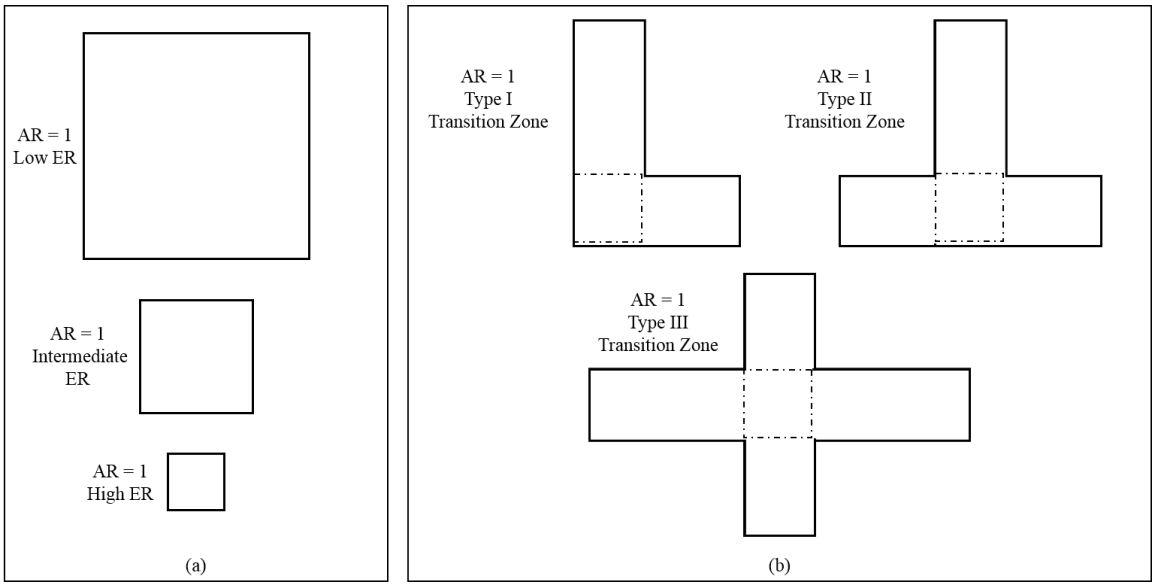

Figure 118: Proposed geometries for investigating the effects of (a) extrusion ratio and (b) transition zone type on the microstructure and properties of aluminum extrusions.

9.2 Deformation Mechanisms in Al 2195

As discussed in Section 2.1, various secondary phases interact differently with dislocations during thermo-mechanical processing; therefore, a change in the initial microstructure or the microstructure during deformation can result in a change in the deformation mechanisms. As reported in Chapter 5, the microstructure of the Al 2195 ingot evolved with time at temperature and with deformation temperature. Transmission electron microscopy (TEM) was performed on select 343°C and 454°C F-temper plates. The mean deformation strain rate for the plates was calculated to be 7.39 s^{-1} based on Equations 2 and 3 as described in Appendix E. Samples were prepared and analyzed as discussed in Section 3.2. Images are shown in Figures 119, 120, 121. At 343°C, deformation appears to have occurred via edge dislocations and slip band formation while at 454°C helical and edge dislocations were observed. At 454°C increased dislocation entanglement was observed in the 8 hour dwell time sample compared to the 1 hour sample. Crooks similarly saw variation in the deformation modes [35]. Microstructures composed of a fine distribution of S' and T_1 were associated with dislocation tangles; whereas, microstructures composed on δ' were associated with shearing of these particles as well as the formation of slip bands [35]. Helical

dislocations form when a quenched in vacancy interacts with a screw or mixed dislocation [154]. A more detailed and systematic TEM investigation would be required to link the deformation temperatures and deformation mechanisms in Al 2195. Possible variations in deformation mode with temperature and strain rate may be responsible for the anomalous strengthening of Al 2195 observed during hot torsion testing.

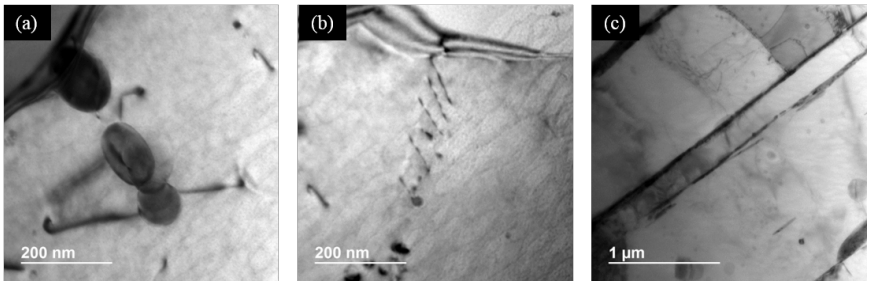

Figure 119: TEM micrographs from the plate rolled at 343°C with 1 hour dwells.

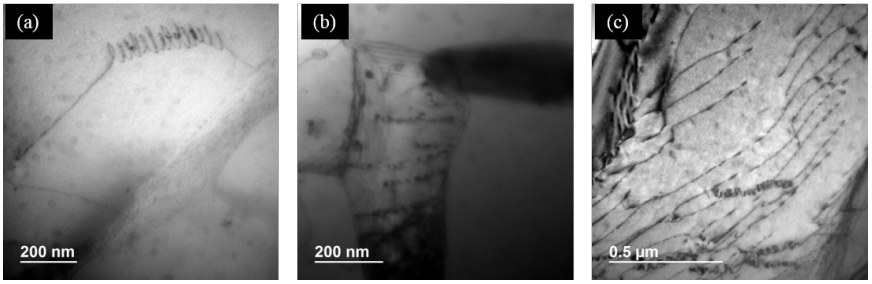

Figure 120: TEM micrographs from the plate rolled at 454°C with 1 hour dwells.

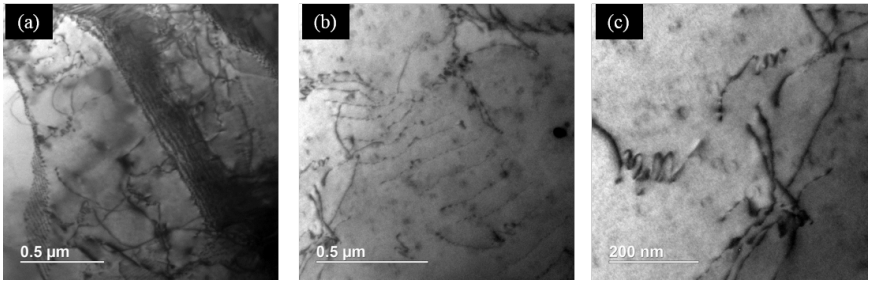

Figure 121: TEM micrographs from the plate rolled at 454°C with 8 hour dwells.

Hot torsion testing was performed at Colorado School of Mines in collaboration with Blake Whitley and Dr. Kip Findley. During this testing, anomalous strengthening was observed at 450°C and strain rates of 0.01/s and 0.1/s as shown in Figure 122. Initially, this behavior was assumed to be due to experimental error. However, a repeated test at 450°C

and 0.1/s confirmed the strengthening behavior. A plot of strain to fracture (Figure 123) revealed that the behavior of Al 2195 at 450°C warrants more detailed investigation. Use of only the 450°C flow stress led to the most accurate prediction of the load curves. This was further indication that the results obtained using hot torsion were not experimental error, but are representative of the actual material behavior. Polarized light optical micrographs of every torsion sample are presented in Appendix H. A TEM study on these hot torsion samples or an in-situ TEM investigation may help elucidate the mechanism behind this anomalous behavior.

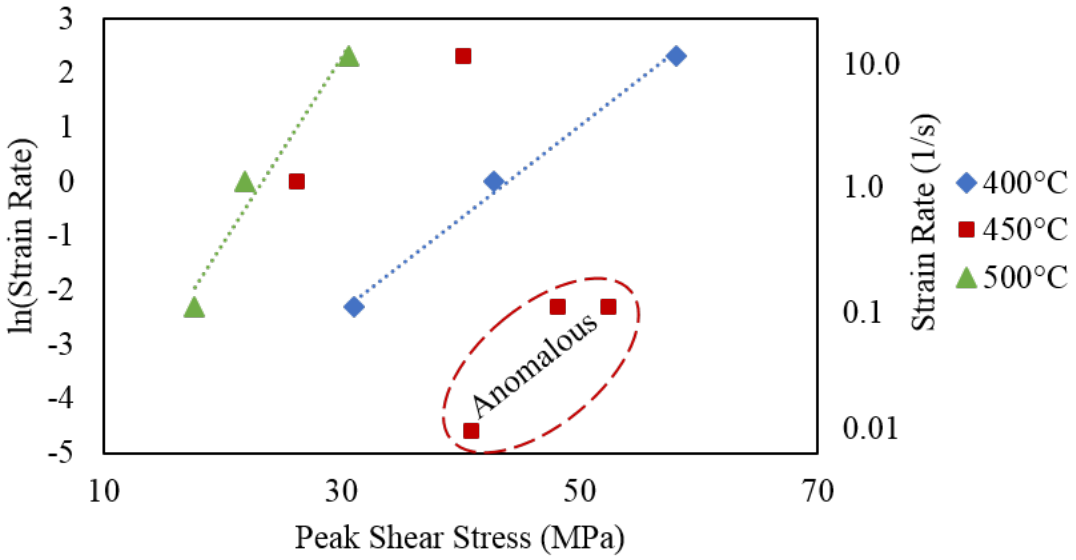

Figure 122: Strain rate versus peak shear stress with anomalous behavior indicated at 450°C.

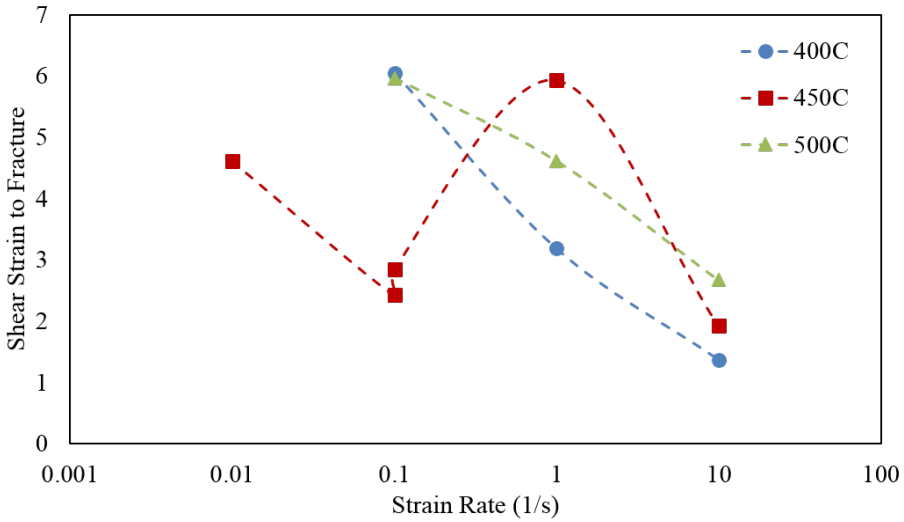

Figure 123: Strain to fracture from Al 2195 hot torsion tests.

9.3 Computational Prediction of Strength Anisotropy and Texture in Extruded Aluminum Alloys

Experimental investigation into the effects of extrusion press parameters, such as ram speed and initial billet temperature, can be costly and ineffective. Despite modern feedback control systems for controlling and monitoring temperatures and speeds, there are always fluctuations between one extrusion and the next. These imperfections in press repeatability make experimental investigation of the effects of individual press parameters on anisotropy ineffective. The appeal of finite element modeling (FEM) is the ability to computationally fix all press variables and then systematically vary the variable of interest, without the limitations of experimental repeatability. Based on the results presented in Chapters 4-5, extrusion speed and initial billet temperature may be used to control crystallographic texture development and thus mechanical properties in Al 2195. Chapter 6 offered a constitutive equation for use in modeling Al 2195 in the commercially available FEM software, HyperXtrude. The accuracy of HyperXtrude's prediction of yield strength was then discussed in Chapter 7. The current models used by HyperXtrude for prediction of grain sizes and yield strengths assume equiaxed grains and cannot predict the variation in yield strengths at various angles from the extrusion direction (see Section 7.2). Integration of a phenomenological model that can predict anisotropy, such as the Barlat Method [152, 153]

would likely lead to more accurate prediction of yield strength anisotropy in aluminum alloy extrusions. Prediction of the mechanical properties of lithium containing alloys, however, would likely necessitate accurate prediction of the crystallographic texture components.

Crystallographic texture development was shown to play a critical role in the development of strength and ductility in aluminum extrusions (Chapter 4). Integration of HyperXtrude and a texture development model for successful prediction of crystallographic texture would allow for computational modeling of the effects of extrusion parameters on texture development. Texture in two phase materials cannot be modeled using Taylor assumptions because there is considerable difference in strength between the two, which creates nonuniform strain; therefore, visco-plastic self-consistent (VPSC) [155] models need to be used [156]. Sidor, Petrov, and Kestens [157] studied the effect of non-deformable particles in hot rolled Al 6016 and, using VPSC, they were able to predict crystallographic texture. Parkar [125] presented preliminary results for successfully predicting texture by integrating HyperXtrude and VPSC. Parkar [125] was able to predict the stress-strain response of a magnesium extrusion in HyperXtrude. This stress-strain response was then fed into the VPSC model along with other relevant parameters. The predicted pole figure closely resembled the experimental one [125]. Parkar [125], however, did not compare the experimental and predicted texture components nor did he show results from varied extrusion speeds and temperatures. Likely, these models might fall short of accurate predictions of specific texture components and their evolution with extrusion parameters. More work is needed to assess the accuracy of these texture predictions.

APPENDIX A

AL 2195 TENSILE DATA

Tables 17 and 18 are all of the data points from tensile tests performed at Deakin University by Dr. Thomas Dorin and Dr. Alireza Vahidgolpayegani. The average values were used and reported in the body of this work. Information regarding heat treatment and tensile testing procedures can be found in Sections 3.4 and 3.5, respectively.

Table 17: Complete data from transverse tensile tests on Al 2195.

Transverse				
Aspect Ratio	Temper	TYS (MPa)	% Elongation	UTS (MPa)
2	Underaged	375.9	6.3	425.7
2	Underaged	412.3	4.8	458.8
2	T3	455.7	2	495.6
3	T3	290	13.8	373.4
3	T3	296.1	17.2	385.3
3	Underaged	396.4	8.4	456.2
3	Underaged	403.5	8	465.1
3	T8	521.6	3.8	558.3
3	T8	508.2	3.9	547.4
5	T3	258.6	12.5	343.6
5	T3	300.3	15.7	390.1
5	Underaged	375.9	10.8	443.1
5	Underaged	376	11.5	442.6
5	T8	520.8	5	555.3
5	T8	522.5	4.9	556.9
7	T3	254.2	14.7	350.9
7	T3	272.9	13.8	365.7
7	Underaged	378.1	9.3	446.3
7	Underaged	404.5	10.1	471.3
7	T8	513.4	4.2	536.7
7	T8	525.3	4.9	552.2
8	Underaged	401.1	10.7	459.8
8	T8	510.1	4.5	535
15	Underaged	416.1	8.7	483.9
15	Underaged	371.5	10.5	433.1
15	T8	519.4	4.7	563.1

Table 18: Complete data from longitudinal tensile tests on Al 2195.

Longitudinal				
Aspect Ratio	Temper	TYS (MPa)	% Elongation	UTS (MPa)
2	T3	340.5	15.6	442.7
2	T3	334.9	14.6	459.8
2	T3	351.9	15.4	463.2
2	Underaged	386.3	8.8	473.2
2	Underaged	432.4	14.2	517.4
2	Underaged	409.0	14.8	525.2
2	T8	575.8	5.3	594.6
2	T8	600.5	4.3	620.8
2	T8	580.3	1.2	601.7
3	T3	325.8	7.3	420.8
3	T3	278.1	10.0	379.7
3	Underaged	364.1	10.1	458.7
3	Underaged	390.6	11.7	470.4
3	T8	562.9	3.3	591.9
3	T8	577.8	5.9	606.5
5	T3	291.2	10.1	404.7
5	T3	309.7	9.1	415.6
5	Underaged	380.8	11.1	460.6
5	Underaged	426.8	9.4	496.8
5	T8	524.7	5.6	559.7
5	T8	573.9	5.7	605.9
7	T3	287.2	12.0	389.2
7	T3	332.5	8.0	431.1
7	Underaged	402.8	10.3	471.9
7	Underaged	389.7	8.6	467.8
7	T8	550.4	5.1	586.7
7	T8	586.7	4.3	607.7
8	T3	330.5	16.0	433.6
8	T3	336.4	14.9	449.5
8	Underaged	467.2	13.8	556.4
8	Underaged	427.5	9.7	536.4
8	Underaged	452.4	11.9	504.0
8	T8	568.6	4.9	602.9
8	T8	579.9	5.6	607.9
8	T8	573.4	4.8	590.7
15	T3	332.4	16.6	456.0
15	T3	325.3	18.5	459.4
15	Underaged	335.9	18.0	464.7
15	Underaged	361.7	17.5	484.4
15	Underaged	379.6	18.9	491.3
15	T8	545.0	5.6	577.8
15	T8	558.3	4.5	587.3
15	T8	547.9	6.2	589.2

APPENDIX B

MTEX COMMANDS

Below are the series of commands used in MATLAB R2014a with MTEX 3.5.0 to generate the presented pole figures and orientation distribution functions. When calculating the ODF, it was observed that the time to convergence would vary and affect the results. Therefore, only solutions which converged in 12-13 seconds were used. What follows is a script for finding the locations and values of maximum intensity along the β-fiber.

```
%Manually change these in the .m file created by the import wizard
cs = symmetry('cubic');
ss = symmetry('triclinic');

%Calculate the ODF
odf=calcODF(pf);

%Export ODF intensities for use in finding local maximums
export(odf, 'filename.txt', 'Bunge', 'varargin',{0:90}, 'resolution', ...
    1*degree);%edit filename for each run

%Save the variables so plots can be edited later without re-calculating ...
    the ODF
save('filename_variables'); %edit filename

fig1 = figure(1);
plotpdf(odf, [Miller(1,1,1), ...
    Miller(2,0,0),Miller(2,2,0)],'complete','contour',0:1:14, ...
    'antipodal');colorbar;

fig2 = figure(2);
```

```
18 plot(odf, 'phi2',[0 5 10 15 20 25 30 35 40 45 50 55 60 65 70 75 80 85 ...
       90]*degree, 'contour',0:1:45,'antipodal');colorbar;
19
20 fig3 = figure(3);
21 plot(odf,'surf3','contour');colorbar
22 caxis(gca,[0,45]);
23
24 %Use for plotting plates
25 figure(4)
26 plotpdf(odf, [Miller(1,1,1)],'complete','contour',0:1:12, ...
       'antipodal');colorbar
27
28 figure(5)
29 plotpdf(odf, [Miller(2,0,0)],'complete','contour',0:1:5, ...
       'antipodal');colorbar
30
31 figure(6)
32 plotpdf(odf, [Miller(2,2,0)],'complete','contour',0:1:9, ...
       'antipodal');colorbar
33
34 %Use for plotting extrusions
35 figure(4)
36 plotpdf(odf, [Miller(1,1,1)],'complete','contour',0:1:9, ...
       'antipodal');colorbar
37
38 figure(5)
39 plotpdf(odf, [Miller(2,0,0)],'complete','contour',0:1:9, ...
       'antipodal');colorbar
40
41 figure(6)
42 plotpdf(odf, [Miller(2,2,0)],'complete','contour',0:1:13, ...
       'antipodal');colorbar
43
44 %texture components with source listed after
45 bs = orientation('Euler',35*degree,45*degree,90*degree,cs,ss);%Engler2010
```

```
s = orientation('Euler',59*degree,33*degree,65*degree,cs,ss);%Engler2010
cu = orientation('Euler',90*degree,30*degree,45*degree,cs,ss);%Engler2010
shear1 = orientation('Euler',45*degree,0*degree,0*degree,cs,ss);%Hales1998
shear2 = orientation('Euler',0*degree,55*degree,45*degree,cs,ss);%Hales1998
shear3 = orientation('Euler',0*degree,35*degree,45*degree,cs,ss);%Hales1998
goss = orientation('Euler',0*degree,45*degree,0*degree,cs,ss);%Engler2010
cube = orientation('Euler',0*degree,0*degree,0*degree,cs,ss);%Hales1998
RC_RD1 = orientation('Euler',0*degree,20*degree,0*degree,cs,ss);%Hales1998
RC_RD2 = orientation('Euler',0*degree,35*degree,0*degree,cs,ss);%Hales1998
RC_ND1 = orientation('Euler',20*degree,0*degree,0*degree,cs,ss);%Hales1998
RC_ND2 = orientation('Euler',35*degree,0*degree,0*degree,cs,ss);%Hales1998
p = orientation('Euler',70*degree,45*degree,0*degree,cs,ss);%Hales1998
q = orientation('Euler',55*degree,20*degree,0*degree,cs,ss);%Hales1998
r = orientation('Euler',55*degree,75*degree,25*degree,cs,ss);%Hales1998
Bs_RX = orientation('Euler',75*degree,25*degree,45*degree,cs,ss);%Hales1998
```

```
%Beta-fiber local maxima
% Searches plus/minus 10 degrees for local maximums around beta-fiber ...
    values given in J.J. Sidor and A.I. Kestens, Scripta Materialia, ...
    2013. Imported filename.txt files only give intensity values for ...
    every degree (no decimals) so location accuracy is plus/minus one  ...
    degree. Script written by Lauren O'Hara and Meghan Toler at Goergia Tech.

function [I] = beta(M)

D = [];
I = [];
F = [];
G = [];
H = [];
J = [];
K = [];
L = [];
N = [];
```

```
P = [];
Q = [];
R = [];

q = importdata('filename.txt');
M = q.data;
[r, c] = size(M);

for i = 1:r;
    phi2 = M(i, 3);
    phi = M(i, 2);
    phi1 = M(i, 1);
    intensity = M(i, 4);
    if phi2 == 45;
        mask1 = phi2 == 45;
        search1 = phi1(mask1);
        search2 = phi(mask1);
        if search1 ≥ 80 & search1 ≤ 90;
            mask2 = search1 ≥ 80 & search1 ≤ 90;
            search3 = search1(mask2);
            search4 = search2(mask2);
            if search4 ≥ 25 & search4 ≤ 45;
                mask3 = search4 ≥ 25 & search4 ≤ 45;
                ifinal = intensity(mask1);
                D = [D; M(i, 1) M(i, 2) M(i, 3) ifinal];
           end
        end
    end
    i = i+1;
end

maxintense = max(D(:, 4));

for i = 1:r
    intensity = M(i, 4);
```

```
    if intensity == maxintense;
        I = [I; M(i, 1) M(i, 2) M(i, 3) maxintense];
    end
end
%%%
```

```
85  end
86  %%%%%%%%%%%%%%%%%%%%%%%%%%%%%%%%%%%%%%%%%%%%%%%%%%%%%%%%%%%%%%%%%%%%%%%%%%%%
87  for i = 1:r;
88      phi2 = M(i, 3);
89      phi = M(i, 2);
90      phi1 = M(i, 1);
91      intensity = M(i, 4);
92      if phi2 == 55;
93          mask1 = phi2 == 55;
94          search1 = phi1(mask1);
95          search2 = phi(mask1);
96          if search1 ≥ 63 & search1 ≤ 83;
97              mask2 = search1 ≥ 63 & search1 ≤ 83;
98              search3 = search1(mask2);
99              search4 = search2(mask2);
100             if search4 ≥ 26 & search4 ≤ 46;
101                 mask3 = search4 ≥ 26 & search4 ≤ 46;
102                 ifinal = intensity(mask1);
103                 G = [G; M(i, 1) M(i, 2) M(i, 3) ifinal];
104            end
105         end
106     end
107     i = i+1;
108 end
109
110 maxintense3 = max(G(:, 4));
111
112 for i = 1:r
113     intensity = M(i, 4);
114     if intensity == maxintense3;
115         I = [I; M(i, 1) M(i, 2) M(i, 3) maxintense3];
116     end
117 end
118 %%%%%%%%%%%%%%%%%%%%%%%%%%%%%%%%%%%%%%%%%%%%%%%%%%%%%%%%%%%%%%%%%%%%%%%%%%%%
119 for i = 1:r;
```

```
    phi2 = M(i, 3);
    phi = M(i, 2);
    phi1 = M(i, 1);
    intensity = M(i, 4);
    if phi2 == 60;
        mask1 = phi2 == 60;
        search1 = phi1(mask1);
        search2 = phi(mask1);
        if search1 ≥ 57 & search1 ≤ 77;
            mask2 = search1 ≥ 57 & search1 ≤ 77;
            search3 = search1(mask2);
            search4 = search2(mask2);
            if search4 ≥ 26 & search4 ≤ 46;
                mask3 = search4 ≥ 26 & search4 ≤ 46;
                ifinal = intensity(mask1);
                H = [H; M(i, 1) M(i, 2) M(i, 3) ifinal];
           end
        end
    end
    i = i+1;
end

maxintense4 = max(H(:, 4));

for i = 1:r
    intensity = M(i, 4);
    if intensity == maxintense4;
        I = [I; M(i, 1) M(i, 2) M(i, 3) maxintense4];
    end
end
%%%
```

```
155     intensity = M(i, 4);
156     if phi2 == 65;
157         mask1 = phi2 == 65;
158         search1 = phi1(mask1);
159         search2 = phi(mask1);
160         if search1 ≥ 51 & search1 ≤ 71;
161             mask2 = search1 ≥ 51 & search1 ≤ 71;
162             search3 = search1(mask2);
163             search4 = search2(mask2);
164             if search4 ≥ 29 & search4 ≤ 49;
165                 mask3 = search4 ≥ 29 & search4 ≤ 49;
166                 ifinal = intensity(mask1);
167                 J = [J; M(i, 1) M(i, 2) M(i, 3) ifinal];
168            end
169         end
170     end
171     i = i+1;
172 end
173
174 maxintense5 = max(J(:, 4));
175
176 for i = 1:r
177     intensity = M(i, 4);
178     if intensity == maxintense5;
179         I = [I; M(i, 1) M(i, 2) M(i, 3) maxintense5];
180     end
181 end
182 %%%%
```

```
190          search1 = phi1(mask1);
191          search2 = phi(mask1);
192          if search1 ≥ 46 & search1 ≤ 66;
193              mask2 = search1 ≥ 46 & search1 ≤ 66;
194              search3 = search1(mask2);
195              search4 = search2(mask2);
196              if search4 ≥ 28 & search4 ≤ 48;
197                  mask3 = search4 ≥ 28 & search4 ≤ 48;
198                  ifinal = intensity(mask1);
199                  K = [K; M(i, 1) M(i, 2) M(i, 3) ifinal];
200             end
201          end
202      end
203      i = i+1;
204  end
205
206  maxintense6 = max(K(:, 4));
207
208  for i = 1:r
209      intensity = M(i, 4);
210      if intensity == maxintense6;
211          I = [I; M(i, 1) M(i, 2) M(i, 3) maxintense6];
212      end
213  end
214  %%%%
```

```
225             mask2 = search1 ≥ 41 & search1 ≤ 61;
226             search3 = search1(mask2);
227             search4 = search2(mask2);
228             if search4 ≥ 29 & search4 ≤ 49;
229                 mask3 = search4 ≥ 29 & search4 ≤ 49;
230                 ifinal = intensity(mask1);
231                 L = [L; M(i, 1) M(i, 2) M(i, 3) ifinal];
232             end
233         end
234     end
235     i = i+1;
236 end
237
238 maxintense7 = max(L(:, 4));
239
240 for i = 1:r
241     intensity = M(i, 4);
242     if intensity == maxintense7;
243         I = [I; M(i, 1) M(i, 2) M(i, 3) maxintense7];
244     end
245 end
246 %%%%
```

```
260             if search4 ≥ 31 & search4 ≤ 51;
261                 mask3 = search4 ≥ 31 & search4 ≤ 51;
262                 ifinal = intensity(mask1);
263                 P = [P; M(i, 1) M(i, 2) M(i, 3) ifinal];
264             end
265         end
266     end
267     i = i+1;
268 end
269
270 maxintense8 = max(P(:, 4));
271
272 for i = 1:r
273     intensity = M(i, 4);
274     if intensity == maxintense8;
275         I = [I; M(i, 1) M(i, 2) M(i, 3) maxintense8];
276     end
277 end
278 %%%%
```

```
295                 Q = [Q; M(i, 1) M(i, 2) M(i, 3) ifinal];
296             end
297         end
298     end
299     i = i+1;
300 end
301
302 maxintense9 = max(Q(:, 4));
303
304 for i = 1:r
305     intensity = M(i, 4);
306     if intensity == maxintense9;
307         I = [I; M(i, 1) M(i, 2) M(i, 3) maxintense9];
308     end
309 end
310 %%%%
```

```
330      end
331      i = i+1;
332  end
333
334  maxintense1 = max(R(:, 4));
335
336  for i = 1:r
337      intensity = M(i, 4);
338      if intensity == maxintense1;
339          I = [I; M(i, 1) M(i, 2) M(i, 3) maxintense1];
340      end
341  end
342  %%%%
```

APPENDIX C

ADDITIONAL TEXTURE DATA

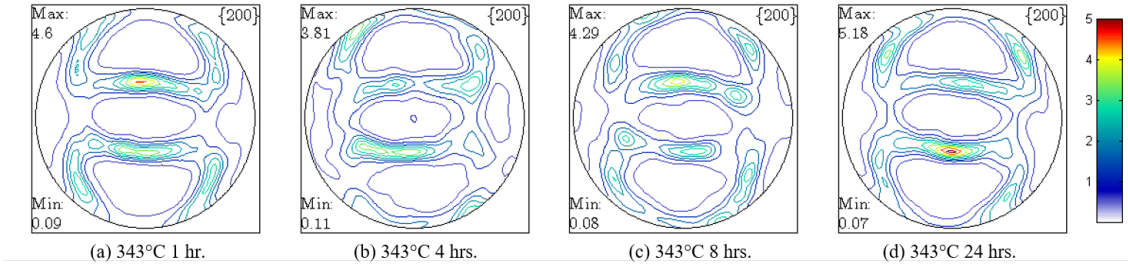

(a) 343°C 1 hr. (b) 343°C 4 hrs. (c) 343°C 8 hrs. (d) 343°C 24 hrs.

Figure 124: {200} Pole figures from F temper Al 2195 rolled at 343°C (650°F) with (a) 1, (b) 4, (c) 8, and (d) 24 hour dwells.

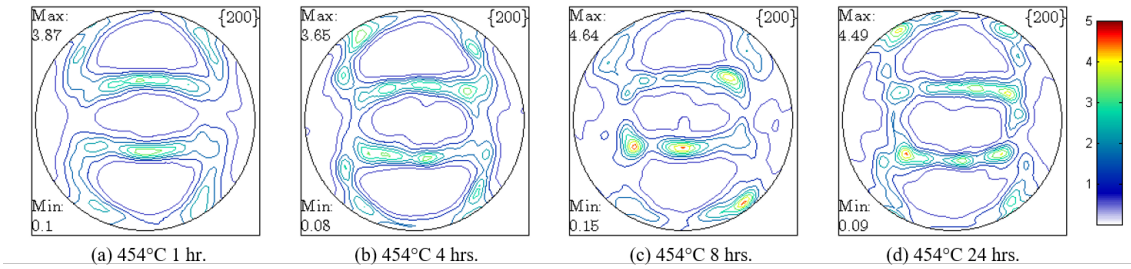

(a) 454°C 1 hr. (b) 454°C 4 hrs. (c) 454°C 8 hrs. (d) 454°C 24 hrs.

Figure 125: {200} Pole figures from F temper Al 2195 rolled at 454°C (850°F) with (a) 1, (b) 4, (c) 8, and (d) 24 hour dwells.

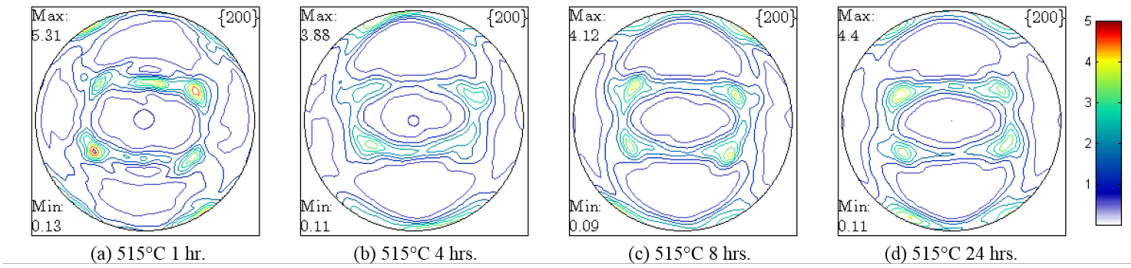

(a) 515°C 1 hr. (b) 515°C 4 hrs. (c) 515°C 8 hrs. (d) 515°C 24 hrs.

Figure 126: {200} Pole figures from F temper Al 2195 rolled at 515°C (959°F) with (a) 1, (b) 4, (c) 8, and (d) 24 hour dwells.

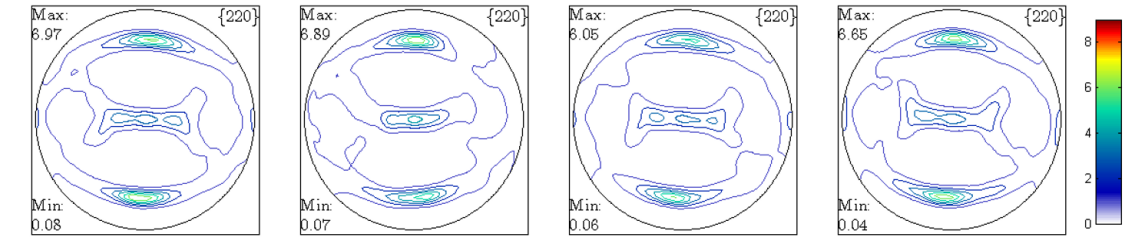

(a) 343°C 1 hr. (b) 343°C 4 hrs. (c) 343°C 8 hrs. (d) 343°C 24 hrs.

Figure 127: {220} Pole figures from F temper Al 2195 rolled at 343°C (650°F) with (a) 1, (b) 4, (c) 8, and (d) 24 hour dwells.

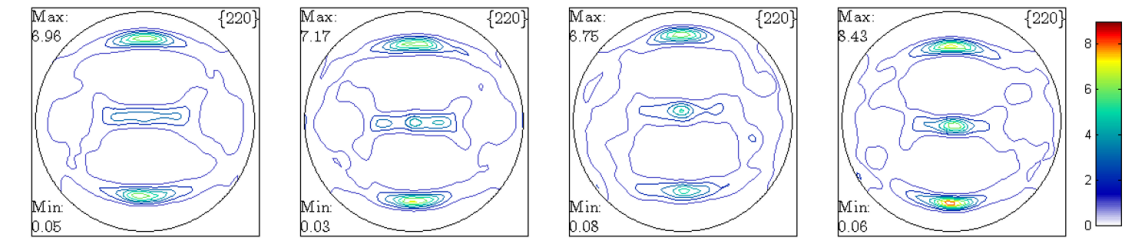

(a) 454°C 1 hr. (b) 454°C 4 hrs. (c) 454°C 8 hrs. (d) 454°C 24 hrs.

Figure 128: {220} Pole figures from F temper Al 2195 rolled at 454°C (850°F) with (a) 1, (b) 4, (c) 8, and (d) 24 hour dwells.

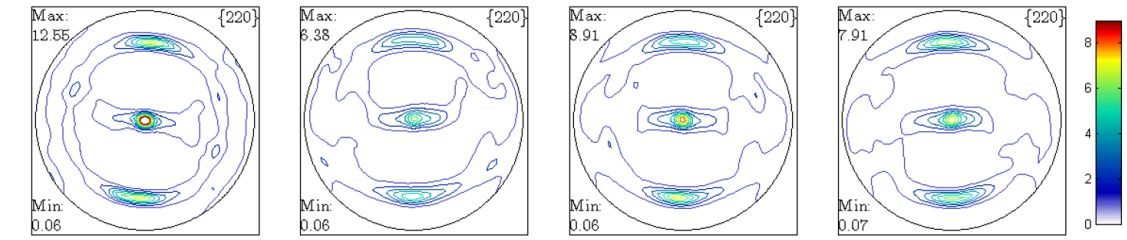

(a) 515°C 1 hr. (b) 515°C 4 hrs. (c) 515°C 8 hrs. (d) 515°C 24 hrs.

Figure 129: {220} Pole figures from F temper Al 2195 rolled at 515°C (959°F) with (a) 1, (b) 4, (c) 8, and (d) 24 hour dwells.

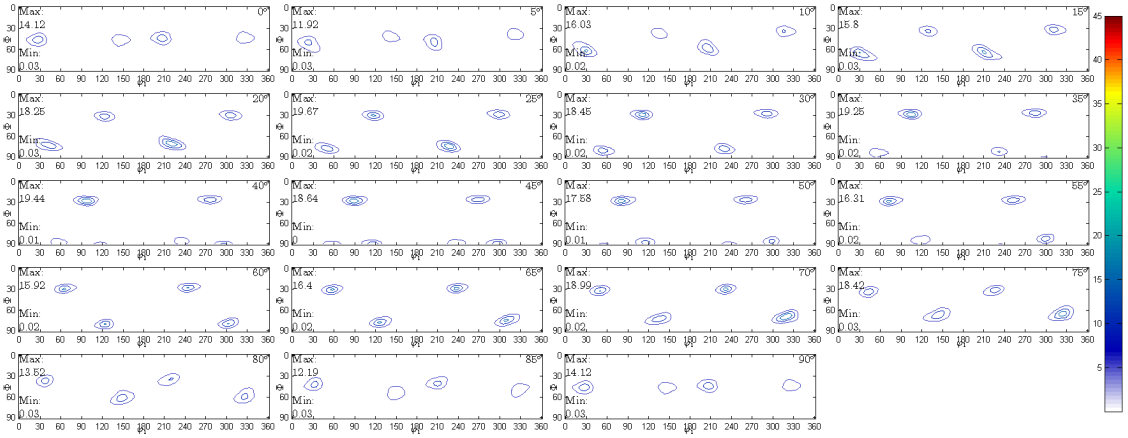

Figure 130: ODF sections along φ_2 of F temper Al 2195 rolled at 343°C (650°F) with 1 hour dwells.

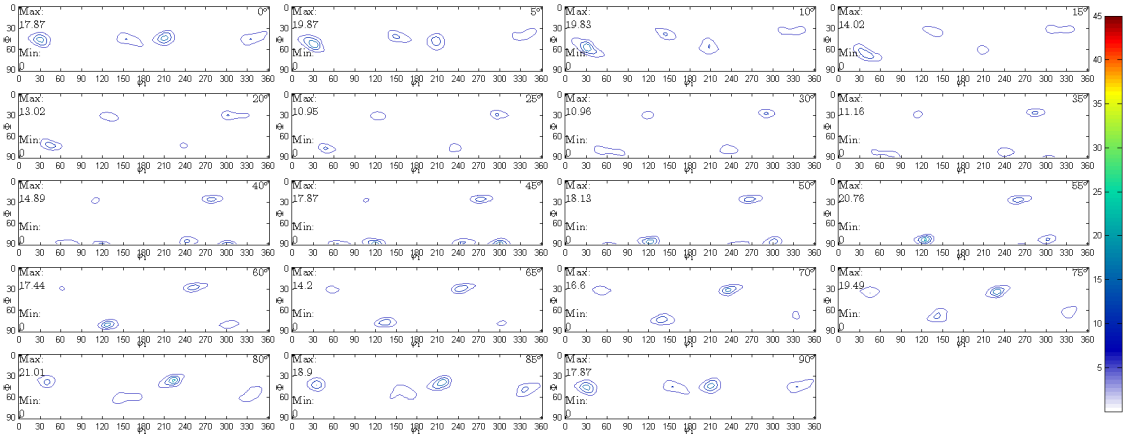

Figure 131: ODF sections along φ_2 of F temper Al 2195 rolled at 343°C (650°F) with 4 hour dwells.

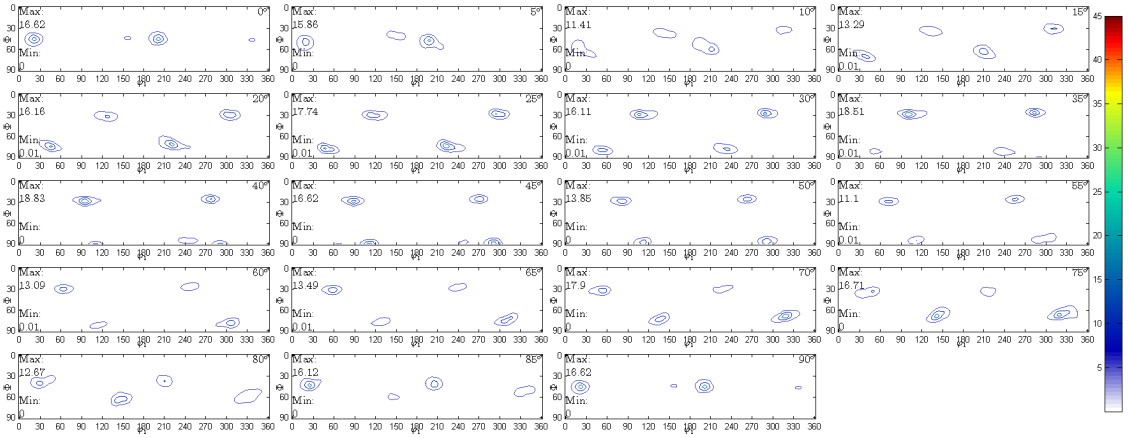

Figure 132: ODF sections along φ_2 of F temper Al 2195 rolled at 343°C (650°F) with 8 hour dwells.

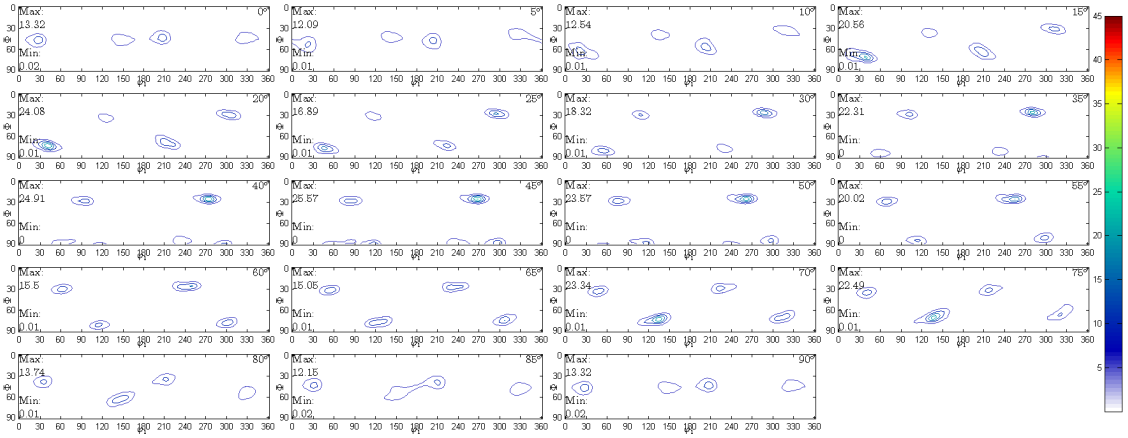

Figure 133: ODF sections along φ_2 of F temper Al 2195 rolled at 343°C (650°F) with 24 hour dwells.

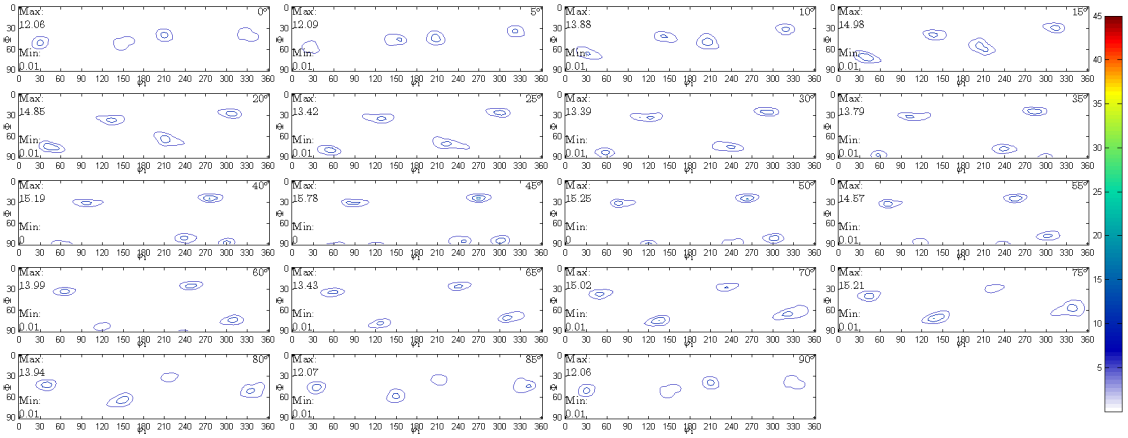

Figure 134: ODF sections along φ_2 of F temper Al 2195 rolled at 454°C (850°F) with 1 hour dwells.

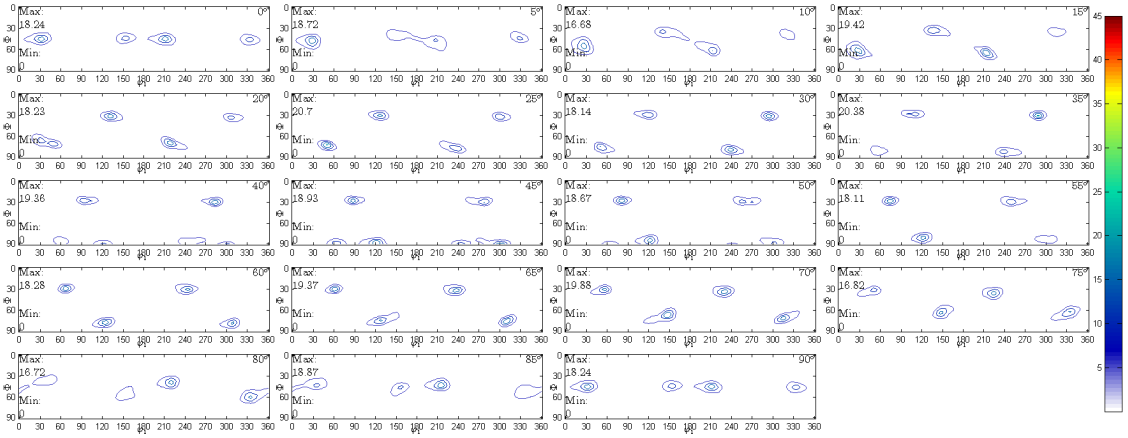

Figure 135: ODF sections along φ_2 of F temper Al 2195 rolled at 454°C (850°F) with 4 hour dwells.

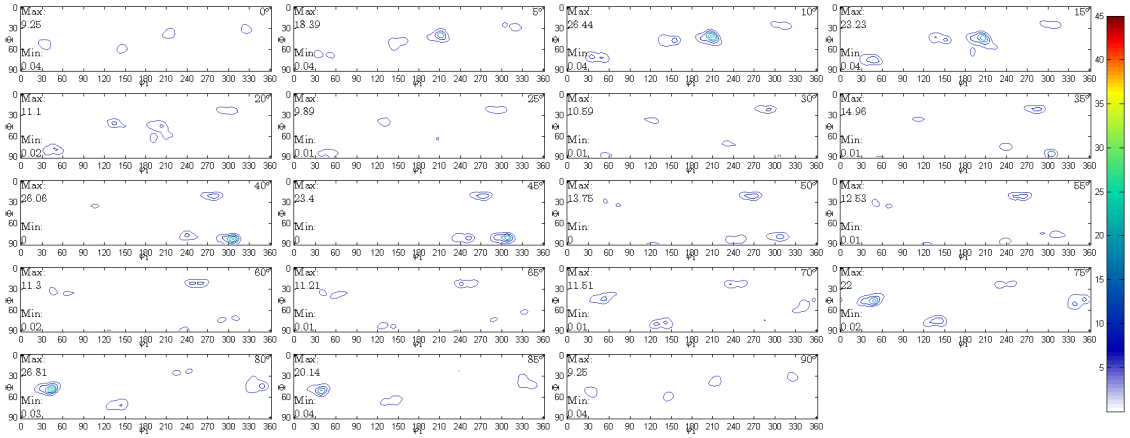

Figure 136: ODF sections along φ_2 of F temper Al 2195 rolled at 454°C (850°F) with 8 hour dwells.

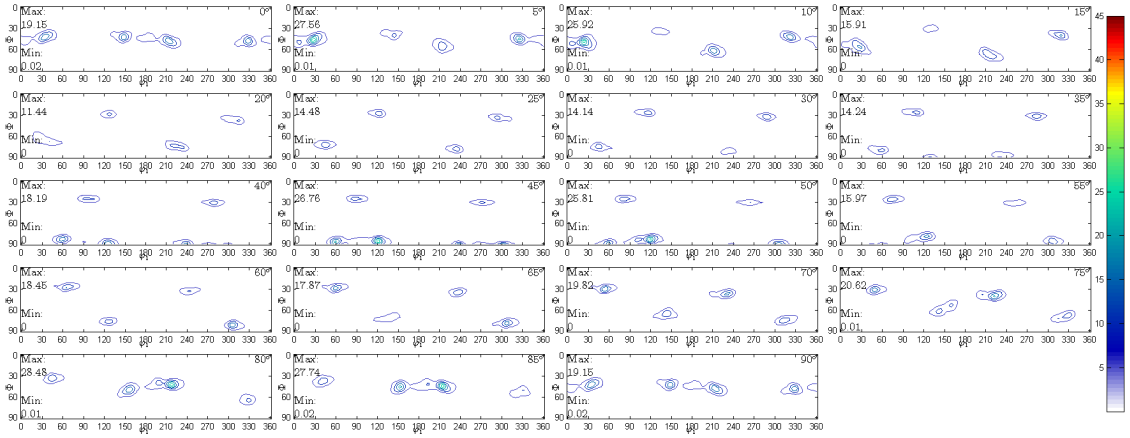

Figure 137: ODF sections along φ_2 of F temper Al 2195 rolled at 454°C (850°F) with 24 hour dwells.

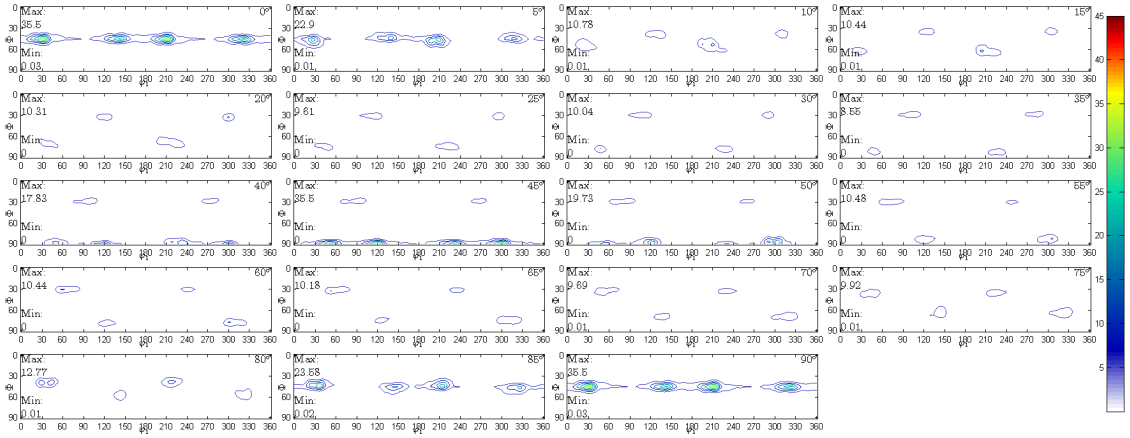

Figure 138: ODF sections along φ_2 of F temper Al 2195 rolled at 515°C (959°F) with 1 hour dwells.

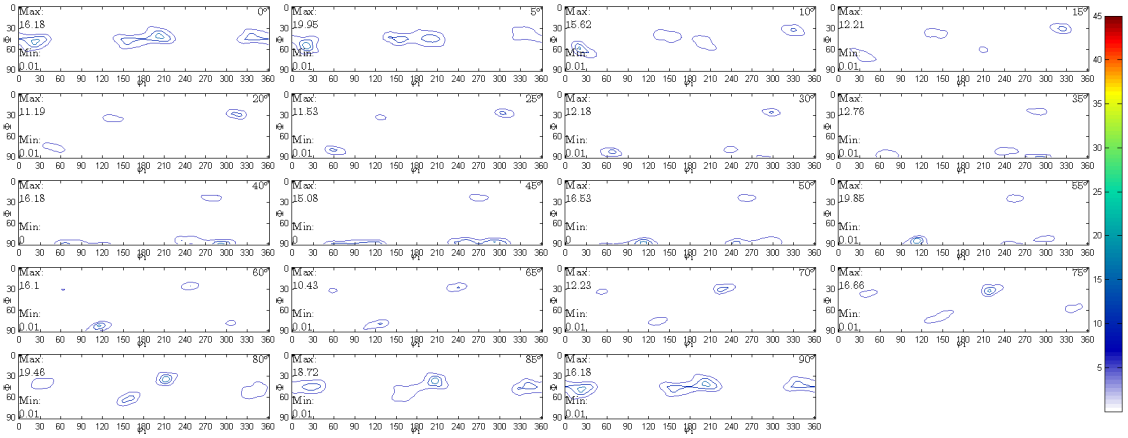

Figure 139: ODF sections along φ_2 of F temper Al 2195 rolled at 515°C (959°F) with 4 hour dwells.

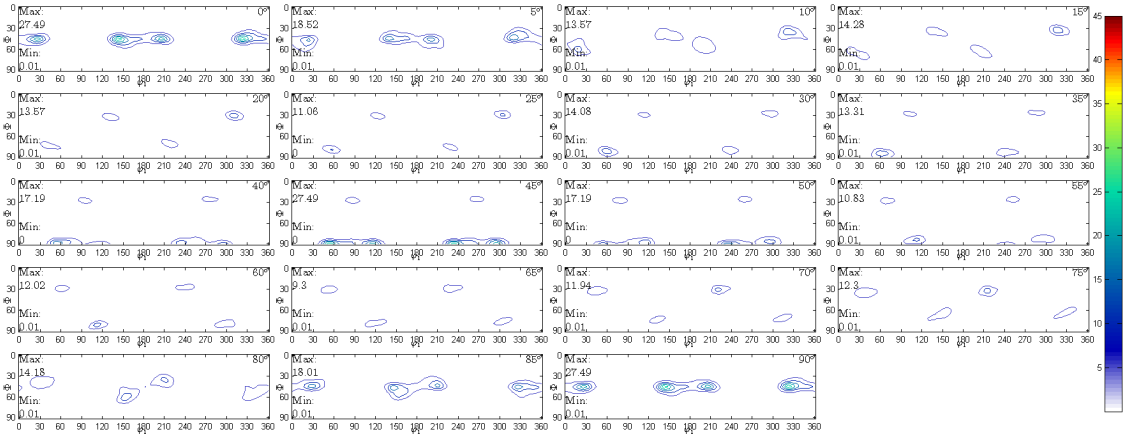

Figure 140: ODF sections along φ_2 of F temper Al 2195 rolled at 515°C (959°F) with 8 hour dwells.

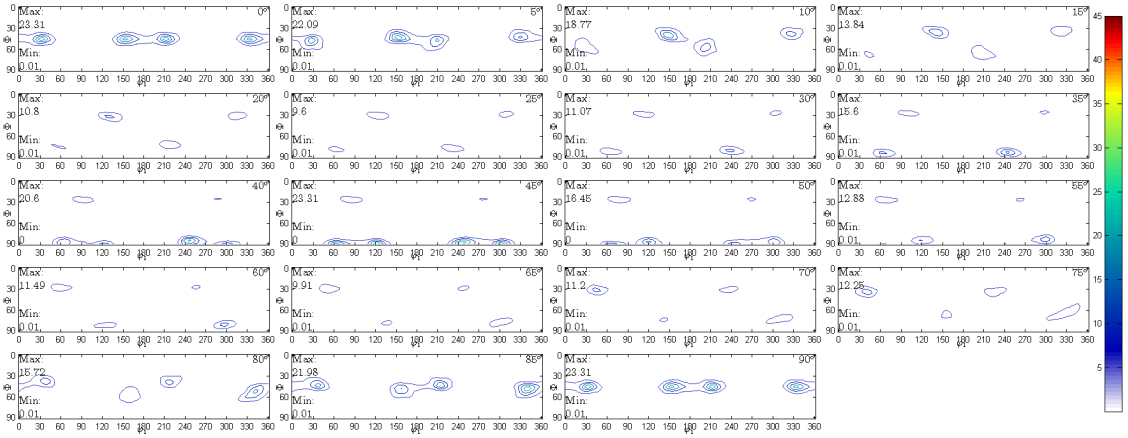

Figure 141: ODF sections along φ_2 of F temper Al 2195 rolled at 515°C (959°F) with 24 hour dwells.

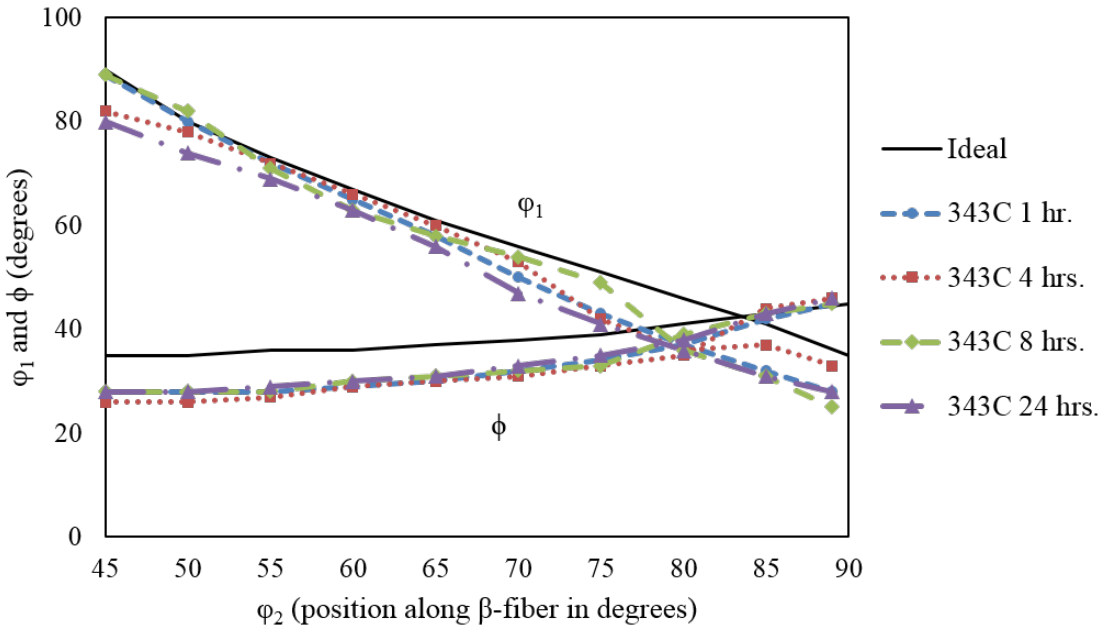

Figure 142: Location of local intensity maximums along the β-fiber for F-temper Al 2195 rolled at 343°C.

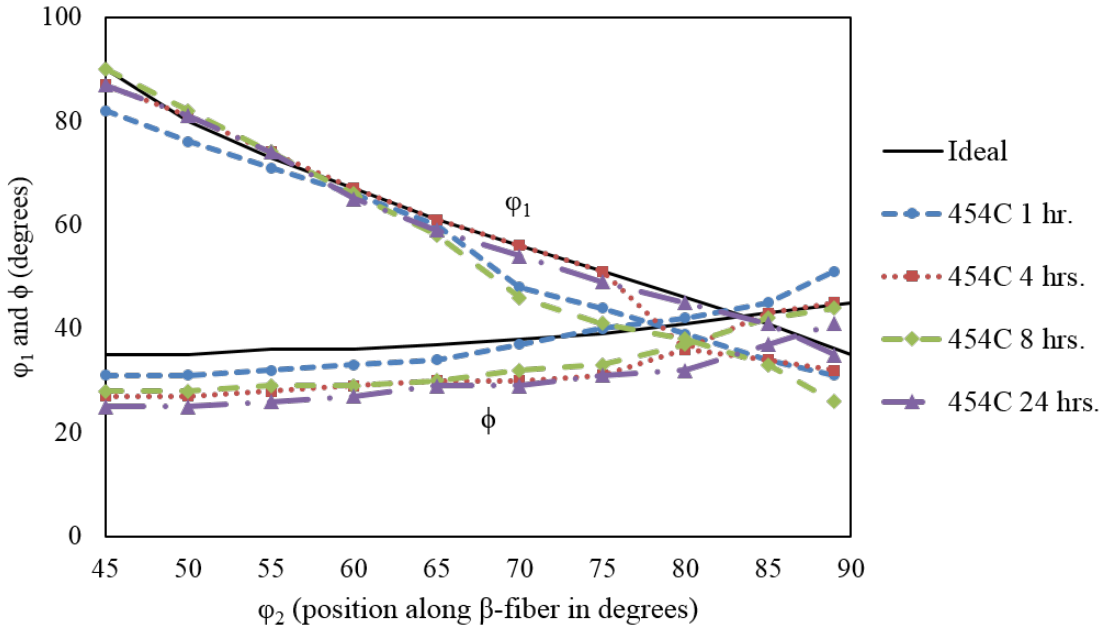

Figure 143: Location of local intensity maximums along the β-fiber for F-temper Al 2195 rolled at 454°C.

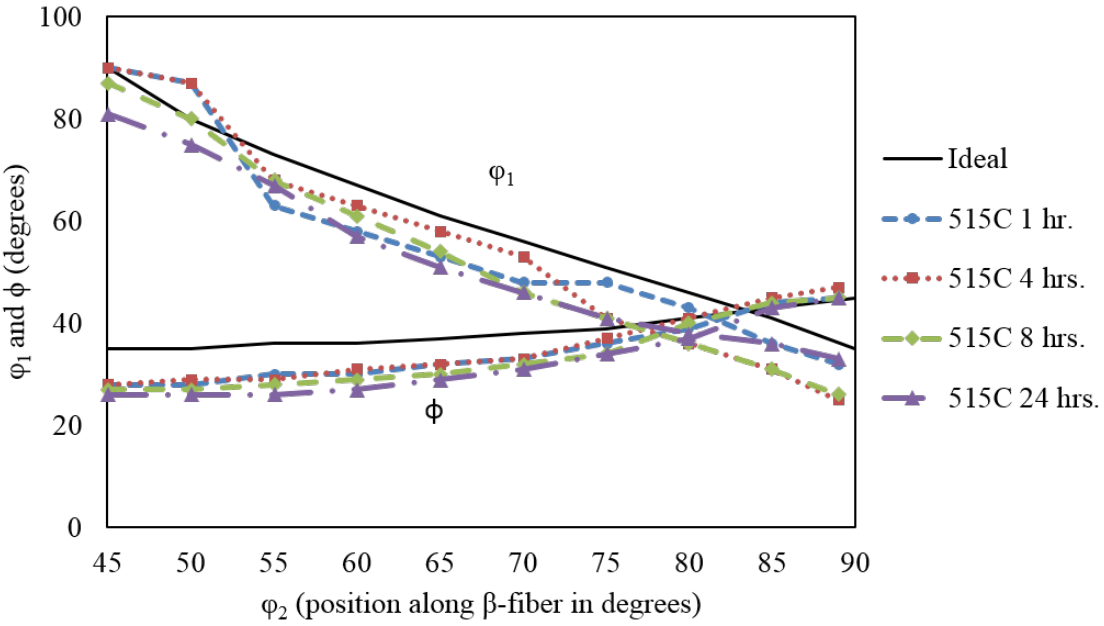

Figure 144: Location of local intensity maximums along the β-fiber for F-temper Al 2195 rolled at 515°C.

APPENDIX D

TEXTURE ALONG THE LENGTH OF AL 7075 EXTRUSIONS

Samples for XRD analysis were taken along the length of Al 7075 AR2 and AR15, F-temper extrusions at the front, middle and rear. These positions corresponded to 22%, 50%, and 78% of the total extrusion length, respectively. There was minimal variation in the texture along the extrusion length as seen in the figures below.

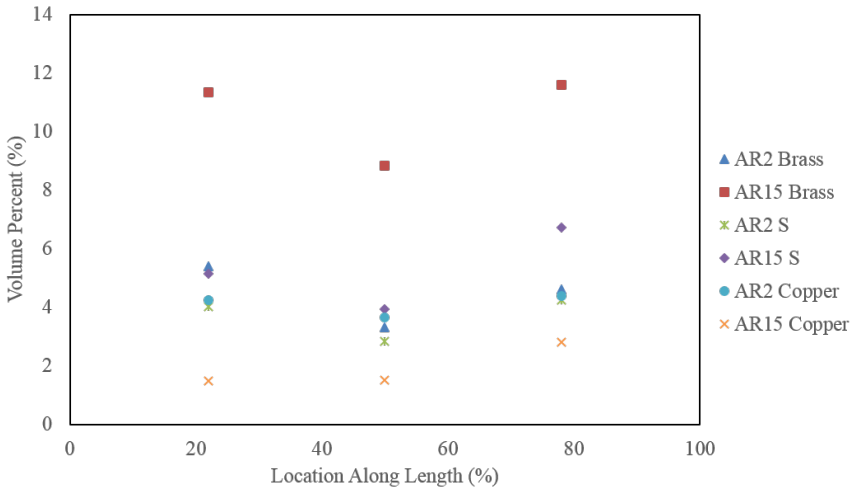

Figure 145: Variation in the volume percent of the Brass, S, and Copper texture components along the length of Al 7075 extrusions.

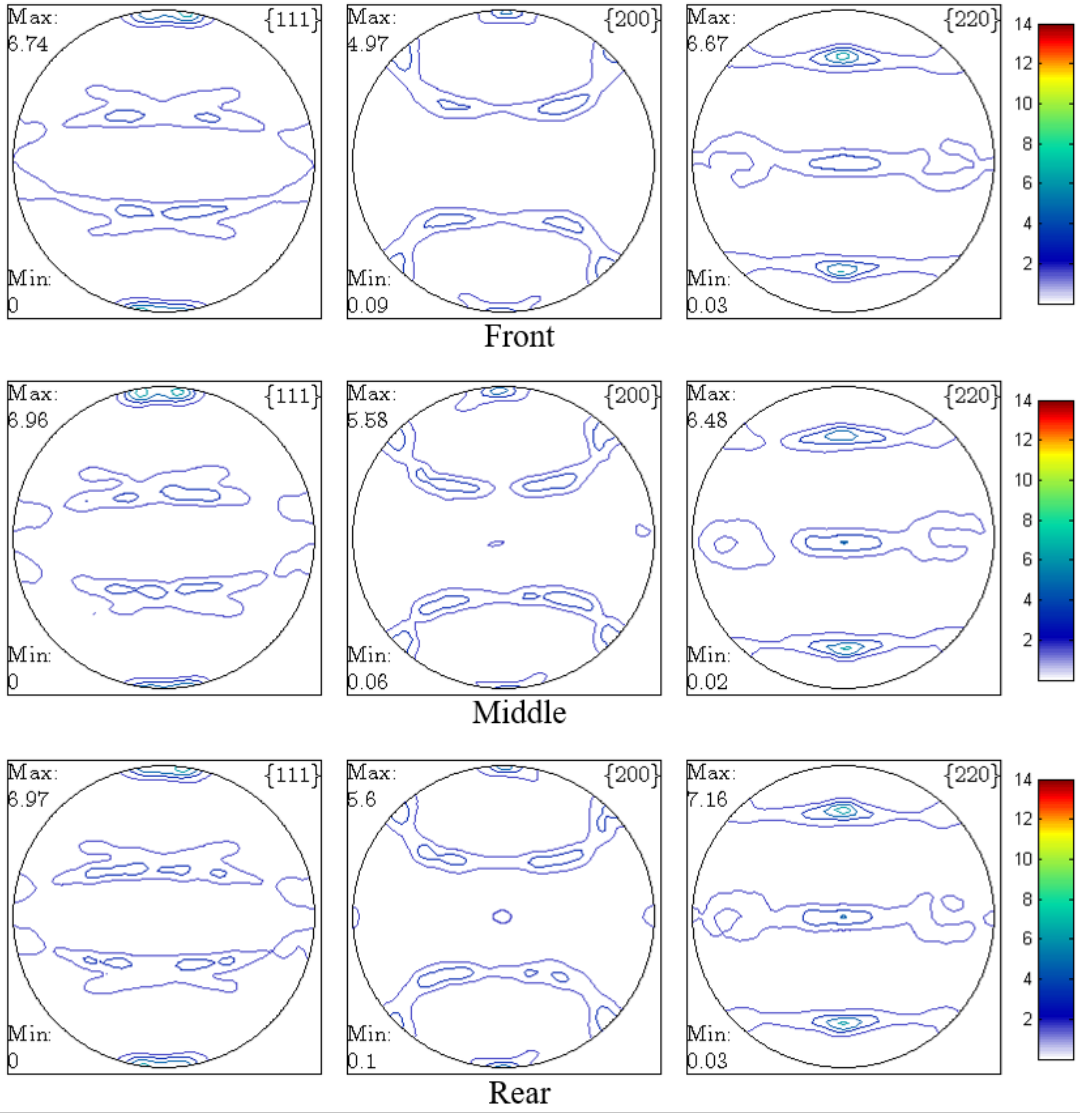

Figure 146: Pole figures along the length of an AR2 Al 7075 extrusion.

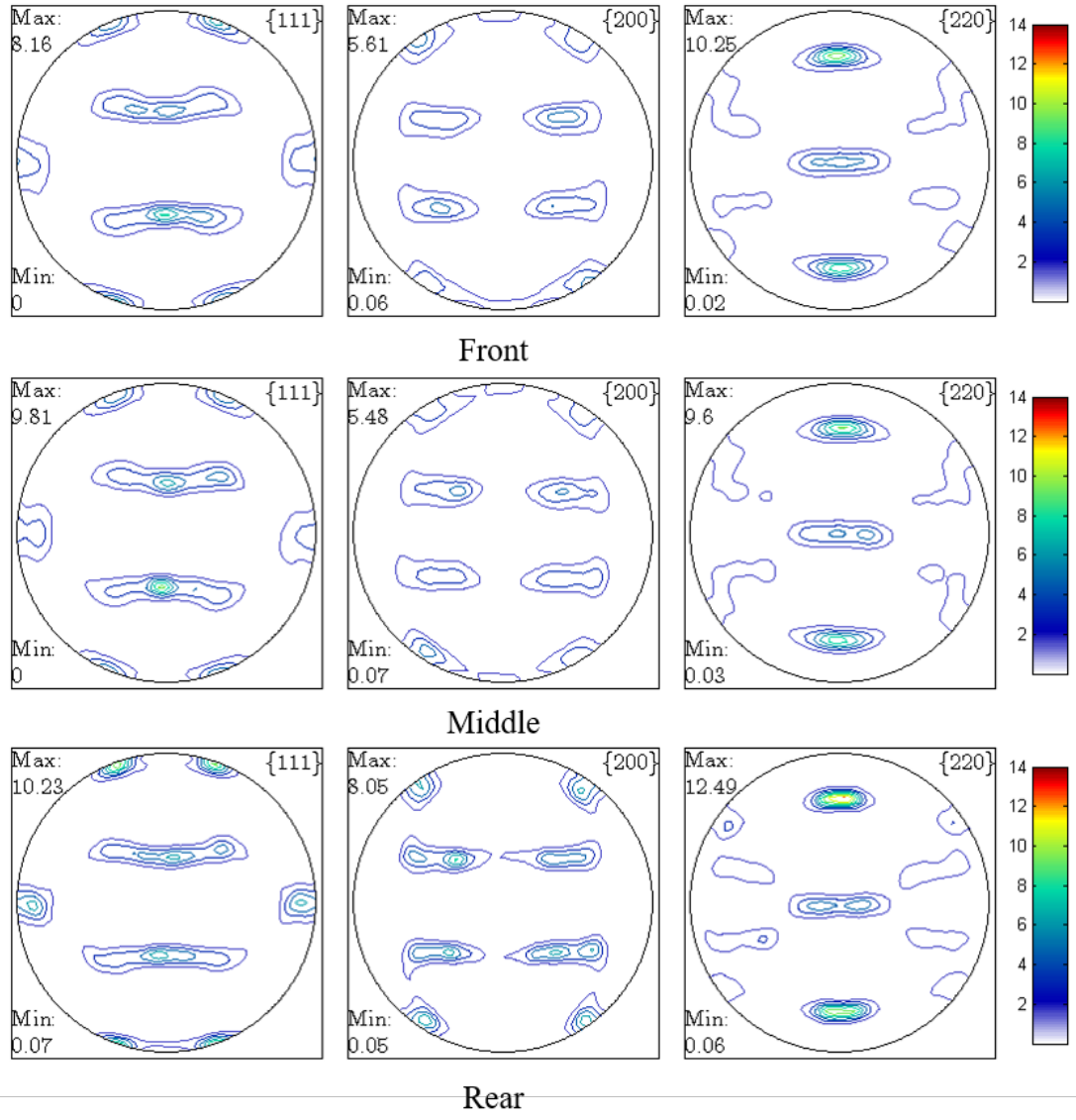

Figure 147: Pole figures along the length of an AR15 Al 7075 extrusion.

APPENDIX E

STRAIN RATE CALCULATIONS

Below is the Mathematica script for finding the average strain rate for 75% rolling reduction on the mill used at Georgia Tech. The mean strain rate was found to be 7.39 s^{-1}.

```
(*ALL IN METERS, SECONDS*)
ho = 0.0200; (*book mold*)
h1 = 0.0150; (*height after pass 1*)
h2 = 0.0100; (*height after pass 2*)
h3 = 0.0050; (*height after pass 3*)

circumference = 1.0922;
radius = circumference/(2*Pi);
Vroll = 0.4080;

strain1 = 1.155 Log[ho/h1]; (*Log in mathematica is Log[E,x]*)
strain2 = 1.155 Log[h1/h2];
strain3 = 1.155 Log[h2/h3];

strainrate1 = (Vroll*strain1)/Sqrt[radius*(ho - h1)];
strainrate2 = (Vroll*strain2)/Sqrt[radius*(h1 - h2)];
strainrate3 = (Vroll*strain3)/Sqrt[radius*(h2 - h3)];

strainrate = (strainrate1 + strainrate2 + strainrate3)/3
```

APPENDIX F

FLOW STRESS DATA

The high temperature flow stress data for Al 7075 from the ASM Hot Working Guide [138] and from hot torsion tests performed at Colorado School of Mines by Blake Whitley are presented in this appendix. Reported values for Al 2195 are equivalent strain and equivalent stress. Stress values are in pascals. When values were not recorded for an exact strain value, a linear interpolation was applied to estimate the value.

Table 19: Flow stress data for Al 7075 from ASM Hot Working Guide [138] as entered in the HyperXtrude material data file.

BEGIN	FLOW	STRESS	DATA			
num_str_val	5					
num_str_rate_val	6					
num_temp_val	6					
list_str_val	0.1	0.2	0.3	0.4	0.5	
list_str_rate_val	0.001	0.01	0.1	1	10	100
list_temp_val	523.15	573.15	623.15	673.15	723.15	773.15
BEGIN	FLOW	STRESS	TABLE			
# strain = 0.100						
1.23E+08	8.21E+07	6.00E+07	4.48E+07	3.23E+07	3.13E+07	
1.23E+08	1.12E+08	7.70E+07	6.00E+07	4.26E+07	3.74E+07	
1.59E+08	1.18E+08	1.01E+08	7.62E+07	7.16E+07	4.36E+07	
1.77E+08	1.35E+08	1.15E+08	1.02E+08	9.24E+07	1.26E+08	
1.74E+08	1.58E+08	1.48E+08	1.22E+08	1.33E+08	9.11E+07	
1.84E+08	1.63E+08	1.44E+08	1.32E+08	1.30E+08	1.18E+08	
# strain = 0.200						
1.24E+08	8.34E+07	5.95E+07	4.40E+07	3.06E+07	3.00E+07	
1.27E+08	1.15E+08	7.71E+07	6.05E+07	4.23E+07	3.76E+07	
1.65E+08	1.20E+08	1.02E+08	7.51E+07	7.09E+07	4.36E+07	
1.89E+08	1.40E+08	1.16E+08	1.02E+08	8.97E+07	1.20E+08	
1.90E+08	1.65E+08	1.57E+08	1.24E+08	1.34E+08	8.68E+07	
1.96E+08	1.78E+08	1.57E+08	1.41E+08	1.35E+08	1.25E+08	
# strain = 0.300						
1.25E+08	1.01E+08	5.95E+07	4.39E+07	3.04E+07	2.88E+07	
1.32E+08	1.17E+08	7.80E+07	5.85E+07	4.16E+07	3.63E+07	
1.67E+08	1.23E+08	1.04E+08	7.56E+07	7.17E+07	4.45E+07	
2.02E+08	1.44E+08	1.18E+08	1.02E+08	8.90E+07	1.13E+08	
1.97E+08	1.72E+08	1.62E+08	1.25E+08	1.38E+08	8.71E+07	
2.00E+08	1.85E+08	1.63E+08	1.48E+08	1.29E+08	1.25E+08	
# strain = 0.400						
1.24E+08	9.98E+07	5.91E+07	4.30E+07	2.99E+07	2.76E+07	
1.31E+08	1.19E+08	7.89E+07	5.82E+07	4.16E+07	3.68E+07	
1.72E+08	1.25E+08	1.05E+08	7.61E+07	7.36E+07	4.38E+07	
2.12E+08	1.48E+08	1.19E+08	1.03E+08	9.24E+07	1.09E+08	
2.08E+08	1.74E+08	1.68E+08	1.25E+08	1.37E+08	8.45E+07	
2.09E+08	1.87E+08	1.65E+08	1.49E+08	1.28E+08	1.18E+08	
# strain = 0.500						
1.25E+08	9.94E+07	5.93E+07	4.30E+07	2.98E+07	2.70E+07	
1.33E+08	1.22E+08	7.97E+07	5.74E+07	4.11E+07	3.77E+07	
1.75E+08	1.28E+08	1.06E+08	7.71E+07	7.44E+07	4.49E+07	
2.24E+08	1.51E+08	1.19E+08	1.04E+08	9.56E+07	1.08E+08	
2.12E+08	1.79E+08	1.72E+08	1.25E+08	1.40E+08	8.18E+07	
2.10E+08	1.91E+08	1.62E+08	1.48E+08	1.28E+08	1.13E+08	
END						

Table 20: Flow stress data, excluding 450°C, for Al 2195 from hot torsion tests performed at Colorado School of Mines as entered in the HyperXtrude material data file.

```
BEGIN FLOWSTRESSDATA
num_str_val 7
num_str_rate_val 3
num_temp_val 2
list_str_val 0.1 0.2 0.3 0.4 0.5 0.6 0.7
list_str_rate_val 0.100 1.000                    10
list_temp_val 673.15                         773.15
BEGIN FLOWSTRESSTABLE
# strain = 0.100
                          4.59E+07   2.46E+07
                          7.28E+07   3.51E+07
                          9.99E+07   4.96E+07
# strain = 0.200
                          5.26E+07   2.52E+07
                          7.03E+07   3.48E+07
                          9.77E+07   5.16E+07
# strain = 0.300
                          5.24E+07   2.47E+07
                          6.87E+07   3.39E+07
                          9.37E+07   5.25E+07
# strain = 0.400
                          5.19E+07   2.41E+07
                          6.72E+07   3.41E+07
                          8.93E+07   5.15E+07
# strain = 0.500
                          5.11E+07   2.53E+07
                          6.37E+07   3.37E+07
                          8.66E+07   5.22E+07
# strain = 0.600
                          5.15E+07   2.62E+07
                          6.21E+07   3.38E+07
                          8.25E+07   5.18E+07
# strain = 0.700
                          4.98E+07   2.64E+07
                          6.19E+07   3.39E+07
                          5.30E+07   5.09E+07
END
```

Table 21: Flow stress data, at 450°C, for Al 2195 from hot torsion tests performed at Colorado School of Mines as entered in the HyperXtrude material data file.

```
BEGIN FLOWSTRESSDATA
num_str_val 7
num_str_rate_val 4
num_temp_val 1
list_str_val 0.1 0.2 0.3 0.4 0.5 0.6 0.7
list_str_rate_val 0.0100 0.100 1.000      10
list_temp_val 723.15
BEGIN FLOWSTRESSTABLE
# strain = 0.100
                              6.94E+07
                              8.26E+07
                              4.53E+07
                              8.65E+07
# strain = 0.200
                              6.74E+07
                              7.98E+07
                              4.43E+07
                              8.75E+07
# strain = 0.300
                              6.63E+07
                              7.83E+07
                              4.37E+07
                              8.55E+07
# strain = 0.400
                              6.29E+07
                              7.68E+07
                              4.30E+07
                              8.40E+07
# strain = 0.500
                              6.10E+07
                              7.38E+07
                              4.17E+07
                              8.23E+07
# strain = 0.600
                              5.99E+07
                              7.19E+07
                              4.19E+07
                              8.13E+07
# strain = 0.700
                              5.94E+07
                              6.99E+07
                              4.18E+07
                              7.88E+07
END
```

APPENDIX G

EFFECTS OF PARAMETERS IN THE HYPERBOLIC SINE LAW ON THE EXTRUSION LOAD CURVE

To investigate the effect of changing parameters in the hyperbolic sine constitutive equation (Equation 27), each parameter was systematically varied in HyperXtrude v14 while all other parameters were held constant. The resulting load curves are given in this Appendix. The activation energy (Q)[1] and reciprocal strain factor (A) shifted the curve uniformly. Changing the stress exponent (n) and stress multiplier (α) not only caused a shift, but also changed the curvature. Changing the strain rate offset, an input parameter in HyperXtrude but a value not found in the hyperbolic sine constitutive equation, by two orders of magnitude caused very little change in the load curve.

$$\dot{\epsilon} = A[sinh(\alpha\sigma)]^n exp(-\frac{Q}{RT}) \tag{27}$$

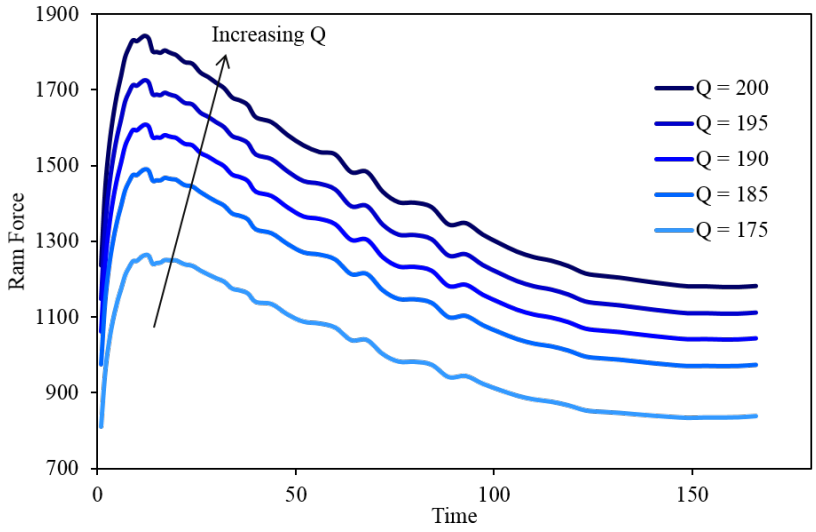

Figure 148: Effect of changing activation energy (Q) on the load curve.

[1]These curves were calculated with a ram acceleration which accounts for the ramping to peak stress observed.

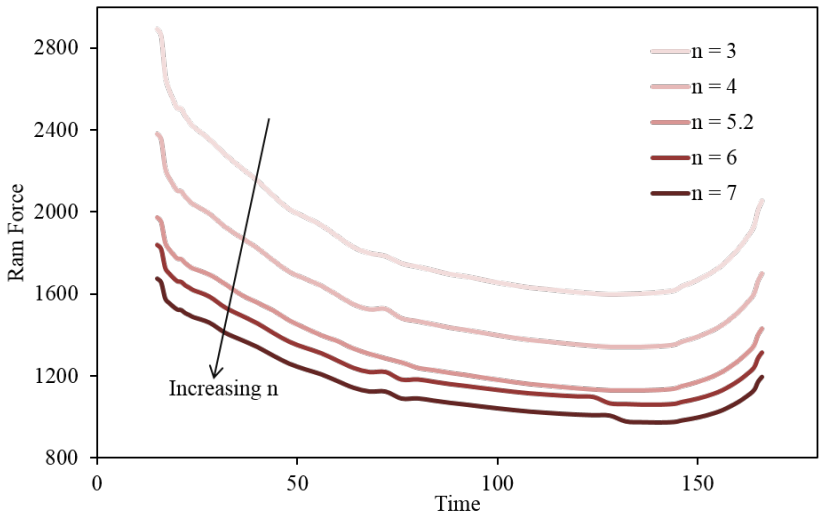

Figure 149: Effect of changing the stress exponent (n) on the load curve.

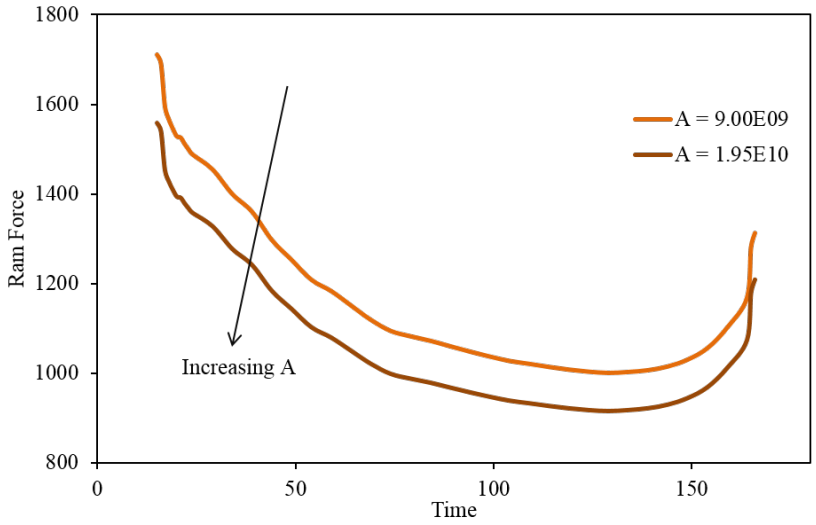

Figure 150: Effect of changing the reciprocal strain factor (A) on the load curve.

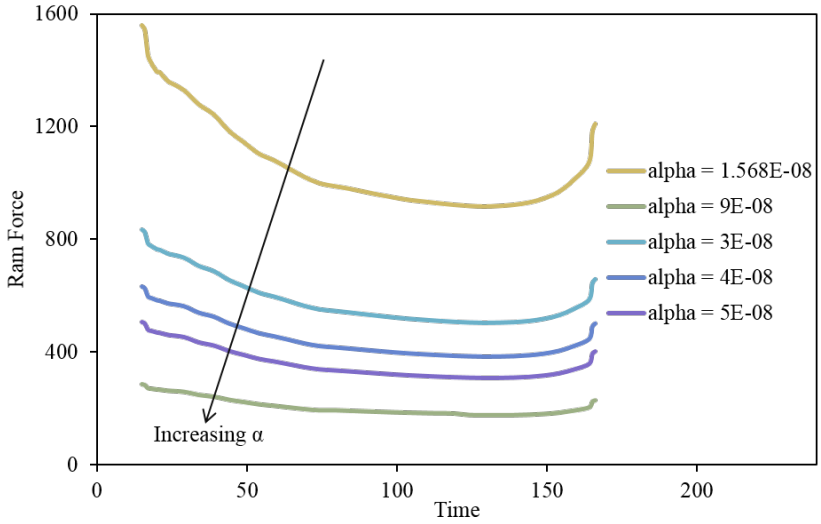

Figure 151: Effect of changing the stress multiplier (α) on the load curve.

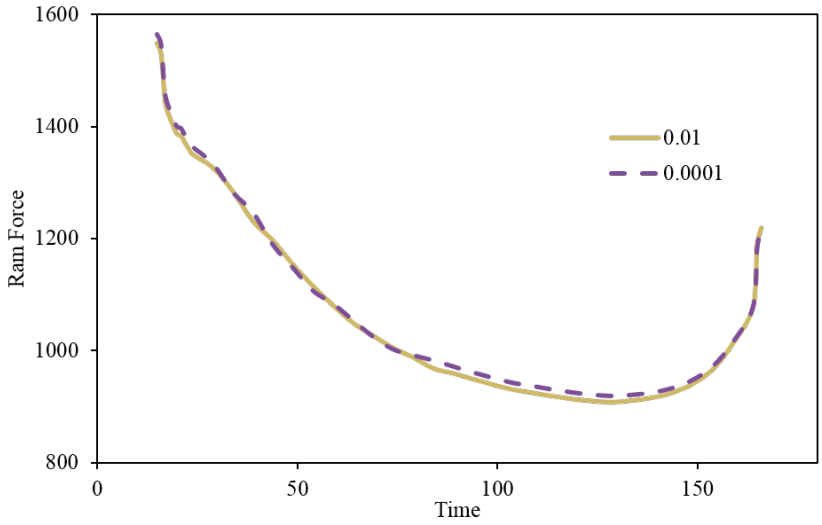

Figure 152: Effect of changing the strain rate offset (HyperXtrude value) on the load curve.

APPENDIX H

MICROGRAPHS FROM HOT TORSION SAMPLES

Hot torsion samples were cross sectioned to reveal the longitudinal microstructure, polished, and Barker's etched for polarized light optical microscopy. The resulting collages are presented in this appendix. Each is oriented with the fracture surface on the right hand side. The end of the gauge region is on the left and a relatively undeformed microstructure can be seen in all of the samples at this gauge end.

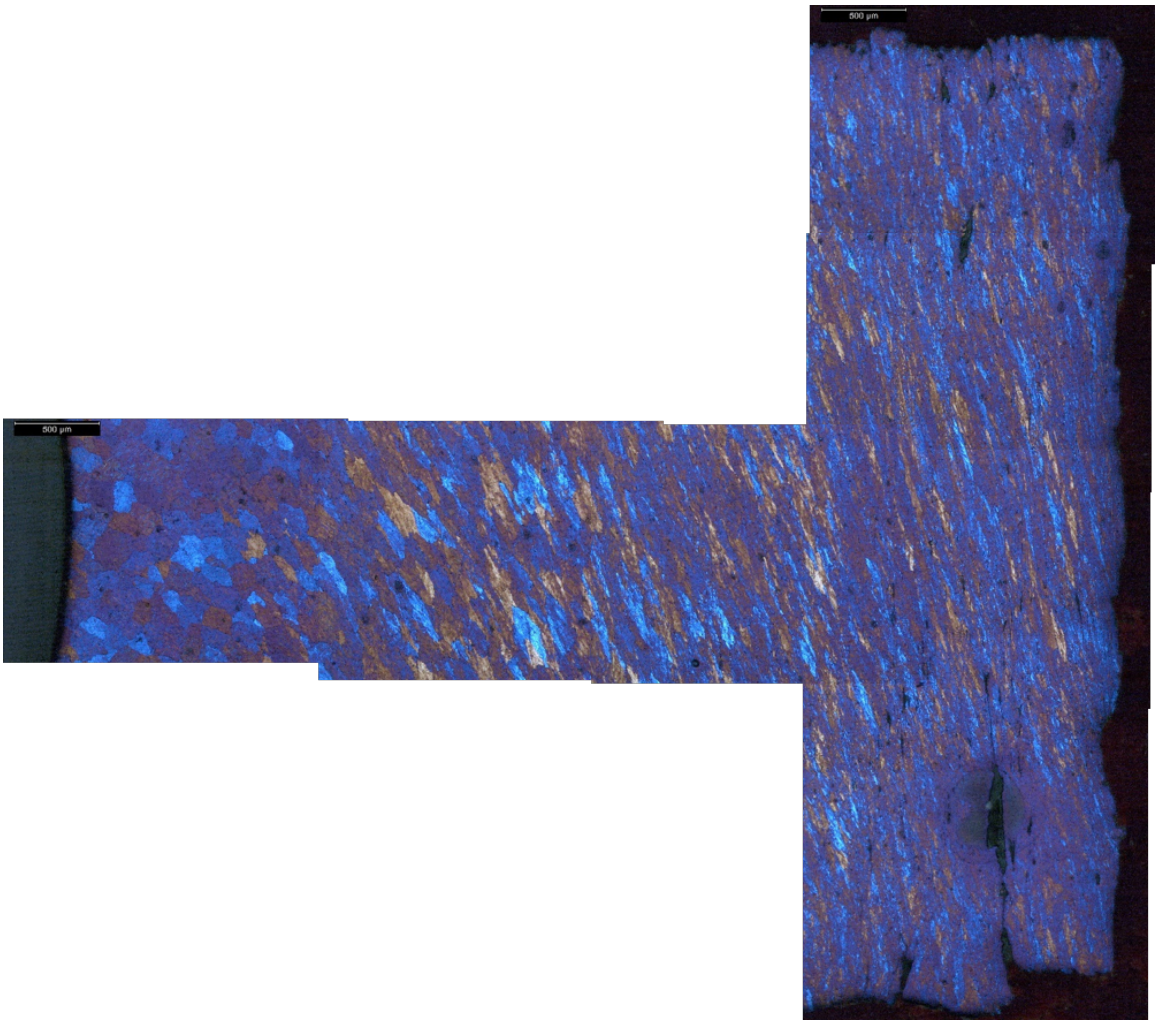

Figure 153: Polarized light micrographs (50X) showing the fracture surface and microstructure into the gauge of the torsion sample deformed at 400°C and 0.1/s.

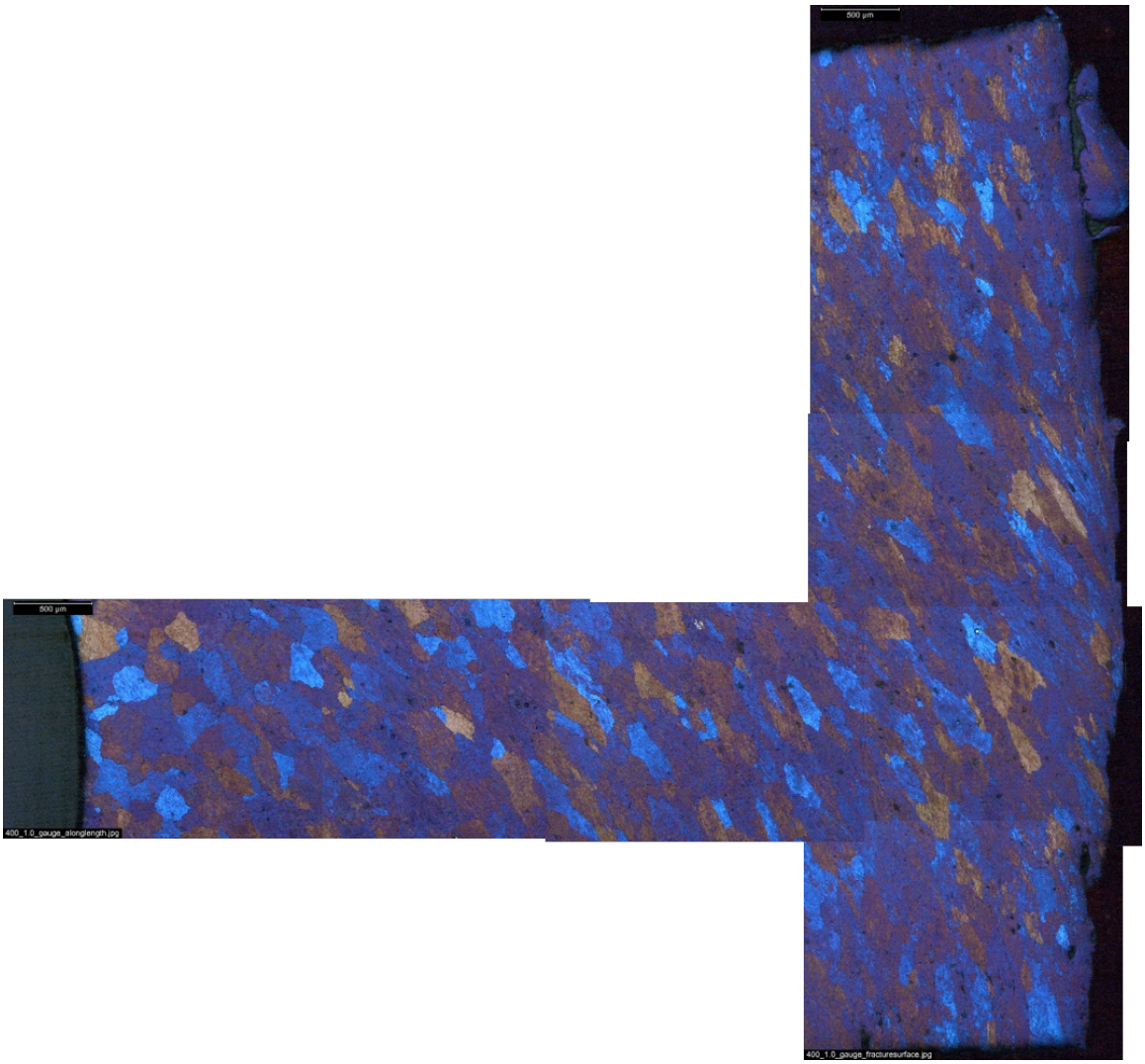

Figure 154: Polarized light micrographs (50X) showing the fracture surface and microstructure into the gauge of the torsion sample deformed at 400°C and 1.0/s.

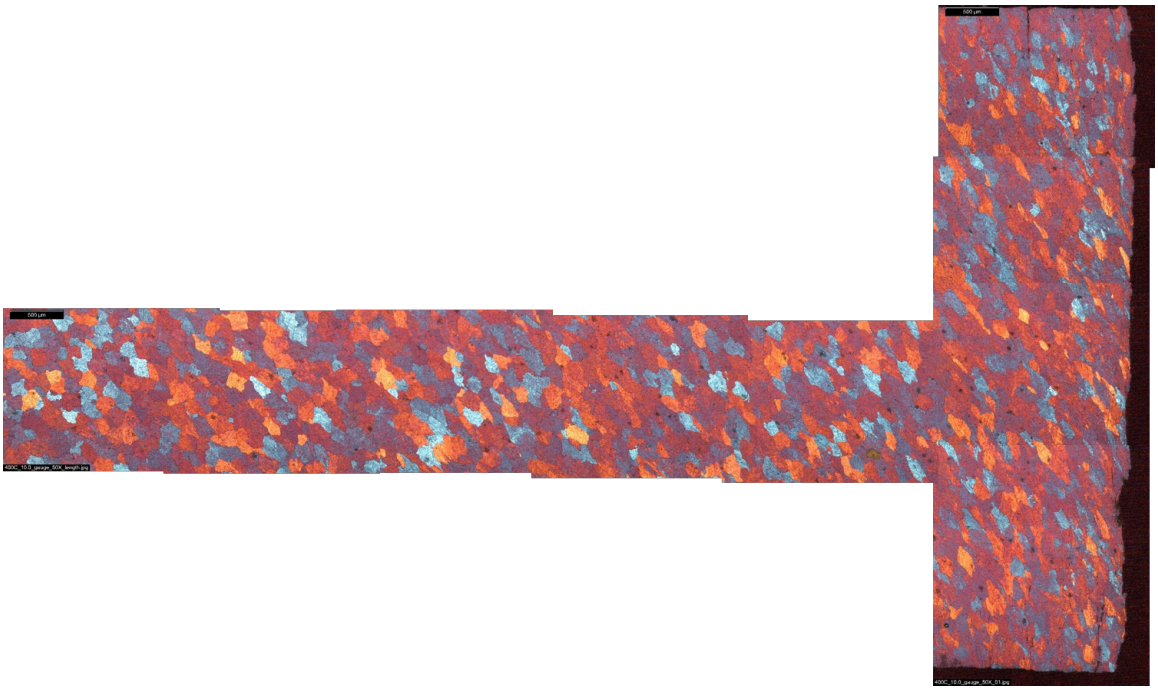

Figure 155: Polarized light micrographs (50X) showing the fracture surface and microstructure into the gauge of the torsion sample deformed at 400°C and 10.0/s.

Figure 156: Polarized light micrographs (50X) showing the fracture surface and microstructure into the gauge of the torsion sample deformed at 450°C and 0.01/s.

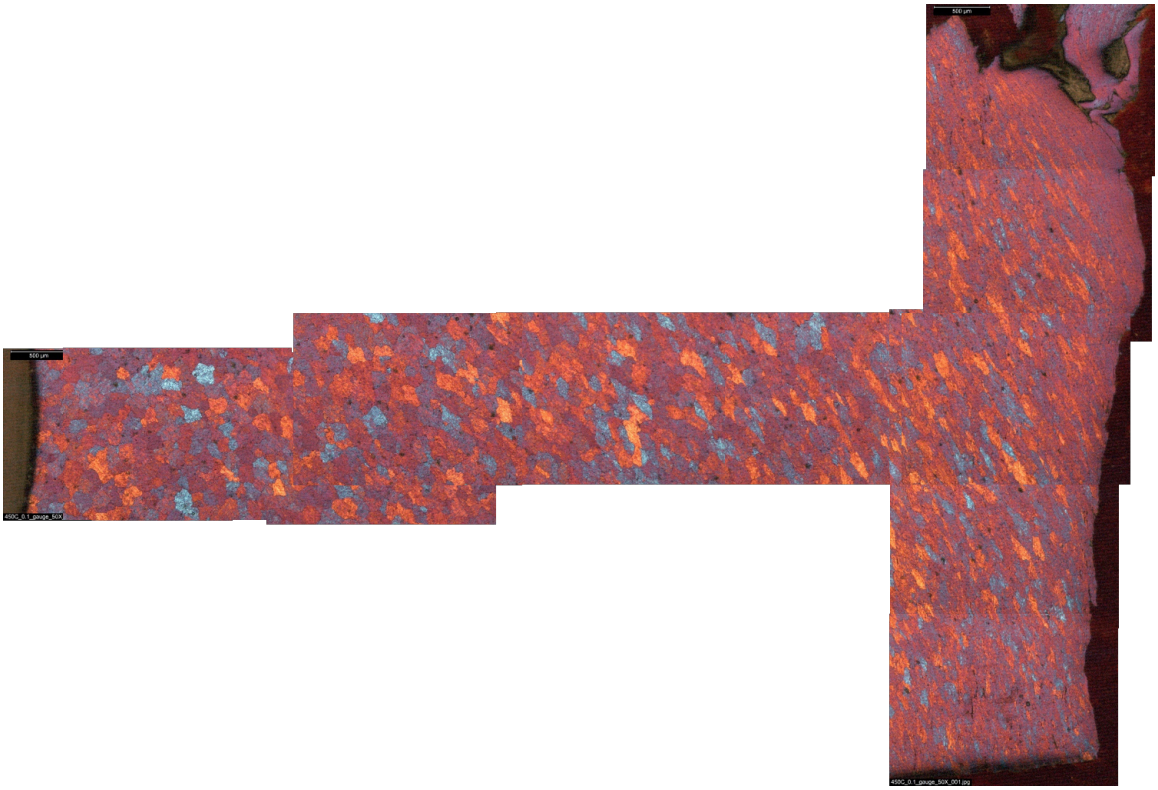

Figure 157: Polarized light micrographs (50X) showing the fracture surface and microstructure into the gauge of the torsion sample deformed at 450°C and 0.1/s.

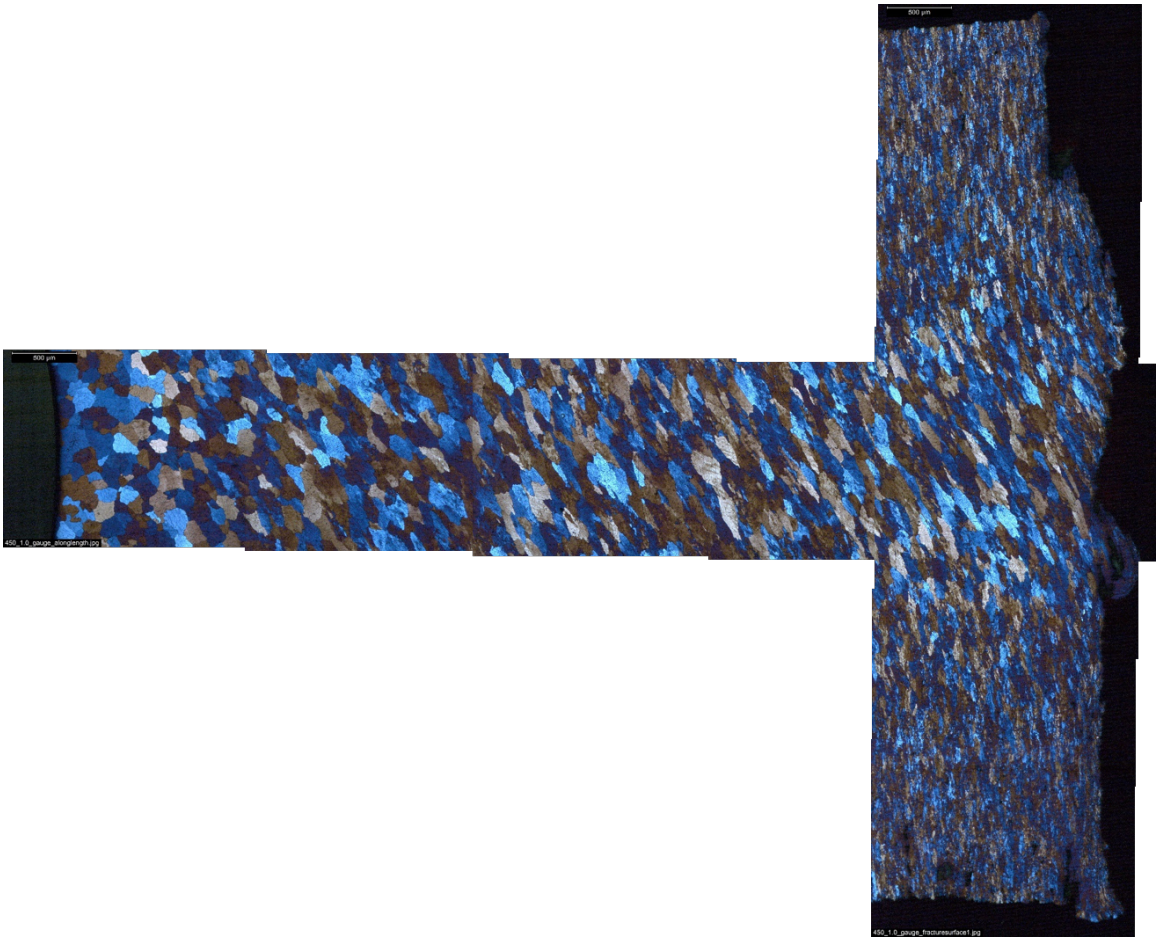

Figure 158: Polarized light micrographs (50X) showing the fracture surface and microstructure into the gauge of the torsion sample deformed at 450°C and 1.0/s.

Figure 159: Polarized light micrographs (50X) showing the fracture surface and microstructure into the gauge of the torsion sample deformed at 450°C and 10.0/s.

Figure 160: Polarized light micrographs (50X) showing the fracture surface and microstructure into the gauge of the torsion sample deformed at 500°C and 0.1/s.

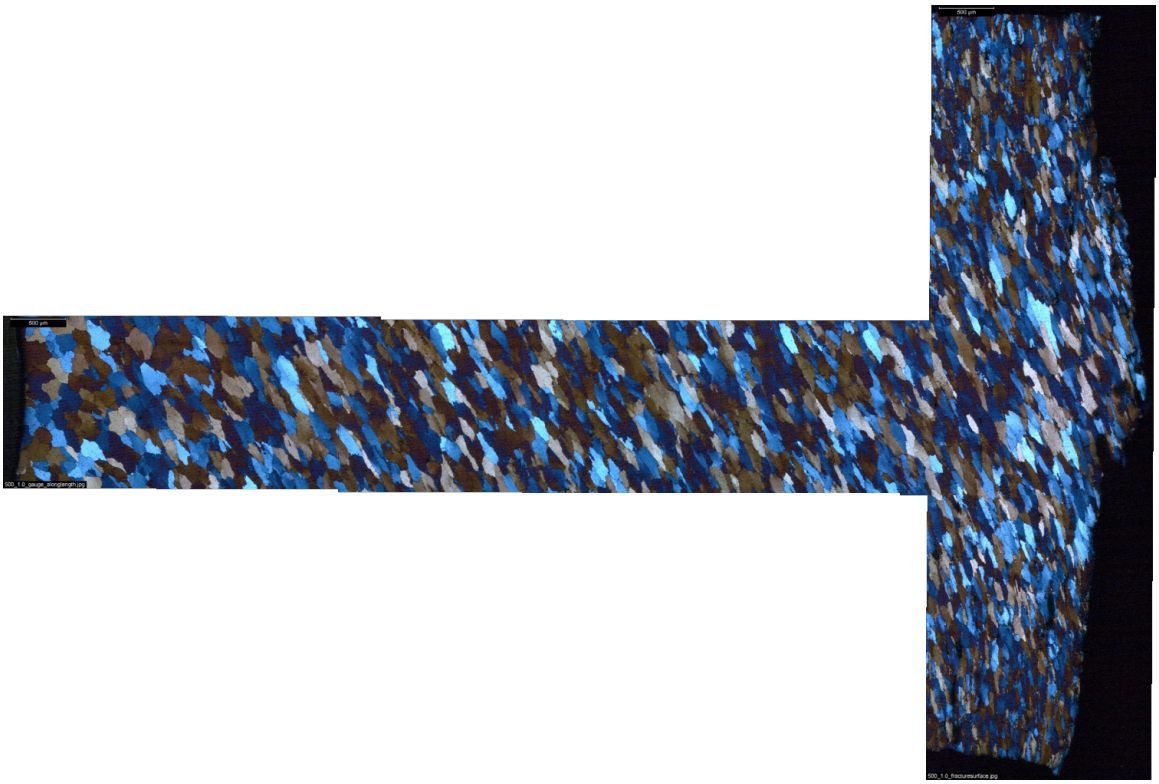

Figure 161: Polarized light micrographs (50X) showing the fracture surface and microstructure into the gauge of the torsion sample deformed at 500°C and 1.0/s.

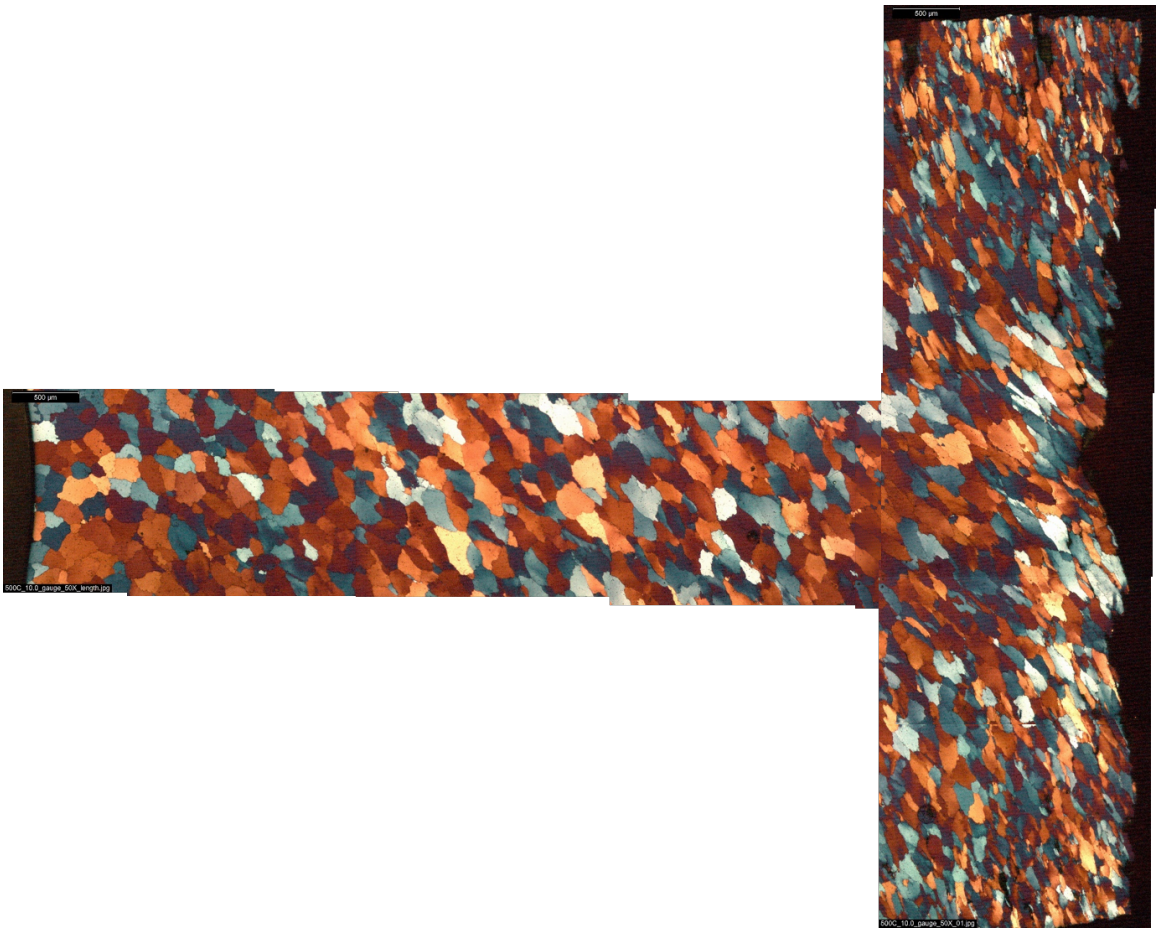

Figure 162: Polarized light micrographs (50X) showing the fracture surface and microstructure into the gauge of the torsion sample deformed at 500°C and 10.0/s.

Bibliography

[1] Gayle, F. W. and Goodway, M., "Precipitation Hardening in the First Aerospace Aluminum Alloy : The Wright Flyer Crankcase," *Science*, vol. 266, pp. 1015–1017, 1994.

[2] The Aluminum Association, "Aircraft and Aerospace," 2014.

[3] Bois-Brochu, A., Blais, C., Tchitembo Goma, F. A., and Larouche, D., "Modelling of Anisotropy for Al-Li 2099 T83 Extrusions and Effect of Precipitate Density," *Mater. Sci. Eng. A*, vol. 673, pp. 581–586, 2016.

[4] Giummarra, C., Thomas, B., and Rioja, R., "New Aluminum Lithium Alloys for Aerospace Applications," in *Proc. Light Met. Technol. Conf.*, 2007.

[5] Rioja, R. J. and Liu, J., "The Evolution of Al-Li Base Products for Aerospace and Space Applications," *Metall. Mater. Trans. A Phys. Metall. Mater. Sci.*, vol. 43, no. 9, pp. 3325–3337, 2012.

[6] Starke, E. A., "Historical Development and Present Status of Aluminum-Lithium Alloys," in *Aluminum-Lithium Alloy. Process. Prop. Appl.* (Prasad, N. E., Gokhale, A. A., and Wanhill, R. J. H., eds.), ch. 1, pp. 3–26, 2014.

[7] The Aluminum Association Inc., "International Alloy Designations and Chemical Composition Limits for Wrought Aluminum and Wrought Aluminum Alloys," 2015.

[8] Armanie, K. P., Rioja, R. J., Denzer, D. K., Brooks, C. E., Gadbery, D. K., and Newell, R., "Extrusion of Aluminum-Lithium Alloys," 2000.

[9] Denzer, D. K., Hollingshead, P., Liu, J., Armanie, K., and Rioja, R., "Texture and Properties of 2090, 8090, and 7050 Extruded Products," *Aluminium-Lithium*, vol. 2, p. 903, 1992.

[10] Ringer, S. P., Muddle, B. C., and Polmear, I. J., "Effects of Cold Work on Precipitation in Al-Cu-Mg-(Ag) and Al-Cu-Li-(Mg-Ag) Alloys," *Metall. Mater. Trans. A*, vol. 26, no. July, pp. 1659–1671, 1995.

[11] Rioja, R. J., Cho, A., and Philip, E. B., "Aluminum-Lithium Alloys Having Improved Corrosion Resitance Containing Mg and Zn," 1990.

[12] Kobayashi, K., Ohsaki, S., Kamio, A., and Tsuji, Y., "Effect of Zn Addition on Corrosion Resistance of 2090 and 2091 Alloys," in *Aluminum-Lithium* (Peters, M. and Winkler, P.-J., eds.), pp. 673–678, 1991.

[13] Rioja, R. J., Bowers, J. A., and James, S., "Aluminum-Lithium Alloys and Method of Making the Same," 1991.

[14] Hatch, J., ed., *Aluminum: Properties and Physical Metallurgy.* American Society for Metals, 1984.

[15] Mondolfo, L., *Metallography of Aluminum Alloys.* New York: John Wiley & Sons, Inc., 1943.

[16] Mondolfo, L., *Aluminum Alloys: Structure and Properties*. Butterworths, 1976.

[17] Chen, P. and Bhat, B. N., "Time-Temperature-Precipitation Behavior in An Al-Cu-Li Alloy 2195," tech. rep., NASA, 1998.

[18] Wang, Z. M. and Shenoy, R. N., "Microstructural Characterization of Aluminum-Lithium Alloys 1460 and 2195," Tech. Rep. February, 1998.

[19] Jiang, N., Gao, X., and Zheng, Z.-q., "Microstructure Evolution of Aluminum-Lithium Alloy 2195 Undergoing Commercial Production," *Trans. Nonferrous Met. Soc. China*, vol. 20, pp. 740–745, may 2010.

[20] Chen, P. S. and Bhat, B. N., "Time-Temperature-Precipitation Behavior in Al-Li Alloy 2195," 2002.

[21] Khushaim, M., Boll, T., Seibert, J., Haider, F., and Al-kassab, T., "Characterization of Precipitation in Al-Li Alloy AA2195 by Means of Atom Probe Tomography and Transmission Electron Microscopy," pp. 1–26, 2015.

[22] Wang, S. C. and Starink, M. J., "Precipitates and Intermetallic Phases in Precipitation Hardening AlCuMg(Li) Based Alloys," *Int. Mater. Rev.*, vol. 50, no. 4, pp. 193–215, 2005.

[23] Hardy, H. and Silcock, J., "The Phase Sections at 500 and 350C of Aluminium-Rich Aluminium-Copper-Lithium Alloys," *J. Inst. Met.*, vol. 84, pp. 423–428, 1955.

[24] Kim, N. J. and Lee, E. W., "Effect of T1 Precipitate on the Anisotropy of Al-Li Alloy 2090," *Acta Met. Mater.*, vol. 41, no. 3, pp. 941–948, 1993.

[25] Jata, K. V., Panchanadeeswaran, S., and Vasudevan, A. K., "Evolution of Texture, Microstructure and Mechanical Property Anisotropy in an Al-Li-Cu Alloy," *Mater. Sci. Eng.*, vol. A257, pp. 37–46, 1998.

[26] Ludwiczak, E. and Rioja, R., "Nucleation Sites of the T2 Phase in Alloy 2090," *J. Mater. Sci.*, vol. 27, pp. 4842–4846, 1992.

[27] Vecchio, K. S. and Williams, D. B., "The Apparent 'Five-Fold ' Nature of Large T2 (Al6Li3Cu) Crystals," *Metall. Trans. A*, vol. 19A, pp. 2876–2884, 1988.

[28] Chen, S.-w., Chuang, Y.-y., Chang, Y. A., and Chu, M. E. N. G., "Calculation of Phase Diagrams and Solidification Paths of Al-Rich Al-Li-Cu Alloys," *Metall. Trans. A*, vol. 22, no. December, pp. 2837–2848, 1991.

[29] Itoh, G., Cui, Q., and Kanno, M., "Effects of a Small Addition of Magnesium and Silver on the Precipitation of T1 phase in an Al-4%Cu-1.1%Li-0.2%Zr Alloy," *Mater. Sci. Eng. A*, vol. 211, no. 1-2, pp. 128–137, 1996.

[30] Dorin, T., Deschamps, A., De Geuser, F., Lefebvre, W., and Sigli, C., "Quantitative Description of the T1 Formation Kinetics in an AlCuLi Alloy Using Differential Scanning Calorimetry, Small-Angle X-ray Scattering and Transmission Electron Microscopy," *Philos. Mag.*, vol. 94, pp. 1012–1030, feb 2014.

[31] Deschamps, A., Decreus, B., De Geuser, F., Dorin, T., and Weyland, M., "The Influence of Precipitation on Plastic Deformation of AlCuLi Alloys," *Acta Mater.*, vol. 61, no. 11, pp. 4010–4021, 2013.

[32] Bois-Brochu, A., Blais, C., Goma, F. A. T., Larouche, D., Boselli, J., and Brochu, M., "Characterization of Al-Li 2099 Extrusions and the Influence of Fiber Texture on the Anisotropy of Static Mechanical Properties," *Mater. Sci. Eng. A*, vol. 597, pp. 62–69, 2014.

[33] Quist, W. and Narayanan, G., "Aluminum-Lithium Alloys," in *Alum. Alloy. - Contemp. Res. Appl.* (Vasudevan, A. and Doherty, R., eds.), p. 219, Academic Press, 1989.

[34] Dorin, T., De Geuser, F., Lefebvre, W., Sigli, C., and Deschamps, A., "Strengthening Mechanisms of T1 Precipitates and Their Influence on the Plasticity of an AlCuLi Alloy," *Mater. Sci. Eng. A*, vol. 605, pp. 119–126, may 2014.

[35] Crooks, R. E., *The Influence of Microstructure on the Ductility of an Aluminum-Copper-Lithium-Magnesium-Zirconium Alloy.* Phd thesis, Georgia Institute of Technology, 1982.

[36] Dorin, T., Deschamps, A., Geuser, F. D., and Sigli, C., "Quantification and Modelling of the Microstructure/Strength Relationship by Tailoring the Morphological Parameters of the T1 Phase in an AlCuLi Alloy," *Acta Mater.*, vol. 75, pp. 134–146, aug 2014.

[37] Wert, J. and Starke, E. J., "Processing and Properties of Advanced Aluminum Alloys," 1989.

[38] Flower, H. M. and Gregson, P. J., "Critical Assessment Solid State Phase Transformations in Aluminium Alloys Containing Lithium," *Mater. Sci. Technol.*, vol. 3, pp. 81–90, 1987.

[39] McAlister, A., "The Al-Li (Aluminum-Lithium) System," in *Bull. Alloy Phase Diagrams*, vol. 3, pp. 177–183, 1982.

[40] Sanders Jr., T. H., A.F. Grandt, J., Hillberry, B., Fragomeni, J., Henkener, J., Kistler, G., McKeighan, P., Pegram, J., Sater, J., and Valentine, M., "An Extrusion Program Designed to Relate Processing Parameters to Microstructure and Properties of an Al-Li-Zr Alloy," in *Proc. Fifth Int. Aluminum-Lithium Conf.*, pp. 273–285, 1989.

[41] Ploetz, J. C., *The Effects of Extrusion Parameters and Composition on the Microstructure and Mechanical Properties of Al-Li-Mg-Cu-Zr Alloys.* PhD thesis, Purdue University, 1987.

[42] Jha, S. C., Jr, T. H. S., Dayananda, M. A., and Lafayette, W., "Grain Boundary Precipitate Zones in Al-Li Alloys," *Acta Met.*, vol. 35, 1987.

[43] Jensrud, O. L. A. and Ryum, N., "The Development of Microstructures in Al-Li Alloys," *Mater. Sci. Eng.*, vol. 64, pp. 229–236, 1984.

[44] Williams, D. and Edington, J., "The Discontinuous Precipitation Reaction in Dilute Al-Li Alloys," *Acta Metall.*, vol. 24, no. 4, pp. 323–332, 1976.

[45] Gu, B. P., Liedl, G. L., Sanders Jr., T. H., and Welpmann, K., "The Influence of Zirconium on the Coarsening of \delta' (Al_3Li) in an Al-2.8 wt.% Li-0.14 wt.% Zr Alloy," *Mater. Sci. Eng.*, vol. 76, pp. 147–157, 1985.

[46] Palmer, I. G., Lewis, R., and Crooks, D., "The Design and Mechanical Properties of Rapidly Solidified Al-Li-X Alloys," in *Aluminum-Lithium Alloy.* (Sanders Jr., T. and Starke Jr., E. A., eds.), (Stone Mountain, GA, USA), 1980.

[47] Ringer, S. P. and Hono, K., "Microstructural Evolution and Age Hardening in Aluminium Alloys: Atom Probe Field-Ion Microscopy and Transmission Electron Microscopy Studies," *Mater. Charact.*, no. 44, pp. 101–131, 2000.

[48] Srivatsan, T., Coyne Jr., E., and Starke Jr., E. A., "Microstructural Characterization of Two Lithium-Containing Aluminium Alloys," *J. Mater. Sci.*, vol. 21, pp. 1553–1560, 1986.

[49] Wolverton, C. and Ozoliš, V., "Entropically Favored Ordering: The Metallurgy of Al2Cu Revisited," *Phys. Rev. Lett.*, vol. 86, pp. 5518–5521, jun 2001.

[50] Ringer, S. P., Hono, K., Polmear, I. J., and Sakurai, T., "Nucleation of Precipitates in Aged Al-Cu-Mg-(Ag) Alloys with High Cu:Mg Ratios," *Acta mater.*, vol. 44, no. 5, pp. 1883–1898, 1996.

[51] Ratchev, P., Verlinden, B., and Houtte, P. V., "S' Phase Precipitation in Al-4wt.%Mg-1wt.%Cu Alloy," *Scr. Metall. Mater.*, vol. 30, pp. 599–604, 1994.

[52] Jena, A. K., Gupta, A., and Chaturvedi, M. C., "A Differential Scanning Calorimetric Investigation of Precipitation Kinetics in the Al-1.53wt%Cu-0.79wt%Mg Alloy," *Acta Met.*, vol. 37, no. 3, pp. 885–895, 1989.

[53] Gregson, P. J., Flower, H. M., Tite, C. N. J., and Mukhopadhyay, A. K., "Role of Vacancies in Coprecipitation of \delta' and S-phases in Al-Li-Cu-Mg Alloys," *Mater. Sci. Technol.*, vol. 2, pp. 349–353, 1986.

[54] Gregson, P. J. and Flower, H. M., "Microstructural Aluminium-Lithium of Toughness Alloys," *Acta Met.*, vol. 33, 1985.

[55] Wert, J. and Wycliffe, P., "Correlation Between S' Precipitation and the Portevin-Le Chatelier Effect in an Al-Li-Cu-Mg-Zr Alloy," *Scr. Metall.*, vol. 19, pp. 463–466, 1985.

[56] Park, J. K. and Ardell, A. J., "Microstructures of the Commercial 7075 Al Alloy in the T651 and T7 Tempers," *Metall. Trans. A*, vol. 14, no. 10, pp. 1957–1965, 1983.

[57] Mukhopdahyay, A., "Microstructure and Properties of High Strength Aluminium Alloys for Structural Applications," *Trans. Indian Inst. Met.*, vol. 62, pp. 113–122, 2009.

[58] Li, X. Z., Hansen, V., Gjénnes, J., and Wallenberg, L. R., "HREM Study and Structure Modeling of the eta' Phase. the Hardening Precipitate in Commercial Al-Zn-Mg Alloys," *Acta Metall.*, vol. 47, pp. 2651–2659, 1999.

[59] Lendvai, J., "Precipitation and Strengthening in Aluminium Alloys," *Mater. Sci. Forum*, vol. 217-222, pp. 43–56, 1996.

[60] Lamb, J., *Decomposition and Its Effects on Mechanical Properties in Al-Zn-Mg-Cu Alloys*. PhD thesis, Georgia Institute of Technology, 2015.

[61] Cogan, S. F., Gayle, F. W., Klein, J. D., Cocks, F. H., and Shepard, M. L., "Extraction and X-Ray Analysis of Phases in Aluminium Alloys," *J. Mater. Sci.*, vol. 13, pp. 2687–2691, 1978.

[62] Wert, J. A., "Identification of Precipitates in 7075 Al After High-Temperature Aging," *Scr. Metall.*, vol. 15, pp. 445–447, 1981.

[63] Martin, J., Doherty, R., and Cantor, B., *Stability of Microstructures in Metallic Systems*. New York: Cambridge University Press, 2nd ed., 1997.

[64] Sellars, M. and Whiteman, J. A., "Recrystallization and Grain Growth in Hot Rolling," *Met. Sci.*, no. April, 1979.

[65] Sweet, E. D., Caraher, S. K., Danilova, N. V., Zhang, X., and Limited, C. A., "Effects of Extrusion Parameters on Coarse Grain Surface Layer in 6xxx Series Extrusions," *Proc. 8th Alum. Extrus. Technol. Semin.*, pp. 115–126, 2004.

[66] Jata, K., a.K. Hopkins, and Rioja, R., "The Anisotropy and Texture of Al-Li Alloys," *Mater. Sci. Forum*, vol. 217-222, pp. 647–652, 1996.

[67] Sanders Jr., T. H., "Factors Influencing Fracture Toughness and Other Properties of Aluminum - Lithium Alloys," tech. rep., Alcoa Laboratories, 1979.

[68] Xu, Y., Zhong, W., Chen, Y., Shen, L., Liu, Q., Bai, Y., and Meyers, M., "Shear Localization and Recrystallization in Dynamic Deformation of 8090 AlLi Alloy," *Mater. Sci. Eng. A*, vol. 299, pp. 287–295, feb 2001.

[69] Lucke, K. and Engler, O., "Effects of Particles on Development of Microstructure and Texture During Rolling and Recrystallisation in FCC Alloys," *Mater. Sci. Technol.*, vol. 6, pp. 1113–1130, 1990.

[70] Engler, O., Hirsch, J., and Lucke, K., "Texture Dvelopment in Al 1.8 wt.% Cu Depending on the Precipitation State–I. Rolling Textures," *Acta Met.*, vol. 37, no. 10, 1989.

[71] Humphreys, F., "Lattice Rotations at Second Phase Particles in Deformed Metals," *Acta Metall.*, vol. 27, pp. 1801–1814, 1979.

[72] Humphreys, F., "A Unified Theory of Recovery, Recrystallization and Grain Growth, Based on the Stability and Growth of Cellular Microstructures- II. The Effect of Second Phase Particles," *Acta mater.*, vol. 45, no. 12, pp. 5031–5039, 1997.

[73] Humphreys, F. and Kalu, P., "Dislocation-Particle Interactions During High Temperature Deformation of Two-Phase Aluminium Alloys," *Acta Met.*, vol. 35, no. 12, pp. 2815–2829, 1987.

[74] Humphreys, F., "The Nucleation of Recrystallization at Second Phase Particles in Deformed Aluminum," *Acta Metall.*, vol. 25, pp. 1323–1344, 1977.

[75] Humphreys, F., "The Interaction of Dislocations with Hard Particles," in *Micromechanisms Plast. Fract.* (Lewis, M. and Taplin, D., eds.), pp. 1–37, Dublin: Parsons Press, 1983.

[76] Engler, O., Heckelmann, I., Rickert, T., Hirsch, J., and Lücke, K., "Effect of pretreatment and texture on recovery and recrystallisation in Al4·5Mg0·7Mn alloy," *Mater. Sci. Technol.*, vol. 10, no. 9, pp. 771–782, 1994.

[77] "Alloy Phase Diagrams," in *ASM Handb.* (Baker, H., ed.), ASM International, 1992.

[78] Last, H., *Precipitation of Dispersoids in Aluminum Alloys.* PhD thesis, Georgia Institute of Technology, 1991.

[79] Suresh, S., Vasudevan, A., Tosten, M., and Howell, P., "Microscopic and Macroscopic Aspects of Fracture in Lithium-Containing Aluminum Alloys," *Acta Metall.*, vol. 35, pp. 25–46, jan 1987.

[80] Ivanov, R., *The Effects of Friction Stir Welding on the Mechanical Properties and Microstructure of a Third Generation Al-Cu-Li.* PhD thesis, McGill University, 2012.

[81] Srivatsan, T. S., "The Influence of Processing on the Microstructure of an Aluminum-Lithium Alloy," *Mater. Lett.*, vol. 4, no. 4, pp. 201–206, 1986.

[82] Backofen, W., *Deformation Processing.* Addison-Wesley Publishing Company, 1972.

[83] Laue, K. and Stenger, H., *Extrusion: Processes, Machinery, Tooling.* American Society for Metals, 1981.

[84] Bauser, M., Sauer, G., and Siegert, K., eds., *Extrusion.* Materials Park, Ohio: ASM International, 2nd ed., 2006.

[85] Saha, P. K., *Aluminum Extrusion Technology.* Materials Park, Ohio: ASM International, 2000.

[86] Sheppard, T., *Extrusion of Alumunium Alloys.* Kluwer Academic Publishers, 1999.

[87] Feltham, P., "Extrusion of Metals," *Met. Treat. Drop Forg.*, vol. 23, pp. 440–444, 1956.

[88] Bastani, A. F., *Modelling of the Flow and Temperature Evolution in Aluminium Extrusion.* PhD thesis, University of Oslo, 2010.

[89] Sheppard, T., "Temperature and Speed Effects in Hot Extrusion of Aluminium Alloys," *Met. Technol.*, 1981.

[90] Sheppard, T. and Wood, E. P., "Effect of Section Geometry on Extrudability of Al-Cu-Mn Alloy," *Met. Technol.*, vol. 7, no. February, pp. 58–66, 1980.

[91] Sheppard, T., Tunnicliffe, P. J., Patterson, S. J., and Summary, I., "Direct and Indirect Extrusion of a High Strength Aerospace Alloy (AA 7075)," *J. Mech. Work. Technol.*, vol. 6, pp. 313–331, 1982.

[92] Sheppard, T. and Paterson, S. J., "Some Observations on Metal Flow and the Development of Structure During the Direct and Indirect Extrusion of Comercial Purity Aluminum," *J. Mech. Work. Technol.*, vol. 7, pp. 39–56, 1982.

[93] Sellars, C. M. and Tegart, W. J. M., "Hot Workability," *Int. Metall.*, vol. 17, pp. 1–24, jan 1972.

[94] Engler, O. and Randle, V., *Introduction to Texture Analysis: Macrotexture, Microtexture, and Orientation Mapping*. CRC Press, 2nd ed., 2010.

[95] Mecking, H., "Textures in Metals," in *Prefer. Orientations Deform. Met. Rocks An Introd. to Mod. Texture Anal.* (Wenk, H., ed.), pp. 267–306, 1985.

[96] Chirsch, J. and Lucke, K., "Interpretation of the Copper-Brass Texture Transition by Quantitative ODF Analysis," in *Prefer. Orientations Deform. Met. Rocks An Introd. to Mod. Texture Anal.* (Wenk, H., ed.), pp. 307–315, 1985.

[97] Hales, S. and Hafley, R., "Texture and Anisotropy in Al-Li Alloy 2195 Plate and Near-Net-Shape Extrusions," *Mater. Sci. Eng. A*, vol. 257, no. 1, pp. 153–164, 1998.

[98] Tempus, G., Calles, W., and Scharf, G., "Influence of Extrusion Process Parameters and Texture on Mechanical Properties of Al-Li Extrusions," *Mater. Sci. Technol.*, vol. 7, 1991.

[99] Hirsch, J. and Lucke, K., "Description and Presentation Methods for Textures," *Texture and Microtextures*, vol. 8 & 9, pp. 131–151, 1988.

[100] Kocks, U., Tome, C. N., and Wenk, H., *Texture and Anisotropy: Preferred Orientations in Polycrystals and their Effect on Materials Properties*. Cambridge University Press, 2000.

[101] Sanders Jr., T. H., "Development of Structure and Properties of 7050 and 7475 Alloys During Direct Extrusion," 1981.

[102] Bois-Brochu, A., Goma, F., Blais, C., Larouche, D., Gauvin, R., and Boselli, J., "Al-Li Alloy 2099-T83 Extrusions: Static Mechanical Properties, Microstructure and Texture," *Adv. Mater. Res.*, vol. 409, nov 2012.

[103] Witters, J. J., Cheney, B. A., and Rioja, R. J., "Low Aspect Ratio Lithium-Containing Aluminum Extrusions," 1992.

[104] Tempus, G., Scharf, G., and Calles, W., "Influence of Extrusion Process Parameters on the Mechanical Properties of Al-Li Extrusions," *J. Phys.*, vol. 48, 1987.

[105] Vasudevan, A., Przystupa, M., and Fricke, W.G., J., "Texture-Microstructure Effects in Yield Strength Anisotropy of 2090 Sheet Alloy," *Scr. Metall. Mater.*, vol. 24, 1990.

[106] Crooks, R., Wang, Z., Levit, V. I., and Shenoy, R. N., "Microtexture, Microstructure and Plastic Anisotropy of AA2195," *Mater. Sci. Eng.*, vol. A257, pp. 145–152, 1998.

[107] Dorward, R. C., "Zirconium vs Manganese-Chromium for Grain Structure Control in an Al-Cu-Li Alloy," *Metall. Trans. A*, vol. 18, no. 10, pp. 1820–1823, 1987.

[108] Vasudevan, A. K., Fricke, W. G. J., Malcom, R. C., Bucci, R. J., Pryzystupa, M. A., and Barlat, F., "On Through Thickness Crystallographic Texture Gradient in Al-Li-Cu-Zr Alloy," *Metall. Trans. A*, vol. 19, 1988.

[109] Trinca, M., Avalino, A., Garmestani, H., Foyos, J., Lee, E., and Es-Said, O., "Effect of Rolling Orientation on the Mechanical Properties and Crystallographic Texture of 2195 Aluminum - Lithium Alloy," *Mater. Sci. Forum*, vol. 331-337, pp. 849–854, 2000.

[110] Rioja, R. J., "Fabrication Methods to Manufacture Isotropic Al-Li alloys and Products for Space and Aerospace Applications," *Mater. Sci. Eng. A*, vol. 257, pp. 100–107, nov 1998.

[111] Rodgers, B. I. and Prangnell, P. B., "Quantification of the Influence of Increased Pre-Stretching on Microstructure-Strength Relationships in the Al-Cu-Li Alloy AA2195," *Acta Mater.*, vol. 108, no. June, pp. 55–67, 2016.

[112] Arehart, T., Timko, M., Yao, T., Wilkins, K., and London, B., *A Process Development Study on Reducing the Anisotropy while Maintaining the Strength of Extruded Aluminum Alloys 2195 through Heat Treatment.* Undergraduate senior thesis, California Polytechnic State University, 2014.

[113] Rollet, A. and Wright, S., "Typical Texture in Metals," in *Texture Anisotropy Prefer. Orientations Polycrystals their Eff. Mater. Prop.* (Kocks, U., Tome, C., and Wenk, H., eds.), ch. 5, pp. 179–238, 2000.

[114] Bastani, A. F., Aukrust, T., and Brandal, S., "Study of Isothermal Extrusion of Aluminum Using Finite Element Simulations," *Int J Mater Form*, vol. 3, pp. 367–370, 2010.

[115] Zhou, J., Li, L., and Duszczyk, J., "3D FEM Simulation of the Whole Cycle of Aluminium Extrusion Throughout the Transient State and the Steady State Using the Updated Lagrangian Approach," *J. Mater. Process. Technol.*, vol. 134, no. 3, pp. 383–397, 2003.

[116] Niu, L. J., Velay, X., and Sheppard, T., "On Material Flow and Aspects of Structural Modification During Direct and Indirect Extrusion of Alumnium Alloy," *Mater. Sci. Technol.*, vol. 28, pp. 397–405, apr 2012.

[117] Kloppenborg, T., Schwane, M., Ben Khalifa, N., Tekkaya, a. E., and Brosius, A., "Experimental and Numerical Analysis of Material Flow in Porthole Die Extrusion," *Key Eng. Mater.*, vol. 491, pp. 97–104, sep 2011.

[118] Chen, H., Zhao, G. Q., Zhang, C. S., and Liu, J. W., "Effects of Welding Chamber Step on Extrusion Process of a Complex Hollow Profile," *Adv. Mater. Res.*, vol. 148-149, pp. 1684–1688, oct 2010.

[119] Zhang, C. S., Zhao, G. Q., Chen, H., and Wang, H., "Numerical Simulation and Die Optimal Design of a Complex Section Thin-Walled Aluminum Profile Extrusion," *Adv. Mater. Res.*, vol. 148-149, pp. 195–199, oct 2010.

[120] Ammu, V. N. S. U. V., Mahendiran, P., Wasnik, S., Rao, K. V. R., and Mukhopadhyay, J., "Optimization of Bearing Lengths for Controlled Material Flow in a Flat Die Aluminium Extrusion," in *Alum. Extruder's Counc.*, (Pune, India), pp. 1–6, 2011.

[121] Farjad Bastani, A., Aukrust, T., and Skauvik, I., "Study of Flow Balance and Temperature Evolution over Multiple Aluminum Extrusion Press Cycles with HyperXtrude 9.0," *Key Eng. Mater.*, vol. 424, pp. 257–264, 2009.

[122] Kumar, S. and Vijay, P., "Die Design and Experiments for Shaped Extrusion Under Cold and Hot Condition," *J. Mater. Process. Technol.*, vol. 190, pp. 375–381, jul 2007.

[123] Kloppenborg, T., Brosius, A., and Erman Tekkaya, A., "Numerical Material Flow Optimization of a Multi-Hole Extrusion Process," *Adv. Mater. Res.*, vol. 83-86, pp. 826–833, dec 2009.

[124] Valberg, H., "Metal Flow in the Direct Axisymmetric Extrusion of Aluminium," *J. Mater. Process. Tech.*, vol. 31, no. 1-2, pp. 39–55, 1992.

[125] Parkar, A. A., "On Modelling and Experimental Validation of Extrusion Process of Lightweight Alloys," 2011.

[126] Parkar, A., Bouvard, C., Marin, E., Wang, P., and Horstemeyer, M., "Comprehensive Thermo-Mechanical Validation of Extrusion Simulation Cycle for Al 1100 Using HyperXtrude," in *TMS 2011*, vol. 2, pp. 229–236, 2011.

[127] Farjad Bastani, A., Aukrust, T., and Brandal, S., "Optimisation of Flow Balance and Isothermal Extrusion of Aluminium Using Finite-Element Simulations," *J. Mater. Process. Technol.*, vol. 211, pp. 650–667, apr 2011.

[128] Pinter, T. and El Mehtedi, M., "Constitutive Equations for Hot Extrusion of AA6005A, AA6063 and AA7020 Alloys," *Key Eng. Mater.*, vol. 491, pp. 43–50, sep 2012.

[129] Ockewitz, a., Sun, D., Andrieux, F., and Mueller, S., "Simulation of Hot Extrusion of an Aluminum Alloy with Modeling of Microstructure," *Key Eng. Mater.*, vol. 491, pp. 257–264, sep 2011.

[130] Sheppard, T., *Extrusion of Aluminum Alloys*. Springer Science and Business Media, 1999.

[131] Crosby, K. E., Mirshams, R. A., and Pang, S. S., "Development of Texture and Texture Gradient in Al-Cu-Li (2195) Thick Plate," *J. Mater. Sci.*, vol. 35, 2000.

[132] Bachmann, F., Hielscher, R., and Schaeben, H., "Texture Analysis with MTEX Free and Open Source Software Toolbox," *Solid State Phenom.*, vol. 160, pp. 63–68, feb 2010.

[133] Hielscher, R. and Schaeben, H., "A Novel Pole Figure Inversion Method: Specification of the MTEX Algorithm," *J. Appl. Crystallogr.*, vol. 41, pp. 1024–1037, nov 2008.

[134] Nikolayev, D. I. and Schaben, H., "Characteristics of the Ultrahyperbolic Differential Equation Governing Pole Density Functions," *Inverse Probl.*, vol. 15, pp. 1603–1619, 1999.

[135] Marlaud, T., Deschamps, A., Bley, F., Lefebvre, W., and Baroux, B., "Evolution of Precipitate Microstructures During the Retrogression and Re-Ageing Heat Treatment of an Al-Zn-Mg-Cu Alloy," *Acta Mater.*, vol. 58, no. 14, pp. 4814–4826, 2010.

[136] Barlat, F. and Richmond, O., "Prediction of Tricomponent Plane Stress Yield Surfaces and Associated Flow and Failure Behavior of Strongly Textured F.C.C. Polycrystalline Sheets," *Mater. Sci. Eng.*, vol. 95, pp. 15–29, 1987.

[137] Mackiewicz, A. and Ratajczak, W., "Principal Component Analysis," *Comput. Geosci.*, vol. 19, no. 3, 1993.

[138] Prasad, Y. V. R. K. and Sasidhara, S., eds., *Hot Working Guide: A Compendium of Processing Maps*. ASM International, 1997.

[139] "Calculation of Flow Stress Data for Aluminum Alloys," *HyperXtrude Solver Documentation by Altair Engineering*, 2014.

[140] Li, B., Pan, Q., and Yin, Z., "Characterization of Hot Deformation behavior of As-Homogenized Al-Cu-Li-Sc-Zr Alloy Using Processing Maps," *Mater. Sci. Eng. A*, vol. 614, pp. 199–206, 2014.

[141] Kassner, M. E., Myshlyaev, M. M., and McQueen, H. J., "Large-Strain Torsional Deformation in Aluminum at Elevated Temperatures," *Mater. Sci. Eng.*, no. A108, pp. 45–61, 1989.

[142] Semiatin, S. L. and Altan, T., "Measurement and Interpretation of Flow Stress Data for the Simulation of Metal-Forming Prcoesses," 2010.

[143] Ryan, N. D. and McQueen, H. J., "Flow Stress, Dynamic, Resotoration, Strain Hardening and Ductility in Hot Working of 316 Steel," *J. Mater. Process. Technol.*, no. 21, pp. 177–199, 1990.

[144] Momeni, A., Dehghani, K., Ebrahimi, G. R., and Kazemi, S., "Developing the Processing Maps Using the Hyperbolic Sine Constitutive Equation," *Metall. Mater. Trans. A Phys. Metall. Mater. Sci.*, vol. 44, no. 12, pp. 5567–5576, 2013.

[145] Canova, G. R., Shrivastava, S., Jonas, J. J., and G'Sell, C., "The Use of Torsion Testing to Assess Material Formability," *Formability Met. Mater. - 2000 AD (ASTM STP 753)*, pp. 189–210, 1982.

[146] Mirzadeh, H., "Constitutive Description of 7075 Aluminum Alloy During Hot Deformation by Apparent and Physically-Based Approaches," *J. Mater. Eng. Perform.*, vol. 24, no. 3, pp. 1095–1099, 2015.

[147] Fulop, S., Cadien, K. C., Luton, M. J., and McQueen, H. J., "A Servo-Controlled Hydraulic Hot-Torsion Machine for Hot Working Studies," *J. Test. Evaluation*, 1977.

[148] Flitta, I. and Sheppard, T., "Nature of Friction in Extrusion Process and Its Effect on Material Flow," *Mater. Sci. Technol.*, vol. 19, pp. 837–846, jul 2003.

[149] "Click2Extrude Grain Size," *HyperXtrude Solver Documentation by Altair Engineering*, 2016.

[150] Hallberg, H., Wallin, M., and Ristinmaa, M., "Modeling of Continuous Dynamic Recrystallization in Commercial-Purity Aluminum," *Mater. Sci. Eng. A*, vol. 527, no. 4-5, pp. 1126–1134, 2010.

[151] Hollinshead, P. and Sheppard, T., "Substructure Morphology in Aluminium Alloys AA 3003 and AA 3004," *Mater. Sci. Technol.*, vol. 3, no. 12, pp. 1019–1024, 1987.

[152] Barlat, F., Lege, D. J., and Brem, J. C., "A Six-Component Yield Function for Anisotropic Materials," *Int. J. Plast.*, vol. 7, pp. 693–712, 1991.

[153] Cazacu, O. and Barlat, F., "Application of the Theory of Representation to Describe Yielding of Anisotropic Aluminum Alloys," *Int. J. Eng. Sci.*, vol. 41, no. 12, pp. 1367–1385, 2003.

[154] Honeycombe, R. W. K., *The Plastic Deformation of Metals*. Edwars Arnold Ltd., 1968.

[155] Tome, C. N. and Lebensohn, R. A., "Manual for Code: Visco-Plastic Self-Consistent (VPSC)," tech. rep., Los Alamos National Laboratory, 2012.

[156] Dunst, D. and Mecking, H., "Analysis of Experimental and Theoretical Rolling Textures of Two-Phase Titanium Alloys," *Zeitschrift für Met.*, vol. 87, pp. 498–507, 1996.

[157] Sidor, J. J., Petrov, R. H., and Kestens, L. A. I., "Modeling the Crystallographic Changes in Processing of Al Alloys," *J. Mater. Sci.*, vol. 49, pp. 3529–3540, 2014.

VITA

Judith "Judy" Dickson was born in Fort Benning, Georgia. She attended Pacelli Catholic High School in Columbus, GA. After high school, she attended the University of Central Florida (UCF) in Orlando, Florida where she received a Bachelor of Science in Mechanical Engineering. While at UCF, she had research assistantships at the Florida Solar Energy Center and the Advanced Materials Processing and Analysis Center as well as an internship with Siemens Energy. She then went to the Georgia Institute of Technology in Atlanta, Georgia to pursue a Doctorate in Materials Science and Engineering. As a graduate student, she spent a summer interning at the Universal Alloy Corporation in Canton, GA and a summer as a teaching assistant at Georgia Tech Lorraine in Metz, France. Judy is also an avid rugby player and played with the Atlanta Harlequins Women's Rugby Football Club throughout her time in graduate school.